THE SOLID-SOLID PHASE TRANSITION IN VANADIUM DIOXIDE THIN FILMS: SYNTHESIS, PHYSICS AND APPLICATION

By

Joyeeta Nag

Dissertation

Submitted to the Faculty of the

Graduate School of Vanderbilt University

in partial fulfillment of the requirements

for the degree of

DOCTOR OF PHILOSOPHY

in

Physics

May, 2011

Nashville, Tennessee

Approved:

Professor Richard F. Haglund Jr.

Professor Leonard C. Feldman

Professor Akunuri V. Ramayya

Professor Sokrates T. Pantelides

Professor Sharon M. Weiss

To my family,

They remain an extraordinary source of inspiration and support through all bright and gloomy days.

ACKNOWLEDGEMENTS

First and above all, my heartfelt thanks to Prof. Richard F. Haglund, Jr., I am fortunate to have known and worked with him and have him as my advisor and the chair of my Ph.D. committee. Apart from giving me a chance to work in his group, without which this thesis would have never materialized, he has been a complete teacher. He has taught me to believe in myself, to be aware of my strengths and work hard on my weaknesses, to be an independent researcher, and above all has inspired me each and every day with his own example of extraordinary hard work.

I am also grateful to the other members of my committee -- Profs. Sharon Weiss, Leonard C. Feldman, Akunuri V. Ramayya, and Sokrates Pantelides for their time and useful scientific and career guidance. They were always there for a helpful discussion, and their never-ending inspiration have helped me and my research in various ways. Special thanks to Prof. Weiss and Prof. Pantelides for encouraging me to collaborate with their respective research groups, which has enriched my knowledge and my research work.

Special thanks to my past and present group members who have been close colleagues and friends: For every single day of my life in the past few years, they have supported me, believed in me, encouraged me and rejuvenated me with very lively scientific discussions and otherwise. They were the ones who cheered me up when things did not look promising, which occurs rather more often in a graduate student's life.

Special acknowledgements also to my very close collaborators and friends without whom a lot of the experiments and theory included in this work wouldn't have seen the light of day. Judson Ryckman, Chris Kang and Petr Markov for the Si photonics project, Stephan Pauli of the Synchrotron facility at the Swiss Light Source, Dr. Andrew Payzant and Karren More of Oak Ridge National Laboratory where a large part of this dissertation work was conducted, Dr. Weidong Luo of Lawrence Berkeley National Laboratory for his density functional calculations, Dr. Bin Wang for his help with crystal structure drawing and Felipe Rivera of Brigham Young University for some of the TEMs and Orientation Imaging Microscopy.

Most of my experiments were conducted at the Vanderbilt Institute of Nanoscale Science and Engineering and it would have been absolutely impossible without the technical expertise and logistical support of the entire VINSE faculty including Prof. Anthony Hmelo, Dr. Bo Choi, Dr. Ben Schmidt and Dr. Bob Geil.

I would also like to take this opportunity to thank all my Physics teachers since high school, in college and graduate school who have not only taught the technicalities, but have instilled in me the love for physics and an urge to learn more. Thanks also to Prof. Ken Schriver for motivating me to become a better teacher and helping me to get there.

I am also indebted in many ways to the undergraduate and junior graduate students who worked with me for their summer research or research rotations: Alex Henegar, Michael Hertkorn, Sarah-Ann Claiborne and Ben Wyatt. They have helped in many ways in getting innumerable small things done for this dissertation. Their fresh outlook, energy and enthusiasm always compelled me to come up with new and interesting research ideas. Special thanks to Michael in helping me prepare many figures and schematics with his excellent expertise with Photoshop.

I also thank National Science Foundation for funding my work; without this support, practically none of this work produced here would have been possible.

Finally, I thank my family and friends in India and US for bearing and being with me through best and worst of my moods. I am extraordinarily fortunate to be blessed with a wonderful family to support and just be there for me – when close and when separated by huge distance and time. My family was always there to remind me that life is larger and more beautiful than whatever happens in one's career. They gave me what is the most needed in every graduate student's life --- a vent after a whole day of unfruitful work. They were there when nothing but VO_2 occupied my life and on days when I wanted to think anything but VO_2.

TABLE OF CONTENTS

LIST OF FIGURES

CHAPTER I

INTRODUCTION

ABSTRACT

We introduce vanadium dioxide (VO_2), a binary strongly-correlated metal oxide that changes phase from semiconductor to metal in response to stimuli like temperature, electric field or doping. We discuss the details of its structure and electronic behavior and the physics behind its phase transition, as far as it is understood from theoretical and experimental studies conducted in the last fifty years. We also review the growth processes of VO_2 thin films and nanoparticles, introduce the concept of epitaxy all of which are essential backgrounds for the rest of the dissertation. We end this chapter with a roadmap for the rest of the dissertation.

1.1 MOTIVATION: TECHNOLOGICAL AND SCIENTIFIC SIGNIFICANCE

Vanadium dioxide (VO_2), a strongly correlated oxide with its first-order metal-insulator transition a little above room temperature, has been well-studied over the last fifty years but its complex physics is less than well understood. This "smart" material is technologically very attractive for its thermal switching at 67C, alterable by doping, its ultrafast (~ 100fs) switching abilities when excited by a laser and also its potential for electric-field induced switching. The details of the physics of this phase transition will be discussed in section 1.2. To understand the challenges that this oxide poses, not only its physics, but the challenges involved in fabrication should also be understood. A review of the growth processes commonly employed in making VO_2 is presented in section 1.3.

To take advantage of the huge technological potential that the multifunctionalities of the strongly-correlated materials, such as VO_2, has to offer, three things need to be addressed – 1) most of the applications involve materials in form of thin films, hence the quality of these films, dependence on growth conditions and defects involved in growth are important to know and understand; 2) the physics of the phase transition has to be well-

understood for reliable and consistent device performances, and 3) there has to be an understanding of how to modify the phase transition to suit specific technological needs.

In this dissertation we have addressed these three issues in the following ways. First, epitaxial thin film growth is the single most important factor in attempting to address all of the above stated issues. We have introduced epitaxy in section 1.4 of this chapter. Our efforts at epitaxial growth on various single-crystalline substrates over varied deposition conditions have shown that we can have oriented films in both smooth and nano-structured morphologies with switching hysteretic performances changing accordingly (Chapter 2). These have specific advantages and disadvantages pertaining to specific technological needs for example, integration in devices might need smoother surfaces whereas sensor applications involve higher surface areas, where nanostructured films might be more desirable. We have shown that room-temperature epitaxial films are of smoother morphology and better performance than their high-temperature grown counterparts which should considerably influence the current state-of-the-art (Chapter 3). To address and understand the physics of the coupled phase transition in VO_2, we have independently studied the structural and electronic hystereses. On comparing and correlating their evolution on the temperature (or energy) scale we have found them to be non-congruent (Chapter 4). Note here that epitaxial films help immensely in studying structural transitions.

Tailoring phase transitions to fit specific technological needs is another important aspect that can be done using doping. Doping to achieve specific functionality is a commonly used technique in the semiconductor world, and Chapter 5 is an example showing how doping VO_2 reduces its femtosecond switching threshold. This work not only helps us address the issue of lower fluence (or energy) requirement in case of ultrafast switching, but also helps us understand how the physics of phase transition is being modified. It can also provide insight into tailoring of the switching-off time of VO_2, which is extremely important from both physics and technological aspects.

From the applications perspective, integration of the two technologically very important materials – Si and VO_2 has been demonstrated in chapter 6 to enhance the optical

response of Si-based optoelectronics, ensuring smaller device footprint, lower power consumption and more robust device performances. This hybrid device has the potential for operating at higher speeds than provided by current technology, by utilizing the ultrafast switching of VO_2.

1.2 VANADIUM DIOXIDE : A REVIEW

In strongly correlated electron systems, observed electronic and structural behavior results from the complex interplay between multiple, sometimes competing degrees-of-freedom and as a result these materials exhibit a variety of unusual behaviors, such as high-temperature superconductivity, colossal magnetoresistance, exotic magnetic, charge and orbital ordering, and insulator-to-metal transitions. Vanadium dioxide is a prototype strongly-correlated material that has been widely-studied by theoretical and experimental condensed-matter and materials community for more than half a century.

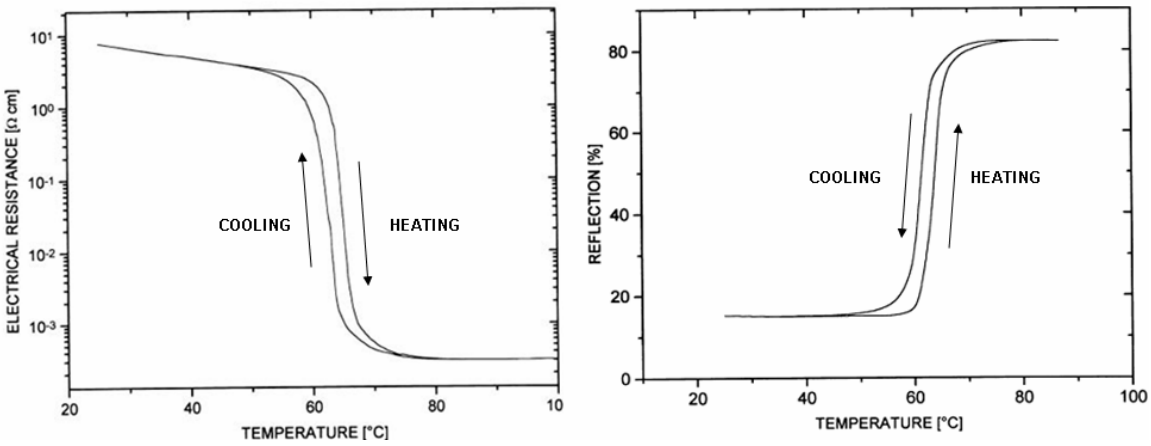

Figure 1.1: Hysteresis curves showing change in resistance (left) and reflection (right) as a function of temperature during phase transition in VO_2.

In 1959, Morin[1] observed that bulk vanadium dioxide crystals exhibit a reversible semiconductor-to-metal transition (SMT) at a critical temperature of about 68^{o}C with change in resistivity and near-infrared transmission spanning several orders of magnitude. Being a transition-metal oxide with narrow *d*-electron bands, this strongly correlated electron system is extremely sensitive to small changes in extrinsic parameters

such as temperature, pressure, or doping. In bulk crystals, the change in resistivity is of order ~10^3-10^5, with a hysteresis width of ~1^{o}C, as seen in figure 1.1. In thin films, on the other hand, hysteresis widths may be in the range of 10^o-15^{o}C, whereas in nanostructures it might be as broad as ~30 – 35^{o}C.

1.2.1 Physical and electronic structure of VO_2

The subtle interplay between atomic structure, charge, spin and orbital dynamics is responsible for the phase transition observed in VO_2. A delicate balance of cooperative interactions of the crystal structure and electronic degrees of freedom drives it into a critical regime where it undergoes a first-order transition from a low-temperature semiconducting phase to a high temperature metallic phase at T_c = 340K. In this case, changes in the electronic band structure are associated with atomic rearrangement between a high-T, more symmetric tetragonal/rutile ($P4_2/mnm$) phase to low-T less symmetric monoclinic ($P2_1/c$) phase due to dimerization of the V atoms.[2] The characteristic feature of this monoclinic phase is the presence of the cation-cation pairs along the $a_m = 2c_r$ axis, leading to the doubling of the unit cell, alternate V-V separations being 2.65Å and 3.12Å rather than the regular 2.87Å spacing in the tetragonal phase (see figure 1.2). This is accompanied by a slight tilting with respect to the c_r-axis to give one shortest vanadium-oxygen separation R_{vo} = 1.76Å perpendicular to the c_r axis, the other cation-anion distances being ~ 2Å. The displacement of a cation toward one or more anions is characteristic of a ferroelectric distortion. Thus the driving mechanism responsible for this transition is an anti-ferroelectric one.

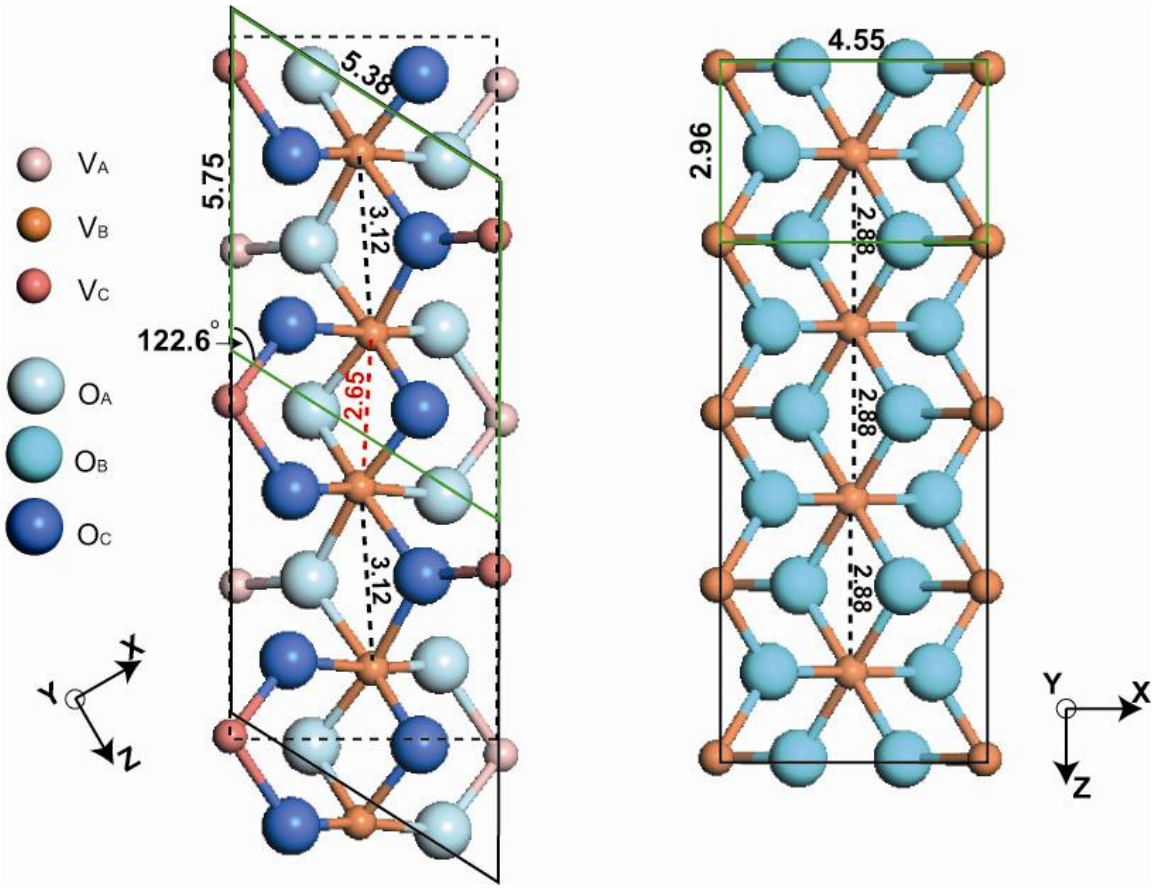

Figure 1.2: Schematic representation of lattices of the two structural phases of VO_2 along directions where their symmetries are most evident. Left: Monoclinic (M1) VO_2. Right: Tetragonal or rutile (R) VO_2. Smaller spheres denote the vanadium ions, which are surrounded by six oxygen ions (bigger spheres). V_B and O_B are atoms in the plane of the paper, whereas V_A, O_A point in to the plane of the paper and V_C, O_C out of the plane of the paper respectively. Unit cells are marked in green. Courtesy: Dr. Bin Wang, Vanderbilt University.

The electronic structure of VO_2 was explained qualitatively long ago by Goodenough.[2] In the rutile structure (space group $P4_2/mnm$), the V atoms are surrounded by O octahedra forming an edge-sharing chain along the *c* axis. The *d*-levels of the V ions are split into lower lying t_{2g} states and e_g states (see figures 1.3 and 1.4). The latter lie higher in energy and are empty. The tetragonal crystal field splits the t_{2g} multiplet into an a_{1g} (d_{II}) state and an e^{π}_g (π^*) doublet. The a_{1g} orbitals are directed along the *c* axis, with strong bonding of the V-V pair along this direction. In the monoclinic phase (space group $P2_1/c$), the dimerization and tilting of the V-V pairs result in two important effects. First, the a_{1g}

band is split into a lower-energy bonding combination and a higher-energy antibonding one. Second, the V_d-O_p antibonding e^{π}_g states are pushed higher in energy, due to the tilting of the pairs increasing the overlap of these states with O states. Thus, in this picture, the single *d* electron occupies the a_{1g}-bonding combination, resulting in a (Peierls-like) band gap.

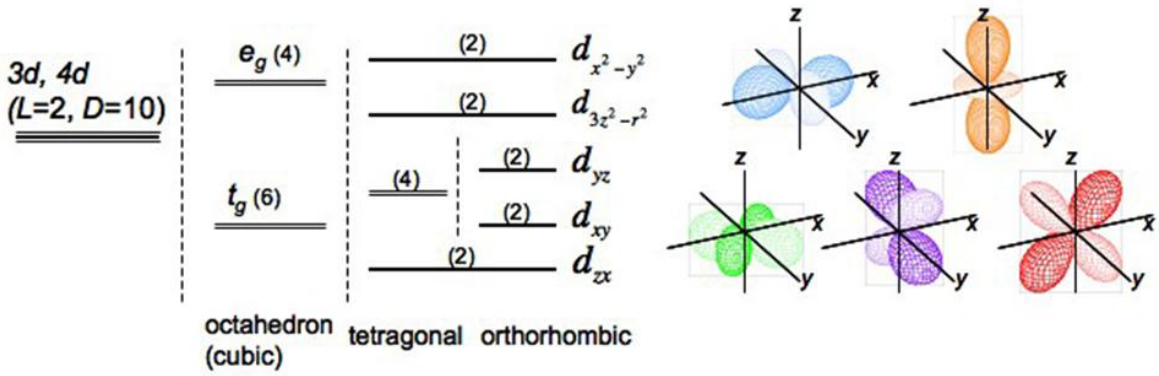

Figure 1.3: d-electron band splitting by crystal fields and their orbitals. The number in the parentheses is the number of degeneracy.[2]

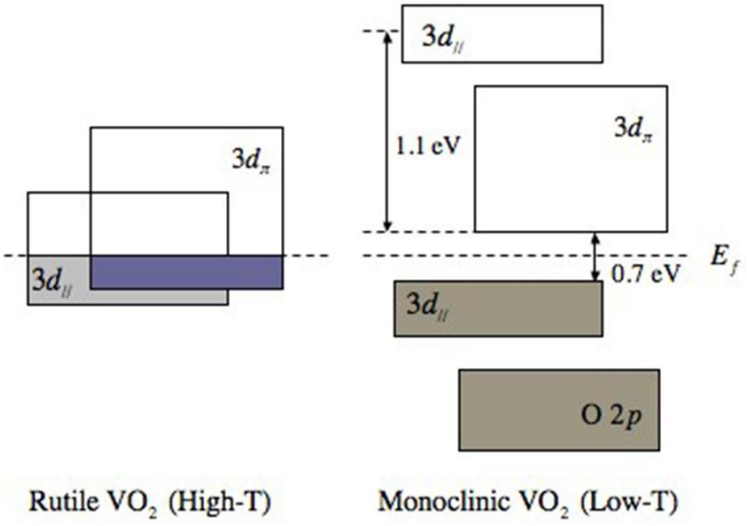

Figure 1.4: Schematic electronic energy bands of VO_2.[2]

1.2.2 Mott *vs* Peierls transition controversy

Whether the structural changes are solely responsible for the insulating nature of the low-*T* phase, or whether correlation effects also play a role, has been a subject of much debate.[3-10] The strong dimerization, as well as the fact that this phase is nonmagnetic,

suggests that VO_2 might be a typical case of a Peierls insulator. However, pioneering experimental work by Pouget *et al*[11, 12] showed that minute amounts of Cr substitutions, as well as uniaxial stress applied to *pure* VO_2 lead to a new phase (M2) in which only half of the V-atoms dimerize, while the other half forms chains of equally spaced atoms behaving as spin-1/2 Heisenberg chains. That this phase is also insulating strongly suggests that the physics of VO_2 is very close to that of a Mott-Hubbard insulator. Zylbersztejn and Mott,[13] Sommers and Doniach,[14] and Rice et al[15] suggested that Coulomb repulsion indeed plays a major role in opening the gap. The table 1.1 below compares and contrasts the Peierls and Mott aspect of this phase transition.

The controversy regarding the driving mechanism of this phase transition still continues unabated as can be seen from the recent works of Tselev et al[16] and Booth et al[17] claiming that the phase transition is purely lattice symmetry-driven, whereas strong evidence is presented in favor of a Mott transition in works of Qazilbash et al[18] and Kim et al.[19]

Table 1.1: Comparison of similarities and differences between the VO_2 SMT and classical metal-insulator mechanisms: a) Peierls mechanism: increased of unit cell opens up a bandgap. (b) Mott-Hubbard Interactions: electron-electron interactions may enhance gap opening.

Features of VO_2 transition	*Peierls Transition*	*Mott-Hubbard Interactions*
consistent with:	○ Doubling of unit cell. ○ Pairing of metal atoms ○ Large lattice transition latent heat	○ Existence of M2 phase ○ Narrowing of *d*-bands ○ Ultrafast phase transition
inconsistent with:	○ Large bandgap (0.7eV) ○ Conductivity jump 10^{-2}-10^{-3} times smaller than experiment ○ $\frac{dT_c}{dP} > 0$	○ Structural change ○ Phonon softening ○ $\frac{dT_c}{dP} > 0$

1.2.3 Applications of VO_2

VO_2 belongs to the class of "smart materials", which generally react to temperature variations, electric or magnetic fields and/or pressure variations and have capabilities of sensing, actuating and switching, relying on an intrinsic property of the material. Thin films and nanoparticles of VO_2 tend to survive the stress generated during repeated cycles of phase transition better than bulk crystals and are therefore suited for many device applications. The large change in resistivity and transmittance/reflectivity during the semiconductor-to-metal (SMT) transition for VO_2 occurs closer to room temperature than any other commonly-known compound and can also be conveniently depressed to about room temperature by doping.[20]

The metal-insulator transition in VO_2 has triggered numerous suggestions and their subsequent realizations for technological applications. These include thermally activated VO_2 thin films and nanoparticles for optical switching[21-23] and beam limiting;[24] resistive switching,[25] thermal relays and energy management devices such as solar cells and smart window coatings; and sensors and actuators.[26-34] It is also being used in optical computing, variable reflectivity mirrors, light modulators, holographic recording media, high-speed solid-state optical displays and in a variety of other modulation, polarization and control functions such as real-time coherent optical data processors and fast, random access scan laser.[35, 36] VO_2 has also been used as the channel layer in field-effect transistors in effort to produce Mott transisitors.[37, 38] VO_2 thin films also have potential applications in the millimeter-wave and microwave portions of the electromagnetic spectrum.[39, 40] Applications for VO_2 nanoparticles, with their plasmonic response in the vicinity of the near-infrared communications wavelengths,[41, 42] ferroelasticity and negative mechanical stiffness,[43] have an even greater range of potential applications that are only beginning to be explored. VO_2 single-crystalline nanobeams have lately opened up a whole new possibility of using switching nanowires with enhanced mechanical strength and stress-resistance.[44] A gas sensor application utilizing the metal-insulator transition in VO_2 has also been realized recently.[45]

1.2.4 Past and recent developments in theory

In case of any strongly correlated oxide, theoretical calculations are complicated by the varied structure, chemistry, defects and impurities present, preventing theorists from accurately capturing the subtle correlation among structure and electronic properties of these materials. In case of VO_2, its monoclinic geometry with pairing and tilting of vanadium atoms complicates any attempt at calculation further. Density functional theory being a 0K theory, by itself cannot predict the bandgap of any system, but electronic structure calculations based on density functional theory within the local density approximation (DFT-LDA) have provided some support for the qualitative description of VO_2 in terms of molecular orbitals.[46] Molecular dynamics calculations by Wentzcovitch *et al*[47] with variable cell shape successfully found the M1 structure to have the lowest total energy, with structural parameters in reasonable agreement with experiment. DFT-LDA calculations fail, however, to produce the opening of the band gap: the top of the bonding $d_{\parallel}$ band is found to overlap slightly with the bottom of the π^* band, and only for a hypothetical structure with larger dimerizations would the band gap open up. Hence, only a theoretical treatment in which structural aspects as well as correlations within V-V pairs are taken into account on equal footing can capture the underlying mechanism for the metal-insulator transition in VO_2.

Dynamical mean-field theory (DMFT)[48] successfully fulfilled this requirement by mapping the many-body lattice problem onto a single-site problem using the Anderson impurity model. This simplifies the spatial dependence of the correlations among electrons and yet accounts fully for their dynamics, *i.e.*, takes into account the local quantum fluctuations that were missing in the static mean-field treatments like the Hartree-Fock approximation. DMFT provides a quantum analog of the classical mean-field theory and satisfactorily describes the Mott metal-insulator transition. It directly addresses the competition between kinetic energy and correlation energy – that is, the wave-like and particle-like character of electrons in the solid. It successfully reproduces the qualitative features of the phase diagram for strongly correlated systems such as vanadium oxide and nickel selenium sulfide. DMFT could perfectly reproduce the phase transition characteristics for pure Mott transition in V_2O_3.

As an extension of DMFT, the electronic structure of VO_2 was successfully reproduced by Biermann et al[49] using a cluster extension of dynamical mean-field theory (C-DMFT) in combination with DFT-LDA calculations within the recently developed *N*th-order muffin-tin orbital (NMTO) implementation. This allowed for a consistent description of both the metallic R phase and the insulating M1 phase and the calculation of a finite band gap which was not achieved in earlier works. Very recently the effect of stress on the phase transition features has been studied within the DMFT framework,[50] and reverse Monte Carlo calculations have been used to model the structural evolution in the region of strong correlation to capture the coexistence of metallic and insulating domains during the first order phase transition.[51] The latter calculations do not support the existence of an intermediate structural state during the phase transition.

1.2.5 Recent experimental results

Phase transitions in VO_2 have been primarily been induced in two different ways: temperature-induced and photo-induced, the former one being an adiabatic and latter being a non-equilibrium preparation of the phase transition.

Adiabatic and non-equilibrium preparation of the metallic state

Electronic transitions occur on a time scale of femtoseconds, because of their low mass and interactions via Coulombic forces, which act almost instantaneously. Electron-electron collisions then bring them to a Fermi-Dirac equilibrium distribution, and attribute a temperature T_e to the electrons in the system, in around tens of femtoseconds. Ions, on the other hand, due to their higher mass take longer to respond to any impulse received and only vibrate about their mean positions in a regular lattice arrangement with vibrational frequencies in the far-infrared regime. Their characteristic response time is of the order of picoseconds. So collisions with excited electrons ascribe a temperature of T_i to the ions in few picoseconds, and after tens of picoseconds the whole lattice settles to a mean equilibrium temperature <T> (when $T_i = T_e$).

During thermally-induced phase transitions, we adiabatically reach a condition of phase transition, in which the changes in temperature are brought about slowly enough to have the thermal equilibrium of the system re-instated at each step, i.e. more than tens of picoseconds of intervals are maintained. To understand the cause and effect relationship between the electronic correlations and the structural transition, and which of these is primarily responsible for the phase transition in VO_2, we need to induce the phase transition in a non-equilibrium situation, for example, by hole-doping during a photoinduced phase transition and probe the transition with femtosecond resolution. Thus ultrafast optical preparation of the non-equilibrium metallic state and probing measurements in the femtosecond regime is another way that can provide useful insight into the VO_2 phase transition puzzle.

Thermal induction of the phase transition has been the most common and popular method till date. All of the early work on VO_2 was done by thermally inducing the phase transition and also recent developments[18, 19, 52, 53] have shed light on VO_2 phase transition mechanism with the first work underscoring the Mott signature of the transition, whereas the others provided a means to interrogate the evolution of the structural and the electronic phase transitions.

Ultrafast optical measurements with visible and THz probes and X-ray diffraction measurements of photoinduced phase transition in VO_2 have been done[54-58] to demonstrate the direct measurement of a femtosecond solid-solid phase transition and the combined measurements of electronic and structural dynamics during phase transition. It has been observed that, at high degree of electronic excitation, transition has been indicated by optical and X-ray data to occur over a macroscopic volume within 100fs or less. This renders VO_2 highly suitable for ultrafast switching applications. Lysenko *et al*[59] have studied the effect of substrate and film morphology on the ultrafast switching and relaxation times. They have also studied the contributions of the non-thermal electronic *vs* phonon-induced thermal components of the light-induced phase transition depending on laser fluence.[60] Also, according to ultrafast investigations by Hilton *et al*,[61] Kim *et al*[62] and Jepsen *et al*[63] there exists a mixture of phases (metallic domains alongside insulating domains) well below transition threshold, and both Maxwell-Garnett and Bruggeman

effective medium theories have been applied to model the macroscopic, effective dielectric properties of VO_2 thin films and nanoparticles in vicinity of transition where composite phases coexist. Another interesting aspect that has been reported in the photoinduced phase transition of VO_2 thin films covering metal nanoparticles is that the changes in dielectric function, changes the position of the surface plasmon resonance and thus the plasmon-photon coupling.[64]

Electric-field induced switching of VO_2 has also been investigated by a large number of groups,[23, 65-69] and is important because of its technological as well as its physics implications. Electric-field (E-field) induced switching of VO_2 underscores the Mott-driven nature of the phase transition and makes VO_2 a strong candidate for the realization of Mott transistors. One of the advantages of a field effect transistor (FET) with VO_2 is that the issue of RC-limitation to the transit time that limits the performance of conventional FETs is no longer relevant in this case.[66] The field-induced switching in VO_2 has been plagued with controversies regarding the actual cause of the switching: that is, if the Joule heating due to the current flowing through the VO_2 and not the carrier injection is the driving mechanism of the phase transition.[70, 71] But recently, a Raman demonstration of the gate-field-induced switching of VO_2,[72] with no current flowing through it, has proved that pure E-field induction of phase transition in VO_2 is possible.

The potential for two and three terminal devices based on E-field induced switching of VO_2 is still an active area of study.[73, 74] A recent study[37] have found that, materials synthesis, especially the VO_2/gate dielectric interface, plays an immensely important role in the response to the gate voltage, and thus controls the functioning of such electrically-controlled devices.

1.2.6 Other phases of VO_2

1.2.6.1 Past developments

The discussion in this subsection is largely based on the seminal paper by Volker Eyert.[46] The understanding of VO_2 and the metal-insulator transition is even more complicated due to the presence of additional phases of this material. They appear on application of

uniaxial stress or on doping of VO_2 with small amounts of Cr, Fe, Al, or Ga of the order of few percent.[11, 12] The phase diagram of Cr doped VO_2 as given by Pouget and Launois[12] is shown in figure 1.5. Later, a similar phase diagram was also reported for $V_{1-x}Al_xO_2$ by Ghedira *et al*[75, 76]. According to Fig. 1.5, Cr-doped VO_2 enters, on cooling, the monoclinic M2 phase in a first order metal-insulator transition.

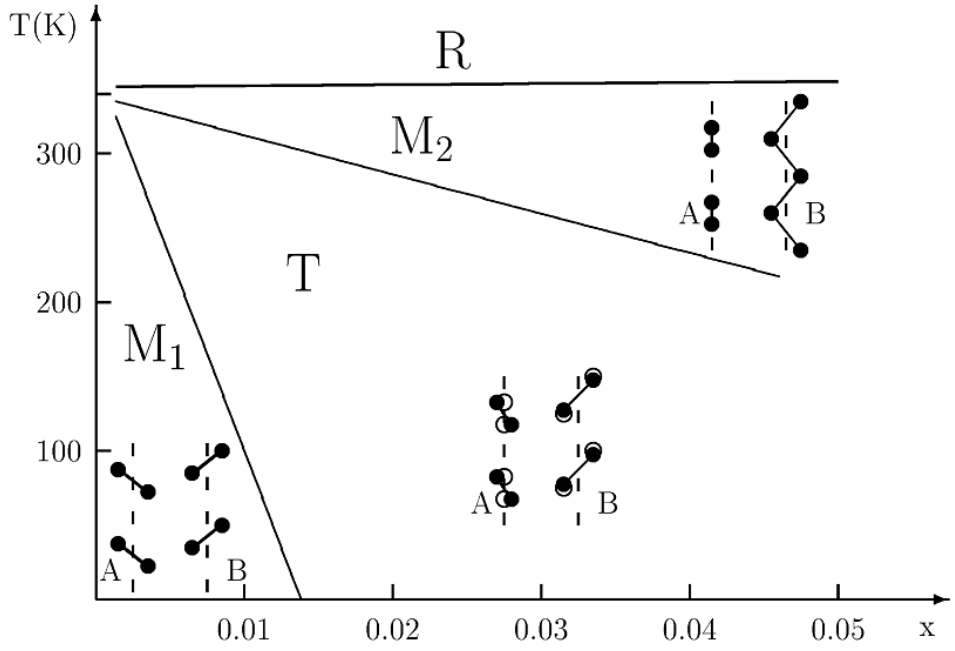

Figure 1.5: Phase diagram of VO_2 showing its structural evolution.[46]

On further lowering of the temperature, transition to the triclinic T phase occurs, which, for chromium concentrations smaller than 0.015, is followed by a first order transition to the monoclinic M1 phase. According to X-ray measurements by Marezio *et al*[77], each of the three low-temperature phases shows a particular distortion pattern of the atomic arrangement especially of the characteristic vanadium chains. The T phase, alternatively also called the M3 phase has also been observed and well-characterized by several groups.[78-80] Whereas in the M1 phase both the metal-metal pairing and the zigzag-type lateral displacement are observed on each chain, in the M2 phase only half of the chains dimerize and the zigzag-type deviations are reserved to the other half of the chains (see figure 1.6). Finally, the T phase is intermediate, as those chains, that in the M2 phase

dimerize, gradually start to tilt, whereas the zigzag chains start to dimerize until distortions in both chains are identical and eventually the M1 phase is reached. Hence, the T and M1 phases can be regarded as superpositions of two M2-type displacements with unequal and equal weights, respectively. The role of the latter displacement pattern as the "fundamental" one may be understood from the symmetry considerations presented by Pouget *et al* as well as by Paquet and Leroux-Hugon.[8, 81] According to these ideas the pairing on one chain is intimately connected with the zigzag-type displacement on the neighbouring chains: If the vanadium atoms pair on one chain, the atoms on the neighbouring chains, which from the outset are vertically displaced by half the rutile *c* axis, move off the chain axis towards the apical oxygen atom whose V neighbours of the first sublattice have pulled apart. For this reason, the zigzag-like displacement may be viewed as being coupled to the metal-metal pairing along the rutile *c* axis. D'Haenens *et al* found from ESR data, that the chromium atoms enter as substitutional Cr^{3+} ions on the zigzag-type chains.[82, 83]

The M2 to T transition was viewed as a bonding or dimerization transition of a linear Heisenberg chain. This interpretation was confirmed by the observed decrease of the magnetic susceptibility at the transition, which is accompanied by an increase of the electrical conductivity by a factor of two. From the existence of well localized 3*d* electrons at the V^{4+} sites, Pouget *et al* concluded that the results should be interpreted in terms of a Mott-Hubbard-type picture. In doing so, they attributed the insulating gap to electronic correlations.

Later on, Pouget *et al* demonstrated that both the M2 and T phases could be likewise stabilized by applying uniaxial stress along either the [110] or the $[1\bar{1}0]$ direction in stoichiometric VO_2 samples.[12] Such uniaxial stress can be viewed as suppressing the zigzag-type displacements on those chains, which have their tilting along the direction of the applied stress, while the respective other chains are not affected. However, from the above symmetry considerations it follows that, as a consequence of the reduced tilt on one half of the chains, the pairing on the other chains will be also reduced.

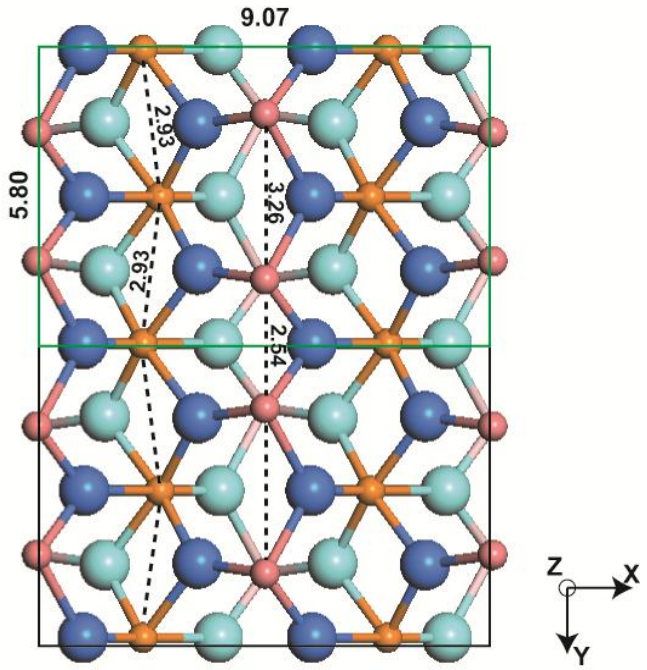

Figure 1.6: Schematic structure of M2 phase of VO_2. Courtesy: Dr. Bin Wang, Vanderbilt University

Pouget *et al* pointed out that the critical uniaxial stress for appearance of the M2 phase is so small that the free energies of the M1 and M2 phases in pure VO_2 must be extremely close at temperatures just below the metal-insulator transition. These authors also pointed to the fact that, although the M2 and T phases involve substantial changes in the vanadium atom positions, they could be stabilized by impurity concentrations as low as 0.2%. According to them the M2 and the T phases therefore must be interpreted as alternative phases of pure VO_2 whose free energies are only slightly higher than that of the M1 phase of the pure material. As a consequence, the M2 phase was regarded as a metastable modification of the M1 phase. In contrast, the T phase appears as a transitional state, which displays characteristics of both monoclinic phases.

The discovery of the M2 phase with its two different types of vanadium chains was difficult to reconcile with the theoretical approaches which had explained the insulating ground state as originating from crystal structure distortions with a predominant influence

of either the pairing or the zigzag-type displacement. Furthermore, from the presence of localized 3*d* electrons on the zigzag chains and the antiferromagnetic ordering of the local moments within non-interacting linear Heisenberg chains many authors concluded that band theory were unable to correctly describe the physics of the M2 and, hence, also of the M1 phase. Instead, electronic correlations were regarded as essential and localized models based on Mott interpretation became necessary. Yet an explanation of the physics of VO_2 purely in terms of a Mott-Hubbard-type picture turned out to be difficult in view of the complex structural changes at the metal-insulator transition, which lead to the same crystal structures as those of the neighbouring metallic transition-metal dioxides.

As Rice et al[15] have pointed out, discussion of the monoclinic M2 phase of VO_2 is essential for a comprehensive understanding of the physics of the metal-insulator transition. The efforts of Eyert in capturing the underlying physics for all these states in VO_2 is notable in this case.[46]

1.2.6.2 Recent Developments: VO_2 nano single-crystals

The ability to synthesize VO_2 in the form of single-crystalline nanobeams and nano- and microcrystals[84, 85] ushered in a new era with measurements and studies being conducted to uncover a number of previously unknown aspects of the metal-insulator transition in bulk or thin films. This one-dimensional form of VO_2, confined in space to smaller than the characteristic domain size, provided a much simplified, elegant platform to study the fundamental physics of the complex phase transition of VO_2 because of the absence of the domain structure, characteristic of thin films. Nanobeams have superior mechanical properties due to absence of defects and much higher stress tolerance. In polycrystalline thin films, mutual interaction of constituent crystallites affect and convolute the nature of the MIT. Strain in thin epitaxial films are redistributed by possible presence of misfit dislocations and grain boundaries, resulting in microscopic domains limiting the phase space accessible in experiments and also complicate the interpretation of results. These problems are absent in one-dimensional nanowire configuration thus providing a much broader scope for fundamental physics interrogation.

Investigation of the phase transition in such a quasi-one-dimensional geometry has led to observation of alternately striped metal and insulator phases,[84] supercooling of the metallic state by almost 50°C,[86] evidence for both the Mott[86] and Peierls[38] character of transition and many such interesting phenomena. Figure 1.7 shows long suspended nanobeams between gold contacts showing buckling and the evolution of metal-insulator transition in these single-domain structures.

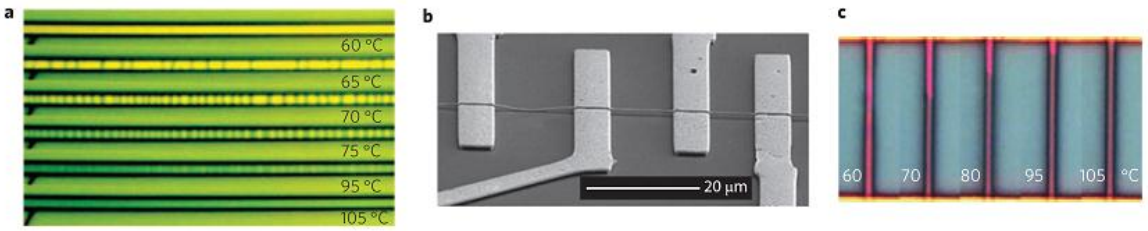

Figure 1.7: Stripes of insulating and metallic phases observed in strained VO_2 nanobeams undergoing phase transition, after Wei *et al*[86]

But the most exciting, unanimous observation from different groups has been the observation of the M2 phase as an intermediate phase during transition which can be stabilized by stress, as observed by Pouget *et al*. Zhang *et al*[38] performed simultaneous Raman and electrical resistivity measurements to extract the temperature dependent resistivity of the M2 phase. Their study also provided evidence in support of a Mott-driven transition by creating metallic M2 and M1 phase, paving the way for design of Mott field-effect transistors, without structural phase transition. Jones *et al*,[87] also with help of Raman and scattering-scanning near field optical microscopy (s-SNOM) studied the influence of the competition between the R, M1 and M2 phase in the MIT in presence of external substrate-induced stress. Taking advantage of the higher yield strengths of the nanobeams, Cao *et al*[88] performed simultaneous micro-XRD and resistivity measurements to map the stress-temperature phase diagram for the different competing phases, in a phase space that is an order of magnitude broader than what could be achieved previously in the bulk without fracturing. They observed that, under tensile stress, the M2 phase self-organizes into twinned superlattices and can be transformed reversibly to the R or M1 phases by varying temperature or stress (see figure 1.8). Micro-XRD, micro-Raman and polarized-light microscopy coupled with Ginzberg-Landau

formalism used by Tselev et al[16] showed that the competition between the M1 and M2 states is purely lattice-symmetry-driven and M2 does not have a special role as an intermediate phase in MIT; it is rather purely stress-induced.

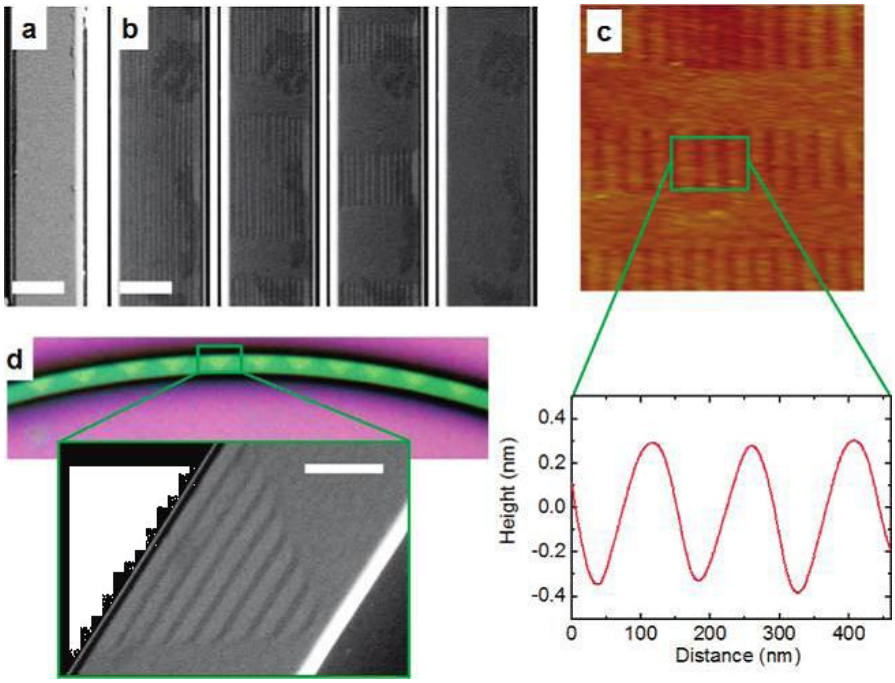

Figure 1.8: Observation of the M1, M2 and R phase stripes in strained VO_2 nanobeams, as measured by Cao *et al*[44]

Recent reports of an intermediate M2 phase in thin films of VO_2 during phase transition have also been made by Okimura *et al*.[52] They observe a third Gaussian peak is required to fit their temperature-variable XRD data near transition, which fit the description of M2. Booth *et al* have reported on the production of substrate-dependent pure phase M2-VO_2 and M1-VO_2.

1.3 A Review in VO_2 Thin Films and Nanoparticles Synthesis

Growing pure phase VO_2 thin films and nanoparticles is a challenge that needs to be overcome for studying and applying its phase transition properties. A brief review of the most common fabrication techniques for VO_2 synthesis is provided in this section.

1.3.1 The phase diagram for VO_2

In addition to vanadium dioxide (VO_2), vanadium sesquioxide (V_2O_3) and vanadium pentoxide (V_2O_5) also exhibit metal-insulator transitions at critical temperatures specific to their stoichiometric phases. But, as the phase diagram of Figure 1.9 shows, there are nearly twenty other stable vanadium oxide phases, such as VO, V_6O_{13}, V_3O_5, V_4O_7 etc. which have no interesting phase transitions but whose phase diagrams are similar to those of VO_2 and V_2O_3, and the existence of these competing oxide phases offers particular challenge to the growth of both bulk and thin films of VO_2.[89, 90] Nevertheless, VO_2 depositions have been done using numerous techniques such as reactive evaporation, several sputtering methods, metal-organic chemical vapor deposition (MOCVD), pulsed laser deposition (PLD), sol-gel deposition, etc. In this section we will concentrate on the five techniques most commonly used nowadays for the fabrication of VO_2 thin films, nanoparticles and nanobeams – sputtering, pulsed laser deposition (PLD), chemical vapor deposition (CVD), sol-gel and physical vapor transport techniques.

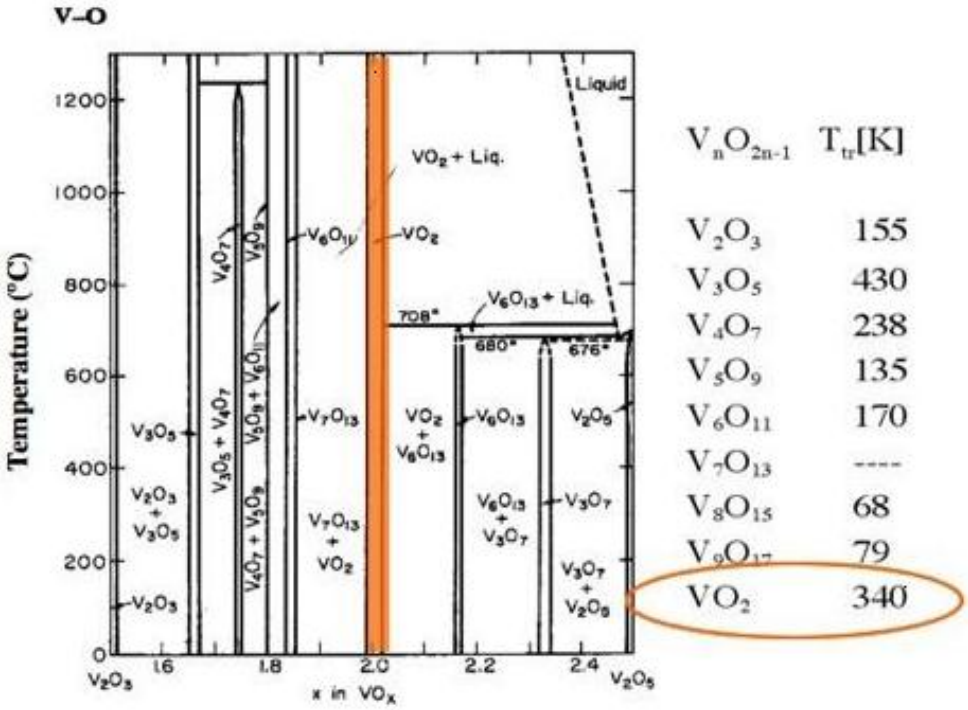

V_nO_{2n-1}	T_{tr}[K]
V_2O_3	155
V_3O_5	430
V_4O_7	238
V_5O_9	135
V_6O_{11}	170
V_7O_{13}	----
V_8O_{15}	68
V_9O_{17}	79
VO_2	340

Figure 1.7: Phase diagram for the vanadium oxygen system.[91]

In passing it should also be noted that techniques such as reactive evaporation have also been extensively employed [92-97] to obtain high-quality VO_2 films. Also, ion implantation was used by Lopez *et al* in order to stoichiometrically co-implant vanadium and oxygen in the near-surface region of fused silica[98] and alumina[99, 100] substrates. The ion-implanted samples were used in the discovery of size-effects, including greatly enhanced hysteresis, in the structural phase transition of VO_2 nanoparticles.[101-103]

1.3.2 Chemical Vapor Deposition

Chemical vapor deposition (CVD) is a common industrial process for depositing high-quality and high-performance thin films. In a typical CVD process, the wafer (substrate) is exposed to one or more volatile precursors, which react and/or decompose on the substrate surface to produce the desired deposit. Frequently, volatile byproducts are also produced, which are removed by gas flow through the reaction chamber. In case of VO_2, most of the time the process has organometallic precursors, and is therefore often called organometallic chemical vapor deposition (OMCVD) or metal-organic chemical vapor deposition (MOCVD).

The first deposition technique used for the deposition of VO_2 thin films appears to have been chemical vapor deposition CVD, and after half a century it is still used extensively. *Koide* and *Takei* in 1966 had grown bulk single crystals of VO_2 by CVD [104], and grew thin films of VO_2 a year later by the same method.[105] They introduced fumes of vanadium oxychloride ($VOCl_3$) carried by N_2 gas into the growth chamber, which was then hydrolyzed on the surface of rutile substrates to give epitaxial VO_2 films. In 1968, MacChesney, Potter and Guggenheim[106] used CO_2 instead of N_2, to carry $VOCl_3$, and V_2O_5 was formed on single crystal sapphire substrates. This V_2O_5 was then reduced to VO_2 by annealing between 500^o and 550^oC, with appropriate oxygen partial pressures, in a controlled atmosphere containing a mixture of CO and CO_2. These same researchers were the first ones to have elucidated the phase diagram for the vanadium-oxygen system. Thin film VO_2 preparation on various substrates by the pyrolysis of vanadium acetylacetonate $(C_5H_7O_2)_4V$ in a controlled atmosphere with appropriate mixtures of

nitrogen and oxygen was accomplished in 1972 by another group.[107]The reaction used by them is as follows:

$$(C_5H_7O_2)_4V \xrightarrow{heat} VO_x + gases$$

They concluded that the composition of the gas carrier was the main factor determining the film composition. Vanadyl tri-isopropoxide ($VO(OC_3H_7)_3$) based CVD was first tried, in open atmosphere, by C.B. Greenberg in 1983,[108] and VO_2 films were made with and without post-annealing on glass substrates.

CVD continues to be one of the most convenient ways of making VO_2, using one of the above pre-cursors. Also, VCl_4 and water have been used as precursors by Manning *et al* in 2002[29] to make intelligent window coatings with VO_2. Maruyama and Ikuta in 1993,[109] first demonstrated atmospheric-pressure CVD (APCVD) from vanadium(III) acetylacetonate and deposited polycrystalline VO_2 films on fused quartz and sapphire single crystals.

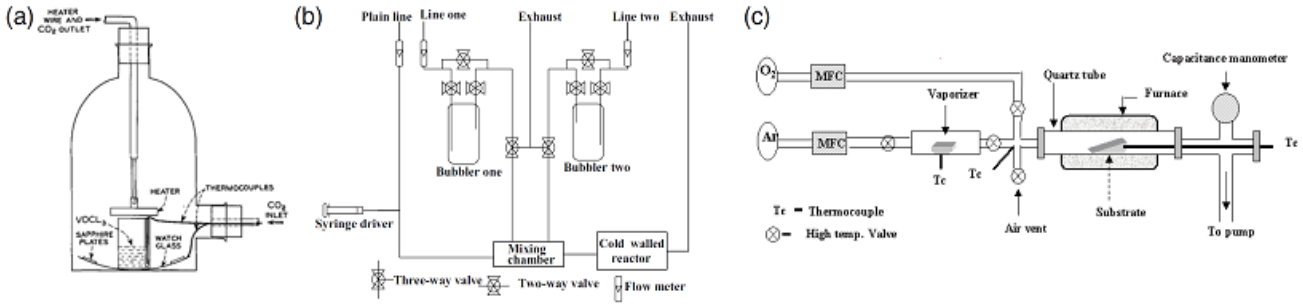

Figure 1.8: (a) MacChesney and Guggenheim's CVD apparatus, (b) CVD apparatus based on VCl_4 and water precursors after Manning *et al*, (c) Low-pressure CVD apparatus as described by Sahana *et al*

Manning *et al*[110-112] have also investigated APCVD in quite details for various purposes, and have successfully demonstrated doping of VO_2 with W, Ti, Mo and Nb. High quality epitaxial VO_2 films were grown on sapphire substrates using low-pressure CVD by Zhang *et al* in 1994,[113] and the substrate and film orientations were studied. Also, in 2001-2002, CVD of VO_2 was performed under low-pressure (LPCVD) by Sahana *et al*,[114, 115] and variation in phase transition characteristics were demonstrated in terms of

the observed film microstructure. Figures 1.10(a), (b) and (c) show three different implementations of the CVD technique as it has evolved.

Recently, aerosol-assisted (AA) CVD has been demonstrated for deposition of VO_2 on glass.[116, 117] In this technique, the pre-cursor (vanadium(III) acetylcetonate and vanadyl (IV) acetylacetonate) is dispersed in a solvent and an aerosol of the solution is generated ultrasonically. The precursor is transported to the substrate through aerosol droplets transported by a carrier gas. The advantage of AACVD over APCVD is that the precursor does not need to be volatile, but just soluble in one of the solvents suitable for aerosol formation.

1.3.3 Sol-Gel Technique

The sol-gel method has been widely employed for depositing VO_2 films because of its many advantages, such as low cost, large area deposition, and the ease of metal-doping. The sol-gel process is a wet-chemical technique for the fabrication of materials (typically a metal oxide) starting from a chemical solution containing colloidal precursors (sol). Typical precursors are metal alkoxides and metal chlorides, which undergo hydrolysis and polycondensation reactions to form a colloid, a system composed of solid particles (size ranging from 1 nm to 1 μm) immersed in a solvent. The sol then evolves towards the formation of an inorganic network containing a liquid phase (gel). Formation of a metal oxide involves connecting the metal centers with oxo (M-O-M) or hydroxo (M-OH-M) bridges, thereby generating metal-oxo or metal-hydroxo polymers in solution, which is then deposited on a substrate or cast in a specific container or used to synthesize powders. A drying process serves to remove the liquid phase from the gel thus forming a porous material, and then a thermal treatment (annealing) may be performed in order to favor further crystallization and enhance mechanical properties.

The precursor sol in case of VO_2 is generally deposited on the desired substrate to form a film (*e.g.* by dip-coating or spin-coating). The sol-gel approach is an inherently low-temperature technique that allows for the fine control on the product's chemical composition, as even small quantities of dopants, can be introduced in the sol and end up

finely dispersed in the final product. Hence sol-gel has been widely used to dope VO_2 with other metals, such as tungsten or niobium, to change its transition temperature.

The method as applied to VO_2 generally consists of a spin coating with a solution of vanadium isopropoxide, $VO(OC_3H_7)_3$ diluted in an alcohol, (e.g., ethanol or isopropanol), and then a subsequent annealing process in a reducing atmosphere. C.B. Greenberg introduced this process for making VO_2 as the gelation-hydrolysis method.[108] It has since been found that using the equivalent n-propoxide vanadium compound gives VO_2 also, and it is likely that a wide variety of organometallics and solvents can be used, since the final oxidation state of the vanadium ion depends on the pyrolysis conditions rather than the starting material.

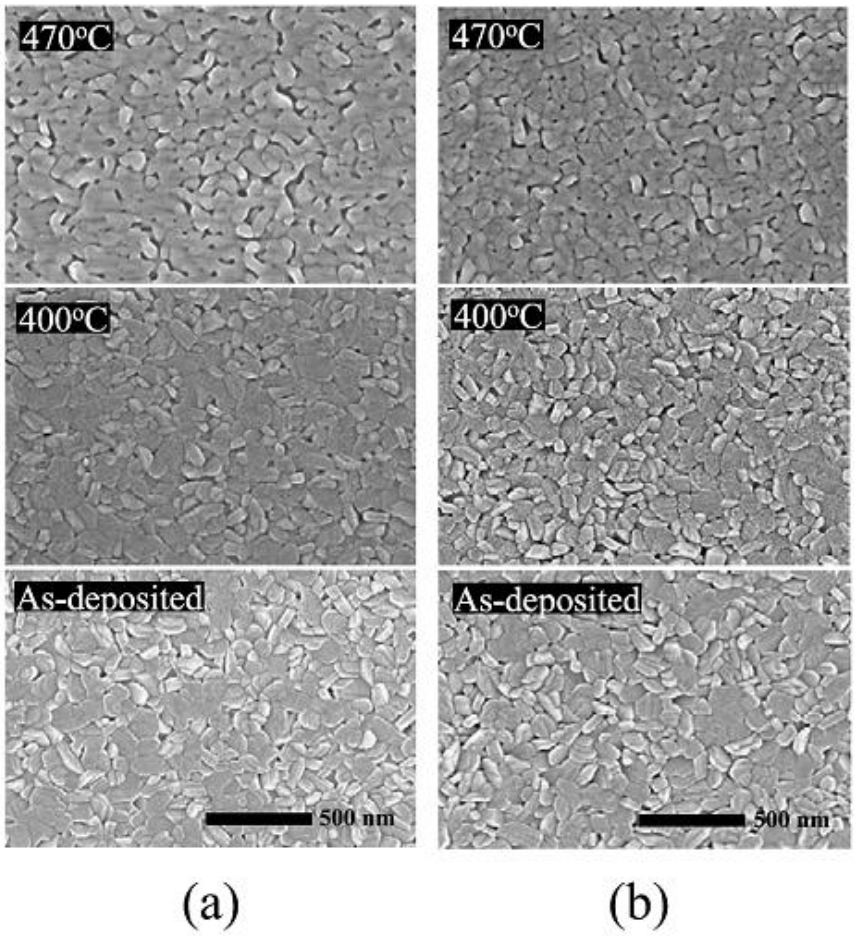

Figure 1.9: SEM images of vanadium oxide films grown on (a) Al_2O_3 $[10\bar{1}2]$ and (b) Al_2O_3 $[10\bar{1}0]$ substrates by sol-gel method.[118]

Another novel method — the inorganic sol-gel method — using V_2O_5 as the precursor was demonstrated by Dachuan *et al.*[119] According to Livage *et al*[120, 121] vanadium oxide gels can be synthesized either via the acidification of aqueous solutions of vanadates, for e.g. $NaVO_3$ or via the hydrolysis of vanadium oxo-alkoxides, $VO(OR)_3$. Application-oriented VO_2 films have been made using sol-gel process by several groups[120, 122-130].

Recently, Chae et al[118, 131] have demonstrated a simplified annealing process, where after using the sol-gel deposition; they formed VO_2 by annealing in a low pressure of oxygen only without a reducing gas, as was required in all of the above processes. Figure 1.11 show the SEMs of their films, as-deposited and after annealing at two different temperatures.

1.3.4 Sputtering

Sputtering, in its many forms, is the most common physical vapor deposition process[132] for growing vanadium dioxide thin films. Vanadium dioxide thin films were first grown by reactive sputtering in 1967 by Fuls, Hensler and Ross of the Bell Telephone Laboratories.[133] They made their films by reactive ion-beam sputtering of a vanadium target in an argon-oxygen atmosphere. Other enhanced sputtering methods used to facilitate the deposition process include RF and DC sputtering and magnetron sputtering. The advantages of sputtering processes are film uniformity, scalability to larger substrate sizes and efficiency of deposition compared to the other methods.

The simplest form of sputtering involves a diode sputtering by energetic ions (usually argon ions) from a gas-discharge plasma bombarding a target that forms the cathode for the discharge. Target atoms bombard the substrate (the anode), forming a coating. There may be three fundamental diode sputtering arrangements, which utilize a DC discharge, a capacitive radio frequency (RF) discharge, and either a DC or a capacitive RF discharges plus a planar magnetron. Figure 1.12(a) shows the essential arrangement for DC sputter deposition, while Figure 1.12(b) shows an RF sputter arrangement with a capacitive, parallel plate discharge, which yields substantially higher RF current. It uses a blocking capacitor to set the DC bias and an impedance-matching network for coupling to the reactive load posed by the plasma. RF sputtering apparatus operates at lower voltage and

lower sputtering gas pressures while producing higher deposition rates and, most importantly, sputtering of an electrically insulating target becomes possible.[134, 135]

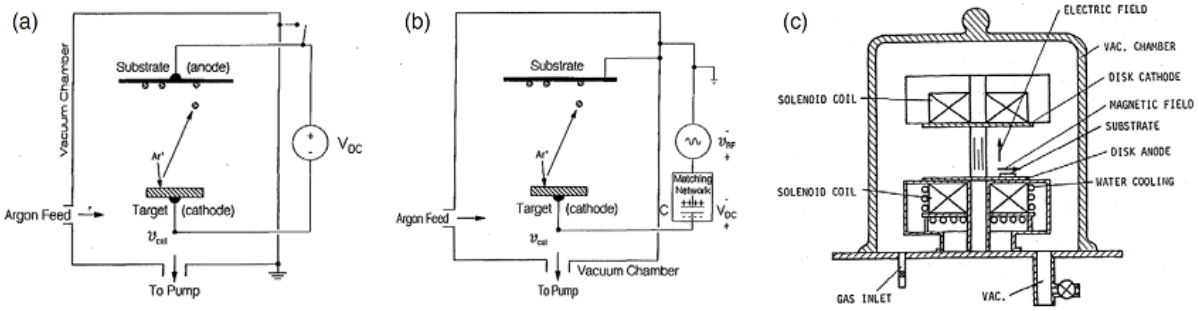

Figure 1.10: Schematic of (a) a DC sputtering apparatus, (b) an RF sputtering apparatus and (c) a magnetron sputtering apparatus[135]

Most contemporary high deposition-rate sources are now based on magnetron sputtering, developed in the 1970s. These sources feature a magnetically assisted discharge, in which a permanent magnet defines lines of magnetic flux perpendicular to the applied electric field from the DC or RF source, and is thus parallel to the surface of the target. The magnetic field concentrates and intensifies the plasma, in the space immediately above the target, by trapping of electrons near the target surface. This magnetron effect results in enhanced ion bombardment by the Ar ions, and thus much higher sputtering rates for both DC and RF discharges. Figure 1.12 (c) is the schematic of a typical magnetron sputtering system.

After the first experiments in VO_2 deposition by reactive sputtering, and further analysis of those samples by Rozgonyi and Hensler,[136, 137] both RF and DC reactive sputtering were studied by Duchene et al.[138] Similar results were obtained in both cases, but since RF sputtering was more suitable for depositing insulating oxides and had the above mentioned advantages over DC sputtering, it became the preferred method for VO_2 deposition. To standardize the fabrication of VO_2 thin films by sputter deposition, numerous studies have detailed the influence of sputter deposition parameters, like temperature, oxygen partial pressure, plasma emission ratio of oxygen and vanadium, etc. on the structure, optical and electrical properties of the deposited VO_2. Worth mentioning amongst these are the works of Chain, Jin *et al*, Razavi *et al*, and others. [139-151] Guinneton *et al* also deposited nanocrystalline VO_2 using RF sputtering.[152, 153]

Inductively-coupled plasma-assisted (ICP) sputtering was reported by Okimura *et al* in 2005 [154, 155] to have produced single phase crystalline VO_2 without any residual V_2O_5 or V_3O_7. Annealing effects on VO_2 thin films deposited by reactive sputtering were also studied in detail by Fu *et al.*[156] Novel methods of making better quality VO_2 thin films by sputter deposition are still being tried by groups in recent publications, showing that this is still an active area of research, which promises an even better fabrication technique for VO_2 thin films in the future.[157] For example, Gurvitch *et al*[158] indicated a precursor oxidation process, where sputter deposited precursor V films were oxidized *in situ*, in the deposition chamber itself to produce high quality VO_2 thin films having switching characteristics close to bulk single crystals of VO_2. VO_2 films for self-lubricating applications were produced using reactive DC magnetron sputter-ion plating physical vapor deposition (MSIP-PVD) by Lugscheider *et al* in 2001.[159]

1.3.5 Pulsed Laser Deposition

Pulsed Laser Deposition (PLD), another physical vapor deposition technique, is a comparatively recent inclusion in the world of thin film depositions, and is especially suited for oxide growth. In PLD a high power pulsed laser beam is focused on a target of the desired composition inside a vacuum chamber. Material vaporized from the target is deposited as a thin film on a substrate, for example Si wafer, facing the target. This process can occur in ultra high vacuum or in the presence of a background gas, such as oxygen which is commonly used when depositing oxides. In recent times it has probably become the most popular technique for VO_2 thin film and nanoparticle fabrication, especially for prototyping. Figure 1.13 shows the schematic of a typical PLD configuration.

While the basic experimental configuration is simple compared to many other deposition techniques, the laser-target interaction phenomenology and film growth are quite complex. When the laser pulse is absorbed by the target, energy is first converted to electronic excitation and then into thermal, chemical and mechanical energy, resulting in evaporation, ablation, plasma formation and even exfoliation. The ejected species expand into the surrounding vacuum in the form of a plume containing many energetic species

including atoms, molecules, electrons, ions, clusters, particulates and molten globules, before depositing on the substrate.[160, 161]

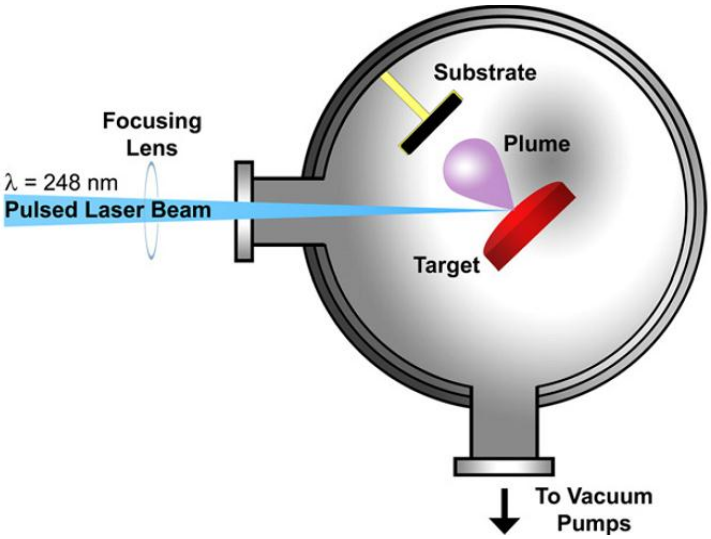

Figure 1.11: A schematic for a typical experimental arrangement for the pulsed laser deposition technique

Pulsed laser ablation as a deposition technique was realized in the late 1980s, and it was first used for VO_2 deposition by Singh *et al* in 1993.[162] They used a KrF pulsed excimer laser (248 nm) to ablate a metallic vanadium target in ultrahigh vacuum deposition chamber with Ar and O_2 (10:1) atmosphere of 100-200 mTorr, and a substrate temperature of about ~500^{o}C. The partial oxygen pressure was found to be critical in preparation of the pure VO_2 phase, for as many as thirteen different phases ranging from V_4O toV_2O_5 could exist in the system. The as-deposited samples were annealed for about an hour at the same temperature and pressure to obtain the VO_2 that switched. Soon after, Kim and Kwok in 1994[163] reported that they were successful in depositing high quality VO_2 films on sapphire by PLD at high temperature *without* post-annealing. Maaza *et al*, in 1999[164] was the first to claim room temperature growth of VO_2 by PLD, and the as-deposited films showed rather sharp phase transitions at around 70^{o}C, though it has not yet been reproduced by any other group. PLD of VO_2 thin films has been done on variety of substrates, including silicon, glass, sapphire, fused silica and quartz.

In 2004, Suh *et al*[165] described the effect of nucleation and growth of VO_2 nanoparticles and thin films on the SMT, where the films and nanoparticles were grown by PLD. They showed that the width and shape of the hysteresis cycle is determined by the competing effects of crystallinity and grain size. Recently, in-situ studies of the initial growth phase of vanadium dioxide films using synchrotron-based X-ray diffraction were reported in detail by Pauli *et al*.[166] They showed that films grown at room temperature are basically amorphous and only crystallize into the VO_2 phase upon thermal annealing in a background of O_2, with the nano-sized islands sometimes having a preferential orientation depending on the match with the substrate crystallography. This leads us to the discussion of hetero-epitaxial growth of VO_2 on substrates which have good lattice match with that of VO_2 thin films.

Studies and manipulations of properties of films of VO_2 deposited by laser ablation is still an area of active research.[167, 168] More of these efforts will be discussed in details in the Chapters 2 and 5.

1.3.6 Physical Vapor Transport

Very recently physical vapor transport process have been employed to make single-crystalline VO_2 nanowires or nanobeams and even microbeams, on which some very interesting physics observations have been made, for example the M2 phase stabilization, etc. as discussed in section 1.2.6.2. In physical vapor transport, generally, bulk VO_2 powder is placed in a quartz boat in the center of a horizontal tube furnace, and temperature (T), pressure (P), evaporation time (t), and argon carrier gas flow rate (k_{flow}) are controlled to obtain the desired product. The reaction product is collected on a substrate downstream from the starting material. Optimum reaction conditions resulting in growth of VO_2 nanowires are achieved in the range T = 900-1100 °C, P = 12-13 Torr, t = 5 h, and k_{flow} ~ 3 sccm. The reliable production of nanowires requires a careful choice of substrate surface.[84] It was reported that the greatest nanowire density is achieved on a Si_3N_4 substrate whereas SiO_2 substrates support very low densities of long wires. This process has been used and perfected by the Cobden, Wu and Tselev groups.[16, 86, 169]

Ordered arrays of *VO_2 nanoparticles* were made with the help of FIB lithography and PLD, and their optical properties were studied by Lopez et al in 2004.[103] These arrays presented novel size-dependences for transition temperatures and optical resonances,[103] which were attributed mainly to VO_2 mesoscale optical properties. Figure 1.14 shows an array of VO_2 nanoparticles deposited by PLD and patterned using conventional FIB lithography. Recently, rod-shaped microcrystals and hexagon-shaped nanocrystals of VO_2 have been produced through one step hydrothermal synthesis.[170] As a demonstration of their potential use, the researchers also demonstrated the VO_2 nanocrystals to infiltrate opaline lattices of polystyrene beads to generate technologically popular inverse opals. Another high-yield two-step process, which yielded high-purity VO_2 was also reported by Booth *et al*.[171]

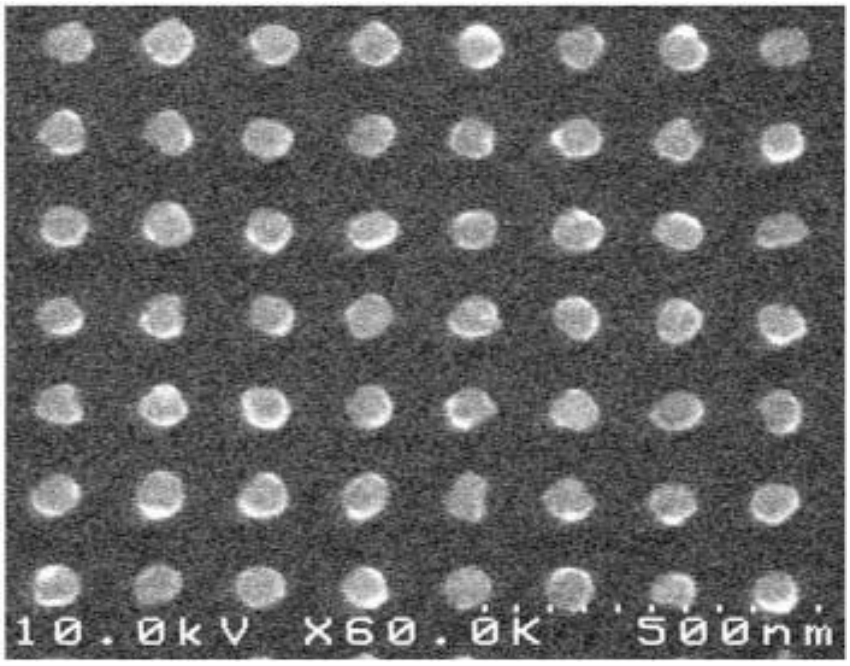

Figure 1.12: Section of a 100 μm x 100 μm array of VO_2 nanoparticles made by focused ion-beam lithography followed by pulsed laser deposition.[103]

1.4 EPITAXY

Epitaxy of VO_2 thin films forms the backbone of this dissertation. Hence we review a few salient features of epitaxy in this section.

1.4.1 Introduction to epitaxy

The term epitaxy (Greek; *epi* "above" and *taxis* "in an ordered manner") describes an ordered crystalline growth on a single-crystalline substrate. Epitaxial films may be grown from gaseous or liquid precursors. Because the substrate acts as a seed crystal, the deposited film takes on a lattice structure and orientation identical to those of the substrate. This is different from other thin-film deposition methods which deposit polycrystalline or amorphous films, even on single-crystal substrates. If a film is deposited on a substrate of the same composition, the process is called homoepitaxy; otherwise it is called heteroepitaxy. Homoepitaxy is used for growing a thin single-crystalline film on top of the bulk substrate and also for fabricating layers with different doping levels.

Heteroepitaxy is a kind of epitaxy performed with materials that are different from each other. In heteroepitaxy, a crystalline film grows on a crystalline substrate or film of another material. This technology is very important in thin-film materials science and semiconductor field because it is often applied to growing crystalline films of materials of which single crystals cannot be obtained and to fabricating integrated crystalline layers of different materials. Figure 1.15 demonstrates heteroepitaxy in film-substrate systems with different crystallographic symmetries.

While homoepitaxy and homoepitaxial layers (appropriately doped) became the basis for present day microelectronics, the heteroepitaxy and heteroepitaxial structures, much more difficult to grow to high perfection, have created present-day semiconductor optoelectronics and opened the way to development for tomorrow's nanoscale electronics.

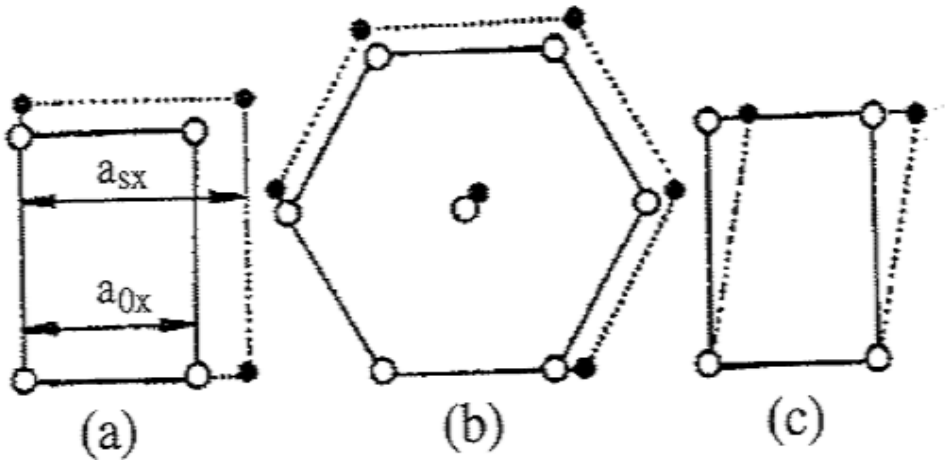

Figure 1.13: Examples of interfacial atomic arrangements in epitaxial film-substrate systems of different crystallographic symmetry. Black dots represent substrate atoms while empty circles stand for overgrowth atoms.[172]

1.4.2 Classic mechanisms of epitaxy

The discussion to follow is based on some of the discussions in the book on Epitaxy by M. A. Herman.[172] Epitaxy occurs only when the film and substrate lattice planes have networks of identical or quasi-identical form and of closely similar spacings. Experimental data indicated that epitaxy occurs if the lattice misfit, defined as corresponding network spacings (lattice constants) in the substrate and the film respectively, is not larger than 15%.[173] During epitaxy, for few monolayers of film deposited, the lattice periods of the film is changed to ensure complete matching at the interface (pseudomorphism). For thicker films the natural lattice periods are preserved in epitaxy (commensurateness) and the differences in the periods are compensated by the appearance of misfit dislocations. Either of these happens depending on the topography and the symmetry of the substrates and deposition parameters.

The growth process of thin epitaxial films is essentially the same as that of bulk crystals, except for the influence of the substrate at the initial stages. This influence comes from the misfit and thermal stress, from the defects appearing at the crystal-film interface and from the chemical interactions between the film and the substrate including segregation of the substrate elements towards the film surface. Refer to figure

1.16 for a schematic representation of strained and relaxed heteroepitaxial growth on a chosen substrate. Five possible modes of crystal growth are commonly distinguished in epitaxy. These are: the Volmer-Weber mode (VW-mode), the Frank-van der Merwe mode (FM-mode), the Stranski- Krastanov mode (SK-mode), the columnar growth mode (CG-mode), and the step flow mode (SF-mode). The mode by which the epitaxial film grows depends upon the lattice misfit between substrate and film, the supersaturation (the flux) of the crystallizing phase, the growth temperature and the adhesion energy.

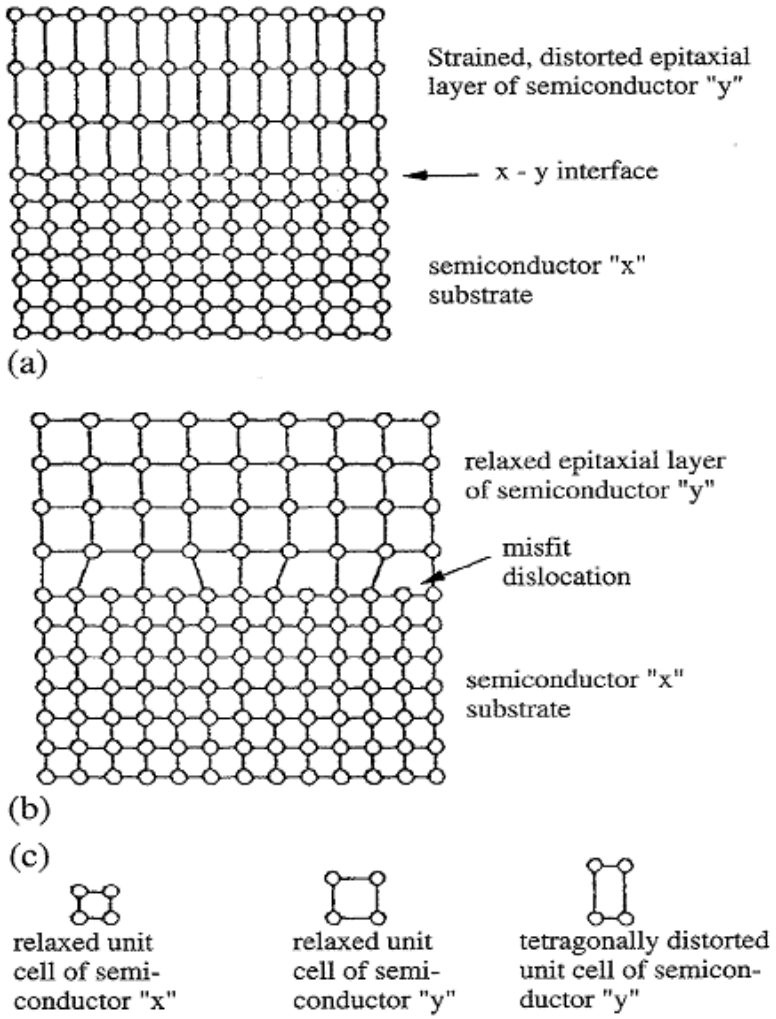

Figure 1.14: Schematic illustrations of (a) strained and (b) relaxed epitaxial layers of a lattice mismatched heterostructure, as well as (c) strained and relaxed unit cells.[172]

The five most frequently occurring modes are illustrated schematically in figure 1.17. In the VW-mode, or island growth mode, small clusters are nucleated directly on the substrate surface and then grow into islands of the condensed phase. This happens when the atoms, or molecules, of the deposit are more strongly bound to each other than to the substrate. This mode is displayed by many systems of metals growing on insulators, including many metals on alkali halides, graphite and other layer compounds such as mica.

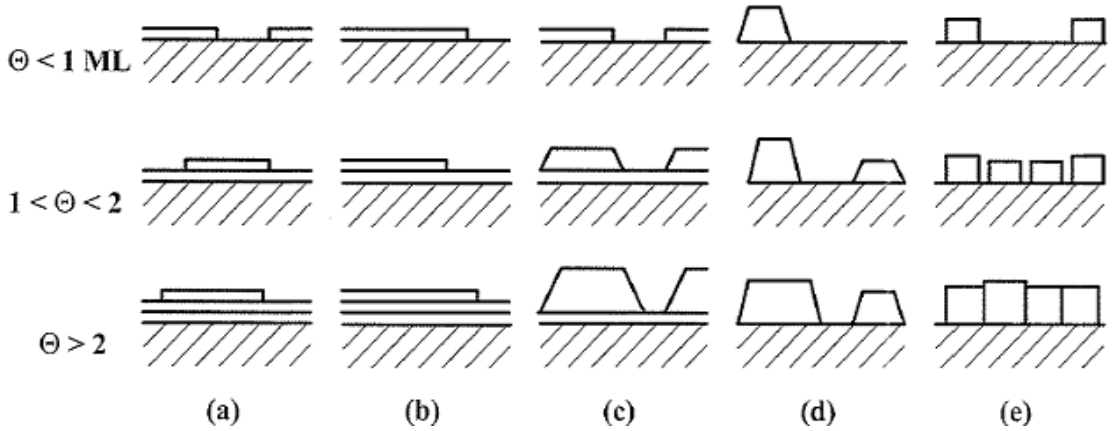

Figure 1.15: Schematic representation of five epitaxial growth modes most frequently occurring on flat surfaces of substrate crystals. (a) Layer-by-layer or Franf-van der Merwe (FM-mode); (b) step-flow (SF-mode); (c) laper plus island or Stranski-Krastanov (SK-mode); (d) island or Volmer-Weber (VW-mode); (e) columnar growth mode (CG-mode) . Θ represents the coverage in monolayers.[172]

The FM-mode displays the opposite characteristics. Because the atoms are more strongly bound to the substrate than to each other, the first atoms to condense form a complete monolayer on the surface, which then becomes covered with a somewhat less tightly bound second layer. Provided the decrease in binding strength is monotonic toward the value for a bulk crystal of the deposit, the layer growth mode is obtained. This growth mode is observed in the case of adsorbed gases, such as several rare gases on graphite and on several metals, in some metal-metal systems, and in semiconductor growth on semiconductors.

The SK-mode, or layer plus island growth mode, is an "intermediate" case of the two growth modes discussed above. After forming the first monolayer, or a few

monolayers, subsequent layer growth becomes unfavorable and islands are formed on top of this intermediate layer. There are several possible reasons for this mode to occur and almost any factor which disturbs the monotonic decrease in binding energy characteristic for layer-by-layer growth may be the cause . It occurs especially in cases when the interface energy is high (allowing for initial layer-by-layer growth) and the strain energy of the film is also high (making reduction of the strain energy by islanding favorable). In the InAs/GaAs material system the SK-mode leads, for example, to formation of dot arrays on the substrate surface [GaAs(100)], as an energetically metastable system with a preferred island size.

The fifth growth mode, the CG-mode, shows some similarities to the SK and VW modes, however, it is fundamentally different because in both these modes, when the film thickens, the condensed phase islands characteristic to these modes tend to merge and to cover the whole substrate surface. Although the grown film may exhibit variations in its thickness and have structural defects at the interfaces where adjacent islands merge, it forms a connected structure in which the density of the film is a continuous function of the position. In contrast, films grown by the CG-mode usually thicken without the merger of columns. As a result, columns usually remain separated throughout the growth process of the film, and the films grown in this way are easily fractured. The CG-mode occurs where low atomic mobility over the substrate surface leads to the formation of highly defective atomic columns of the deposited material on the substrate.

Three factors are important from the point of view of the mutual relation between the substrate and the heteroepilayer. Lattice constant matching, or mismatch, is the first, crystallographic orientation of the substrate is the second, and surface geometry, or surface reconstruction, is the third. The crucial problems of heteroepitaxy are, however, related to lattice mismatch which is the major factor in determining the critical thickness of the epitaxial film that can be grown pseudomorphically, as will be discussed in the following section.

1.4.3 Critical thickness

The following treatment is after that in the web-version of Sergey Smirnov's dissertation.[174] The basic principle of strained-layer pseudomorphic epitaxy is that a certain amount of elastic strain can be accommodated by any material without generating dislocations or defects. It takes energy to accommodate an epitaxial layer of lattice-mismatched material. The energy depends on both the thickness and the size of the lattice mismatch. It also requires energy to create a dislocation that will relieve the lattice mismatch strain. If the thickness of the epitaxial layer is kept small enough to maintain the elastic strain energy below the energy of dislocation formation, the strained-layer structure will be thermodynamically stable against dislocation formation. The unstrained state of the lattice-mismatched layer is energetically most favorable, but the strained structure is stable against transformation to the unstrained state by the energy barrier associated with the generation of enough dislocations to relieve the strain.

A fundamental assumption underlying many of the critical thickness calculations is the a priori assumption that the equilibrium configuration of the strain induced dislocations is that of a regular, non-interacting, rectangular array. Critical layer thicknesses are then computed by requiring that the total strain energy per unit area ε_T be a minimum with respect to the in-plane strain e.

$$\left(\frac{\partial \varepsilon_T}{\partial |e|} \right) = 0 \tag{1.1}$$

evaluated at $|e| = f$, where f is the mismatch between the film and the substrate. Here ε_T is defined as a sum

$$\varepsilon_T = \varepsilon_H + \varepsilon_D \tag{1.2}$$

of the homogeneous strain energy density ε_H :

$$\grave{o}_H = 2G\left(\frac{1+\nu}{1-\nu}\right)e^2 h \tag{1.3}$$

and the areal energy density of the dislocation ε_D :

$$\grave{o}_D \equiv \frac{E_l}{p} \tag{1.4}$$

Here G is the shear modulus, h is the film thickness, E_l the energy per unit length of a given dislocation line, and p is the spacing between the dislocations in the assumed rectangular array. It should be noted that E_l is independent of the in-plane strain e in the film and in fact ε_D only depends on the strain in the film through of the strain-dependence of the effective interfacial width p. The spacing between dislocations in the array is given by

$$p = \frac{b}{f - |e|} \tag{1.5}$$

where b is the magnitude of Burgers vector. Equations (3)-(5) in conjuction with the mechanical equilibrium condition (1) yield the following equation for the critical thickness h_c:

$$h_c = \frac{b}{4\pi f(1+\nu)}\left[\ln\left(\frac{h_c}{b}\right)+1\right] \qquad (1.6)$$

It is assumed that dislocation formation requires in a dislocation formation energy ε_D. As the thickness of a film approaches its critical value, some fraction of the homogeneous strain energy ε_H will be used to supply this dislocation formation energy.

One of the main goals of current research in the field of highly strained heterostructures is to increase the transition thickness h_c below which layer-by-layer growth can be maintained. A reasonable way to avoid the formation of 3D islands is to use kinetic limitations to prevent the substrate/epilayer system from reaching equilibrium. In other words, the mass transport at the substrate surface, and thus the surface diffusion length should be reduced. Usually, the surface diffusion length is reduced by lowering the growth temperature. However, this in turn may have a deleterious effect on the device quality of the epitaxially grown material. Another approach, which seems to be very promising, is the use of surfactants that kinetically inhibits the formation of islands.

Since we will be dealing with VO_2 epitaxy in the next few chapters, we have calculated using equation (1.6), the critical thicknesses for pseudomorphic epitaxial VO_2 films with lattice mismatches relevant to our chosen substrates. With the Burgers vector B chosen to be ~ 0.3 nm, of the same order as the lattice constant and $\nu = 0.2$, as assumed by Guiton *et al*, for a mismatch factor of f = 0.008, we get that h_c = 11.5 nm. With increasing f, h_c continuously decreases to atomic dimensions of 0.5 nm for f = 0.06. The range of mismatches investigated here pertains to those occurring in case of growth on TiO_2 planes where the mismatch is in the range of ~0.85% - 1% and in case of growth on various sapphire planes with lattice mismatches close to 5%.

1.5 CONTENTS OF THIS DISSERTATION

This dissertation in the next few chapters will give an overview of studies in VO_2 growth, physics behind the phase transition and an application. Chapter 2 will discuss the epitaxial VO_2 film growth efforts on a six different substrates. Chapter 3 is a systematic study of the dependence of film morphology and phase transition behavior of films on different process parameters for example temperature and laser power. Chapter 4 will be a discussion of the physics of correlation between the structural and electronic transition of VO_2. Chapter 5 is a transition showing how doping of VO_2 films can not only help us with better applications of VO_2 but also facilitate our understanding and control over the complex VO_2 phase transition. Chapter 6 deals with an application of VO_2 in the field of Si-nanophotonics to improve the state-of-the-art by using the metal-insulator transition in VO_2. We will conclude with summary and future directions for VO_2 studies in Chapter 7.

CHAPTER II

EPITAXIAL VO_2: FABRICATION AND CHARACTERIZATION

ABSTRACT

We start this chapter with recapitulation of the work that has been done previously in growing epitaxial thin films of VO_2. Then we discuss in-detail the fabrication and characterization of epitaxial VO_2 films on three different planes of sapphire and three planes of TiO_2, that were grown using the pulsed laser deposition system at Vanderbilt. We discuss the effect of substrate-surface treatment on epitaxy and conclude with evidences of switching in ultrathin epitaxial films of VO_2.

2.1 EXISTING LITERATURE ON VO_2 EPITAXY

Fabrication of high-quality VO_2 thin films is crucial for technologies that capitalize on the IMT. It is well known that film microstructure,[175] the film-substrate interface[176] and localized strain[50, 133] can all affect the hysteretic response of this first-order phase transition. Epitaxial films are generally expected to produce spatially homogeneous films with phase transition behavior close to that of bulk crystals, as the defined crystallographic growth direction(s) lead to more consistent and efficient performance in devices.

The process of making high-quality, defect-free, thin film samples of VO_2 is complicated not only by the presence of oxygen defects, but also by the narrow temperature-pressure window in phase space for stoichiometric VO_2, due to multiple valence states of vanadium. Note also that, when grown directly at high temperature or annealed after being grown at room temperature, the film crystallizes as stoichiometric, tetragonal VO_2, and transitions to monoclinic form only during cooling, involving considerable stress-driven rearrangement giving rise to a variety of defects and dislocations.

The substrate plays an important role in the quality of the epitaxial films and their microstructures, because of the existence of lattice mismatch – the differences from either lattice constant or angle of the lattice vectors between substrate and grown film. Usually same crystallographic crystal is chosen as the substrate, as that reduces the angle mismatch to zero, thereby largely reducing the lattice misfit, which is then only determined by the difference in lattice constants. But in some cases, it is hard to choose a same crystallographic crystal for the substrate, as for the monoclinic VO_2 crystal system. VO_2 is monoclinic at room temperature, with lattice angles of $\alpha = \gamma = 90^o$ and $\beta = 122.6^o$, making it pseudohexagonal and rendering hexagonal sapphire a preferred substrate for epitaxial thin film growth.

Sapphire, the single-crystal form of Al_2O_3 , especially the R-cut plane $(01\bar{1}2)$ and the C-cut plane (0001) of Al_2O_3, has been the preferred substrate for epitaxial growth of VO_2 due to its easy availability, stability at high temperatures, and less reactivity with the oxides. It was used in early days of VO_2 deposition by CVD by MacChesne (1968),[106] and remained popular in the process of growing epitaxial VO_2 by different sputtering methods,[177] sol-gel methods,[118, 131] PLD technique[175] and others like Activated Reactive Evaporation (ARE).[92] But, the very first researchers Koide and Takei (1967)[105] to grow VO_2 thin films, by means of CVD, reported the growth of epitaxial VO_2 single crystal films on rutile crystals. Also, Rozgonyi and Hensler in 1968,[136] reported the growth of textured VO_2 films on sapphire, by reactive sputtering.

Epitaxial films of VO_2 on sapphire were deposited by reactive sputtering and characterized by Rogers *et al*[178]in 1991 followed by the work of Jin *et al*[142, 143] on VO_2 and W-doped VO_2 epitaxial films by magnetron sputtering. Singh *et al* in 1993[162] first showed that strongly oriented and single-phase VO_2 with (200) planes parallel to the R-cut sapphire substrate can be grown using PLD. Their films exhibited a bulk-like transition width of 2K, and resistivity change of $3x10^4$.

Zhang *et al*[113] produced epitaxial VO_2 films on sapphire in 1994 using MOCVD and studied the orientation relationships of substrate and film in detail. Garry *et al* in 2004[179] attempted epitaxial growth of VO_2 on both R- and C- sapphire planes , and found that

VO_2 films on R-planes exhibit a sharper electrical transition at a lower temperature than those deposited on C-plane; optical transmission of those films also confirmed the electrical results.

In the last few years, a lot of work has been devoted to understanding the structural properties of VO_2 on Al_2O_3, and includes quite a few publications from the group of Z.P.Wu and H.Naramoto.[176, 180, 181] Notably, in 2001, Muraoka *et al*[182] reported epitaxial growth of VO_2 on TiO_2 (001) and (110) planes, where the lattice mismatch is ~0.85%, and showed that the transition temperature of the deposited epitaxial VO_2 films had a strong dependence on the substrate orientation. Also, ultrathin films of VO_2 grown epitaxially on TiO_2 by PLD was reported by Nagashima *et al* in 2006,[183] and effect of strain on switching properties was observed. Anisotropy of dielectric properties of VO_2 films on TiO_2 (011) substrates was also studied by Lu *et al*.[184, 185]

Recently the group of J. Narayan has pioneered the use of different kinds of buffer layers to grow epitaxial VO_2 thin films.[186-188] The buffer layers range from the typical Mott insulator NiO, tetragonal yttrium-stabilized zirconia to ZnO and antiferromagnetic Cr_2O_3.

2.2 TOOLS USED FOR FABRICATION AND CHARACTERIZATION

In this section, a brief discussion of the tools primarily used for the synthesis and characterization of epitaxial VO_2 thin films will be provided.

2.2.1 Pulsed Laser Deposition

Pulsed laser deposition (PLD) is an application of laser ablation, the generic process of laser-induced material removal, to the growth of thin films from elemental or compound targets. A powerful laser beam impinges on the target material, undergoes absorption, and vaporizes a thin surface region. One of the most common PLD lasers, and the one used in this work, is the krypton fluoride (KrF) excimer (excited dimer) laser operating at an ultraviolet (UV) wavelength of λ = 248 nm (5 eV). Short-wavelength photons are strongly absorbed by most materials and have sufficient energy to induce photochemical reactions and break molecular bonds. For an in-detail description and discussion of the

pulsed laser deposition technique, please consult the referenced Ph.D. dissertations.[64, 189] PLD is the primary fabrication technique for all our thin films that will be discussed in this dissertation.

2.2.2 X-ray Diffraction

XRD is a powerful non-destructive technique for the characterization of crystallinity of materials. It provides the information on the structure, phase, preferred crystal orientation (texture) and other structural parameters, such as average grain size, strain and crystal defects.

When a monochromatic X-ray beam with wavelength λ, on the order of lattice spacing d, is projected onto a crystalline material at an angle θ, X-ray diffraction peaks are produced by constructive interference of monochromatic beam scattered from each set of lattice planes at specific angles. Constructive interference gives the diffraction peaks according to Bragg's law,

$$2d\ sin\ \theta\ =\ n\lambda \tag{2.1}$$

By varying the angle θ, the Bragg's law condition is satisfied by different d-spacings in polycrystalline materials. Plotting the angular position and intensities of the resultant diffracted peaks of radiation produces a pattern, characteristic of the material. The full width at half maximum (FWHM) of the peak, Δ (2θ) (in radians), is a measure of the grain size d in a polycrystalline film or the mosaic blocks in an epitaxial layer, as described by Scherrer's formula:

$$d = \frac{0.89\lambda}{\Delta(2\theta)cos\theta} \tag{2.2}$$

In case of epitaxial or strained films, the broadening of the peaks is not only a function of the size distribution of the grains, but also the residual strain in the films.

Figure 2.1 shows the schematic representation of a standard Bragg-Brentano diffractometer, with the Cu K_{α} (λ= 0.15418 nm) source and a scintillation detector. In the most frequently used θ-2θ or ω-2θ scan, for structural characterization, the detector

rotates twice as fast and in the same direction around the diffractometer axis as the sample. In θ-2θ scans, the reflections from the planes parallel to the substrate surface are detected helping to determine the orientation along the growth direction of a (epitaxial or polycrystalline) films with respect to the substrate.

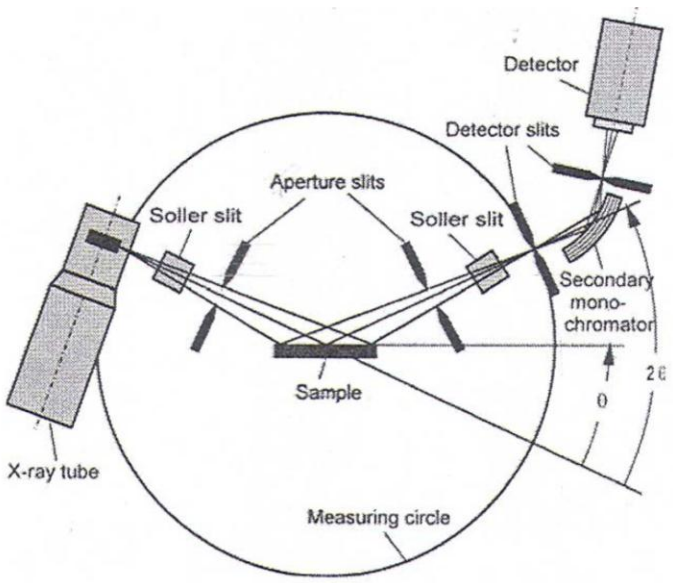

Figure 2.1: Schematic Representation of Bragg-Brentano Diffractometer.[190]

Reciprocal space mapping measurements are also performed with XRD for structural analysis. It is generally performed using an Eulerian cradle four-circle diffractometer, allowing access to a large volume of reciprocal space. A schematic of the four-circle geometry is shown in figure 2.2. The horizontal plane *H* is defined by the incident and diffracted beams; ψ is defined as the angle between the sample surface and plane *H* and ψ=0 when they are parallel. We have performed x-ray reciprocal space maps of symmetric Bragg reflection measurements using fixed ψ and varying ω about the 2θ value of a known peak.

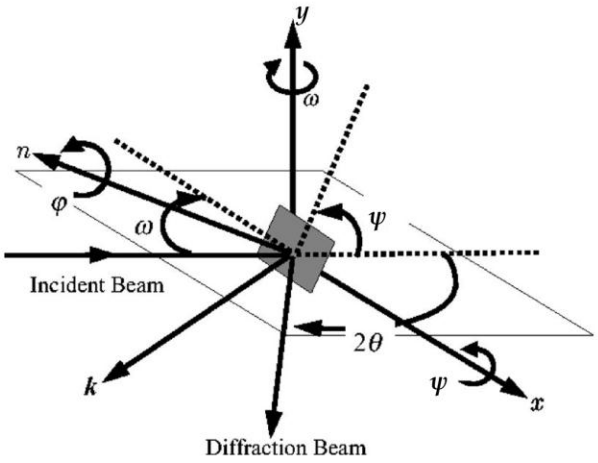

Figure 2.2: Schematic of a four-circle X-ray diffractometer.[191]

Preferred orientation is best described by means of a *Pole Figure*. A pole figure is a graphical representation of the orientation of objects in space. Pole figures in the form of stereographic projections are used to represent the orientation distribution of lattice planes in crystallography and texture analysis in materials science.

If we consider a plane of the object, the orientation of the plane can be given by its normal line. The intersection of the normal line and the sphere is the *pole***.** The orientation of the object is fully determined by the use of poles of two planes that are not parallel. A pole figure is a stereographic projection which shows the variation in pole density with pole orientation for a selected set of crystal planes. This method of describing texture was first used by the German metallurgist Wever in 1924.

2.2.3 Atomic Force Microscopy

In an atomic force microscope (AFM) an atomically sharp tip is scanned over a surface with feedback mechanisms that enable the piezo-electric scanners to maintain the tip at a constant force (to obtain height information), or height (to obtain force information) above the sample surface.[190, 192] Tips are typically made from Si_3N_4 or Si, and extended down from the end of a cantilever. The nanoscope AFM head employs an optical detection system in which the tip is attached to the underside of a reflective cantilever. A diode laser is focused onto the back of a reflective cantilever. As the tip scans the surface of the sample, moving up and down with the contour of the surface, the laser beam is

deflected off the attached cantilever into a dual element photodiode.The photodetector measures the difference in light intensities between the upper and lower photodetectors, and then converts to voltage signal. Feedback from the photodiode difference signal, through software control from the computer, enables the tip to maintain either a constant force or constant height above the sample.

In this work, the primary purpose of using AFM was to study the topography of the sample surfaces and quantitatively measure surface roughness (RMS or average surface roughness). Also, the AFM has scanners that are used to translate either the sample under the cantilever or the cantilever over the sample. By scanning in both directions, the local height of the sample is measured. Three dimensional topographical maps of the surface are then constructed by plotting the local sample height versus horizontal probe-tip position. Figure 2.3 shows a schematic of how an atomic force microscope functions.

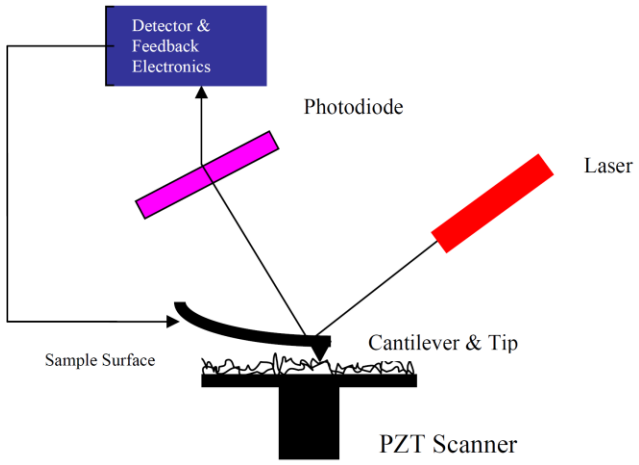

Figure 2.3: Schematic of an atomic force microscope.[190]

2.2.4 Transmission Electron Microscopy

The following discussion is adapted from the open source wikipedia article named Transmission Electron Microscopy[193] and the book by Williams and Carter.[194]

Transmission electron microscopy (TEM) is a microscopy- technique in which a beam of electrons is transmitted through an ultra thin specimen, interacting with the specimen as it passes through. An image is formed from the interaction of the electrons transmitted through the specimen; the image is magnified and focused onto an imaging device, such as a fluorescent screen, on a layer of photographic film, or on the sensor of a CCD camera.

TEMs are capable of imaging at a significantly higher resolution than visible light microscopes, owing to the small de Broglie wavelength of electrons. This is the biggest advantage of electron microscopes in general, allowing one to view finer details — even as small as a single column of atoms, which is four orders of magnitude smaller than the smallest resolvable object in a light microscope, making them indispensable in nanophysics and nanotechnology. The first TEM was built by Max Knoll and Ernst Ruska in 1931.

Electrons are usually generated in an electron microscope by a process known as thermionic emission from a filament, usually tungsten, or alternatively by field-electron emission. The electrons are then accelerated by an electric potential and focused by electrostatic and electromagnetic lenses onto the sample. The transmitted beam contains information about electron density, phase and periodicity and is used to form an image. Figure 2.4 is a schematic of the essential components of a transmission electron microscope.

From the top down, the TEM consists of an emission source, which may be a tungsten filament, or a lanthanum hexaboride (LaB_6) source. By connecting this gun to a high voltage source (typically ~100-300 kV) the gun emits electrons either by thermionic or field-electron emission into the vacuum. Once extracted, the upper lenses of the TEM allow for the formation of the electron probe to the desired size and location for later interaction with the sample.

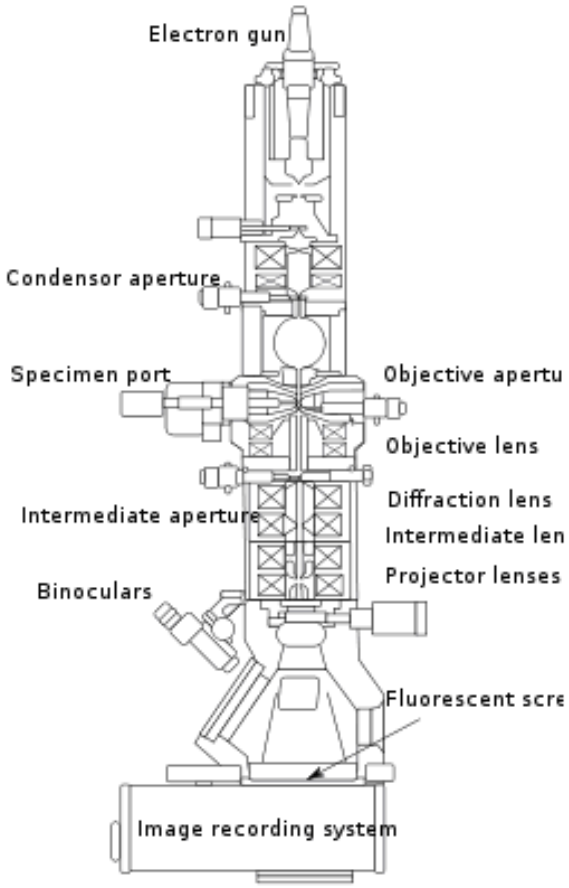

Figure 2.4: Schematic of a transmission electron microscope. [193]

Manipulation of the electron beam is performed using two physical effects. The use of magnetic fields allows for the formation of a magnetic lens of variable focusing power, the lens shape originating due to the distribution of magnetic flux. Additionally, electrostatic fields cause the electrons to be deflected through a constant angle. Coupling of two deflections in opposing directions with a small intermediate gap allows for the formation of a shift in the beam path, this being used in TEM for beam shifting, and is extremely important to STEM. The optical configuration of a TEM can be rapidly changed, unlike that for an optical microscope, as lenses in the beam path can be enabled, have their strength changed, or be disabled entirely simply by rapid electrical switching, the speed of which is limited by effects such as the magnetic hysteresis of the lenses.

Imaging methods in TEM utilize the information contained in the electron waves interacting during transmission through the sample to form an image. A set of projector lenses assist in the correct positioning of this electron wave distribution onto the viewing system. The observed intensity of the image, I, assuming sufficiently high quality of imaging device, can be approximated as proportional to the time-averaged amplitude of the electron wavefunctions, where the wave which form the exit-electron-beam is denoted by ψ.

$$I(x) = \frac{k}{t_1 - t_0} \int_{t_0}^{t_1} \psi\psi^* \mathrm{d}t \tag{2.3}$$

Different imaging methods therefore attempt to modify the electron waves exiting the sample in a form that is useful to obtain information with regards to the sample, or beam itself. From the previous equation, it can be deduced that the observed image depends not only on the amplitude of the beam, but also on the phase of the electrons, although phase effects may often be ignored at lower magnifications.

Higher resolution imaging requires thinner samples and higher energies of incident electrons. When the sample is thin enough it can safely be assumed, that it no longer absorbs electrons, via a Beer's law effect, instead the sample can be modeled as an object that does not change the amplitude of the incoming electron wavefunction, rather modifies the phase of the incoming wave; this model is known as a pure phase object. Thus for sufficiently thin specimens phase effects dominate the image, complicating analysis of the observed intensities.

Contrast formation in the TEM depends greatly on the mode of operation. Complex imaging techniques, which utilise the unique ability to change lens strength or to deactivate a lens, allow for many operating modes. Aberration-corrected lenses in recent times have greatly enhanced the ability to resolve and obtain more useful information from TEM imaging.

Bright field

The most common mode of operation for a TEM is the bright-field imaging mode. In this mode the contrast formation, when considered classically, is formed directly by occlusion

and absorption of electrons in the sample. Thicker regions of the sample, or regions with higher atomic numbers appear dark, while regions with no sample in the beam path appear bright – hence the term "bright field". The image is in effect assumed to be a simple two-dimensional projection of the sample down the optic axis, and to a first approximation may be modeled via Beer's law.

Diffraction contrast and dark-field

Samples can exhibit diffraction contrast, whereby the electron beam undergoes Bragg scattering, which in the case of a crystalline sample, disperses electrons into discrete locations in the back focal plane. By placement of apertures in the back focal plane, i.e. the objective aperture, the desired Bragg reflections can be selected (or excluded), thus only parts of the sample that are causing the electrons to scatter to the selected reflections will end up projected onto the imaging apparatus. If the reflections that are selected do not include the unscattered beam (which appear at the focal point of the lens), then the image will appear dark wherever no sample scattering to the selected peak is present. This is known as a dark-field image.

TEMs are also equipped with specimen holders that allow the user to tilt the specimen through a range of angles in order to obtain specific diffraction conditions, and apertures placed above the specimen allow the user to select electrons necessary for the purpose.

High-resolution TEM or Phase contrast microscopy

Crystal structure can also be investigated by high resolution transmission electron microscopy (HRTEM), also known as phase contrast microscopy. Image formation is given by the complex modulus of the wave function of incoming electron beams. As such, the image is not only dependent on the number of electrons hitting the screen, but also on the phase of the waves, making direct interpretation of phase contrast images more complex. However this effect can be used to an advantage, as it can be manipulated to provide more information about the sample, such as by complex phase retrieval techniques. When passing through a sample of uniform thickness, differences in phase of an electron wave is caused by specimen interaction. This phase difference is converted to contrast for image formation by comparison with a reference wave.

Selected Area Diffraction

By adjusting the magnetic lenses such that the back focal plane of the lens rather than the imaging plane is placed on the imaging screen a diffraction pattern can be generated. For crystalline samples, this produces an image that consists of a pattern of dots in the case of a single crystal, or a series of rings in case of a polycrystalline material. For the single crystal case the diffraction pattern is dependent upon the orientation of the specimen and the structure of the sample. This selected area electron diffraction (SAED) pattern provides information about the space group symmetries in the crystal and the crystal's orientation to the beam path. This is typically done without utilizing any information but the position at which the diffraction spots appear and the observed image symmetries.

Z-contrast STEM

Scanning Transmission Electron microscopy (STEM) is a type of aberration-corrected transmission electron microscopy (TEM) and is distinguished from conventional transmission electron microscopes by focusing the electron beam into a narrow spot which is scanned or rastered over the sample.

The rastering of the beam across the sample makes these microscopes suitable for analysis techniques such as mapping by energy dispersive X-ray (EDX) spectroscopy, electron energy loss spectroscopy (EELS) and annular dark-field (ADF) imaging. These signals can be obtained simultaneously, allowing direct correlation of image and quantitative data.

By using a STEM and a high-angle detector, it is possible to form atomic resolution images where the contrast is directly related to the atomic number (Z-contrast image). The directly interpretable Z-contrast image makes STEM imaging with a high-angle detector appealing. This is in contrast to the conventional high resolution electron microscopy technique, which uses phase-contrast, and therefore produces results which need interpretation by simulation. Figure 2.5 shows the basic differences between the operations of a TEM and an STEM.

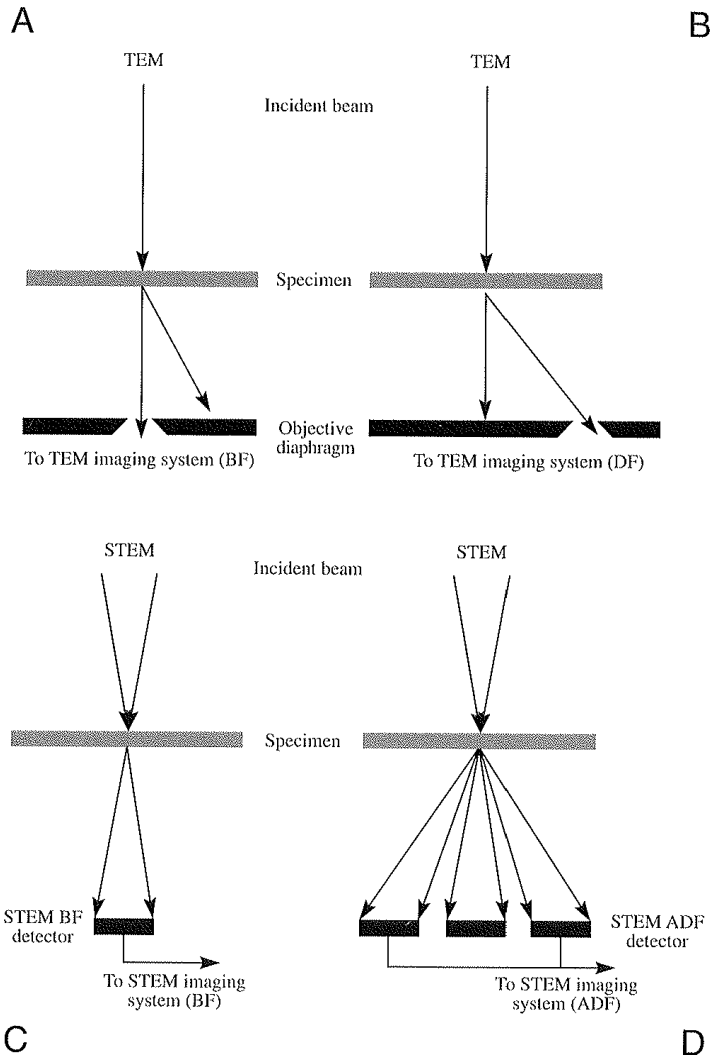

Figure 2.5: Comparison of TEM and STEM imaging conditions.[194]

Electron Energy Loss Spectroscopy (EELS)

In electron energy loss spectroscopy (EELS) a material is exposed to a beam of electrons with a known, narrow range of kinetic energies. Some of the electrons undergo inelastic scattering, which means that they lose energy and have their paths slightly and randomly deflected. The amount of energy loss can be measured using an electron spectrometer and interpreted in terms of what caused the energy loss. Inelastic interactions include phonon excitations, inter- and intra- band transitions, plasmon excitations, inner shell ionizations, and Čerenkov radiation. The inner-shell ionizations are particularly useful for detecting the elemental composition of a

material. Looking at a wide range of energy losses, one can determine the types of atoms, and the numbers of atoms of each type, interacting with the electron beam. The scattering angle (the deflection of the electron path) can also be measured, giving information about the dispersion relation of the material that caused the inelastic scattering. Figure 2.6 shows typical EELS data on our epitaxially-grown VO_2 films and compared to existing literature.

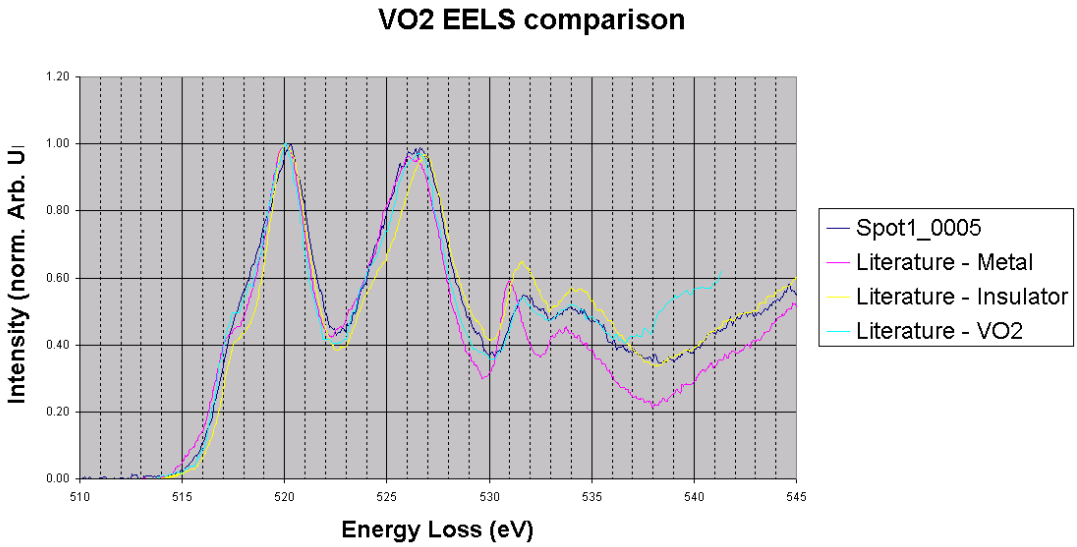

Figure 2.6: VO_2 EELS data obtained from our epitaxial films compared to existing literature. Courtesy: Felipe Rivera, Brigham Young University.

2.2.5 Scanning Electron Microscopy

The following discussion is along the lines of discussion found in MS thesis of Felipe Rivera.[195] The Scanning Electron Microscope (SEM) is a tool that allows for the imaging of micro and nanoscale objects with the use of electron beam, just as in case of transmission electron microscopy. The creation, acceleration and focusing of the electron beam in the scanning electron microscope is usually achieved in a similar way as discussed above for TEM. The electron beam then passes through a set of scanning or deflector coils that cause the beam to raster so that it may scan the sample (hence the name Scanning Electron Microscope). The beam is then allowed to interact with the sample and an image is formed by the interactions that take place between the electron-beam and the sample as the beam is scanned.

The interactions between the electrons and the sample allow for a rich amount of information that might be obtained in the SEM like in the case of TEM. Secondary electrons, backscattered electrons, characteristic X-rays, Auger electrons, and visible light are some of the results of the interaction during the scanning process. Depending on the detectors available, the SEM can be used to obtain a wealth of information regarding the specimen. Typically, the image is formed by using a secondary electron detector but more information can be extracted depending on the type of detector being used.

Under a typical imaging mode (secondary electron detector), the surface of the specimen is imaged without any other data collected. Another useful aspect of the SEM under imaging mode is the ability to tilt the specimen. Imaging a surface where the electron beam is normal to the thin film is commonly called a "plan-view." Imaging where the sample is placed so that beam is parallel to the films is commonly referred to as a "cross-sectional view." Tilts in the specimen anywhere between a plan and a cross-sectional view is referred to as tilted views[195]. For a thin film, imaging the surface at different angles can give information regarding the morphology of the thin film, as well as an estimate of the surface roughness. A tilted sample is required in order to obtain Electron Back-Scattered Diffraction (EBSD) patterns, and to perform Orientation Imaging Microscopy (OIM) analysis.

Electron Back-Scattered Diffraction and Orientation Imaging Microscopy

As the electron beam interacts with the sample, the electrons in the beam scatter in all directions (but mainly in the direction of the beam). If the sample is crystalline, then several of the scattered electrons inside the sample will find themselves in the Bragg condition. These electrons will scatter multiple times while remaining in the Bragg condition. This creates a "channeling" effect that allows electrons to escape the sample creating observable contrast.

These multiple scattering events (along with the radial symmetry rising from having electrons scattered in all directions) creates Kossel cones (see figure 2.7). Since most of the electrons that enter the sample scatter in the forward direction a tilted sample provides

the benefit of having a larger number of the scattered electrons close to the surface and able to exit the sample.[196]

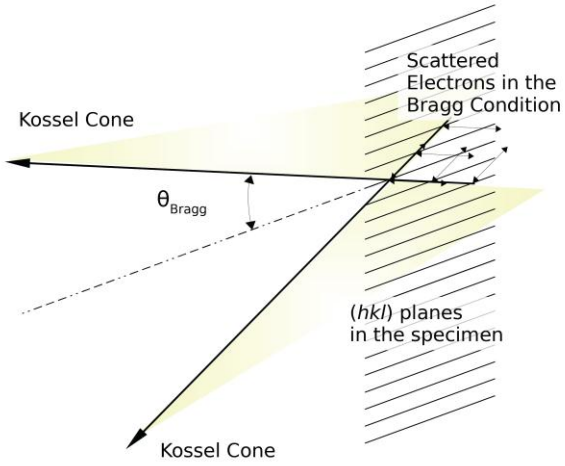

Figure 2.7: Kossel cone: Created by all electrons scattering under Bragg condition.[195]

The intersection of the Kossel cone with the Ewald sphere creates the condition necessary to observe a set of Kikuchi lines. Figure 2.8 shows a diagram of the Kossel cones, the (hkl) plane they represent, and the observed Kikuchi lines. Since the Kikuchi lines are formed by the intersection of a plane with a cone, they are conic sections (in this case, hyperbolas). However, since the angle between the plane and the Kossel cone is small, the Kikuchi bands look like lines.

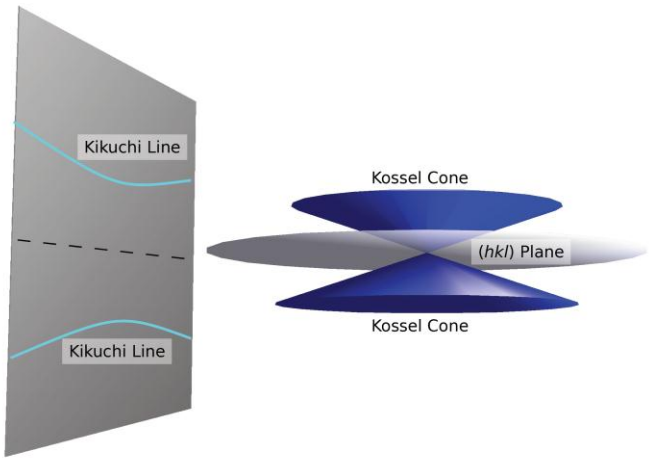

Figure 2.8: Kikuchi lines: the intersections of the Kossel cones with the phosphor screen.[195]

A full Electron Back-Scattered Diffraction (EBSD) pattern is formed by all the Kikuchi lines that intersect the phosphor screen (see figure 2.9). A full Orientation Imaging Micrograph (OIM) can then be obtained. This is done by letting the software collect EBSD patterns while a scan of the surface is being performed.

By this method, a map of the surface is created where individual grains are selected by sections of the scan having the same orientation. This method helps determine orientation of the grains in the surface, misorientations between grains, and grain sizes. The attainable resolution depends on factors such as the beam size, scan parameters, and quality of the sample.

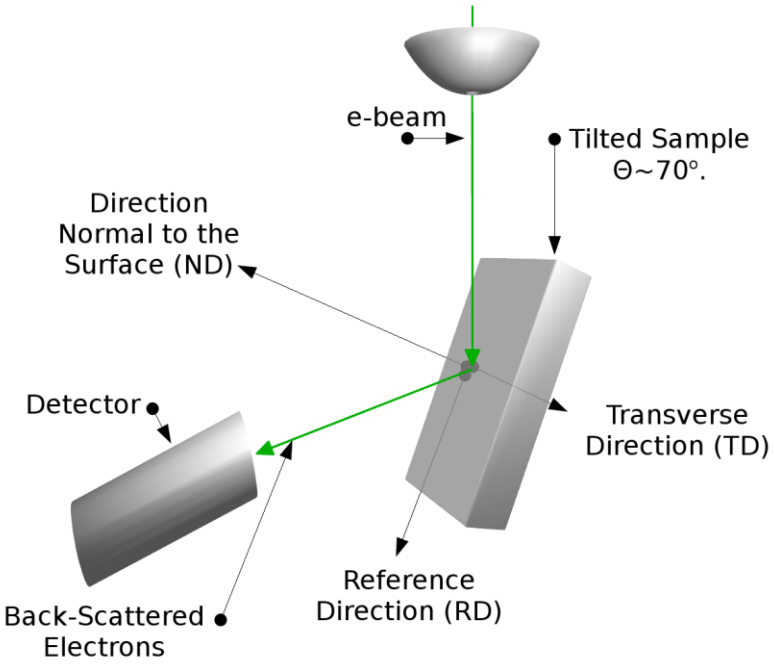

Figure 2.9: OIM: Kikuchi patterns are recorded and indexed simultaneously with the imaging scan.[195]

Electron Back-Scattered Diffraction (EBSD) patterns may also be simulated as they depend on the structure of the material being observed. Since EBSD is a diffraction technique, it can be used to index different crystallographic structures. The software

available for OIM uses these calculated diffraction patterns to compare them with obtained EBSD patterns. Some of the characteristics that are used for indexing the patterns include the angle between bands, distance among zones, and number of zones seen in the pattern. As observed from various calculations and experiments,[195] the change in symmetry of VO_2 yields some missing bands, but otherwise, the monoclinic and rutile VO_2 patterns are rather similar.

2.3 EPITAXIAL VO_2: GROWTH AND CHARACTERIZATION

Efforts at epitaxy at Vanderbilt started with trying to grow films on different planes of sapphire, or single-crystalline Al_2O_3, the advantages of which as a substrate have been stated earlier in section 2.1. This comparatively cheaper substrate was used to standardize the recipe for epitaxial growth. On the other hand, the lattice mismatches of sapphire and VO_2 are quite large. In spite of that, the fabrication and characterizations of epitaxial VO_2 films on sapphire helped our understanding about VO_2 epitaxy immensely and hence we will report in detail these characterization efforts in section 2.3.1. We then also tried to grow epitaxial VO_2 on different planes of single-crystalline rutile TiO_2, which have smaller mismatches because the lattice matches very closely with the high-temperature rutile phase of VO_2. In the section 2.3.2, we will describe the epitaxy on different planes of TiO_2 and their characterizations using different microscopy and diffraction techniques and also optical characterizations.

2.3.1 VO_2 on C-cut , A-cut and R-cut sapphire

The lattice planes of the C-cut (0001), A-cut $(11\bar{2}0)$ and R-cut $(1\bar{1}02)$ sapphire have been illustrated on the left-hand figures in figure 2.10, superposed with the unit cells of the VO_2 planes that epitaxially grow on top of them. The individual out-of-plane orientations of VO_2 are also schematically represented in the right-hand figures.

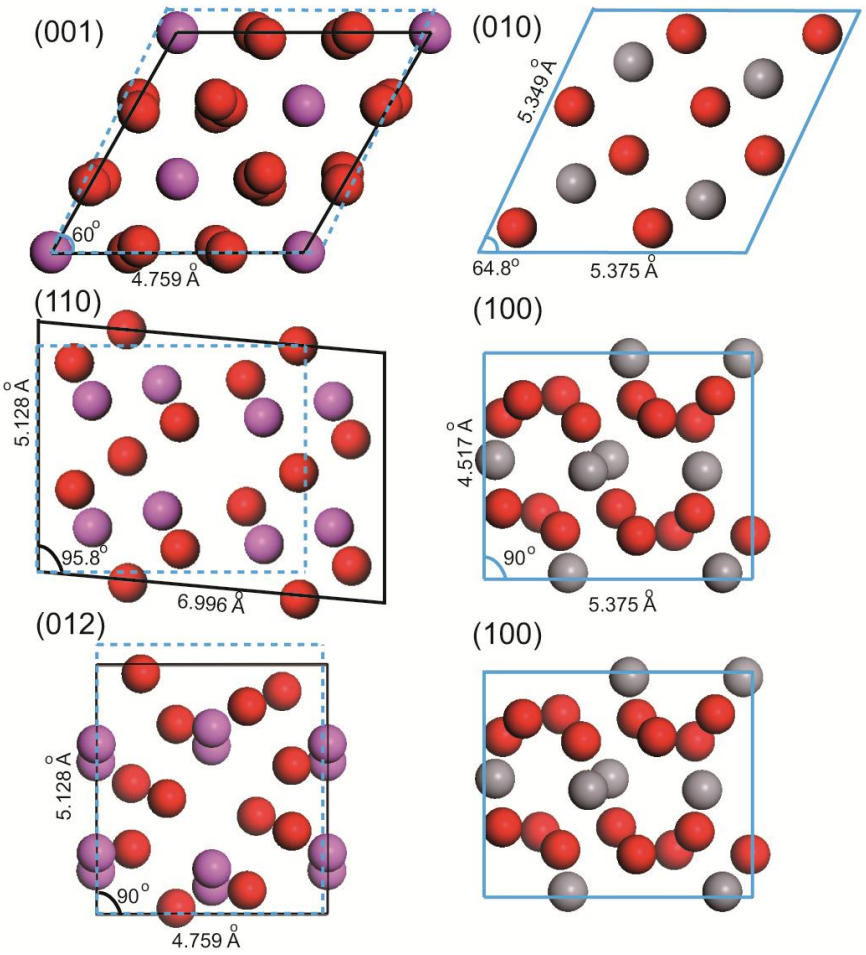

Figure 2.10: From top to bottom, schematic of lattice planes of C-, A- and R- cut sapphire used as substrates (left) and the corresponding planes of VO_2 film (right) that grow on top. The purple spheres indicate Al, grey spheres indicate V and red spheres correspond to oxygen atoms. The blue dotted lines are the VO_2 unit cells superposed on top of sapphire unit cells (black). Courtesy: Dr. Bin Wang, Vanderbilt University.

Note that R-cut has the closest lattice match with the VO_2 plane that orients itself on it whereas the match is worst in case of film on a-cut sapphire.

The following cleaning and deposition steps were found to yield good-quality epitaxial VO_2 on the chosen substrates:

1) Clean substrate: Ultrasonication for 5 minutes in solvents (TCE, acetone, methanol/IPA, deionized water)

2) Deposit VO_2 by PLD: V-metal target; 385 mJ pulses focused to ~0.3 cm^2 on target surface; 5 cm target-to-substrate distance; 50 mtorr O_2; substrate temperature : 500^oC.

When viewed in transmission against white light, a “switchable" VO_2 should appear dark golden-yellow to greyish-yellow, depending on thickness, roughness, etc.

To test for good-quality VO_2 material we performed the optical switching characterization in the vicinity of 340 K. The sharpness, contrast, and hysteresis of the IR transmission across the metal-insulator transition are directly related to the morphology and strain in the film. The transmission setup we used has the following components: (i) fiber-coupled light source, either an IR laser at λ = 1330 nm or a white-light tungsten-halogen lamp (a 3000K blackbody); (ii) mechanical chopper connected to a lock-in amplifier through a frequency generator; (iii) beamsplitter and CCD camera for visual inspection of the interrogated area via reflected and scattered light from the sample surface; (iv) one focusing and one collection low-magnification micro-objectives, with the sample in-between; (v) pinhole aperture (0.5 mm) for stray-light rejection; (vi) Thorlabs PDA10CS InGaAs IR detector with responsivity (amp/watt) greater than 10 % for λ = 700-1800 nm; (vii) lock-in amplifier, with input signals from the chopper and the detector, and output of amplified and filtered DC signal proportional to the intensity of the transmitted light. The sample with the film to be interrogated is mounted on a copper sample holder with a center hole for transmission and heated and cooled by a Peltier thermoelectric element. The temperatures are measured by a precision thermocouple (K-type calibrated from Omega Engineering, Inc.) in contact with the copper sample holder.

2.3.1.1 Epitaxial VO_2 on C-cut (0001) sapphire

The films grown on C-plane of sapphire have been characterized by white-light transmission measurements, X-ray diffraction (θ-2θ scans and reciprocal space mapping), SEM (regular, EBSD and OIM) and TEM (regular, HRTEM, SAED/FFT), AFM, etc.. We give a brief description and implication of each of them below.

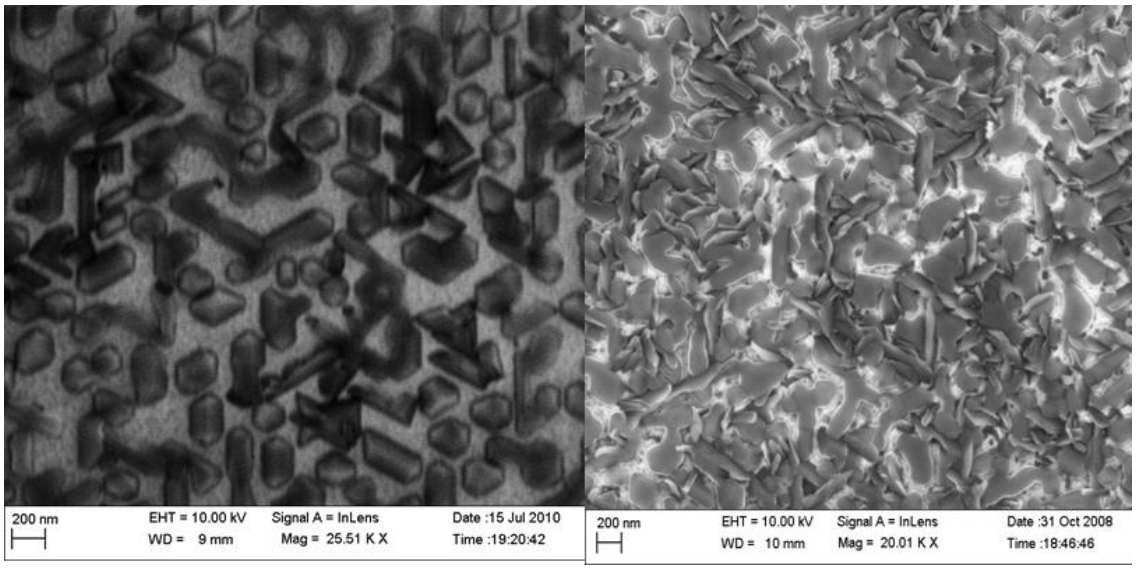

Figure 2.11: SEMs on thin (left) and thick (right) films of VO_2 on C-sapphire

Figure 2.11 shows the SEM of a thin (~35nm) and thick (~80nm) VO_2 film grown on (0001) sapphire grown following the high-temperature recipe. In the thinner film the six-fold symmetry of the film as it grows on sapphire is evident. Typical transmission hystereses obtained from these thin and thick epitaxial films on C-sapphire are shown in figure 2.12.

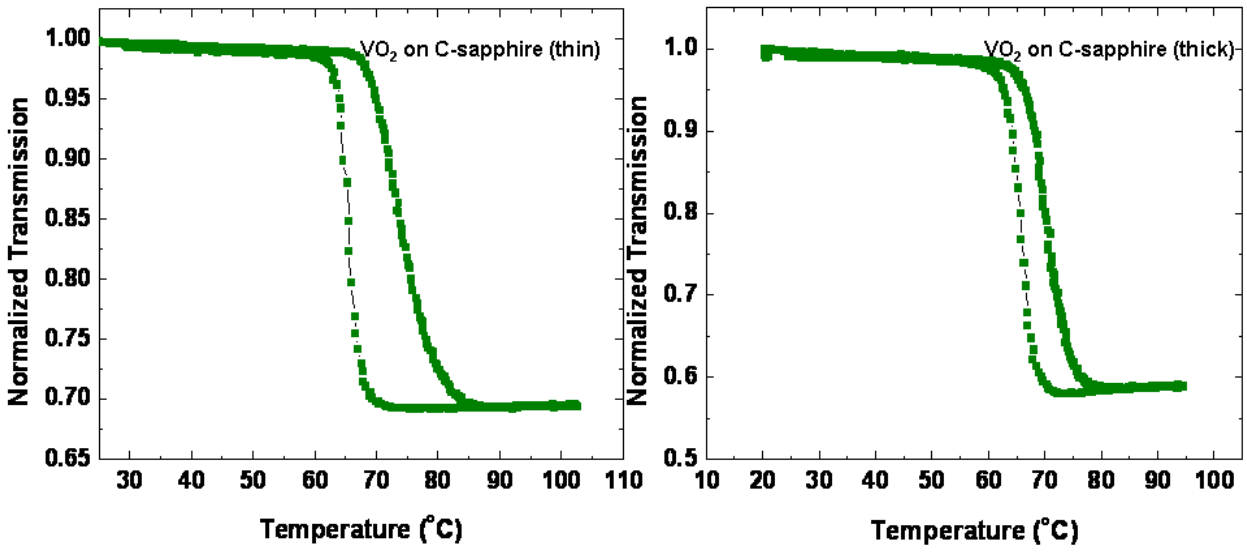

Figure 2.12: White-light transmission hystereses on thin (left) and thick (right) epitaxial VO_2 films on C-sapphire

The transition temperatures (T_c) and hystersis widths (ΔH) for the thin and thick films were measured to be T_{cthin} = 69.5 C, T_{cthick} = 70 C and ΔH_{thin} = 9 C, ΔH_{thick} = 6 C.

The out-of-plane and in-plane epitaxy of films grown on c-sapphire were determined using regular θ-2θ scans (as shown in figure 2.13) from which it is evident that (010) VO_2 grows out-of-plane on (0001) sapphire. The reciprocal space map (RSM) in figure 2.14 shows the RSM as ω-2θ rocking curves; these could equally well be plotted as k_x *vs* k_y plots. The intensities at specific positions on the RSM show that the film is epitaxial and specifies the in-plane epitaxial relationship between the film and the substrate where the center peak is the sapphire (116) peak and the triplet film peak corresponds to the (220) M1-VO_2. Thus (220) of M1-VO_2 aligns itself with (116) of sapphire.

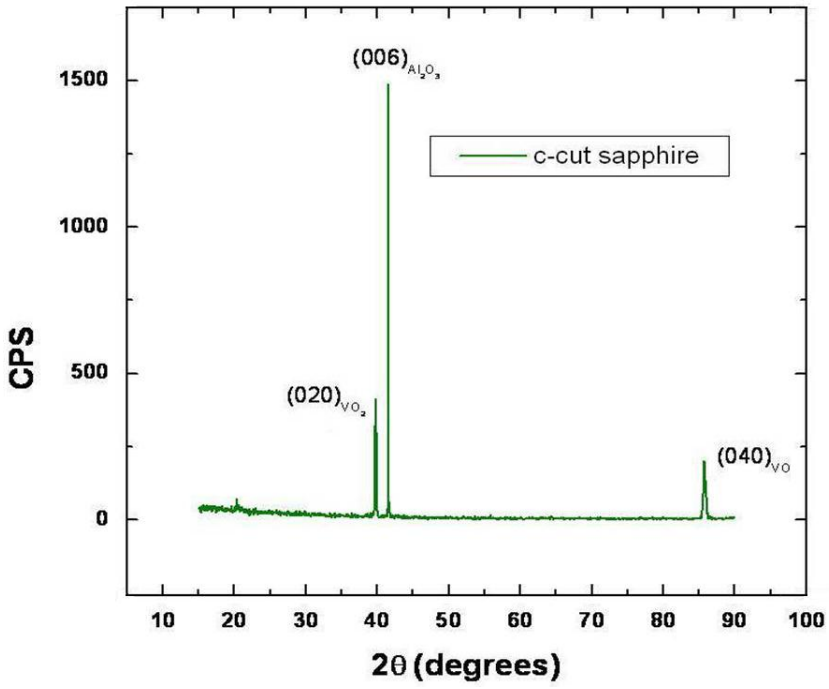

Figure 2.13: θ-2θ X-ray diffraction of a typical epitaxial VO_2 film on C-sapphire

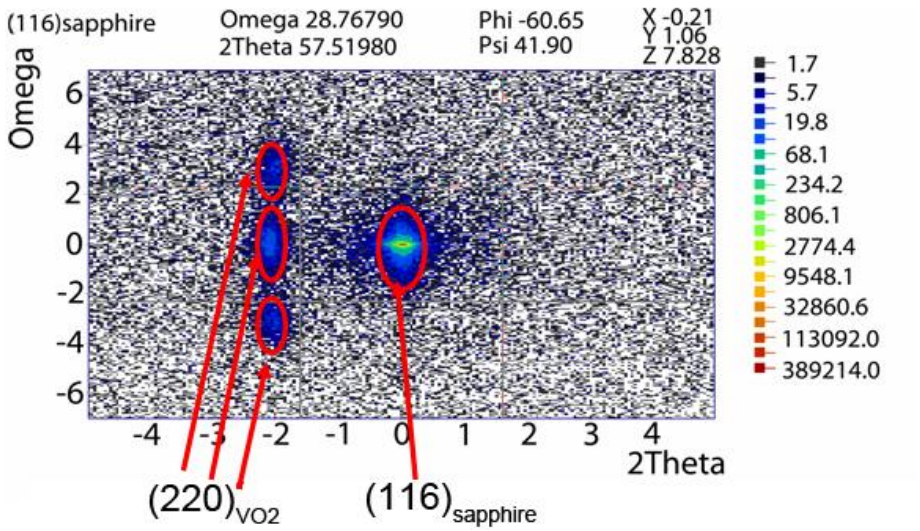

Figure 2.14: XRD reciprocal space map of epitaxial VO_2 film on C-sapphire about (116) direction of Al_2O_3

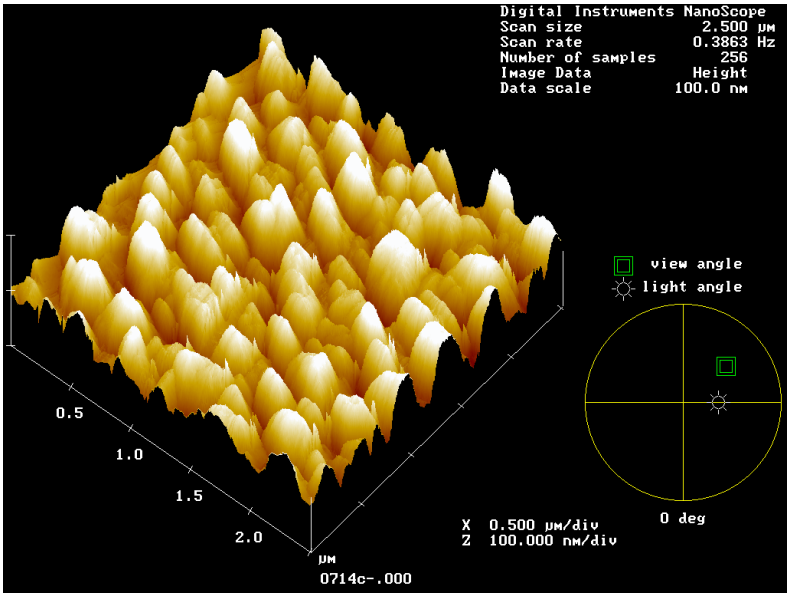

Figure 2.15: Atomic force microscopy image of epitaxial VO_2 film on C-sapphire

Atomic force microscopy on these films (figure 2.15), over 2.5 μm^2 area show that a film of 80 nm nominal thickness has about 23.5 nm RMS roughness. The autocovariance was

measured to be ~536 nm^2, which gives a measure of the lateral correlation length or long-range surface roughness parallel to the surface.

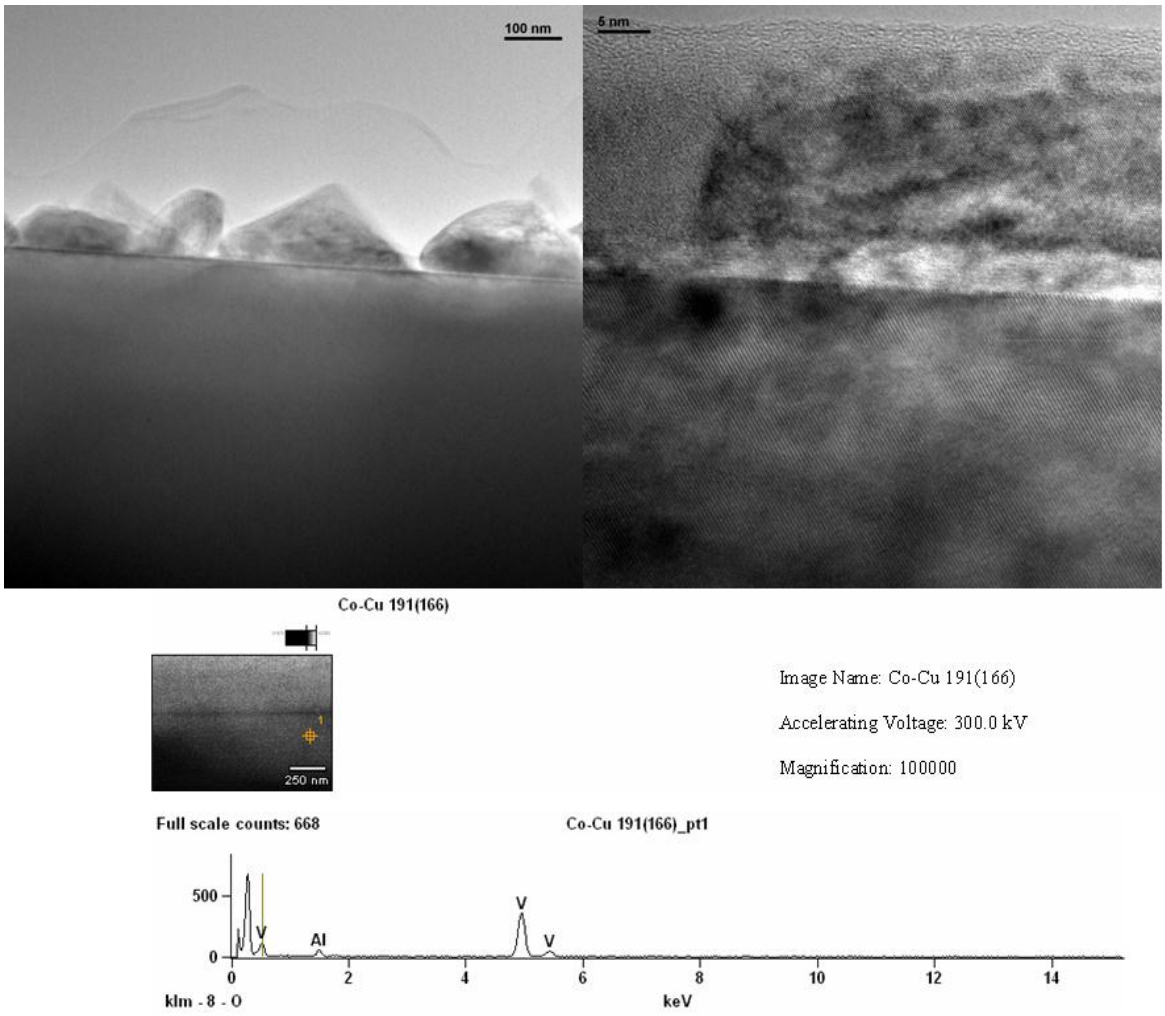

Figure 2.16: (a) TEM and (b) HRTEM of the VO_2-Al_2O_3 interface, and (c) energy dispersive spectroscopic scan taken across the interface

Our high-temperature growth recipe results in films that follow the island-growth mode with the pyramids being evident in the AFM in figure 2.15 as well as TEM in figure 2.16(a). Figure 2.16(b) is a high-resolution TEM (HRTEM) image of the interface between C-cut sapphire and VO_2 film on top of it. Evidently, this HRTEM and energy-dispersive spectroscopic measurement (figure 2.16 (c)) reveals an interdiffusion or buffer layer near each grain where Al, V and O are all present in non-stoichiometric proportions.

This interdiffusion layer exhibits a lattice spacing of 2.24 Å, a value in between that of the C-plane of sapphire (2.16 Å) and the (020) plane of VO_2 (2.42 Å). The Fast Fourier Transform (FFT) pattern (figure 2.17) taken across film-substrate interface show that the film is epitaxial, having definite in-plane orientation with respect to the substrate as the diffraction spots from the film, the interdiffusion layer (in HT-grown VO_2 only), and substrate line up or almost overlap.

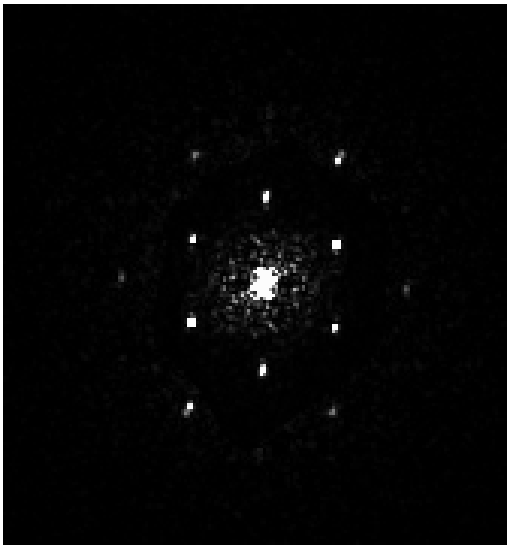

Figure 2.17: Fast Fourier transform image acquired across the film-substrate interface of epitaxial VO_2 on C-sapphire

Below is a Z-STEM picture of the interface of a VO_2 film on C-sapphire (figure 2.18). Since the vanadium atoms have large atomic mass compared to that of oxygen only the V columns are visible in the VO_2 film whereas both Al and O atoms are seen in the alumina substrate.

An EELS spectrum (figure 2.19) taken across the film-substrate interface shows that near the interface a V_2O_3 signal is obtained rather than VO_2, indicating that the VO_2 bonds to the Al_2O_3 surface through a V_2O_3 layer.

Figure 2.18: Z-contrast Scanning Transmission Electron Microscopy image of the VO_2-C-sapphire interface. Courtesy: Dr. Gerd Duscher, Oak Ridge National Laboratory.

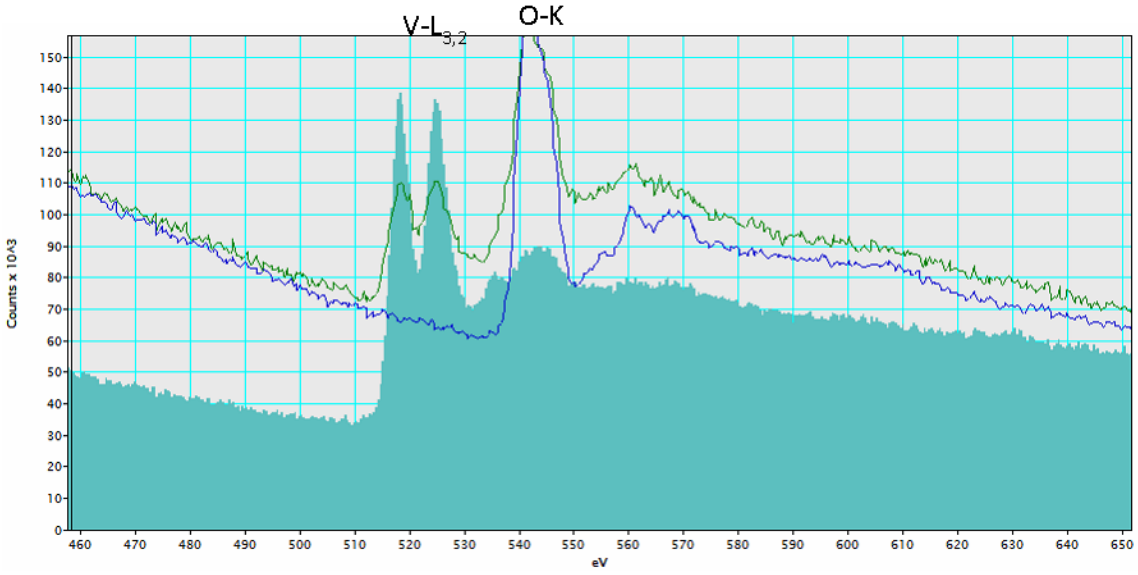

Figure 2.19: Electron energy loss spectra of the VO_2-C-sapphire interface. Courtesy: Dr. Gerd Duscher, Oak Ridge National Laboratory.

The electron backscattered diffraction (EBSD) pattern shown in figure 2.20, shows that (0001) of sapphire and (010) of VO_2 lines up exactly thus verifying the out-of-plane orientation of our films on C-sapphire.

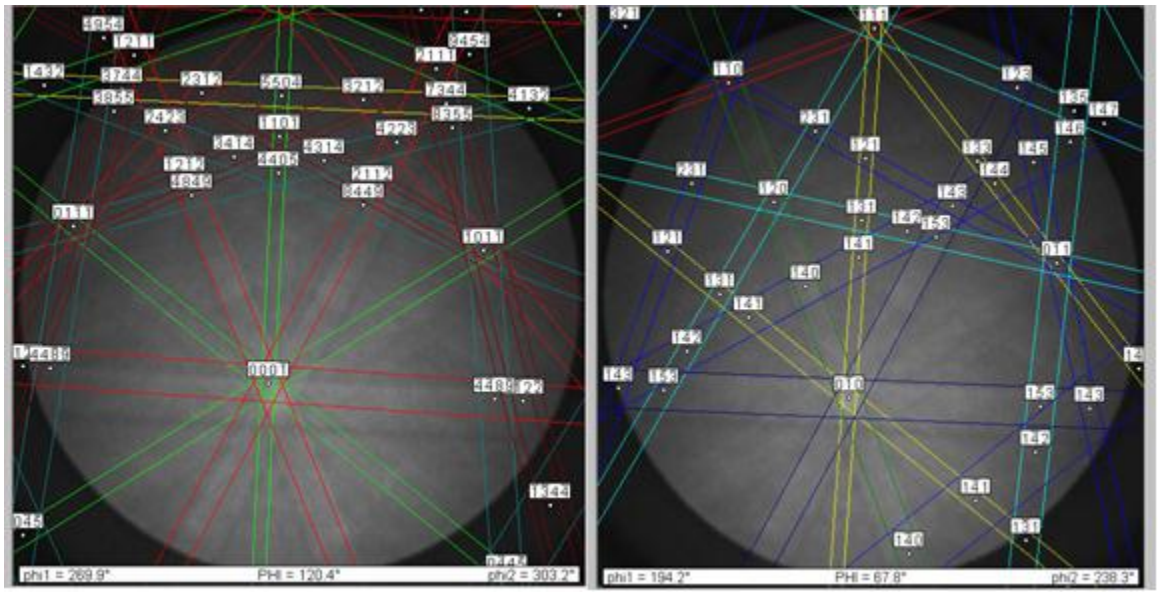

Figure 2.20: Indexed EBSD pattern showing the Kikuchi lines obtained on the substrate (left) and on the epitaxial VO_2 film (right) growing on C-sapphire. Courtesy: Felipe Rivera, Brigham Young University.

Orientation imaging microscopy (OIM) was also performed on the VO_2 films on c-sapphire in their high-temperature tetragonal phase, and the figures below represent the pole figures obtained (figure 2.21). We already know that (010) plane of VO_2 orients out-of-plane on c-sapphire. From the pole figures we see that (001) of VO_2 lies in the plane because its signature is observed only at a tilt angle of 90^o from the normal direction implying that it is completely in-plane. The (110) signatures appear at 45^o out-of-plane, consistent with the above results. For a schematic of the normal direction, transverse direction and reference direction refer back to figure 2.9.

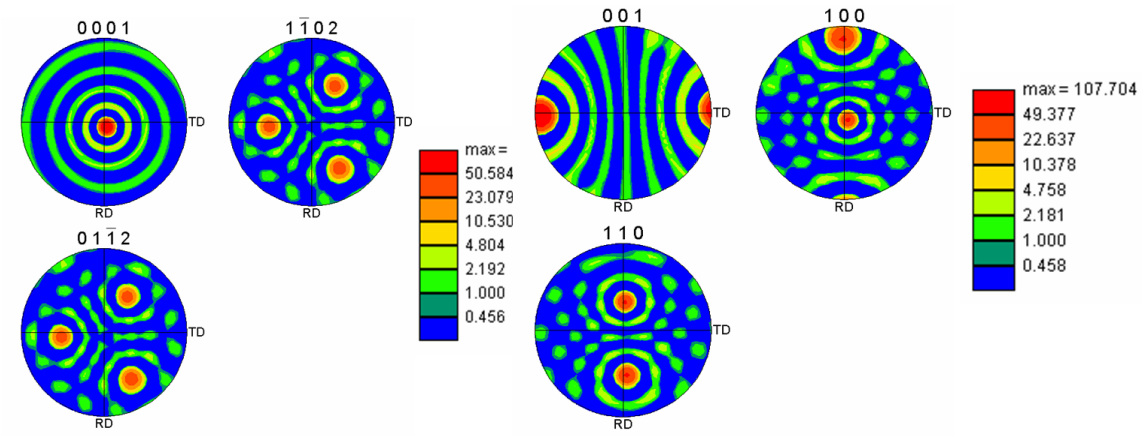

Figure 2.21: Orientation Imaging microscopy pole figures of the C-sapphire substrate (left) and the VO_2 film(right) showing the epitaxial relationship between the film and the substrate.Courtesy: Felipe Rivera, Brigham Young University.

2.3.1.2 Epitaxial VO_2 on A-cut $(1\bar{1}02)$ *sapphire*

Following similar lines of characterization as for the epitaxial VO_2 film on c-cut sapphire , now we report on the epitaxy on A-cut sapphire, that is, the $(1\bar{1}02)$ plane of sapphire. In the following figure 2.22 we see the typical SEM of a thin and a thick film of VO_2 on A-sapphire.

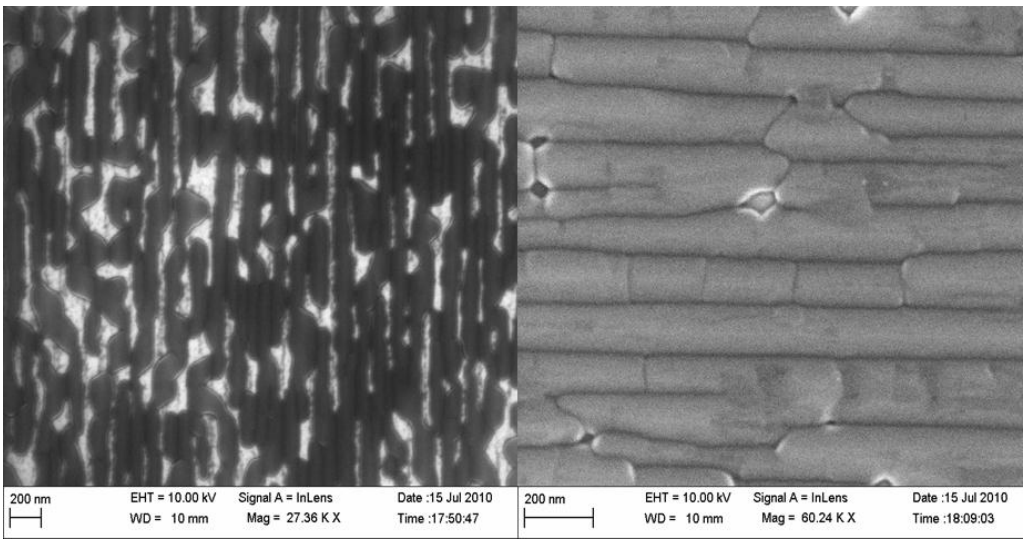

Figure 2.22: SEM of thin (left) and thick (right) epitaxial VO_2 films on A-sapphire

Atomic force microscopy image on one such film (figure 2.23), over 2.5 μm^2 area show that a film of about 50 nm nominal thickness has about 12nm RMS roughness. The autocovariance was measured to be ~514 nm^2, giving a measure of the lateral correlation length or long-range surface roughness parallel to the surface.

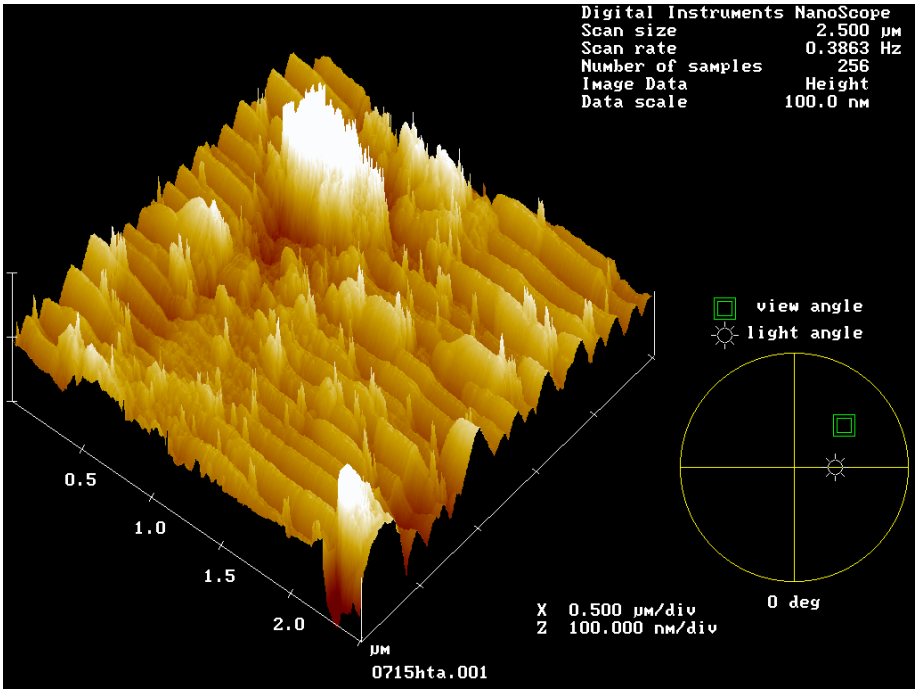

Figure 2.23: AFM image of a 35-40 nm thick epitaxial VO_2 film on A-sapphire

Typical white light transmission hystereses on a thin (~40 nm) and a thick (~80 nm) film on A-sapphire are presented in figure 2.24.

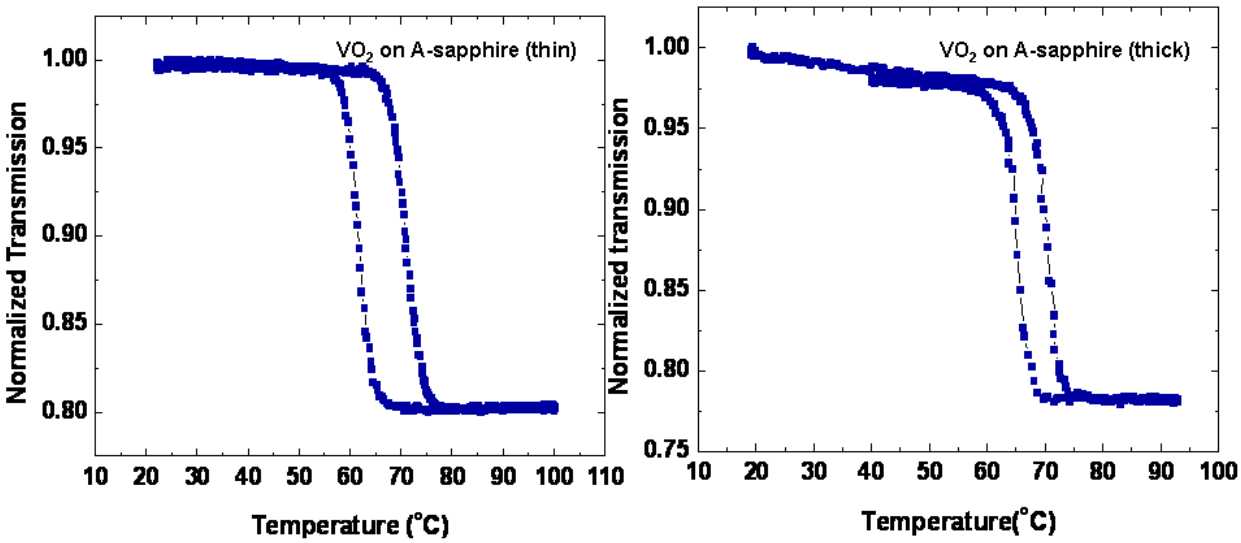

Figure 2.24: Typical transmission hystereses of thin (left) and thick (right) epitaxial VO_2 films on A-sapphire

The transition temperatures (T_c) and hystersis widths (ΔH) for the thin and thick films were measured to be T_{cthin} = 66.5 C, T_{cthick} = 70 C and ΔH_{thin} = 9 C, ΔH_{thick} = 8 C.

The out-of-plane orientation of films on A-sapphire obtained using XRD is shown in figure 2.25.

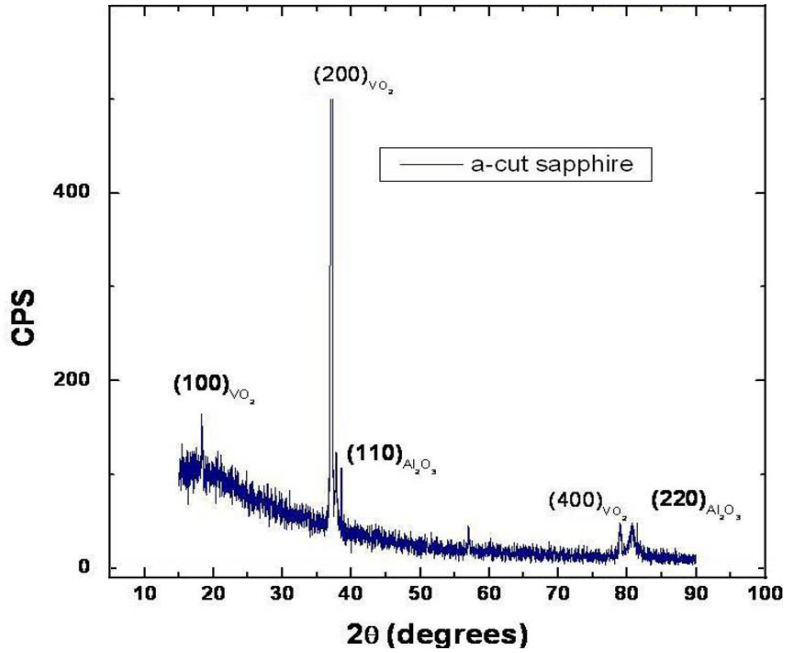

Figure 2.25: θ-2θ XRD spectrum of a typical epitaxial VO_2 film on A-sapphire

OIM maps of VO_2 on A-sapphire gives the complete orientation information of the films as is evident from figure 2.26.

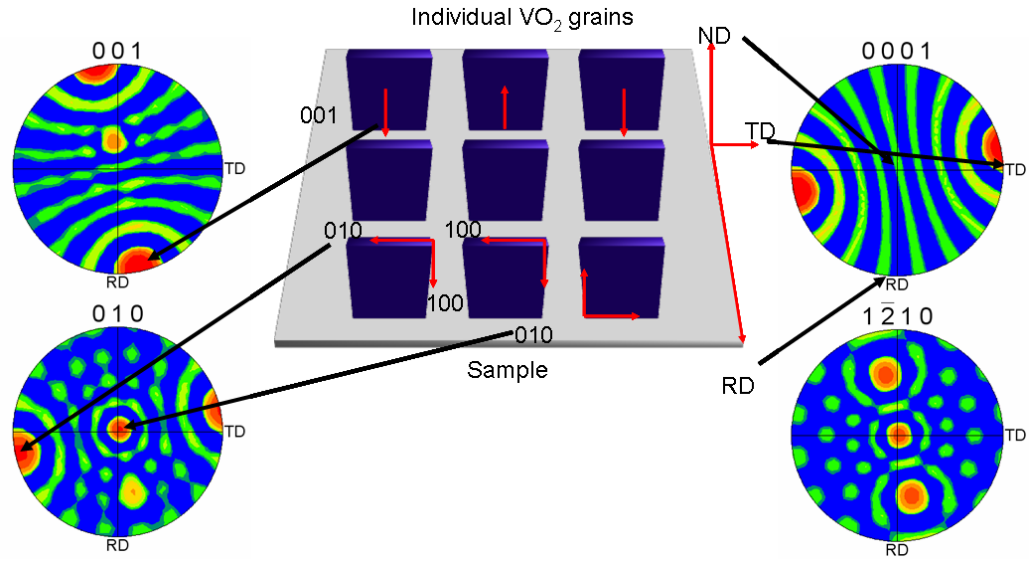

Figure 2.26: Orientation imaging microscopy images of VO_2 film (left) and A-sapphire (right) completely specifying the orientation of the film on the substrate as shown in the schematic in the middle. Courtesy: Felipe Rivera, Brigham Young University.

2.3.1.3 Epitaxial VO_2 on R-cut ($1\bar{1}02$) sapphire

For epitaxial VO_2 films grown on R-sapphire, figure 2.27 represents the SEM morphologies of very thin films in early growth stages to thick continuous films. The AFM image of a typical film of intermediate thickness is shown in figure 2.28. Over 2.5 μm^2 area, the film of about 80 nm nominal thickness has about 14.2 nm RMS roughness and an autocovariance of ~224 nm^2; for the thinner ~40nm thick film , RMS roughness of 7.5 nm and ~59 nm^2 autocovariance were recorded.

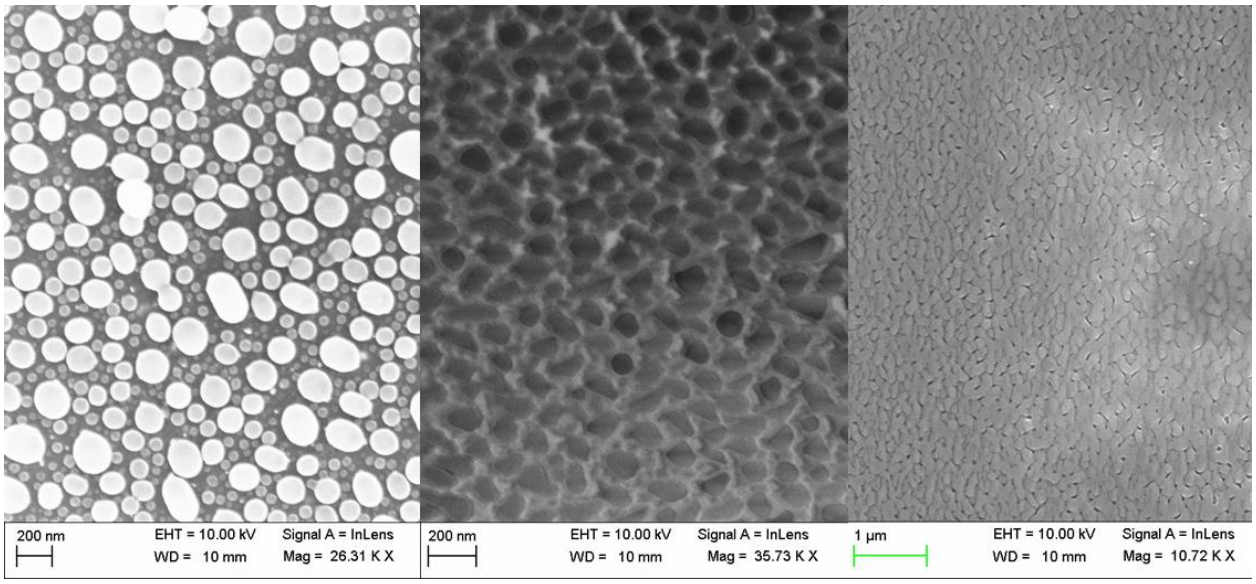

Figure 2.27: SEM morphologies of epitaxial VO_2 films on R-sapphire as thickness increase from left to right

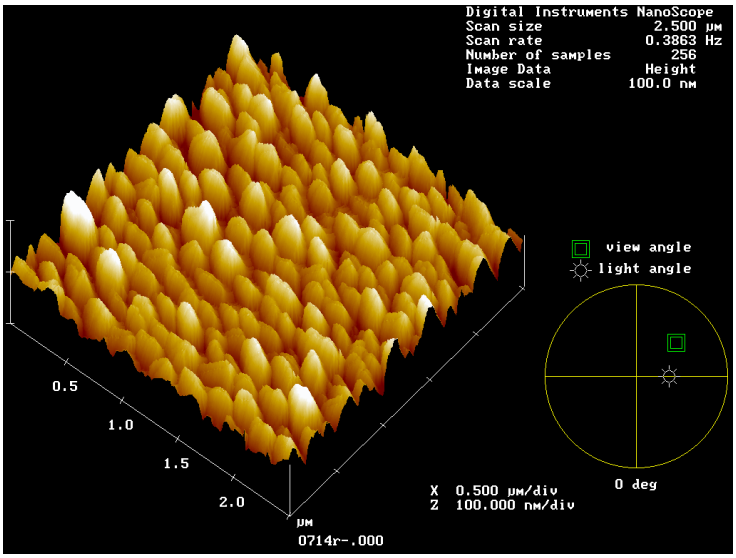

Figure 2.28: AFM image of the thinnest film on R-sapphire showing similar out-of-plane tendencies like films on C-sapphire in the early growth stages

Typical transmission hystereses of a thin and a thick epitaxial film on R-sapphire are shown in figure 2.29. The kink observed in the cooling curve of the hystersis for the thinner film is consistently present in all such films prepared and is attributable to the presence of two distinct sizes of grains, transitioning at two different temperatures.[197]

Transition temperatures (T_c) and hystersis widths (ΔH) for thin and thick films were measured to be T_{cthin} = 67 C, T_{cthick} = 60 C and ΔH_{thin} = 19 C, ΔH_{thick} = 2 C.

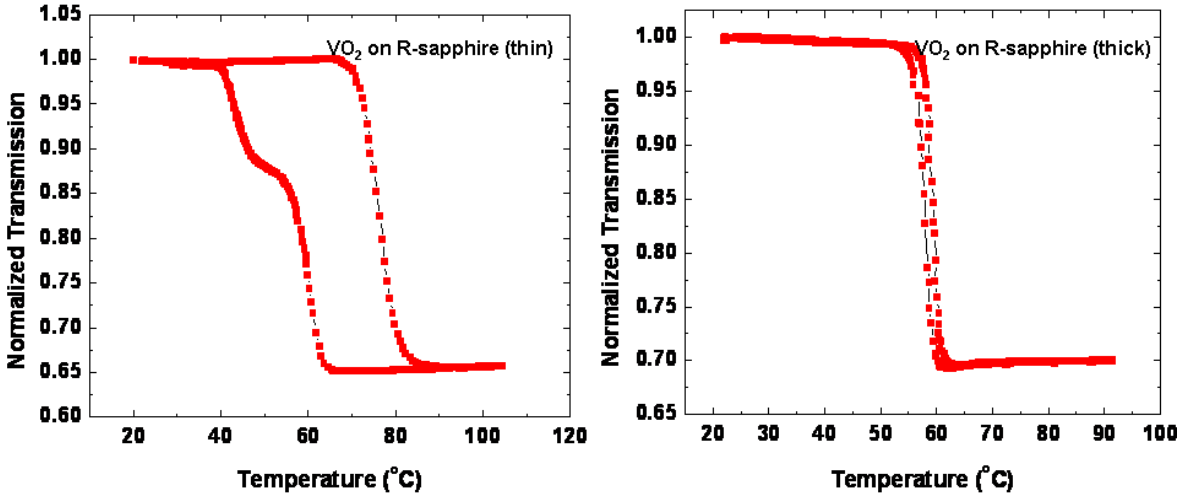

Figure 2.29: Transmission hystereses of thin (left) and thick (right) epitaxial VO_2 films on R-sapphire

The out-of-plane orientation of a film on R-sapphire is the same as that on A-sapphire as seen in figure 2.30, where (200) is again the out-of-plane orientation the VO_2 film as in the case of growth on A-sapphire.

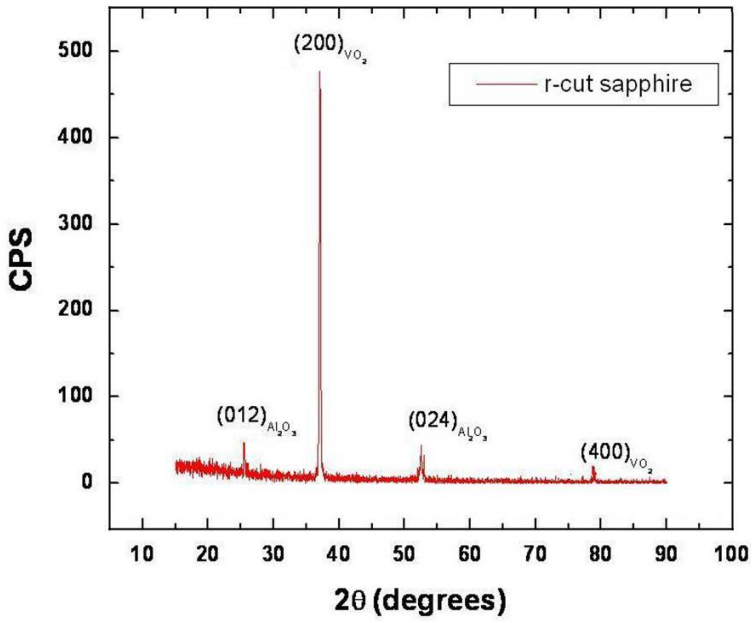

Figure 2.30: θ-2θ XRD spectrum giving the out-of-plane orientation of an epitaxial VO_2 film on R-sapphire

The TEMs below (figure 2.31) show the columnar growth of VO_2 grains on R-sapphire and figure 2.32 shows a clean interface with no evidence of intermixing as in case of C-sapphire.

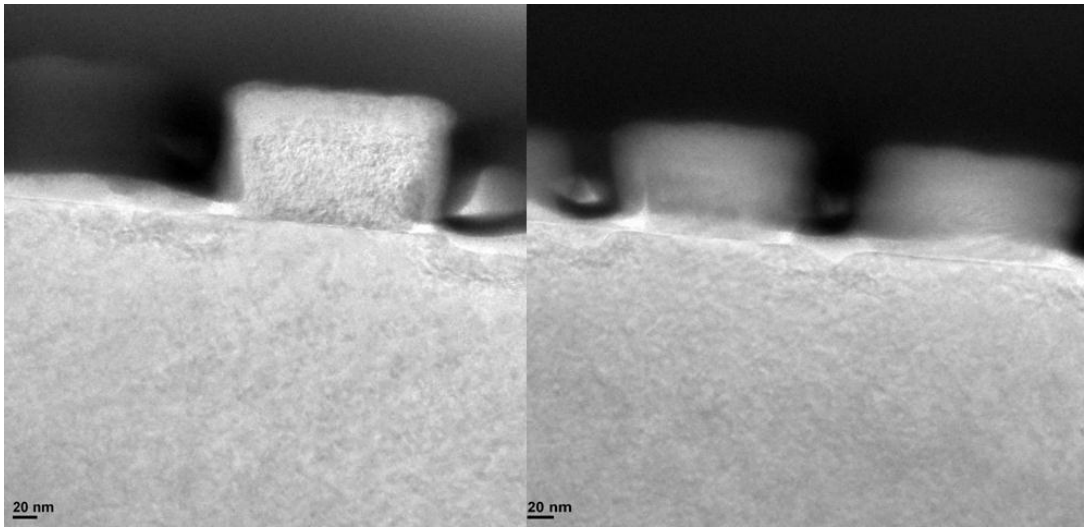

Figure 2.31: TEMs of the VO_2-R-sapphire interface showing rectangular columnar growth of the VO_2 grains

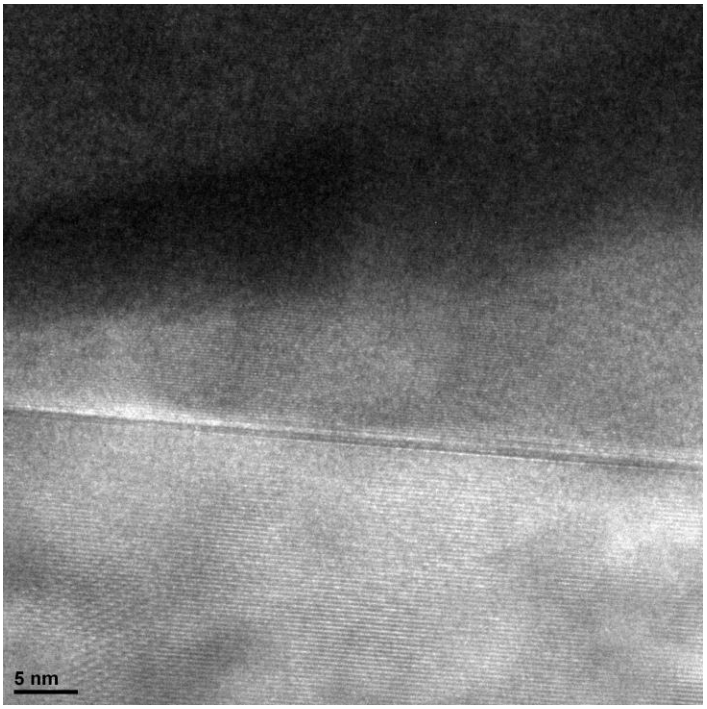

Figure 2.32: HRTEM of the VO_2-R-sapphire interface showing a clean interface

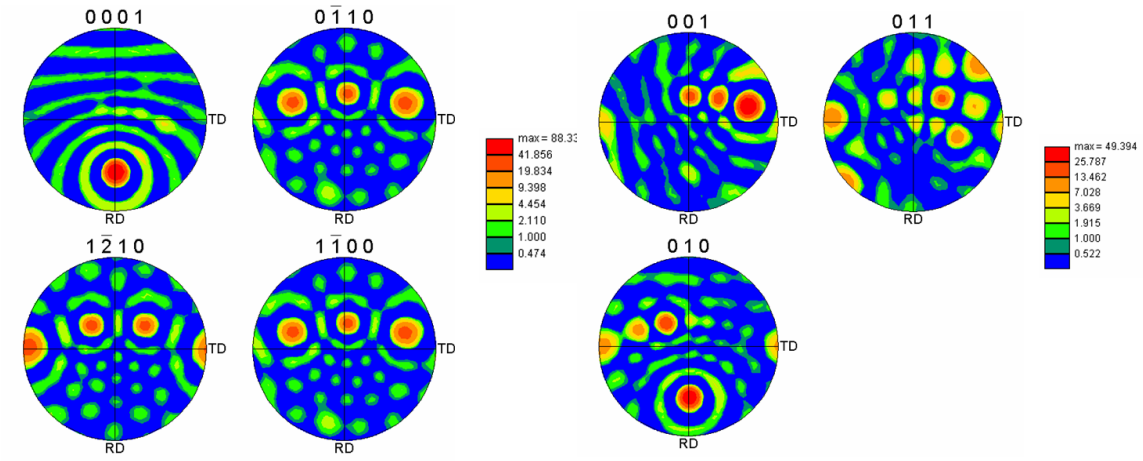

Figure 2.33: OIM pole figure of R-sapphire (left) and VO_2 (right) growing on top of it indicating the epitaxial preference. Courtesy: Felipe Rivera, Brigham Young University.

As is evident from the OIM pole figures in figure 2.33, the epitaxial orientation preference of the VO_2 films on sapphire substrates is that -- (010) of VO_2 always aligns with the (0001) direction of sapphire, be it out-of-plane like in case of C-sapphire or in-plane like in case of A and R-sapphire.

2.3.2 Epitaxy on different planes of TiO_2

Ti is a neighboring element of V in the periodic table. Its most stable oxide, rutile TiO_2 has a unit cell with lattice parameters closest to that of VO_2 as well. We have grown VO_2 on these very low (<1%) mismatch substrates – the three different planes of TiO_2 – (001), (110) and (100). Figure 2.34 shows the unit cell matching of the respective TiO_2 substrate planes and the VO_2 film planes that grow on top.

Note that two unit cells of TiO_2 (001) fit almost perfectly with the VO_2 ($\bar{4}02$) unit cell and four unit cells of TiO_2 (110) fit almost exactly with VO_2 (011) unit cell whereas even the match between TiO_2 (100) and VO_2 (010) though not perfect is pretty small to allow nice epitaxial growth.

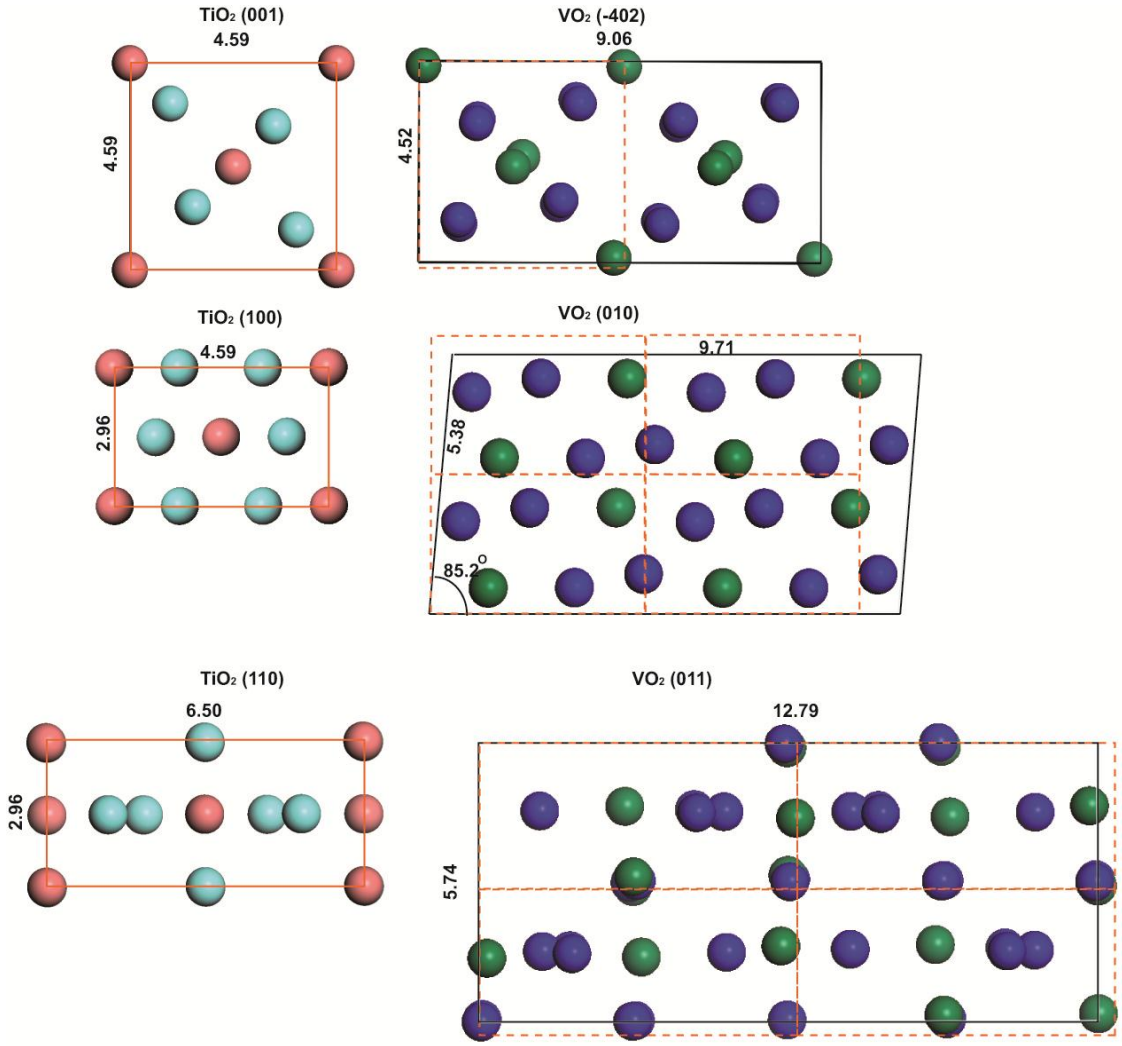

Figure 2.34: Schematic representation of the TiO_2 substrate planes and the respective VO_2 planes that grow on top of them. Courtesy: Dr. Bin Wang, Vanderbilt University

2.3.2.1 Epitaxial VO_2 on TiO_2 (001)

The probable interfacial bonding of VO_2 on top of TiO_2 (001) is schematically represented in figure 2.35.

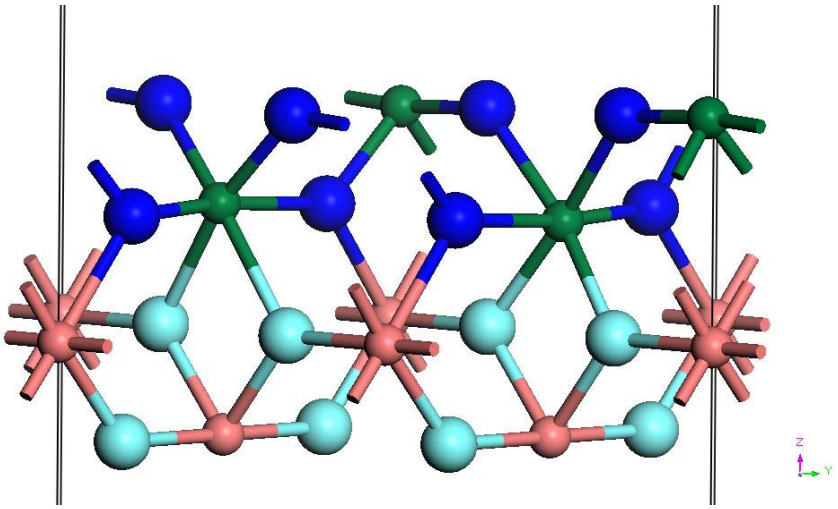

Figure 2.35: Schematic of the idealized interface bonding for VO_2 on top of TiO_2 (001). Courtesy: Dr. Bin Wang, Vanderbilt University.

Following the same lines as above the films on TiO_2 have also been characterized using SEM, AFM, white light transmission measurements, XRD, OIM, etc. Figures 2.36-2.39 give the morphology and hysteresis behavior of such films.

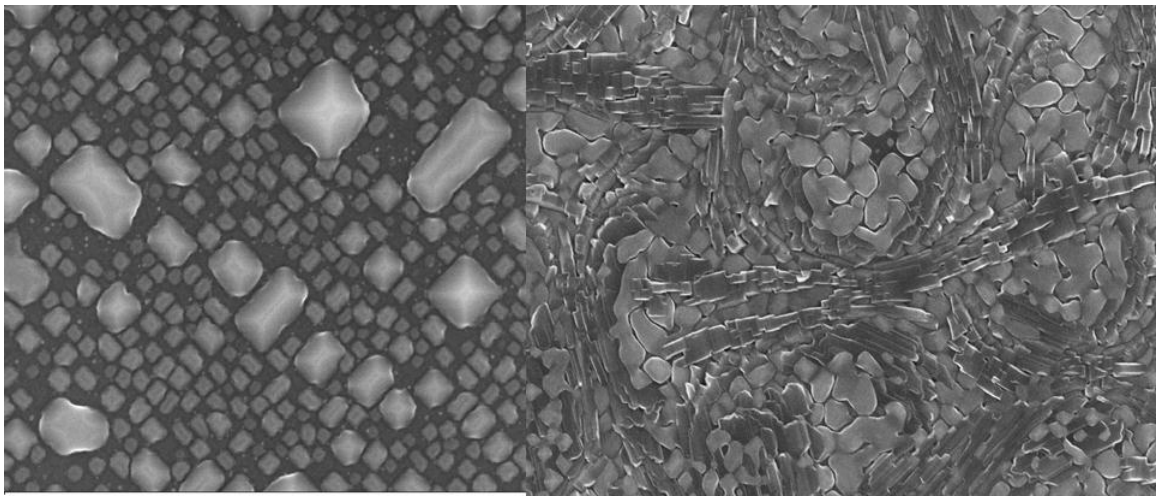

Figure 2.36: SEM morphologies of thin (left) and thick (right) epitaxial VO_2 films on TiO_2 (001)

The transition temperatures (T_c) and hystersis widths (ΔH) for the thin and thick VO_2 films on TiO_2 were measured to be T_{cthin} = 52.5 C, T_{cthick} = 58.5 C and ΔH_{thin} = 6 C, ΔH_{thick} = 3.5 C.

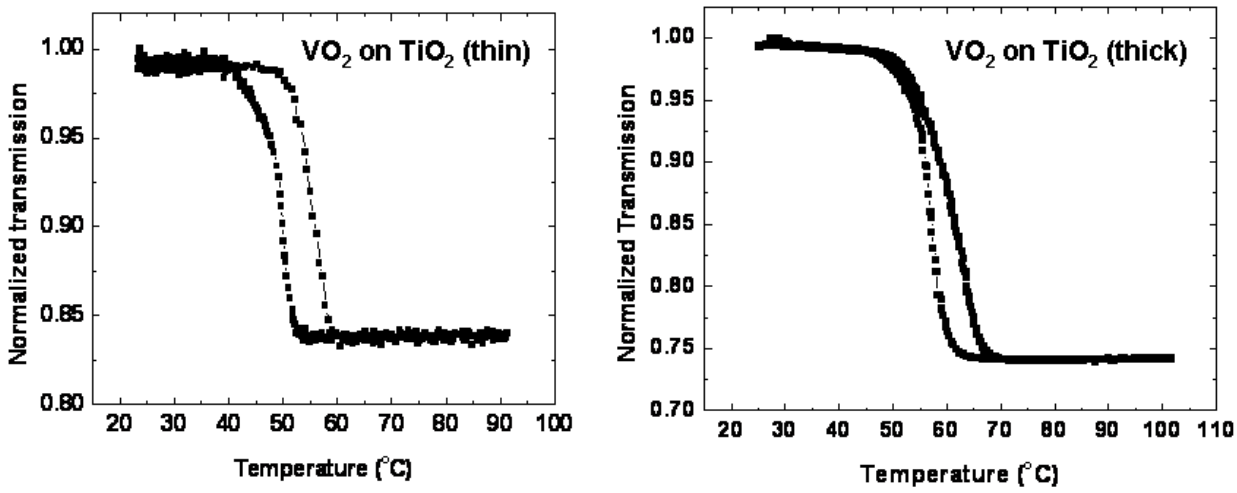

Figure 2.37: Transmission hystereses of thin (left) and thick (right) epitaxial VO_2 films on TiO_2 (001)

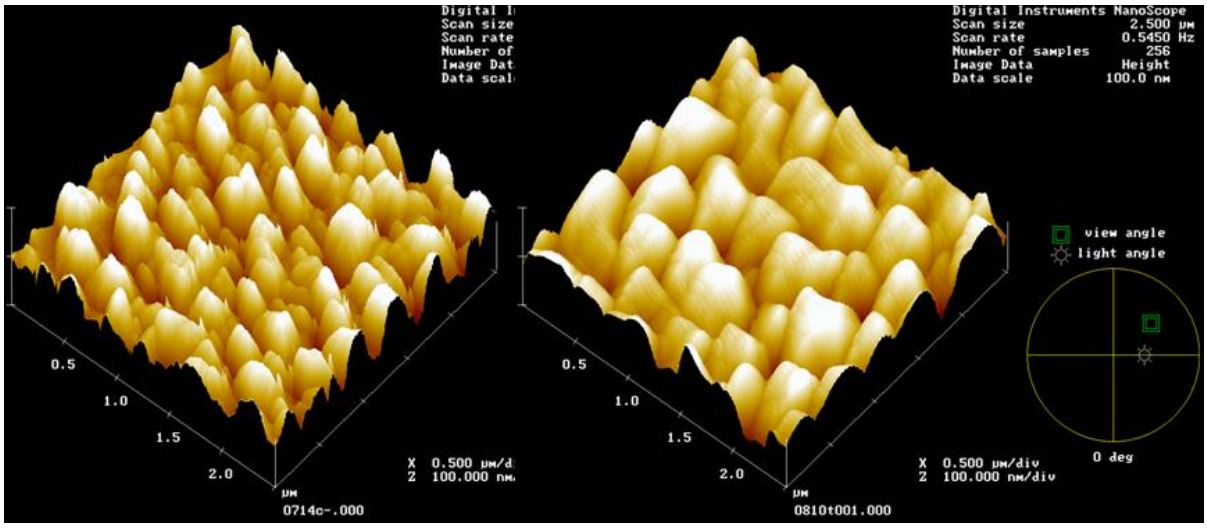

Figure 2.38: AFM images of thin (left) and thick (right) epitaxial VO_2 films on TiO_2 (001)

Atomic force microscopy on these films (figure 2.38), over 2.5 μm^2 area show that a film of about 80 nm nominal thickness has about 16 nm RMS roughness and an autocovariance of about ~270 nm^2 and a film of about ~200 nm thickness has ~39 nm RMS roughness and autocovariance of ~ 1258 nm^2.

To determine the epitaxial relationship between the film and the substrate, a regular θ-2θ XRD as in figure 2.39 was obtained. For in-plane epitaxial orientation information, figure

2.40 was obtained at a tilt angle of $\psi = 42.5^{o}$ for (111) direction of TiO_2 and close to it a (012) monoclinic peak is obtained which corresponds to the (111) plane of rutile VO_2. This indicates that during growth the (111) direction of VO_2 prefers to orient itself with the (111) direction of VO_2. This trend was observed for growth on all the three planes of TiO_2.

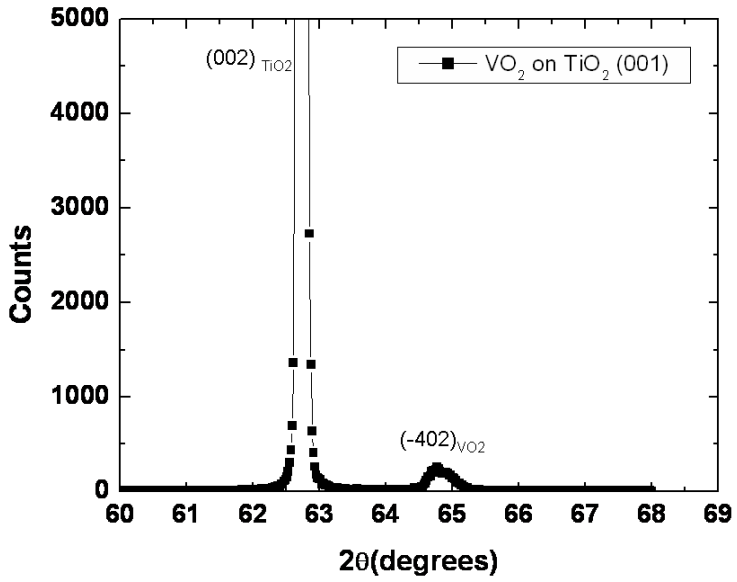

Figure 2.39: θ-2θ XRD on epitaxial VO_2 on TiO_2 showing a preferential orientation of $(\bar{4}02)$ of VO_2 on TiO_2 (001)

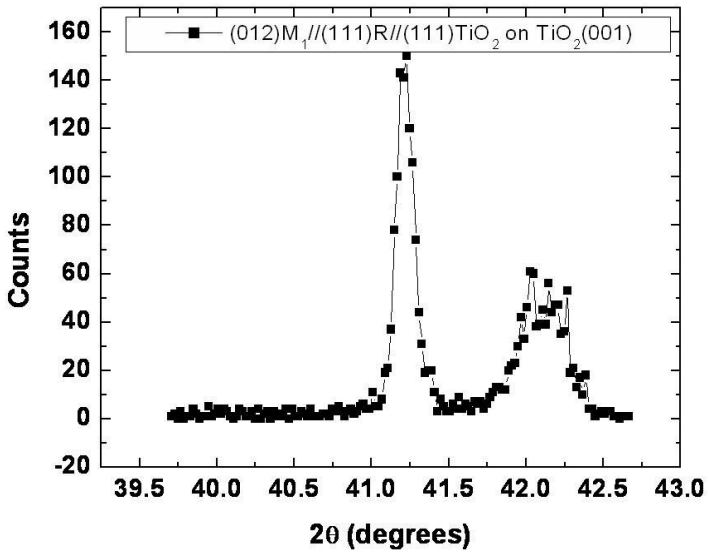

Figure 2.40: XRD at $\psi = 42.5^{o}$ for (111) plane of TiO_2, with a VO_2 (012) peak close to it showing the preferential orientation

The OIM pole figures (in figure 2.41) of the film (left) and substrate (right) shows the complete epitaxial relationship of an epitaxial VO_2 film on TiO_2.

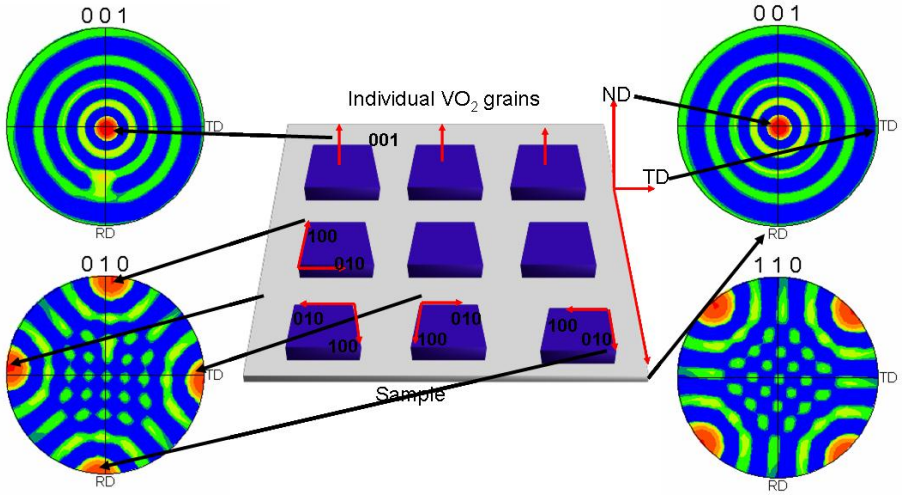

Figure 2.41: OIM pole figures of the film (left) and substrate (right) giving the complete orientation of the VO_2 film on TiO_2 (001), as shown in the middle. Courtesy: Felipe Rivera, Brigham Young University.

2.3.2.2 Epitaxial VO_2 on TiO_2 (110)

The match of the (011) VO_2 that grows on top of (110) TiO_2 has a near-perfect interface as seen in figure 2.42.

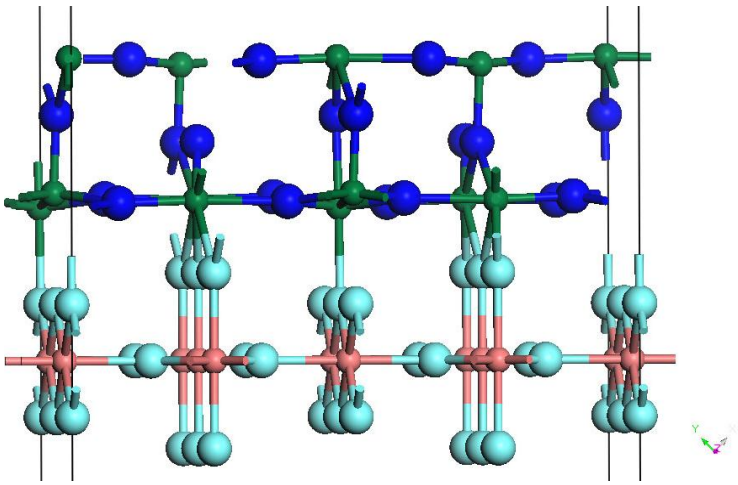

Figure 2.42: Schematic of the idealized interface of (011) VO_2 that grows on top of TiO_2 (110). Courtesy: Dr. Bin Wang, Vanderbilt University.

Figures 2.43-2.46 show the surface morphology and hysteresis behavior of thin and thick epitaxial VO_2 film on TiO_2(110).

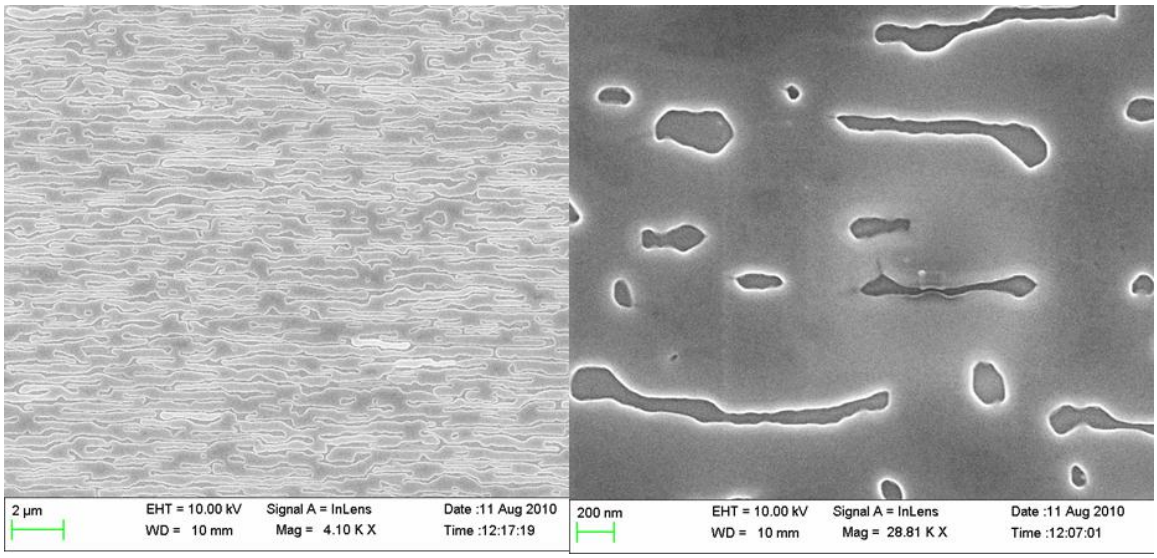

Figure 2.43: SEM images of thin (left) and thick (right) epitaxial VO_2 films growing on TiO_2(110)

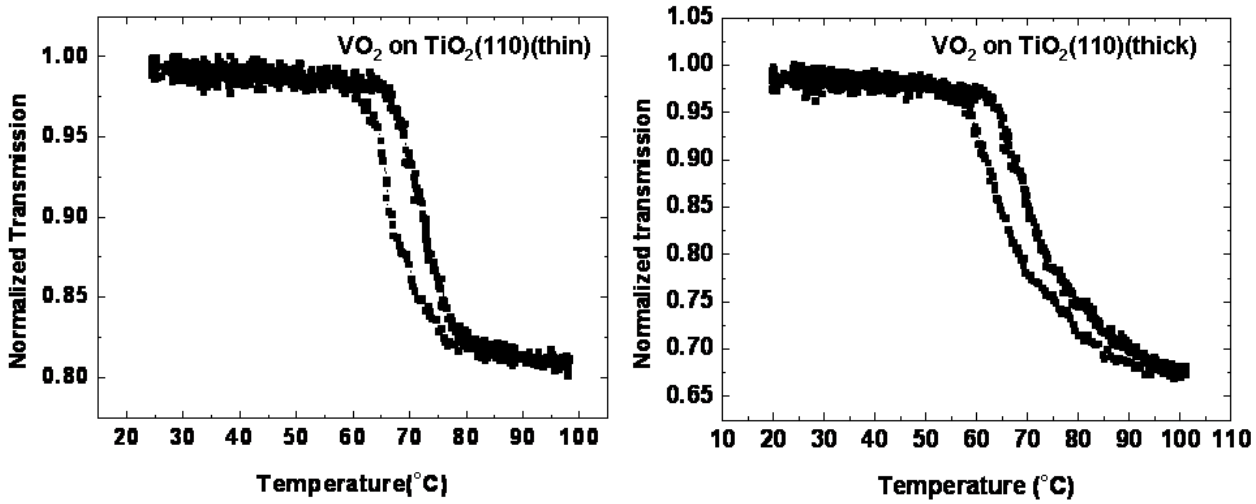

Figure 2.44: Transmission hystereses of thin (left) and thick (right) epitaxial VO_2 films growing on TiO_2(110)

The transition temperatures (T_c) and hystersis widths (ΔH) for the thin and thick films were measured to be T_{cthin} = 69.5 C, T_{cthick} = 68.5 C and ΔH_{thin} = 5 C, ΔH_{thick} = 6 C.

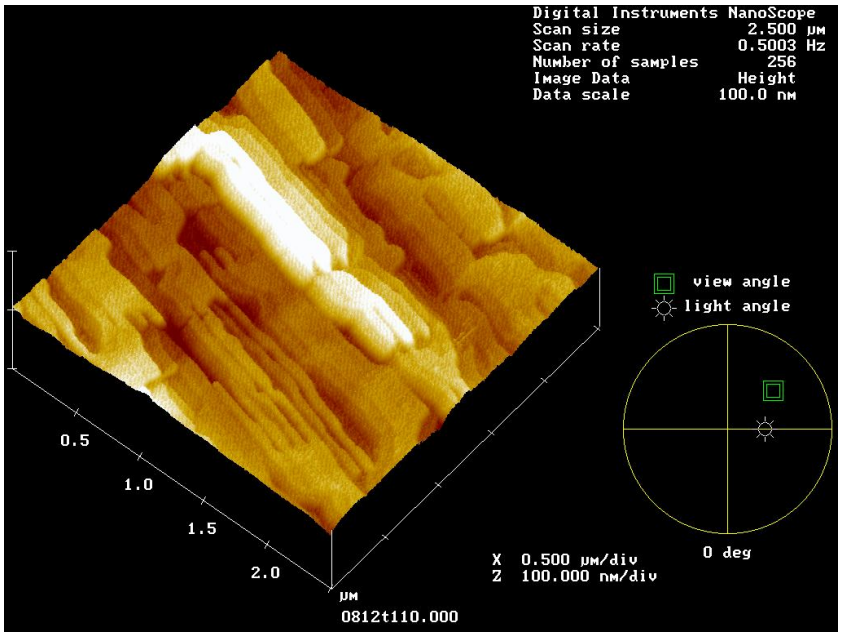

Figure 2.45: AFM image of a thin epitaxial film of VO_2 on TiO_2(110)

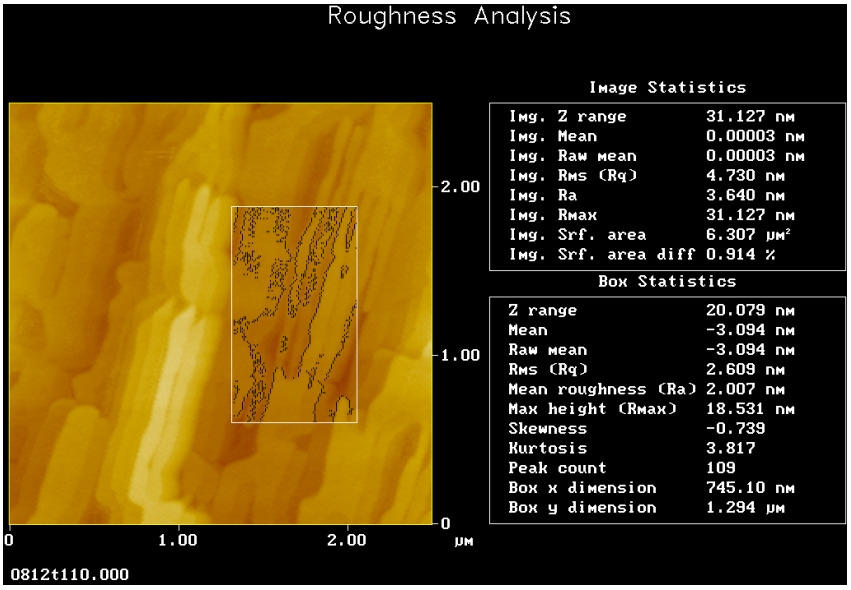

Figure 2.46: A two-dimensional AFM image on the same film as in figure 2.46 showing the roughness of these films to be about ~2.5 nm

A thin film of ~ 40 nm nominal thickness has an RMS roughness of ~ 1.4 nm with an autocovariance of ~ 5 nm^2 whereas a thicker film close to ~ 80 nm thickness has

roughness of 2.6 nm RMS roughness with autocovariance of 17.4 nm^2, as shown in figure 2.46.

Regular θ-2θ XRD scan showing that the (011) M1-VO_2 grows out-of-plane on TiO_2(110) is shown in figure 2.47.

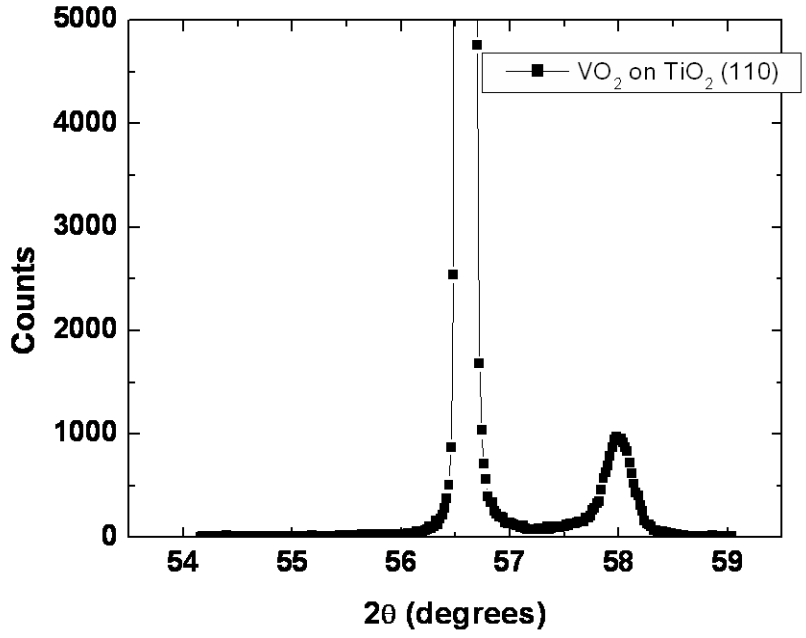

Figure 2.47: θ-2θ XRD of VO_2 on TiO_2 (110) showing that the (011) plane of VO_2 grows out-of-plane

Tilting by $\psi = 47.5^o$ to find the (111) peak of TiO_2, we also find the (012) peak of M1-VO_2 which corresponds to the (111) of rutile-VO_2, hence again showing the in case of TiO_2 the epitaxial growth prefers alignment along the (111) direction (see figure 2.48).

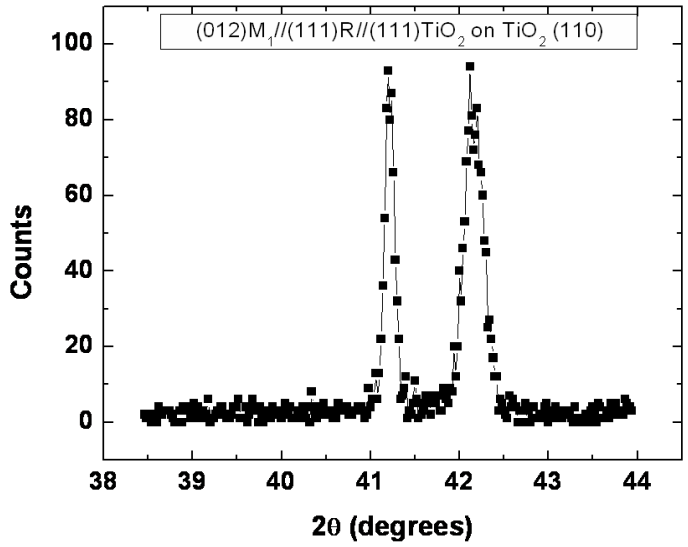

Figure 2.48: XRD at $\psi = 47.5^{o}$ for (111) plane of TiO_2, with a VO_2 (012) peak close to it showing the preferential orientation

A partial ϕ-scan of 180 degrees was performed about the (012) M1-peak and only a single peak was found indicating that it has a two-fold symmetry along this direction (figure 2.49).

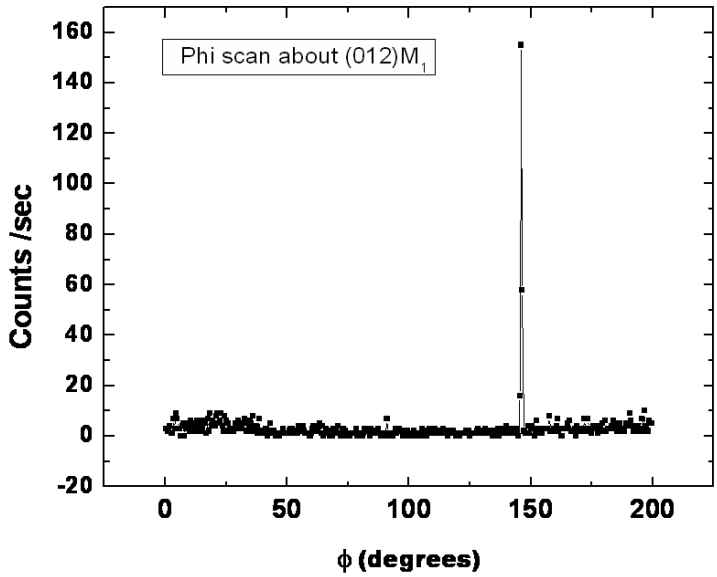

Figure 2.49: XRD - 180 degree ϕ-scan about the (012) M1 peak of VO_2 showing that only one (012) is present reflecting the two-fold symmetry of the monoclinic geometry

2.3.2.3 Epitaxial VO_2 on TiO_2(100)

VO_2 on TiO_2 (100) was found to grow with the (010) out-of-plane direction. Taking that into account here is a schematic of the interface between VO_2 on TiO_2 (100) (figure 2.50).

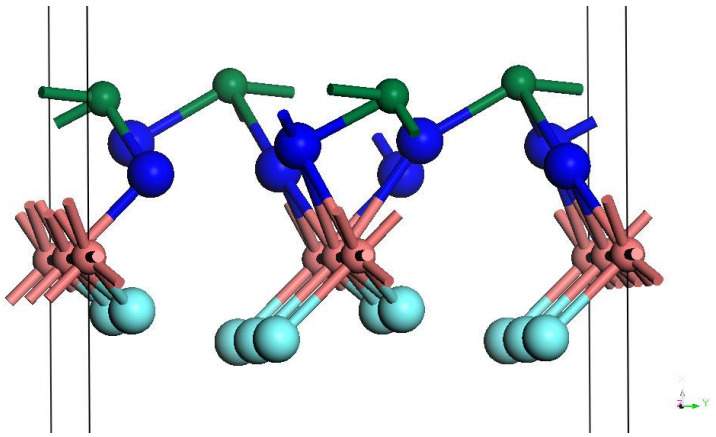

Figure 2.50: Schematic representation of the idealized interface between VO_2 (010) and TiO_2 (100). Courtesy: Dr. Bin Wang, Vanderbilt University

Figures 2.51-2.53 show the morphologies and hysteretic behavior of the epitaxial VO_2 film on TiO_2 (100).

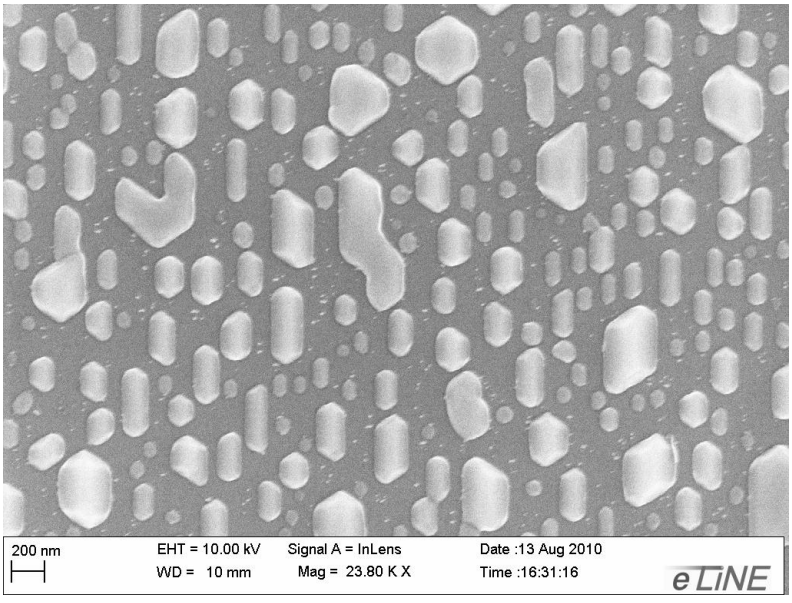

Figure 2.51: SEM morphology of a thin epitaxial VO_2 in its early growth phase on TiO_2 (100)

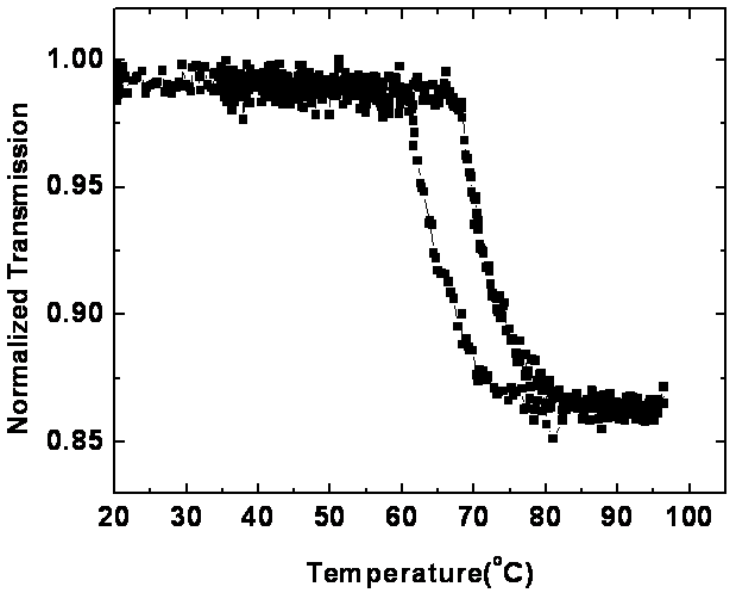

Figure 2.52: Typical transmission hysteresis of a thin epitaxial VO_2 film on TiO_2 (100)

The transition temperature (T_c) and hystersis width (ΔH) for the typical epitaxial film was measured to be T_c = 67.5 C, and ΔH = 7 C.

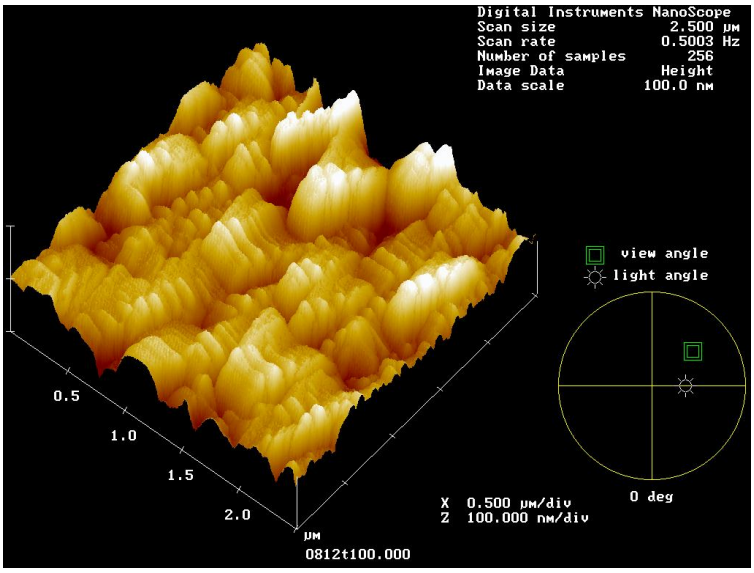

Figure 2.53: AFM image of a thin epitaxial VO_2 film in its early growth phase on TiO_2 (100)

AFM image on one such film (figure 2.53), over 2.5 μm^2 area show that a film of about 80 nm nominal thickness has about 12.5 nm RMS roughness and an autocovariance of about ~232 nm^2.

A typical θ-2θ scan reveals the out-of-plane growth direction of VO_2 on TiO_2(100), as shown in figure 2.54. The (010) VO_2 grows out-of-plane as indicated in the figure 2.54.

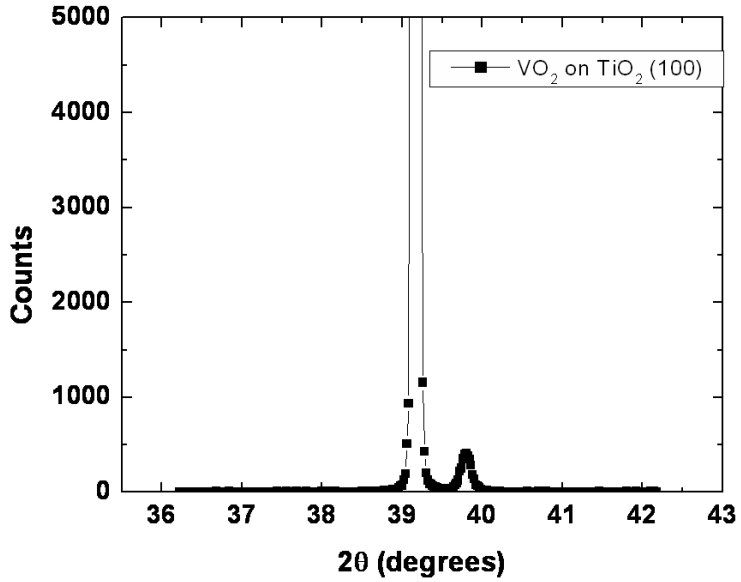

Figure 2.54: θ-2θ XRD scan of epitaxial VO_2 on TiO_2 (100) indicating (010) of VO_2 grows out-of-plane

2.3.3 Effect of oxygen plasma cleaning of substrates on epitaxy

There is an observable difference in morphologies of films grown epitaxially on substrates that are oxygen-plasma cleaned prior to deposition compared to the ones which are not as shown in figures 2.55 -2.61 for various substrates. An oxygen plasma cleaning consists of exposing the organically cleaned substrates to an oxygen plasma for 30 minutes just before deposition.

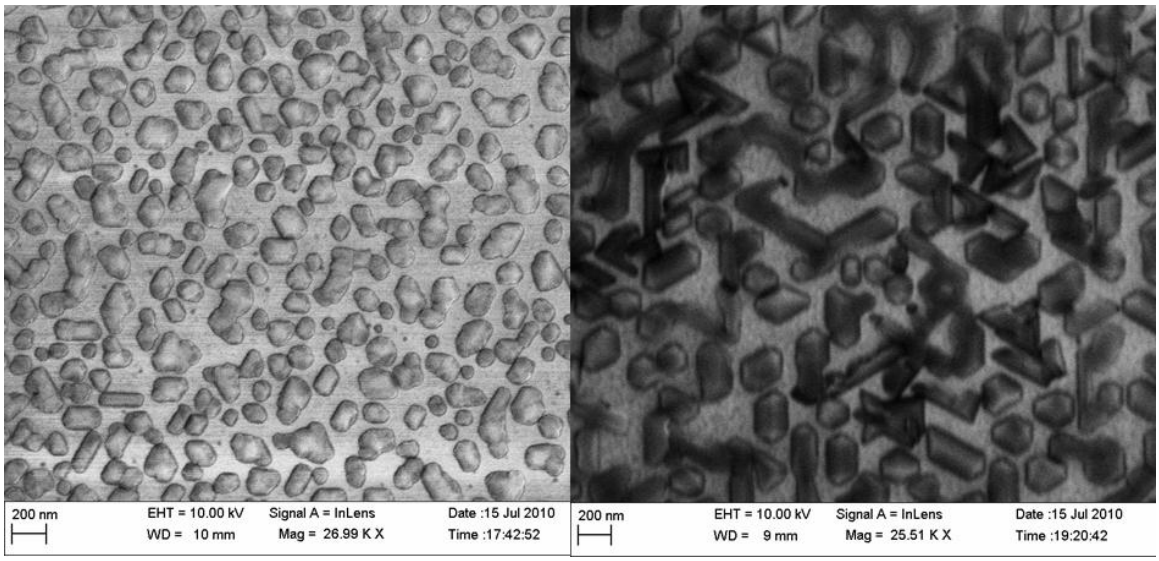

Figure 2.55: SEM morphologies of films grown on pristine (left) and oxygen-plasma-treated (right) C-sapphire substrates of almost similar thicknesses

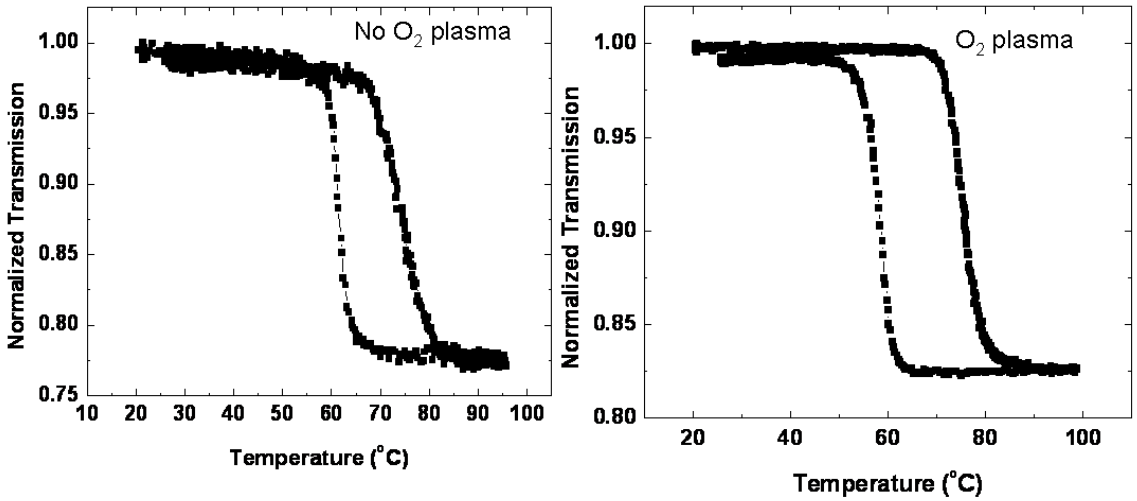

Figure 2.56: Transmission hystereses of films grown on pristine (left) and oxygen-plasma-treated (right) C-sapphire substrates of almost similar thicknesses

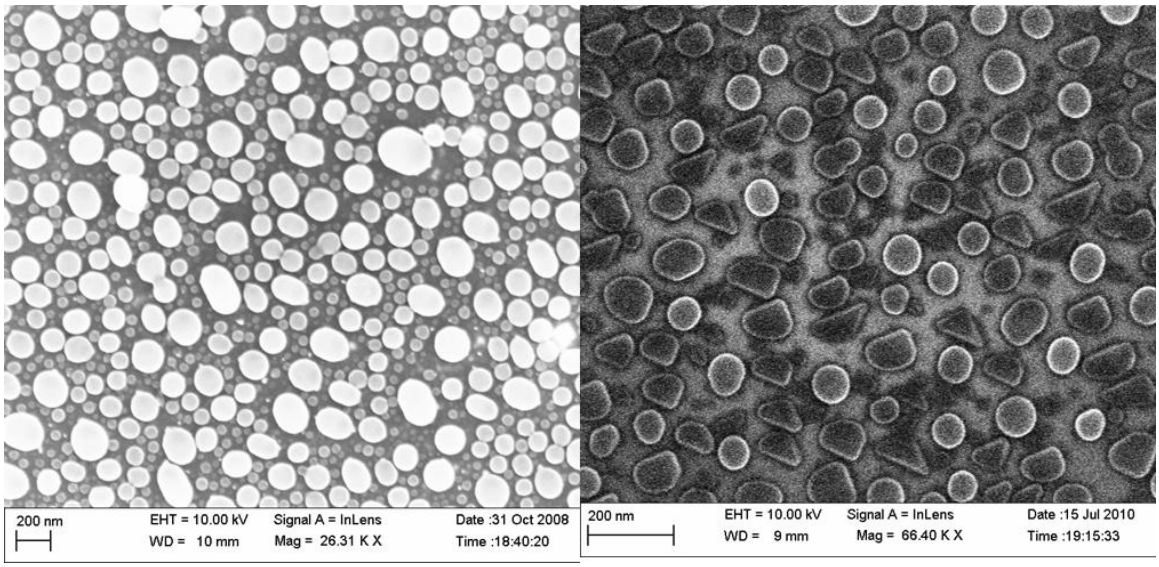

Figure 2.57: SEM images of films grown on pristine (left) and oxygen-plasma-treated (right) R-sapphire substrates of almost similar thicknesses

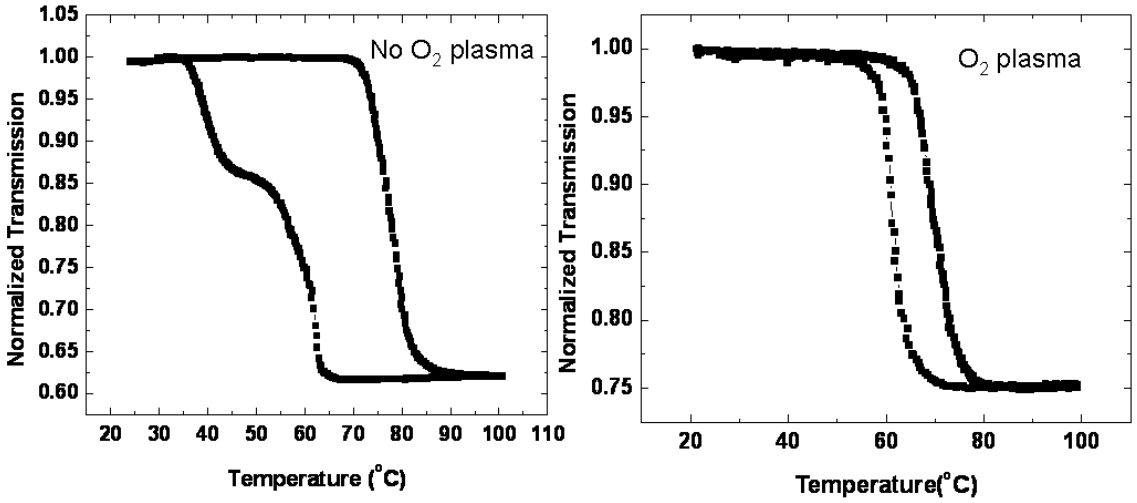

Figure 2.58: Transmission hystereses of films grown on pristine (left) and oxygen-plasma-treated (right) R-sapphire substrates of almost similar thicknesses

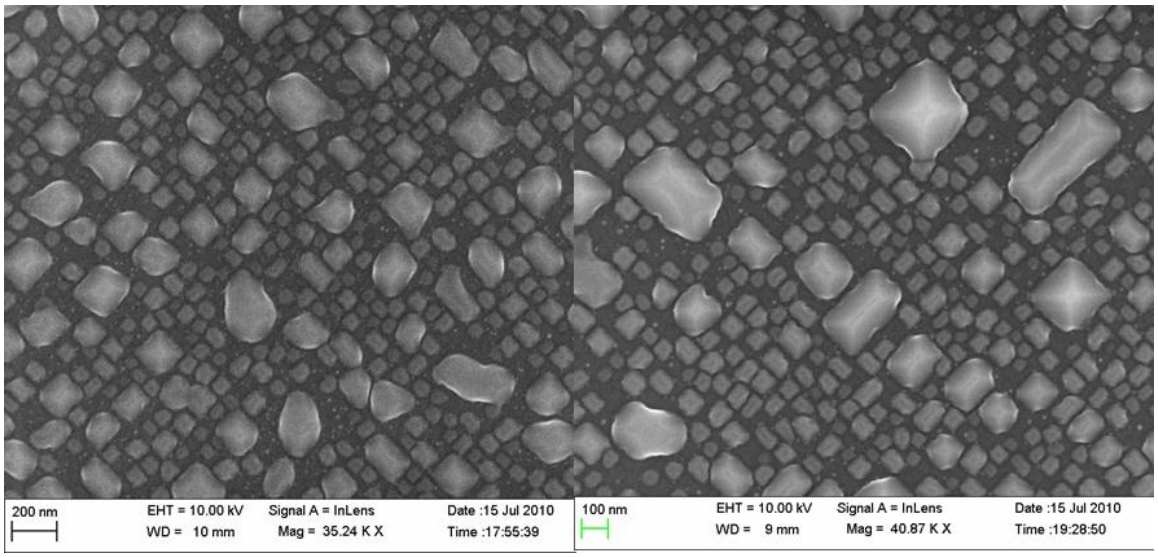

Figure 2.59: SEM morphologies of films grown on pristine (left) and oxygen-plasma-treated (right) TiO_2(001) substrates of almost similar thicknesses

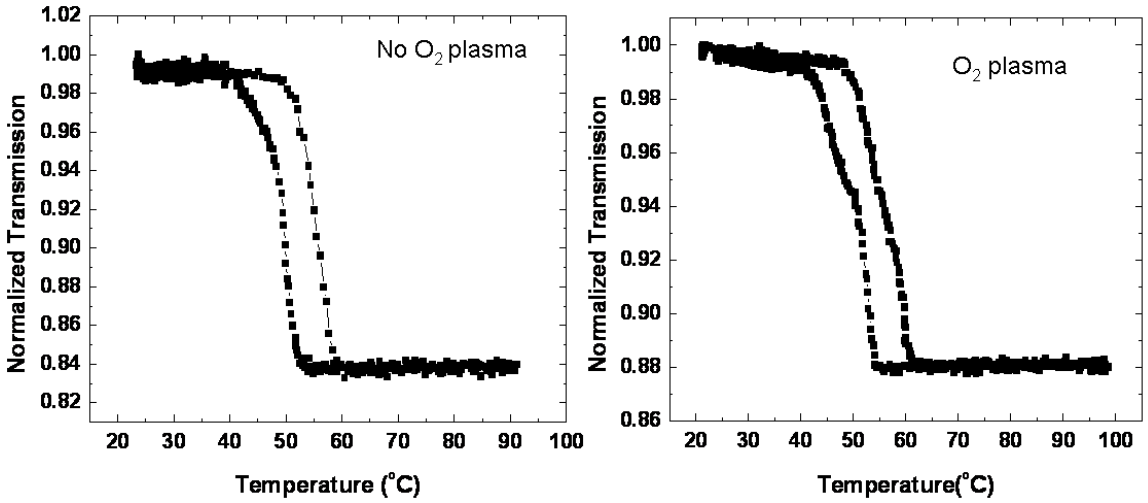

Figure 2.60: Transmission hystereses of films grown on pristine (left) and oxygen-plasma-treated (right) TiO_2 (001) substrates of almost similar thicknesses

We note here that when exposed to atmosphere, even Al or Ti terminated planes of substrates satisfy most of their dangling bonds with ambient oxygen, but cleaning with oxygen plasma ensures the oxygen termination of all exposed bonds. Probably this promotes more directional and sharply-defined faceted growth and hence the observed differences in morphologies.

2.3.4 Switching of ultrathin epitaxial films

As has been observed in literature several times, VO_2 films thinner than 20 nm are not known to switch, but here we have observed switching in ultrathin films (5 and 10 nm nominal thicknesses) of epitaxial VO_2 on c-sapphire and TiO_2 (001), as shown in figures 2.61-2.66.

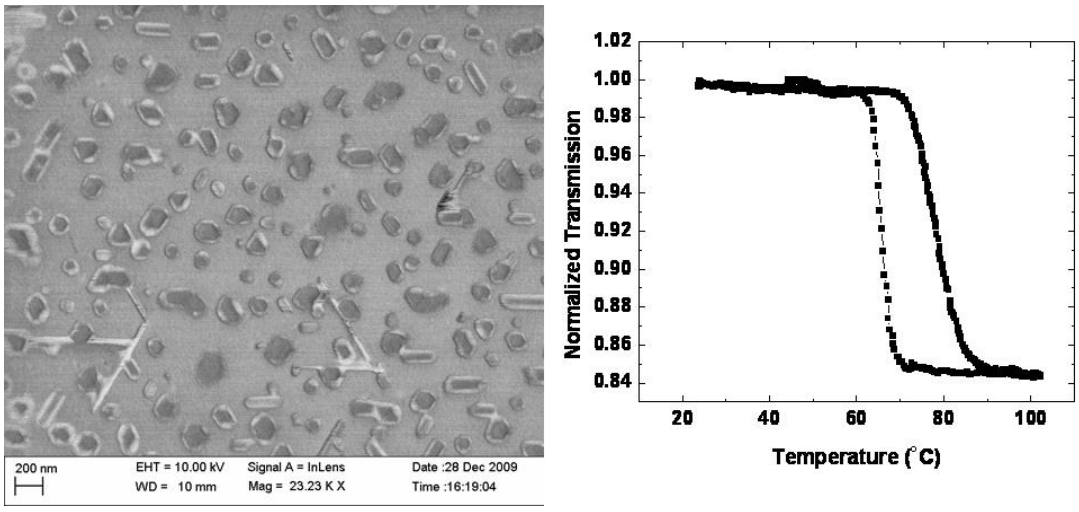

Figure 2.61: SEM image and transmission hysteresis of a 10 nm epitaxial VO_2 film on C-sapphire

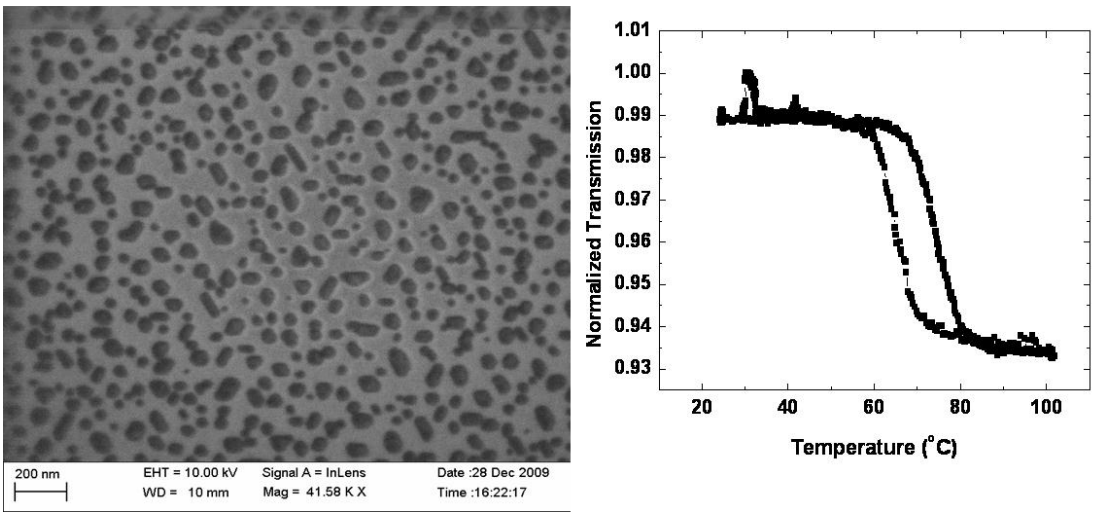

Figure 2.62: SEM image and transmission hysteresis of a 5 nm epitaxial VO_2 film on C-sapphire

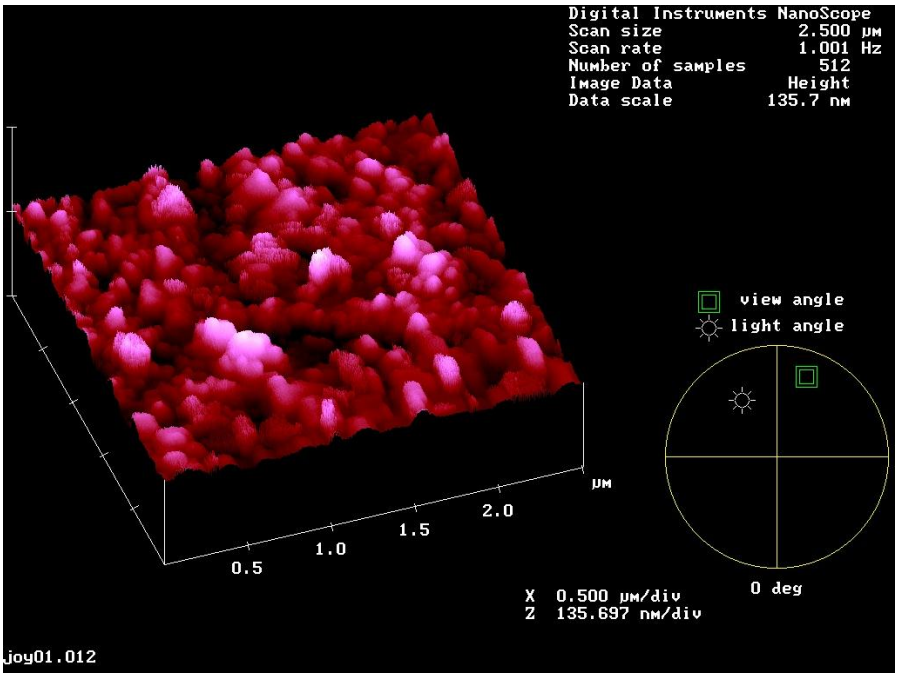

Figure 2.63: AFM image of a 5 nm epitaxial VO_2 film on C-sapphire

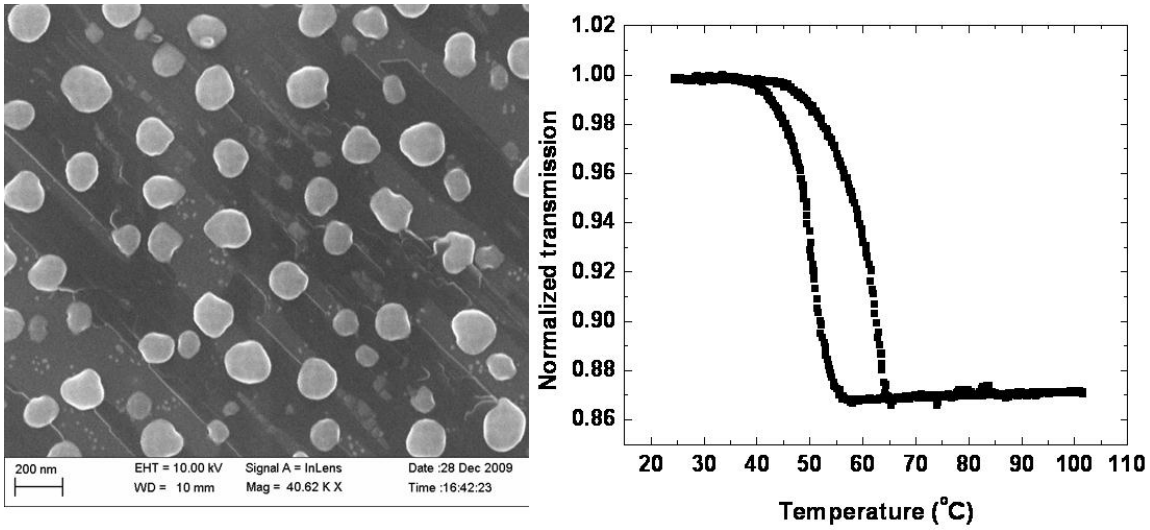

Figure 2.64: SEM image and transmission hysteresis of a 10 nm epitaxial VO_2 film on TiO_2 (001)

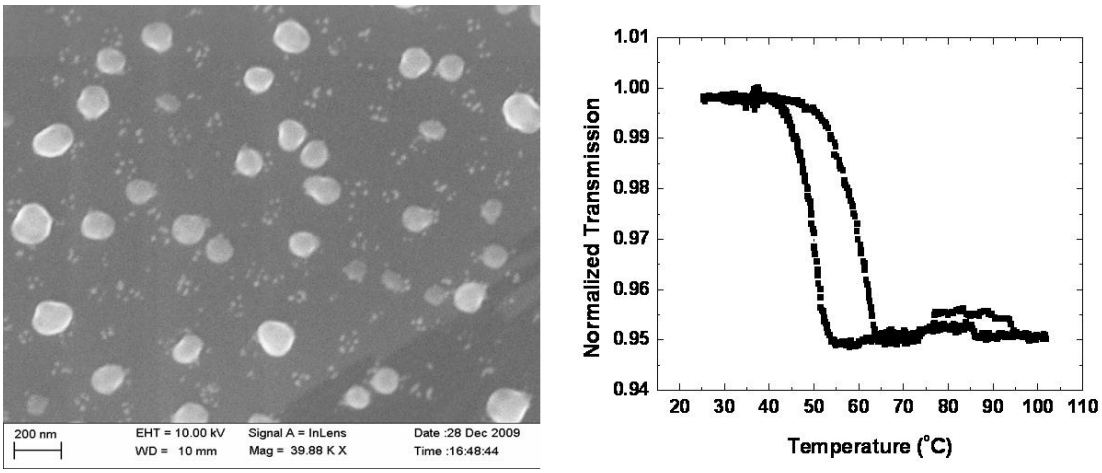

Figure 2.65: SEM image and transmission hysteresis of a 5 nm epitaxial VO_2 film on TiO_2 (001)

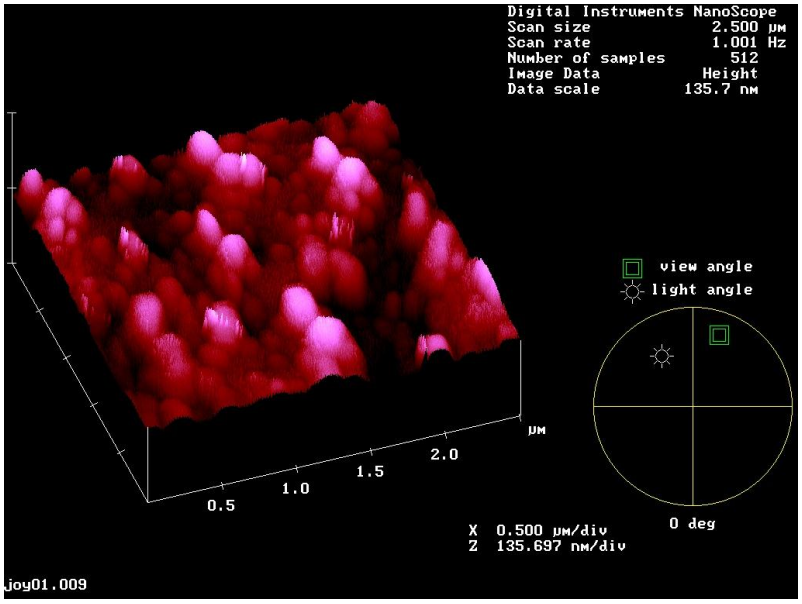

Figure 2.66: AFM image of a 5 nm epitaxial VO_2 film on TiO_2 (001)

We note here that even though the equivalent mass thicknesses are 5 nm and 10 nm, the actual thicknesses of the isolated grains are quite a bit larger, for example ~50 nm thick, and hence we have a sparse collection of isolated, switchable VO_2 grains giving us the transmission hysterses observed. Also, note here that these are directly grown at high-temperatures and not deposited and annealed in two steps, in the latter case it becomes a lot harder to anneal very low volumes of deposited amorphous film.

CHAPTER III

EFFECT OF DEPOSITION PARAMETERS ON EPITAXY

ABSTRACT

Vanadium dioxide (VO_2) in bulk, thin film and nanostructured forms exhibits an insulator-to-metal transition accompanied by structural reorganization, induced by temperature, light, electric fields, doping or strain. We have grown epitaxial films of VO_2 on c-plane (0001) of sapphire using two different procedures involving (1) room-temperature growth followed by annealing and (2) direct high-temperature growth. Strain at film-substrate interface due to growth at different temperatures leads to interesting differences in morphologies and transition characteristics. Observations indicate that contrary to conventional wisdom, the room-temperature grown films have smoother morphologies and better switching performances, consistent with the observed behavior of epitaxially-grown conventional semiconductors. We observe similar effects in epitaxial films on other substrates as well. We have also discussed the effect of laser parameters on epitaxy in the last section.

3.1 EFFECT OF SUBSTRATE TEMPERATURE DURING DEPOSITION

3.1.1 On epitaxially-grown VO_2 on C-cut sapphire

Fabrication of high-quality thin films is crucial for technologies that capitalize on the IMT. It is well known that film microstructure,[175] the film-substrate interface[176] and localized strain[50] can all affect the hysteretic response of this first-order phase transition. Moreover, the process of making high-quality, defect-free, thin film samples of VO_2 is complicated not only by the presence of oxygen defects, but also by the narrow temperature-pressure window in phase space for stoichiometric VO_2, due to multiple valence states of vanadium. Epitaxial films are generally expected to produce spatially homogeneous films with phase transition behavior close to that of bulk crystals, as the defined crystallographic growth direction(s) lead to more consistent and efficient

performance in devices. Epitaxial films are conventionally grown at higher temperatures, to facilitate better surface kinetics during growth process. In this letter, by following the very early stages of thin film growth, and comparing morphologies and switching response of epitaxial VO_2 films synthesized at two different temperatures, we observe that the lower-temperature process produces thin films of superior quality.

Here we will first discuss growth of epitaxial VO_2 on C-cut sapphire. Refer to figure 3.1 for the schematic of the probable interfacial atomic arrangement of VO_2 on Al_2O_3. Evidently the unit cell of VO_2 along (010) direction is pretty large compared to that of VO_2 and thus should lead to a huge compressive strain in case of pseudomorphic epitaxial growth. In fact, this clearly indicates why the critical thickness of VO_2 film on sapphire is extremely small and hence instead of a single crystal growth, we obtain many single crystals disjoint from one another but oriented along the same direction.

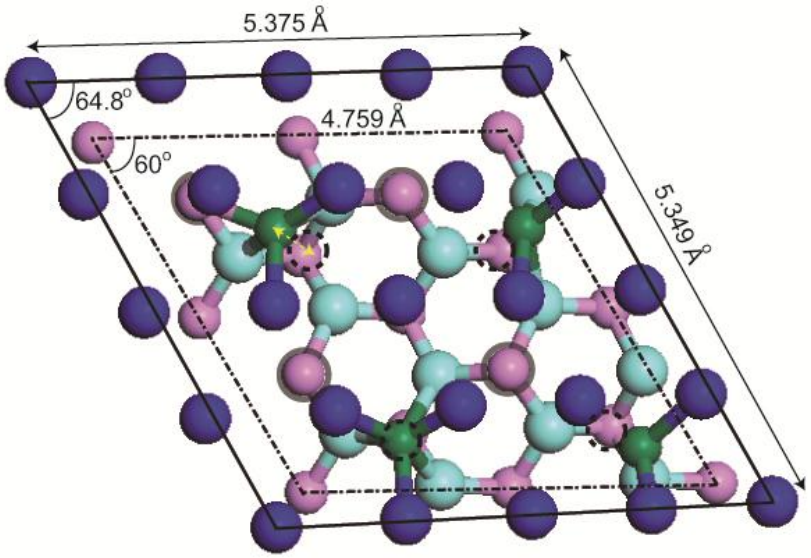

Figure 3.1: Schematic of a probable interface between VO_2 (010) and (0001) plane of sapphire. The V atoms are in green, Al atoms in pink, O atoms from sapphire in light blue and O atoms from VO_2 in dark blue. The lower left V atom has been placed at the strained position and the upper left one shows the distortion that has to occur in the lattice for the V atom to be in the right interfacial bonding conditions. Courtesy: Dr. Bin Wang, Vanderbilt University.

We fabricated, epitaxial VO_2 films of 80 nm nominal thicknesses on c-cut sapphire using two different processes: (1) RT-growth process: 99.99% pure vanadium metal target was pulsed laser ablated at room temperature in a background of 10 mTorr of oxygen, with a target-substrate distance of 8 cm, to produce an amorphous, oxygen-deficient film of $VO_{1.7}$. Subsequent annealing of this sub-stoichiometric film in 250 mTorr of oxygen at 450^{o}C for 45 minutes yielded stoichiometric, crystalline VO_2. (2) HT-growth process: Similar pulsed laser deposition at high temperature (~500^{o}C), with a background gas pressure of 50 mTorr oxygen and a target-substrate distance of 5 cm.

The stoichiometry and crystallinity of the films were determined by Rutherford back scattering (RBS) and powder X-ray diffraction (XRD). XRDs of both the films show (010) out-of-plane orientation on C-plane of sapphire [a typical XRD is shown in figure 2.13]. The epitaxial character of the films was confirmed by reciprocal space mapping using a PANalytical X'pert Pro MRD and images acquired in the HF 3300 transmission electron microscope (TEM). The metal-insulator transition in both RT and HT VO_2 thin films was observed by measuring the infrared transmission using a mechanically chopped white light source (3000 K blackbody) and an InGaAs detector; the chopped signal (frequency 190 Hz) was fed as the reference to a lock-in amplifier that recorded the signal from the detector. The films were heated and cooled during optical characterization by a Peltier thermoelectric element. The temperature was measured with a precision thermocouple in thermal contact with the VO_2 surface.

The TEMs in figures 3.2(a) and (b) show the smoother morphology of the RT-grown film compared to the HT-grown film.

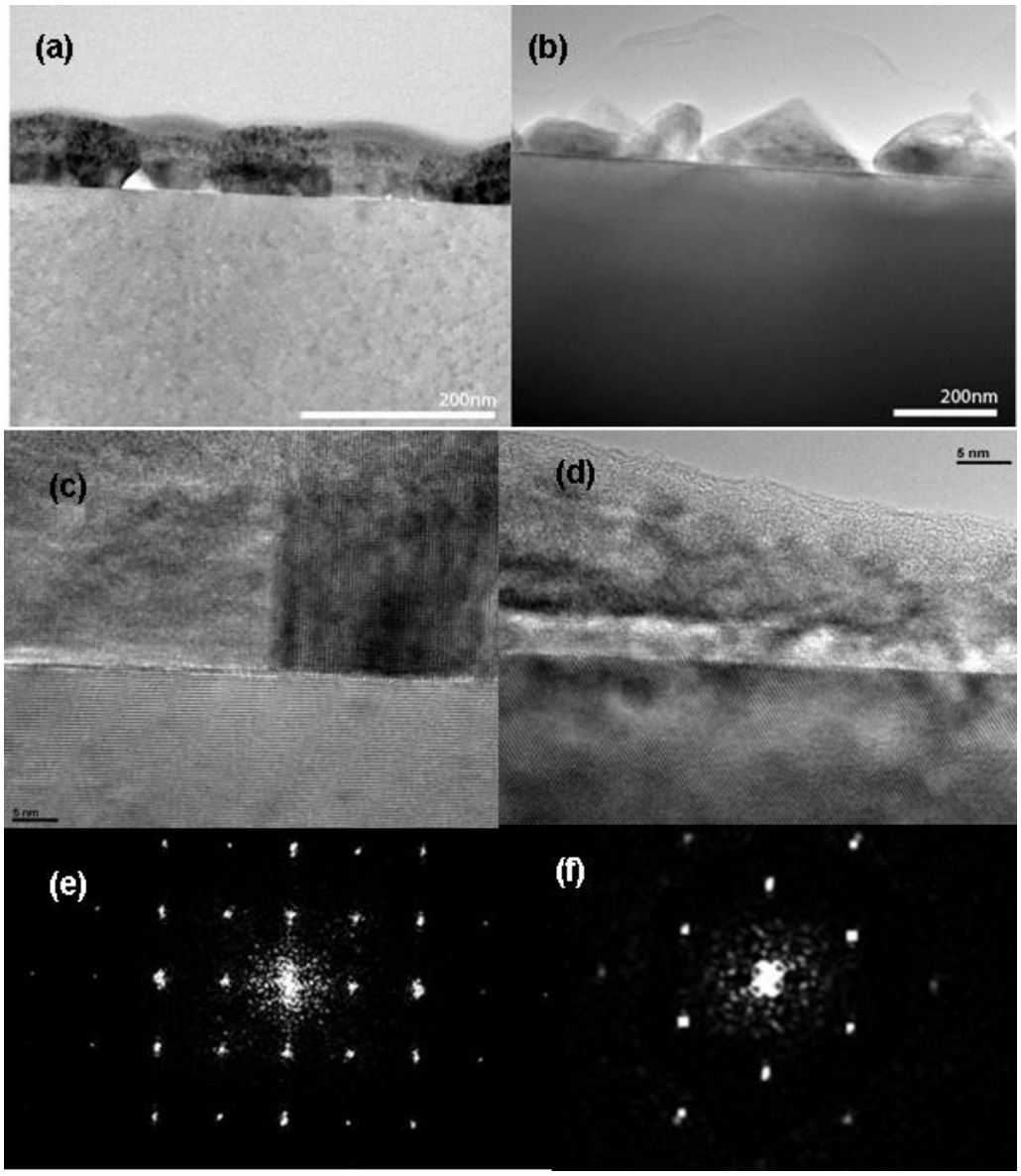

Figure 3.2: TEMs of (a) RT-grown and (b) HT-grown films. High resolution TEMs of the film-substrate interface for (c) RT-grown film and (d) HT-grown film. SAED patterns along film-substrate interface (e) along <100> zone axis of RT-grown film and (f) along <010> zone axis on HT-grown film, showing that the film diffraction pattern follows the substrate lattice diffraction pattern very closely

Atomic force microscopy on these films [figure 3.3], over 2.5 μm^2 area show that the roughness of the RT-grown films is about 4.5 nm, compared to about 23.5 nm roughness for HT grown films, for nominal film thicknesses of 80nm. The autocovariance for HT

grown films was measured to be ~536 nm^2, whereas for RT-grown films it was 29 nm^2, this gives a measure of the lateral correlation length or long-range roughness parallel to the surface. This is also evident from fig.3.2(b) for HT films showing non-contiguous, single-crystalline pyramidal nanoparticles, separated by wide, deep valleys in contrast to the continuous RT-grown film [figure 3.2(a)].

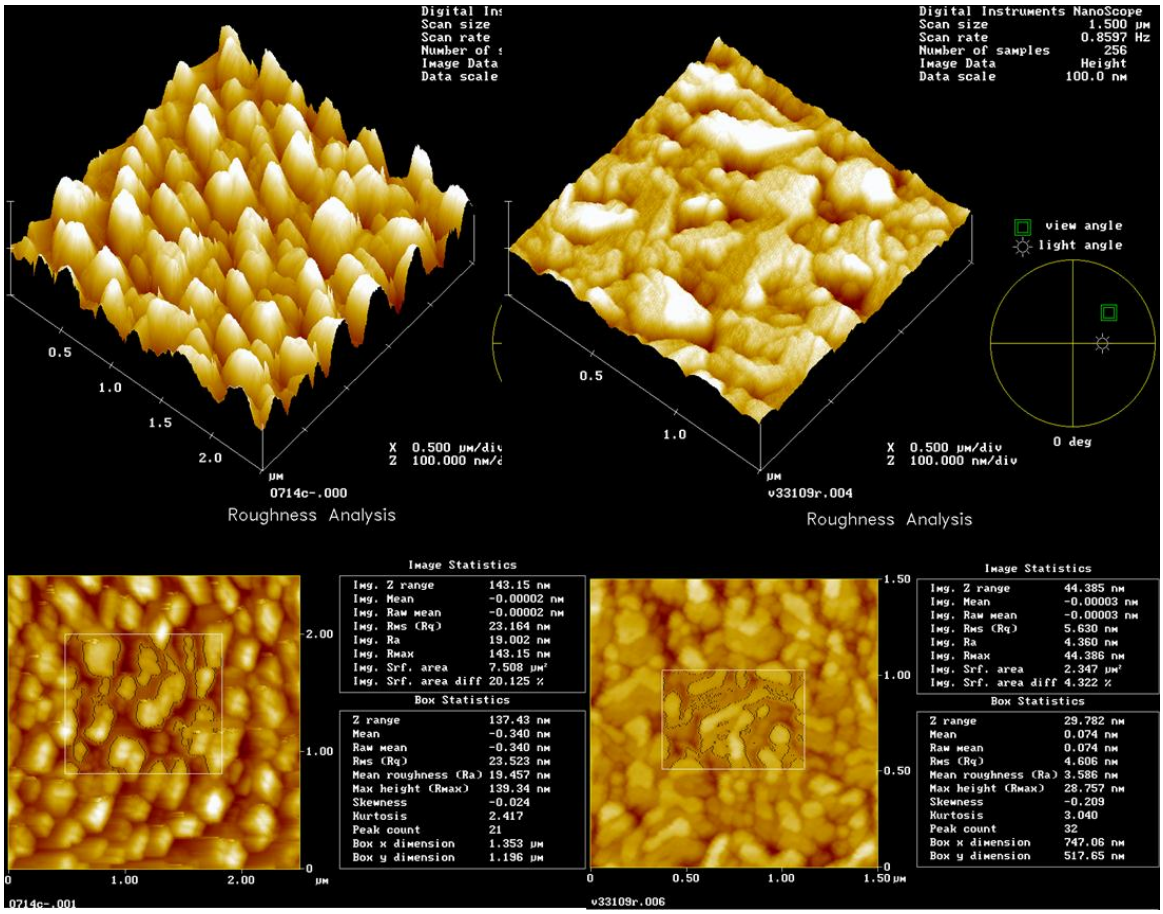

Figure 3.3: AFM images of the HT-grown (left) and RT-grown films (right) on C-sapphire

Figures 3.2 (c) and (d) are high-resolution TEM of grains and grain boundaries in RT-grown and HT-grown films respectively. For RT-grown films, neighboring grains form a clean interface with the substrate. In the HT-grown films, on the other hand, as discussed previously, the HRTEM and energy-dispersive spectroscopic measurement reveals an interdiffusion or buffer layer near each grain where Al, V and O are all present in non-stoichiometric proportions. This interdiffusion layer exhibits a lattice spacing of 2.24 Å,

a value in between that of the c-plane of sapphire (2.16 Å) and the (020) plane of VO_2 (2.42 Å). The selected area electron diffraction patterns taken across film-substrate interfaces in figures 3.2(e) and (f) show that both RT-grown and HT-grown films are epitaxial, having definite in-plane orientation with respect to the substrate as the diffraction spots from the film, the interdiffusion layer (in HT-grown VO_2 only), and substrate line up or almost overlap.

Figure 3.4 shows the STEM bright field images of RT and HT grown film-substrate interfaces. It is clearly evident that the RT grown films exhibit a columnar growth whereas the HT grown films follow an island-like growth mode making them more rough compared to their RT grown counterparts.

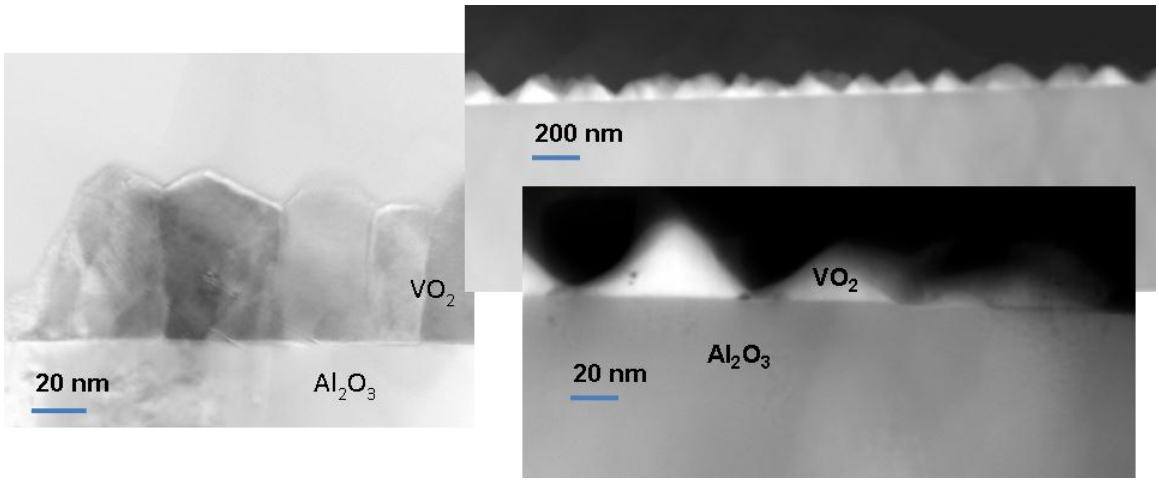

Figure 3.4: Bright field STEM images of RT-grown (left) and HT-grown (right) films

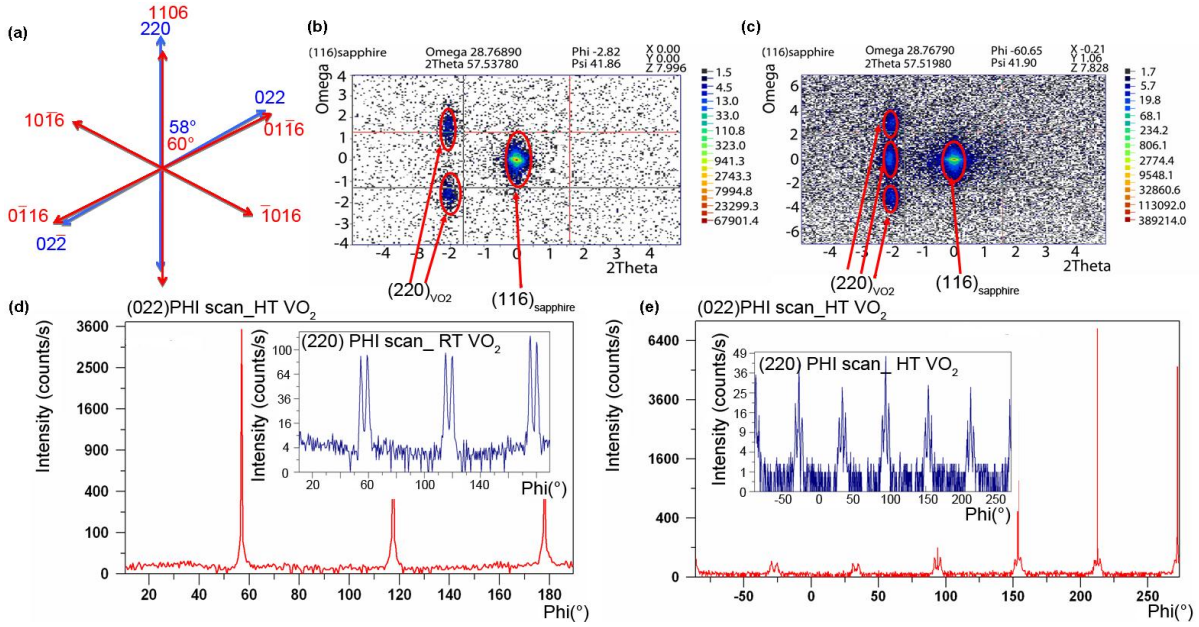

Figure 3.5: XRD RSM and PHI scans on RT and HT-grown films. (a) Line diagram demonstrating slight orientational difference between (220) and (022) of VO_2 with respect to (116) direction of sapphire. Reciprocal space maps on (b) RT grown and (c) HT grown sample about the (116) axis of sapphire, indicating the in-plane orientations with respect to the substrate. ϕ–scans about (022) peak of VO_2 [and (220) peak in the inset] for (e) RT-grown and (f) HT-grown films confirming the slight differences in orientation of the two films.

Monoclinic VO_2 is pseudohexagonal, the angle between the (220) and (022) planes of VO_2 being approximately 58.5˚ instead of 60˚ as in the perfect hexagonal lattice of Al_2O_3 [figure 3.5(a)]. To investigate the in-plane epitaxy of these two films, reciprocal space maps (RSMs) and ϕ–scans were measured. Figures 3.5(b) and (c) show the RSMs as ω-2θ rocking curves; these could equally well be plotted as k_x *vs* k_y plots. The ϕ–scans — rotations about the axis normal to the sample surface, keeping the 2θ and tilt angle of the sample ψ fixed for a certain set of diffraction planes — are shown in figures 3.5(d) and (e)] for the RT-grown and HT-grown films respectively.

For the RT-grown sample, the ϕ–scan about the (022) peak [figure 3.5(d)] shows that the (022) peak is aligned with the (1106) peak of sapphire and a pair of (220) peaks [figure 3.5(d) inset] are generated on either side of it by twinning. This is confirmed by the RSM

[figure 3.5(b)] where the two (220) peaks are observed at 1.5 degrees from each other as expected for the 58.5^{o} angle between the (022) and (220) planes.

For the HT-grown sample, the (022) peak is not aligned with the (1106) of sapphire but is rather at a ~2^{o} offset on either side of (1106) sapphire [figure 3.5(e)]. These (022) peaks in turn give rise to a pair of (220) peaks on either side and hence causes the triplets to appear in (220) ϕ–scans [figure 5(e) inset] with the central peak twice as intense as the satellites. This is confirmed by the appearance of three (220) peaks in the RSM as well [figure 3.5(c)] with the most-intense central peak having satellite peaks at 3^{o} on either side accounting for the 1.5^{o} twinning on either side of the (022) planes.

This difference in alignment and morphology is observed in several films, making it likely that growth parameters, in particular, growth temperature, rather than some other parameter such as substrate miscut, controls the epitaxial alignment. Note also that, when grown directly at high temperature, the film grows as stoichiometric, tetragonal VO_2, and transitions to monoclinic form only during cooling, involving considerable stress-driven rearrangement, whereas during room temperature growth, it first grows as a smooth film subsequently crystallizing to stoichiometric VO_2 during anneal.

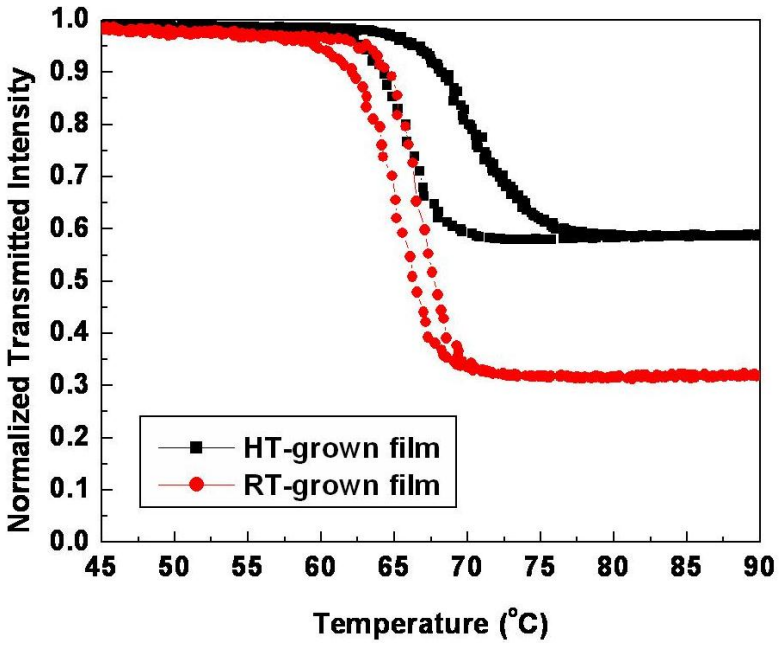

Figure 3.6: White light transmission hystereses for RT-grown (red) and HT-grown (black) epitaxial VO_2 films

These differences in morphologies, residual strains and orientation of the films lead to the distinctive IMT characteristics seen in the transmission curves in figure 3.6. As is evident from the figure, the RT-grown films in general have a lower critical temperature and higher contrast than the HT-grown films. The asymmetry in hysteresis evident in the HT-grown film can be attributed to the stress in the film.[197] The hysteresis features of these films are compared in Table 1.[175]The comparison is done on the basis of ten films of both kinds varying from thicknesses 50 – 100 nm for RT grown films and 40 – 100 nm for HT grown films. With increasing thickness, the trend observed in both kinds of films is that the critical temperature (T_c) and hysteresis width (ΔH) decreases and slope of transition (ΔT) and transition amplitude (ΔA) increases, as expected.

Table 3.1: Comparison of transition characteristics, viz., critical temperature (T_c), hysteresis width (ΔH), slope of transition (ΔT) and transition amplitude (ΔA) for RT and HT grown films.

Hysteresis parameters	*RT-grown film*	*HT-grown film*
T_c	$(64.9 \pm 1.46)^oC$	$(67.8 \pm 2.0)^oC$
ΔH	$(2.4 \pm 1.2)\ ^oC$	$(9.8 \pm 2.3)\ ^oC$
ΔT	$(0.045 \pm 0.005)/^oC$	$(0.018 \pm 0.003)\ /^oC$
ΔA	0.53 ± 0.05	0.29 ± 0.06

Theorists have only recently begun to study the effects of strain on the phase-transition characteristics of VO_2.[9] However, earlier Tersoff *et al* had observed that strained epitaxial layers can relax by two competing mechanisms depending on substrate mismatch and film-growth temperature.[198] Thermally-activated strain-induced surface modulation, generically known as "roughening," has an activation barrier ε that scales with misfit as ε^{-4}. Hence for large misfits, roughening, in form of sharp grooves or pits, allows for easier nucleation of dislocations than by the modified Frank-Read mechanism in which nucleation occurs at defects, by "multiplication" of preexisting smaller misfit dislocations.

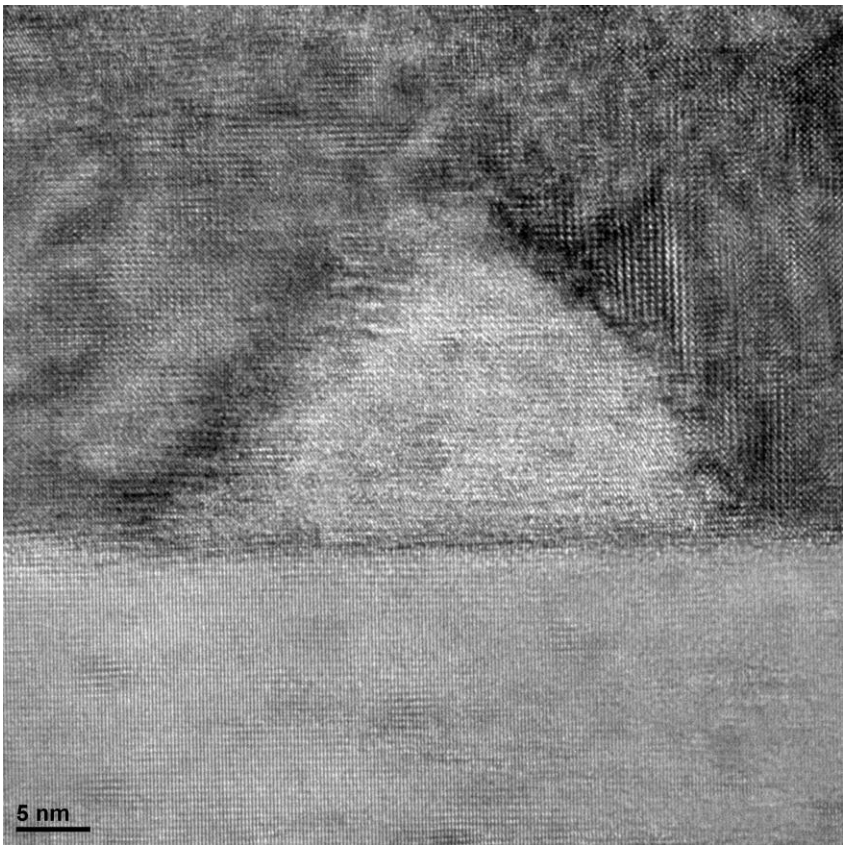

Figure 3.7: HRTEM of a pyramidal pit formed in a thick epitaxial HT-grown VO_2 film on C-sapphire

Nucleation of dislocations via surface roughening, kinetically favored at large misfits, was demonstrated both theoretically and experimentally in the growth of SiGe on Si and InGaAs on GaAs. Calculations showed that the appearance of islands or pits had a nearly equivalent cost in energy, with pit formation being favored when higher-order terms were taken into account. But if nucleation occurs before the film is thick enough to support pits, islands form instead. For thick epitaxial films we have observed with HRTEM and energy dispersive spectroscopy, the formation of triangular-shaped pits as well, as shown in figure 3.7. But the formation of islands at the early stages seems more common in case of HT growth. In SiGe films with large substrate mismatches, the film roughens *before* reaching equilibrium critical thickness required to nucleate dislocations. Even after the film grows thicker and dislocations form, the roughness remains evident. We observe the

exact analog of this in case of HT-grown VO_2 on C-cut sapphire substrates, where sharp, faceted islands grow because of thermal activation and a large misfit with the substrate.

Surface roughness is undesirable especially in electronic or optical applications; hence this comparison of HT- and RT-growth leads to the conclusion that the latter is the preferred growth condition for epitaxial films of VO_2 on C-cut sapphire. Not only does RT growth involves fewer complications in achieving perfect stoichiometry, the RT grown films on C-cut sapphire are epitaxial, continuous and smoother than the HT grown films, switching at lower temperatures. Hence, the RT grown epitaxial films may well be the more suitable ones for applications given their smooth morphology, higher optical contrast and and lower transition temperatures.

3.1.2 On other substrates – A-, R- sapphire, TiO_2 (001) and TiO_2 (110)

In this section we will illustrate some similar effects observed in epitaxial films on the other substrates for example, A-sapphire, R-sapphire, TiO_2 (001) and TiO_2 (110). Most of the hystereses are plotted for films with similar thicknesses.

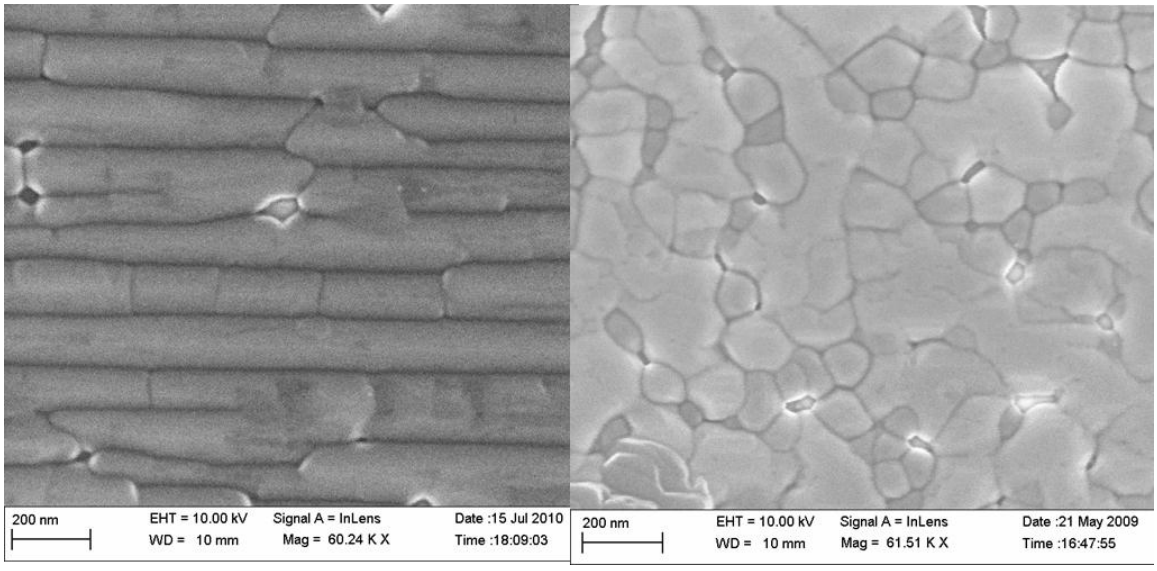

Figure 3.8: SEM morphologies for HT-grown (left) and RT-grown (right) films of similar thicknesses on A-sapphire

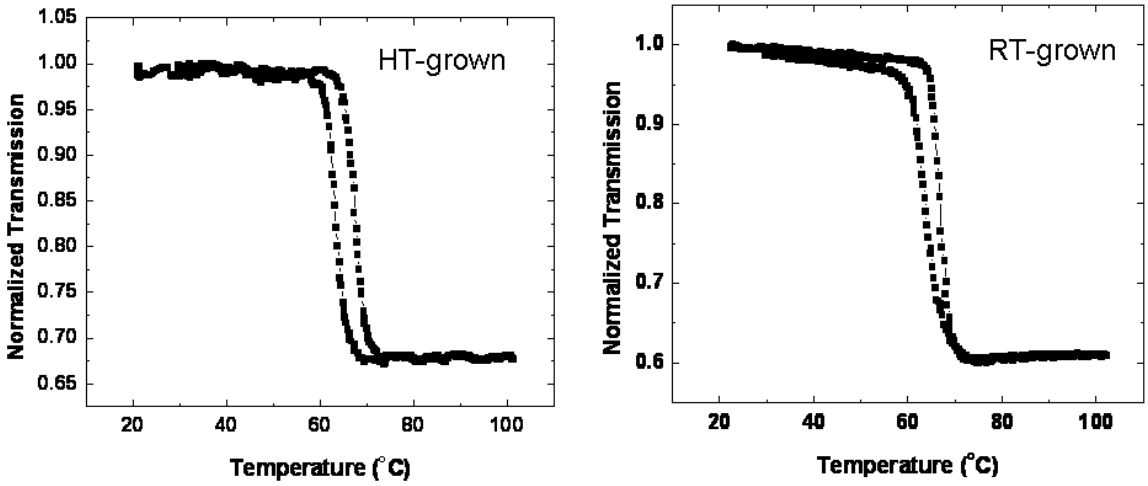

Figure 3.9: Transmission hystereses for HT-grown (left) and RT-grown (right) films of similar thicknesses on A-sapphire

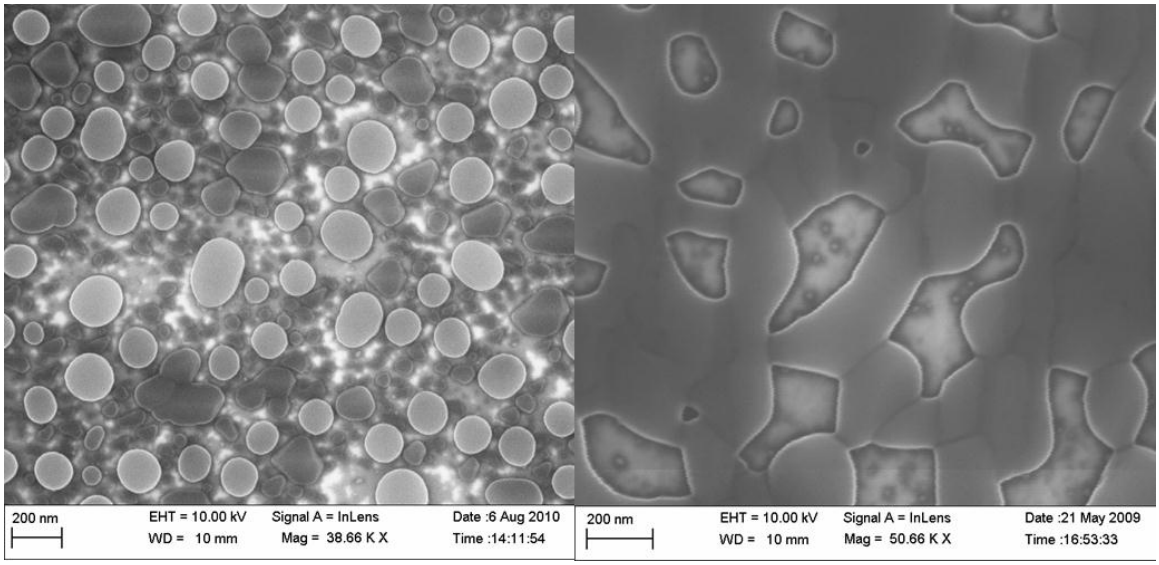

Figure 3.10: SEM morphologies for HT-grown (left) and RT-grown (right) films of similar thicknesses on R-sapphire

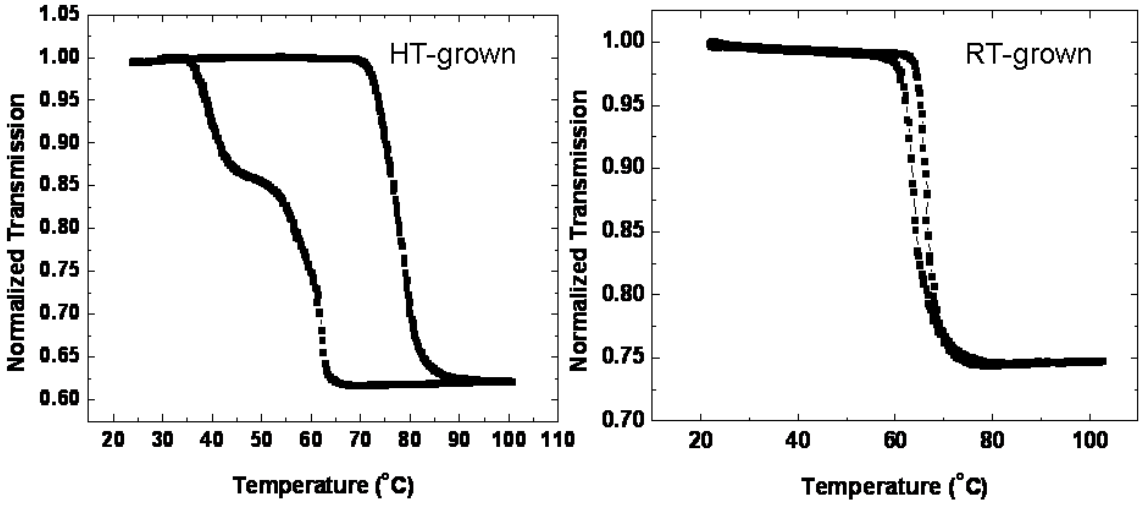

Figure 3.11: Transmission hysterses for HT-grown (left) and RT-grown (right) films of similar thicknesses on R-sapphire

Note here that the kink present in the cooling side of the curve for HT-grown film is not observed in case of the RT-grown sample. In case of HT-growth, possibly during the deposition process itself, two very different-sized island grains nucleate and form. In case of RT-growth, a smooth amorphous film grows first and later during annealing, crystallizes in conformity with the substrate template but the kinetics of crystal formation is different and does not result in the same kind of island growth as in case of HT process.

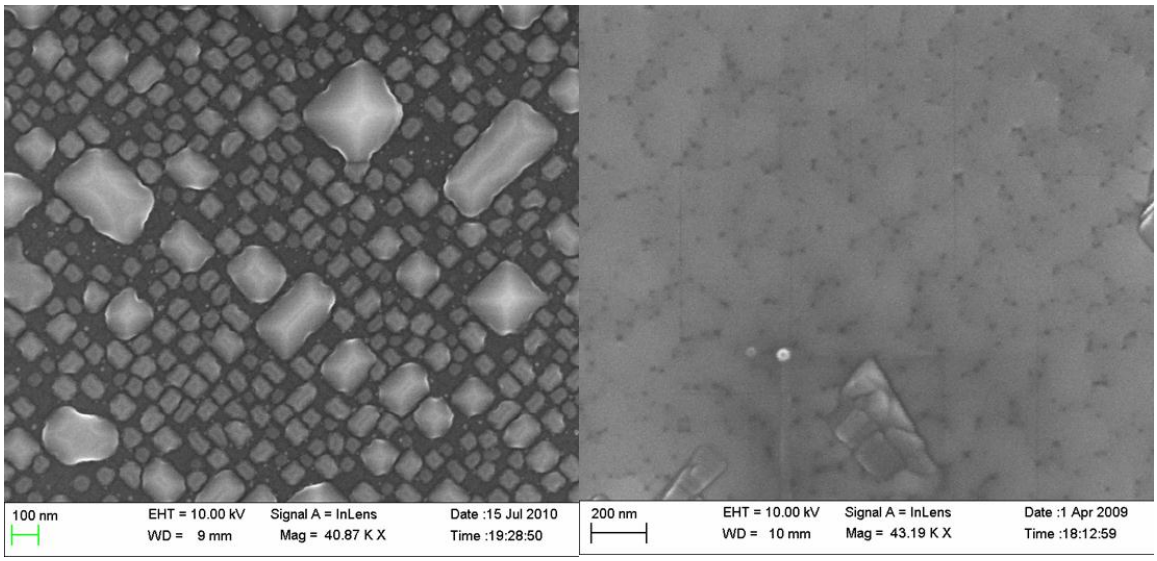

Figure 3.12: SEM morphologies or HT-grown (left) and RT-grown (right) films of similar thicknesses on TiO_2 (001)

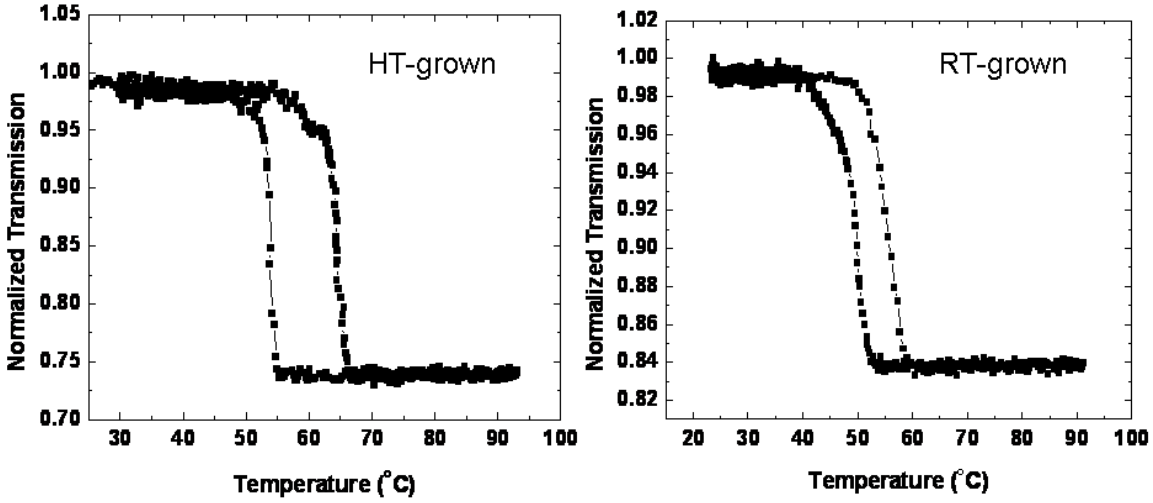

Figure 3.13: Transmission hystereses for HT-grown (left) and RT-grown (right) films of similar thicknesses on TiO_2 (001)

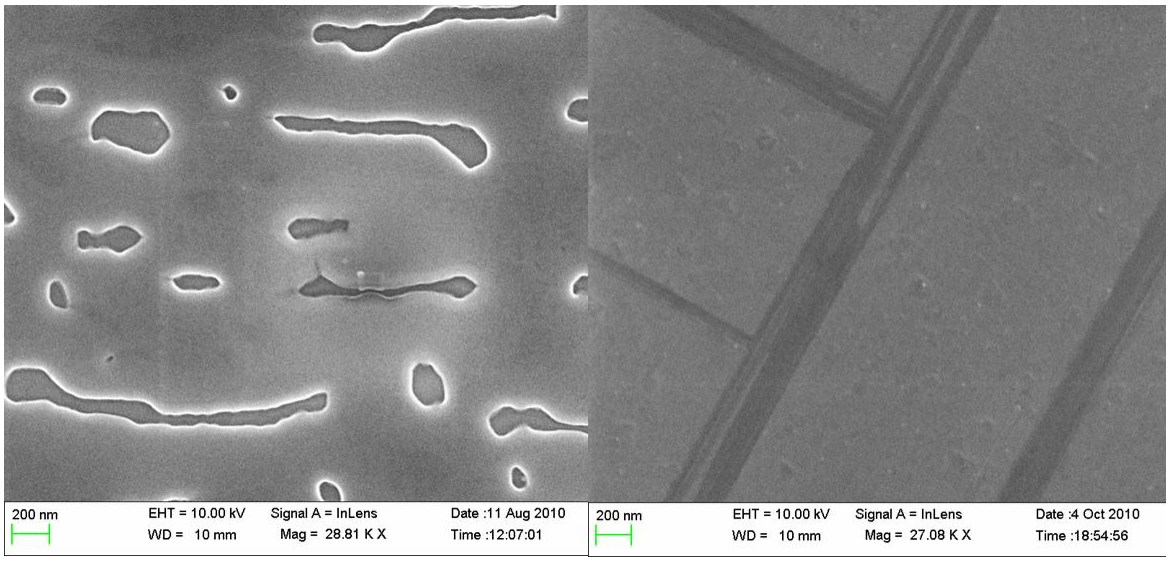

Figure 3.14: SEM morphologies for HT-grown (left) and RT-grown (right) films of similar thicknesses on TiO_2 (110)

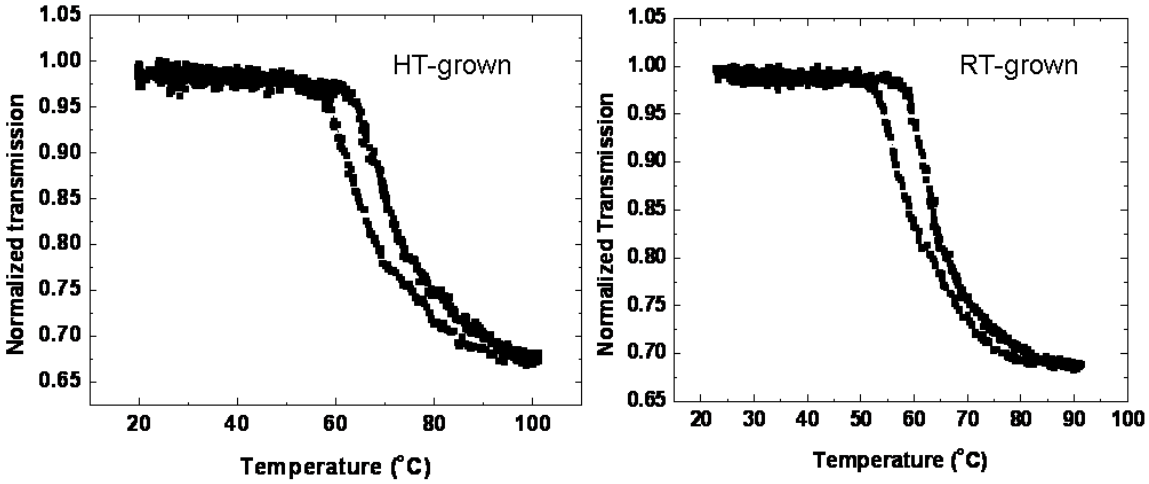

Figure 3.15: Transmission hystereses for HT-grown (left) and RT-grown (right) films of similar thicknesses on TiO_2 (110)

Practically no difference is observed in the hysteretic behavior of HT and RT-grown films on TiO_2 (110).

3.2 EFFECT OF LASER PARAMETERS ON EPITAXY

3.2.1 Effect of repetition rate of laser pulses

The effect of laser pulse repetition rate on film growth is discussed in this section. The morphologies are indistinguishable in the SEM, hence we discuss only the hysteresis differences for films of similar thicknesses here.

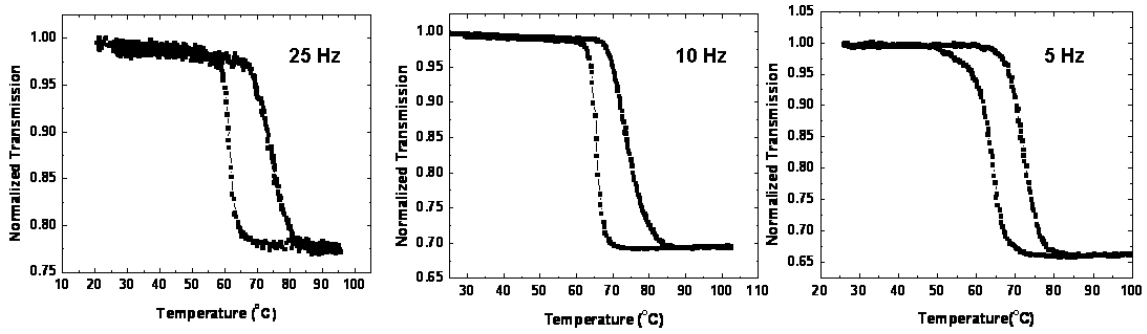

Figure 3.16: Transmission hystereses behavior for HT-grown VO_2 films on C-sapphire as laser repetition rate is decreased

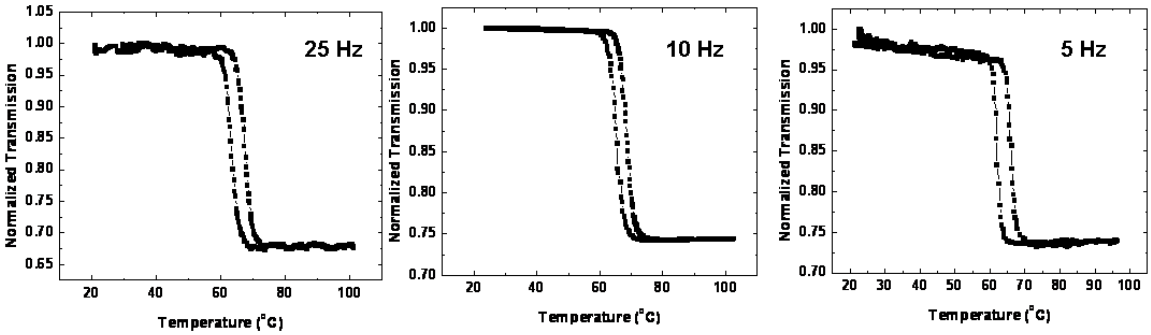

Figure 3.17: Transmission hystereses behavior for HT-grown VO_2 films on A-sapphire as laser repetition rate is decreased

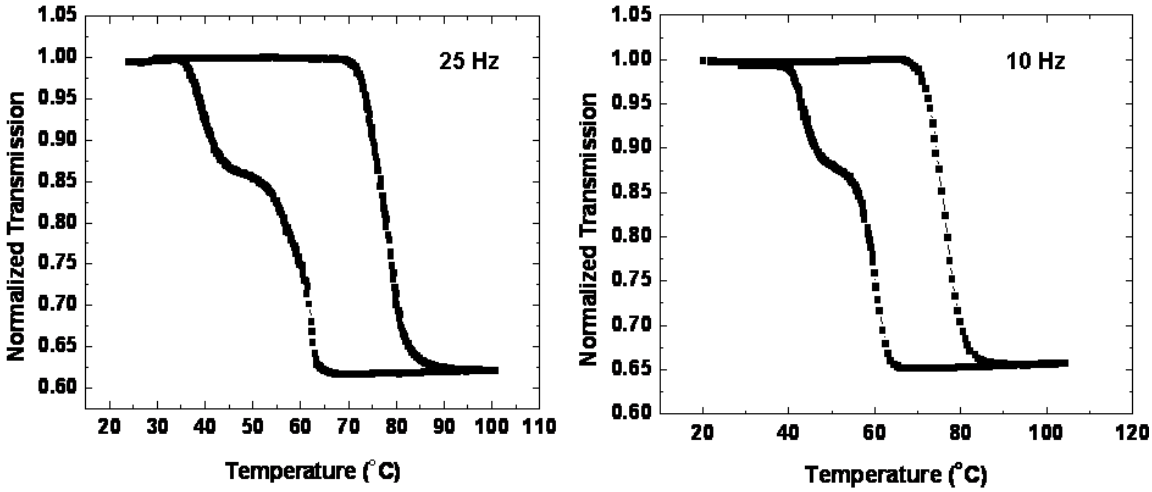

Figure 3.18: Transmission hystereses behavior for HT-grown VO_2 films on R-sapphire as laser repetition rate is decreased

From the figures 3.16 – 3.18, we observe that 10 Hz is probably close to the optimum repetition rate for films grown on A-cut and R-cut sapphire as it corresponds to narrowest, bulk-like hysteretic behavior, whereas for C-cut sapphire 5 Hz seemed to work best.

3.2.2 Effect of laser pulse energy

A small variation in the laser pulse energy resulted in considerable differences in the hystereses behavior of HT-grown films on C and R-sapphire as shown in figures 3.19 and 3.20.

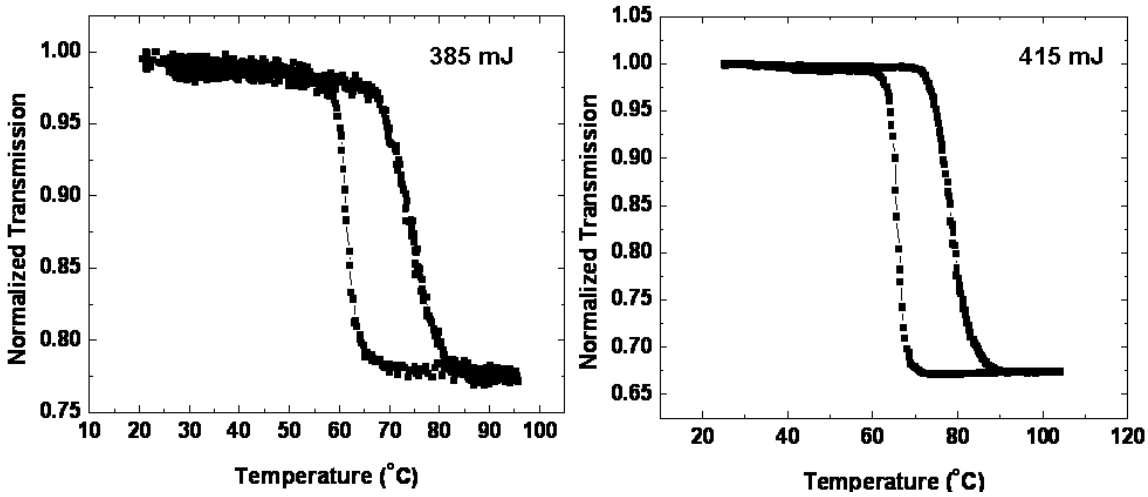

Figure 3.19: Transmission hystereses of HT-grown films grown with two different laser pulse energies on C-sapphire

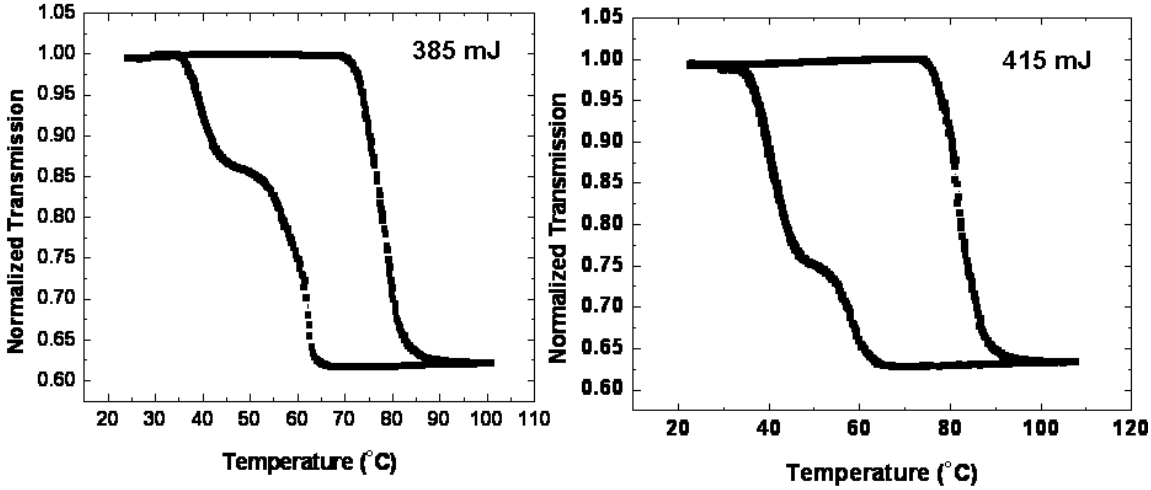

Figure 3.20: Transmission hystereses of HT-grown films grown with two different laser pulse energies on R-sapphire

The hysteretic behavior of the film on R-sapphire at pulse energy of 415 mJ has the kink in the cooling cycle at a different temperature from the film deposited with laser energy of 385 mJ, indicating that a size variation in the VO_2 grain growth occurs with differing laser pulse energies.

CHAPTER IV

NEW INSIGHTS INTO STRUCTURAL AND ELECTRONIC PHASE TRANSITIONS IN VO_2

ABSTRACT

The multifunctional properties of vanadium dioxide (VO_2) arise from coupled first-order phase transitions: an insulator-to-metal transition (IMT) and a structural phase transition (SPT) from monoclinic to tetragonal. The characteristic signatures of the IMT and SPT are the hysteresis loops that track the phase transition from nucleation and growth of the new phase to stabilization at macroscopic length scales. A long-standing question about the mechanism of the phase transition is how the almost-simultaneous electronic and structural transitions are related. Here we report independent measurements of the IMT and SPT hystereses in epitaxial VO_2 films with differing morphologies. We show that the hystereses are not congruent, that the structural change requires more energy to reach completion, and that these results are independent of nanoscale morphology, so that the non-congruence is an intrinsic property of the VO_2 phase transition. This experimental result is supported by effective-medium calculations of the dielectric function incorporating the measured volume fractions of the monoclinic and tetragonal states. The results are consistent with the existence of an intermediate metallic state in which the electron-electron correlations characteristic of the monoclinic state begin to disappear before the transition to the tetragonal structural state. Synchrotron measurements and evidence for an intermediate structure are also presented at the end of the chapter.

4.1 NON-CONGRUENCE OF THERMALLY-INDUCED STRUCTURAL AND ELECTRONIC TRANSITIONS IN VANADIUM DIOXIDE

4.1.1 Introduction

Vanadium dioxide (VO_2) exhibits an insulator-to-metal transition (IMT) at ~67^{o}C with abrupt changes in transport and optical properties, coupled to structural phase transition (SPT) from monoclinic (M_1) to tetragonal (R). The complex physics of the VO_2 phase transition has long been debated, as discussed in Chapter 1. Unlike other strongly

correlated materials[199] exhibiting an IMT, such as V_2O_3[200, 201] or manganites[202], where phase transitions are satisfactorily explained by Mott mechanism alone, the IMT in VO_2 is complicated by an accompanying spin-Peierls instability[49] that leads via strong electron-phonon coupling to the formation of spin-singlet states that incorporate the bonding-antibonding splitting of the $d_{x^2-y^2}$ bands.

A critical question, so far unanswered, is whether the structural and electronic phase transitions in VO_2 occur congruently. For non-equilibrium phase transformations in thin VO_2 films, induced by ultrashort laser pulses, it was reported that the electronic IMT leads the SPT,[62] and that the SPT presents a kinetic bottleneck for the transition.[58] It was also observed that for the shortest attainable excitation pulses, a coherent phonon associated with a breathing mode of the VO_2 lattice appears simultaneously with the IMT.[57] Ultrafast electron diffraction measurements on single-crystal VO_2 excited by femtosecond near-IR laser pulses demonstrated the existence of transitional structural states with lifetimes up to hundreds of picoseconds [203].

On the other hand, in the case of adiabatic, thermally induced phase transitions, Qazilbash *et al*[18] have recently reported an intermediate electronic state characterized by strongly correlated metallic nanopuddles with properties distinct from those of the high-temperature tetragonal metal. Intermediate structural states of monoclinic M_2 and triclinic T phases [11, 12, 204] in doped or uniaxially stressed VO_2 in bulk single crystals have also been reported. A recent study by Okimura *et al*[52] of temperature-dependent XRD on thin VO_2 films on sapphire (0001) substrates suggests the possibility that the M_2 structure may be an intermediate state during phase transition. Micro-X-ray diffraction studies[19] of epitaxial VO_2 on (1010) sapphire substrate have shown evidence for the existence of a monoclinic metallic phase. Taken together, these observations indicate the possibility of local energy minima other than the M_1 and R phases in the region of strong correlation.

An important complement to these previous experiments is a direct comparison of the the characteristic hysteretic signatures of the IMT and SPT. In this experiment, we used near-IR transmission to measure the IMT hysteresis through the phase transition on well-characterized epitaxial thin films of VO_2 on (0001) sapphire; on the same samples, we

then employed high-temperature X-ray diffraction (HTXRD) to follow hysteresis in the SPT, and from these measurements extracted the relative monoclinic fraction as a function of temperature. To complete the analysis, we then calculated the dielectric function of VO_2 in the region of strong correlation using Bruggeman effective medium theory. We observe that the dielectric function calculated on the basis of structural phase is not consistent with the optical signature of the electronic transition: the hysteresis in the SPT is always wider than the hysteresis of the IMT. This inconsistency may imply the existence of an intermediate electronic state.

Our results are demonstrated over macroscopic areas of two types of epitaxial films: continuous epitaxial VO_2 (CE VO_2) and noncontiguous epitaxial VO_2 (NCE VO_2) films grown on c-cut (0001) sapphire having quite *distinct nanoscale morphologies*, suggesting that the differences between the structural and electronic phase transitions is *not* a local or dimensional effect, but can be viewed as inherent to the materials physics underlying the VO_2 phase transition. The measured differences in the energy required to complete the IMT *vs* the SPT may correspond to the existence of two correlation lengths in the region of strong correlation, as proposed by Pergament.[9]

4.1.2 Experimental details

CE and NCE VO_2 films approximately 80±10 nm thick on c-cut (0001) sapphire substrates were grown following two different protocols. The continuous epitaxial (CE) VO_2 films were produced in two steps. First, a 99.99% pure vanadium metal target was ablated at room-temperature in a background of 10mTorr of oxygen, following a standard recipe for pulsed laser deposition (PLD). A second step of annealing the amorphous, sub-stoichiometric film in 250mTorr of oxygen and 450^{o}C, for 30-45 minutes yields stoichiometric, single-phase, crystalline VO_2 . The non-contiguous epitaxial (NCE) films were grown in a one-step PLD process at high temperature (~500^{o}C), using the same target with a background gas pressure of 50 mTorr oxygen and a target-substrate distance of 5 cm.

The epitaxial nature of both films was confirmed by reciprocal space mapping (RSM) using the PANalytical X'pert Pro MRD at the Center for Nanophase Materials Science

(CNMS) and the transmission electron microscopy (TEM) using the HF 3300 TEM; at the SHaRE facility both located at Oak Ridge National Laboratory (ORNL). These RSMs and TEMs are shown in figure 4.1 (c) - (f). The morphological differences in the CE and NCE films are evident from the comparison of the two SEMs respectively in figures 4.1 (a) and (b) and TEMs in figures (c) and (d). The CE film grown at room temperature with subsequent annealing has a smoother surface than the discrete, pyramid-like structure of the NCE film grown at high temperature. But both films are epitaxial — that is, both have a definite orientational relationship to the substrate — as evident from the reciprocal space maps shown in figures (e) and (f).

Epitaxial films are more uniform in orientation and morphology over macroscopic length scales and exhibit more bulk-like phase transition behavior, typified by narrower, sharper hystereses.[175] Epitaxial growth thus minimizes strain and morphological inhomogeneities characteristic of polycrystalline thin films and use volume-averaged optical measurements in different ranges of the electromagnetic spectrum — that is, XRD and infrared transmission — over the same spot of the films to draw inferences about their phase transition characteristics. Moreover, epitaxial films produce X-ray or electron diffraction patterns with spot patterns rather than concentric rings typical of randomly-oriented polycrystalline, allowing extraction of significantly more detailed structural information.

The electronic component of the metal-insulator transition was tracked by measuring the transmission from a white-light source (3000 K blackbody, give manufacturer and model number) during heating/cooling, using an InGaAs detector (950-1600nm, make and model) coupled to a lock-in amplifier. The films were heated and cooled by a Peltier thermoelectric heater. The temperature was measured with a precision thermocouple in thermal contact with the VO_2 surface.

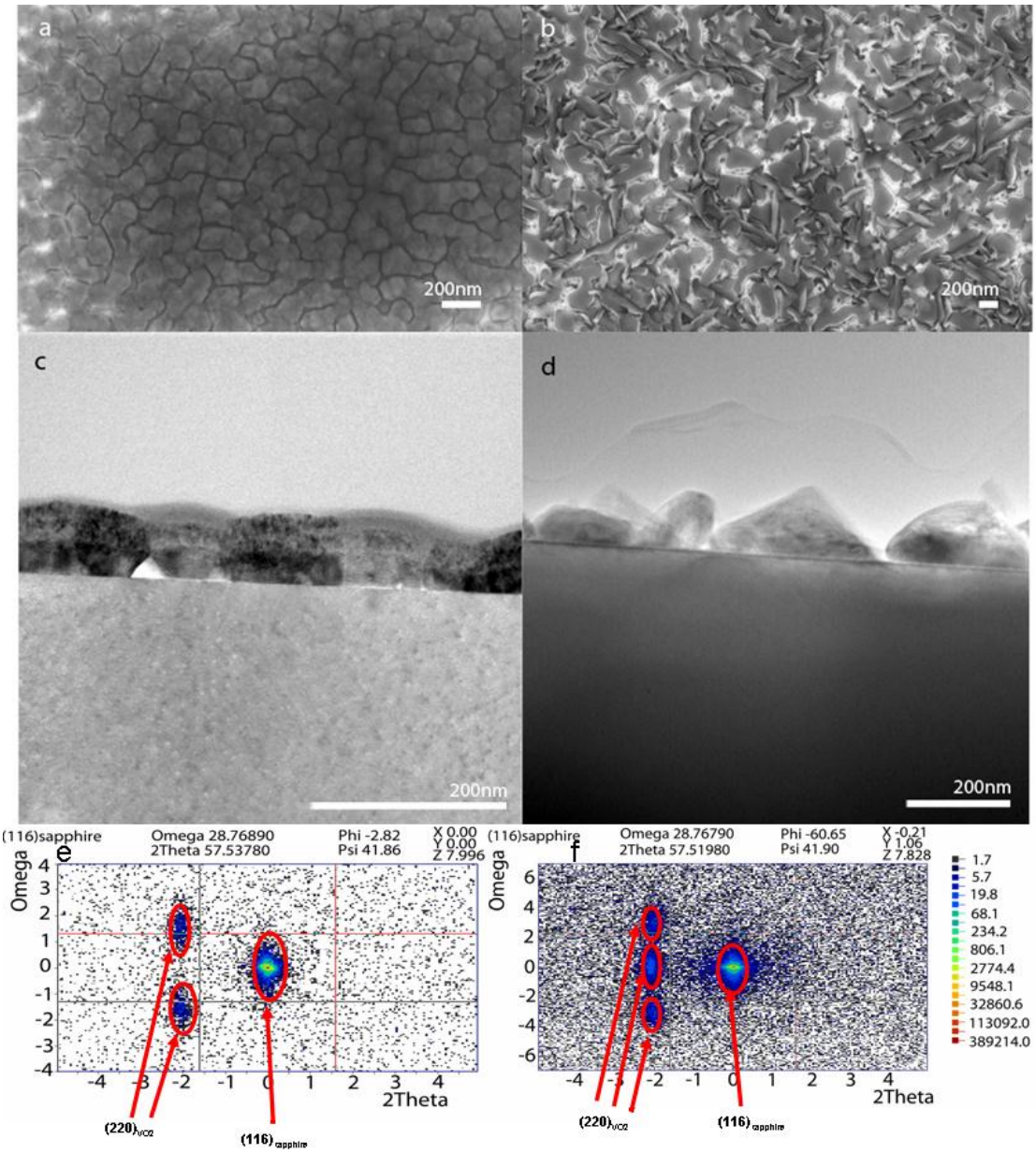

Figure 4.1: (a), (b) Top-view SEM, (c), (d) cross-sectional TEM and (e), (f) X-ray diffraction reciprocal space map of typical CE-VO_2 and NCE-VO_2 films respectively.

The *in-situ* high-temperature XRD data for tracking the structural transition were collected using a different two-axis XRD instrument (PANalytical X'Pert Pro MPD) with Anton Paar XRK900 Reaction Chamber also at the Center for Nanophase Materials Science (CNMS) at ORNL. The ratio of areas under XRD peaks corresponding to different phases of a single material gives the ratio of the volumes of each phase present

in the multi-phase film. The areas were calculated after subtracting the background, then filtering out the Cu-$K_{\alpha 2}$ peaks and applying a Pseudo-Voigt profile fitting method using the X'pert High Score Plus software. The results are shown in figure 4.2.

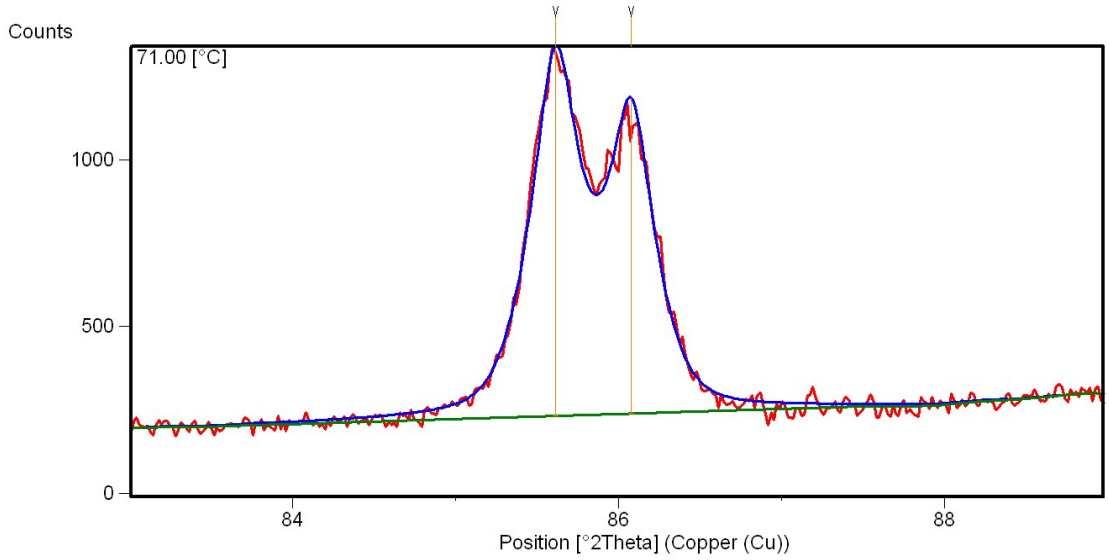

Figure 4.2: A typical spectrum at 71°C during the phase transition of the NCE-film and its profile fitting for calculation of area under the curve. The blue curve shows the fit to our experimental data (red curve) by the Voigt profile fitting method to calculate the area under individual peaks. The green baseline denotes the background.

4.1.3 Experimental results

During the transition, we tracked the evolution of the monoclinic (040) peak for VO_2, located at 86.05˚ on the 2θ–axis, for the CE VO_2 film; the corresponding tetragonal peak is located at 85.73˚. Figure 4.3(a) shows the isoline 3D view of the X-ray spectra indicating the way the selected VO_2 peak shifts during the entire monoclinic-tetragonal-monoclinic transition. The superposition of the 2θ–spectra for the five temperatures over which almost the entire transition is completed is shown in figure 4.3(b). Starting at 69°C, the area under the monoclinic peak decreases as the tetragonal fraction in the film grows; evidently both phases coexist in almost equal fractions at 71°C, and the film is almost entirely tetragonal at 73°C. The slight shift in peak position during the transition can be attributed to the thermal expansion of the sample holder, substrate and the VO_2 lattice. Figure 4.3(c) shows the monoclinic fraction in the sample at each temperature, calculated

from the XRD peak areas as a function of temperature. White light transmission measurements of the MIT [figure 4.3(d)] in this film show narrow, high-contrast hysteresis similar to those of bulk VO_2. This is the signature of the insulator-metal transition, the electronic component of the phase transition.

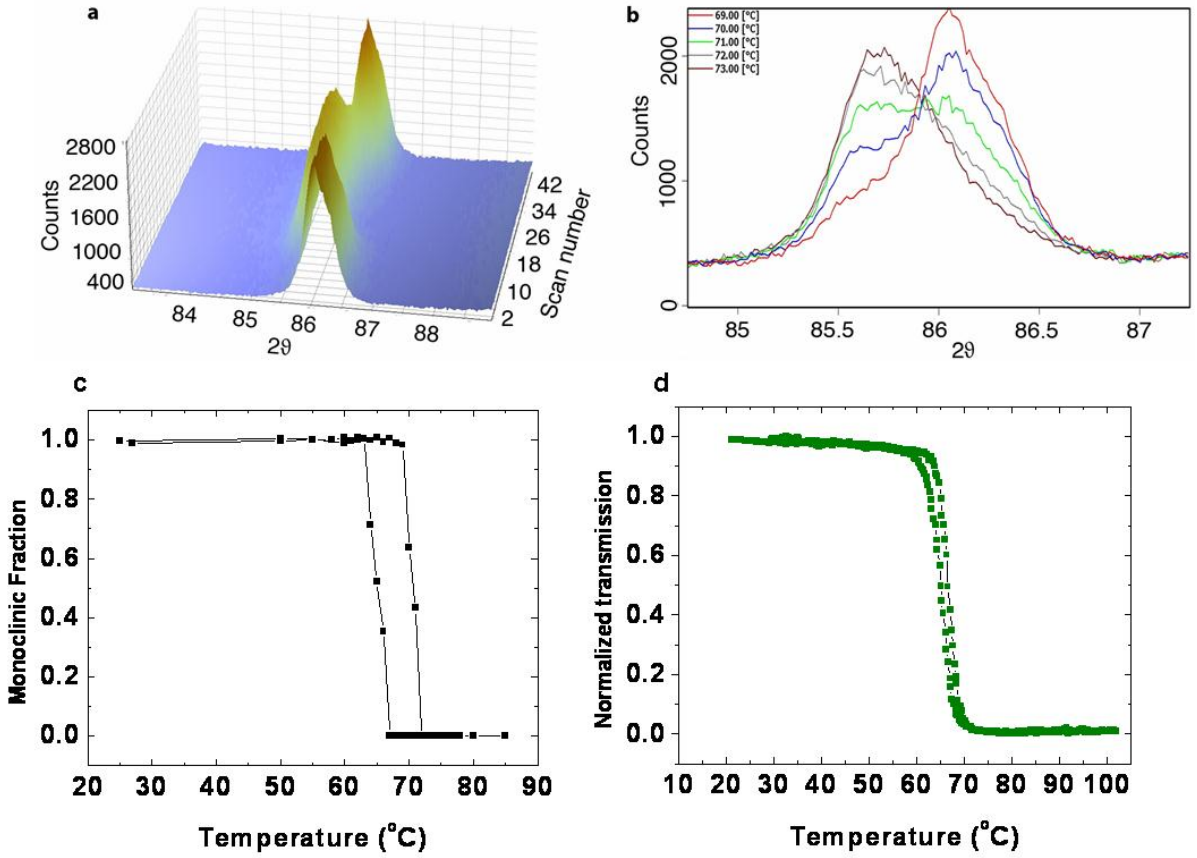

Figure 4.3: HTXRD measurements on CE VO_2 on c-sapphire: (a) Evolution of the reversible structural phase transition (monoclinic-tetragonal-monoclinic) as a function of temperature, (b) evolution of the monoclinic and tetragonal peaks between 69°C and 73°C, and (c) hysteresis in the monoclinic fraction as a function of temperature and (d) hysteresis in the white light optical transmission as a function of temperature measured on the same sample.

Figures 4.4(a) and (b) illustrate the corresponding SPT and transmission hystereses. respectively, observed for NCE-VO_2 films on c-cut sapphire.

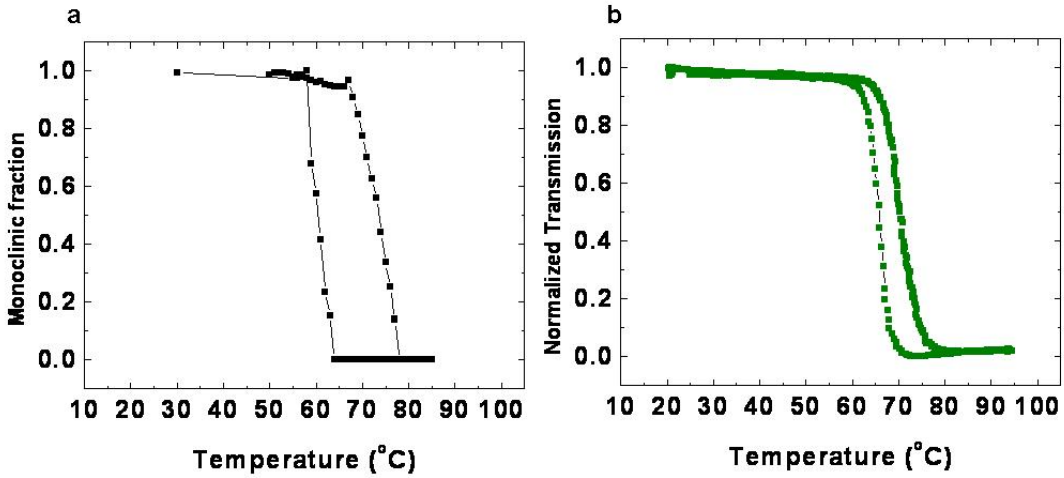

Figure 4.4: HTXRD measurements on NCE VO_2 on c-sapphire: (a) Hysteresis of the monoclinic phase as a function of temperature and (b) optical transmission hysteresis as a function of temperature taken on the same sample.

The hysteresis width is a more fundamental quantity than the onset temperature of phase transition, because absolute temperature comparisons might be convoluted with systematic errors and minor variations in thermometry for the two thermocouples employed. Thus in Table 1 we compare the hysteresis widths, which shows that for epitaxial films with very different nanoscale morphologies on c-sapphire, the SPT hysteresis width is about 2.5 times that of the IMT hysteresis within an error range of ±10%. To ascertain whether or not this ratio is a constant over other epitaxial VO_2 films, will involve more such measurements on epitaxial films on other substrates. For example, hysteresis measurements on a different plane of sapphire, or a different substrate altogether, such as TiO_2, can be expected to generate very different film-substrate strain affecting the SPT.

Table 4.1: IMT and SPT hysteresis width comparison

VO_2 film	*IMT hysteresis width ΔH_{IMT} (in ^oC)*	*SPT hysteresis width ΔH_{SPT} (in ^oC)*	*$\Delta H_{SPT}/\Delta H_{IMT}$*
CE-VO_2	4.83	13	2.69
NCE-VO_2	2.49	6	2.41

4.1.4 Modeling results

To provide a way of interpreting our experimental data and have a comparison basis for the two seemingly different quantities — the experimentally measured monoclinic fraction and normalized transmission intensity — we model here the structural data to yield the evolution of the dielectric function, assuming that only the structural change was responsible for it. We then compare with the measured change in dielectric function by superposing it on the infrared transmission hysteresis.

The phase transition in semiconducting VO_2 is initiated at nucleation sites from which metallic domains then evolve up to and beyond the transition temperature. In the strong correlation region near the transition temperature, semiconducting and metallic domains coexist, and this spatial inhomogeneity strongly influences the effective dielectric properties of the film. We use Bruggeman effective medium theory (EMT)[205] to model the optical properties of VO_2 thin films[206 207] rather than Maxwell Garnett EMT [208 63], since the latter assumes a small volume fraction of metallic inclusions. The effective dielectric constant in the Bruggeman theory for ellipsoidal inclusions is given by:

$$f\frac{\tilde{\varepsilon}_m(\lambda)-\tilde{\varepsilon}_{eff}(\lambda)}{\tilde{\varepsilon}_m(\lambda)+\frac{1-q}{q}\tilde{\varepsilon}_{eff}(\lambda)}+(1-f)\frac{\tilde{\varepsilon}_i(\lambda)-\tilde{\varepsilon}_{eff}(\lambda)}{\tilde{\varepsilon}_i(\lambda)+\frac{1-q}{q}\tilde{\varepsilon}_{eff}(\lambda)}=0 \qquad (4.1)$$

so that

$$\varepsilon_{eff}=\frac{\tilde{\varepsilon}_m(f-q)-\tilde{\varepsilon}_i(f+q-1)+\sqrt{\left[\tilde{\varepsilon}_i(f+q-1)-\tilde{\varepsilon}_m(f-q)\right]^2+4(1-q)q\tilde{\varepsilon}_m\tilde{\varepsilon}_i}}{2(1-q)} \qquad (4.2)$$

where $\tilde{\varepsilon}_i$ and $\tilde{\varepsilon}_m$ are the wavelength-dependent dielectric constants in the insulating and metallic states of VO_2 respectively [209], f is the metallic volume fraction obtained from the XRD peak areas, and q is a shape-dependent depolarization factor for the inclusions. The metallic fraction f was calculated from the experimentally-obtained HTXRD spectra. The depolarization or shape-factor is taken to be continuously varying from 0.2-0.5 assuming nearly spherical metallic regions at low concentrations and thin, flat disks at higher concentrations relative to overall film thickness.[210]

Figure 4.5 (a) and (b) show respectively the evolutions of the real and imaginary parts of the dielectric function spectra for a typical NCE-VO_2 film as it goes through the thermally-induced insulator-to-metal transition, as calculated following the above procedure. From the dielectric function components we calculate the refractive indices (n) and the absorption co-efficients (k) for each film using the equations:

$$n = \frac{1}{\sqrt{2}}\left[\varepsilon_1 + \left(\varepsilon_1^2 + \varepsilon_2^2\right)^{1/2}\right]^{1/2} \tag{4.3}$$

$$k = \frac{1}{\sqrt{2}}\left[-\varepsilon_1 + \left(\varepsilon_1^2 + \varepsilon_2^2\right)^{1/2}\right]^{1/2} \tag{4.4}$$

Note that the real and imaginary parts of the dielectric function, and thus n and , evolve with temperature in opposite ways, making VO_2 a lossy metal in its high temperature state. Figure 4.5 (c) shows the evolution of the reflection co-efficient R of the VO_2 film as given by the equation:

$$R = \frac{(n-1)^2 + k^2}{(n+1)^2 + k^2} \tag{4.5}$$

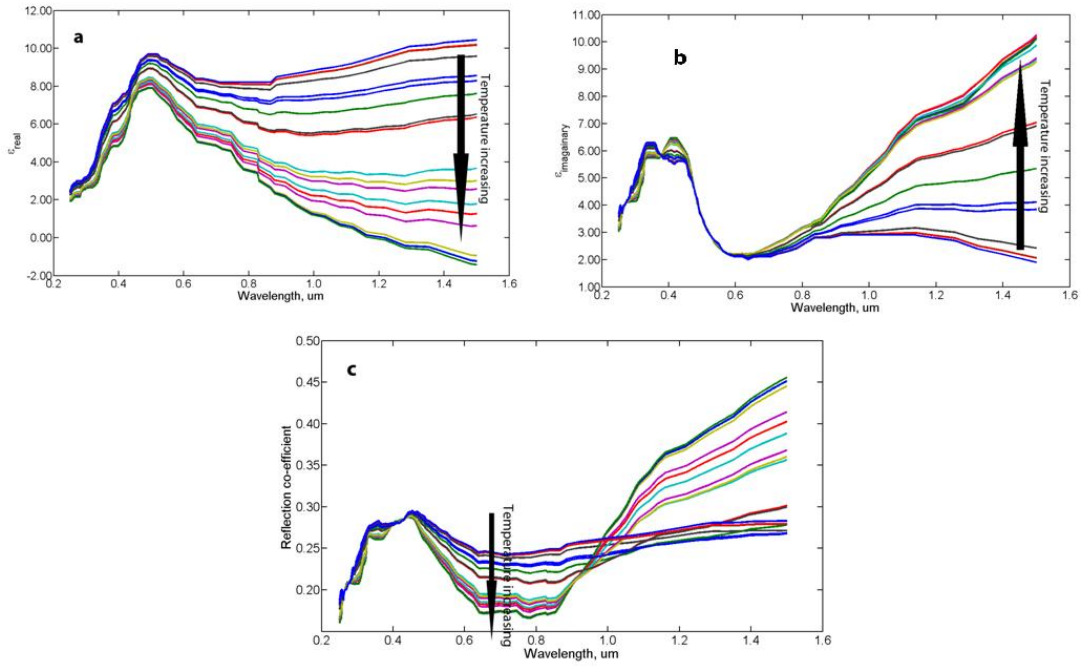

Figure 4.5. For NCE-VO_2, (a) real and (b) imaginary parts of the dielectric function as a function of temperature extracted from Ref. 33 using a Bruggeman mean-field model parametrized by the HTXRD measurements. (c) The reflectivity spectrum for varying temperatures calculated from (a) and (b). The arrows indicate the trends in the evolution of the dielectric functions as a function of temperature.

Figure 4.6 shows the real (*n*) and imaginary (*k*) parts of the refractive index of both NCE VO_2 and CE VO_2 films calculated using equation (2), and the modeled transmission using equation (3). The transmission calculated from the Bruggeman model is,

$$T_B = (1-R)e^{-\alpha z} = (1-R)e^{-4\pi kz/\lambda} \tag{4.6}$$

where R is the reflection coefficient (calculated from n and k), α is the absorption coefficient, both being functions of wavelength λ, and *z* is the thickness of the film, set to 90 nm in our calculations. Cross-sections of the n, k spectra for specific wavelengths are shown in the figures 4.5(a, b) and (d, e) [black continuous lines] to make the temperature hystereses in n and k values evident over the entire spectrum. The hystereses are more

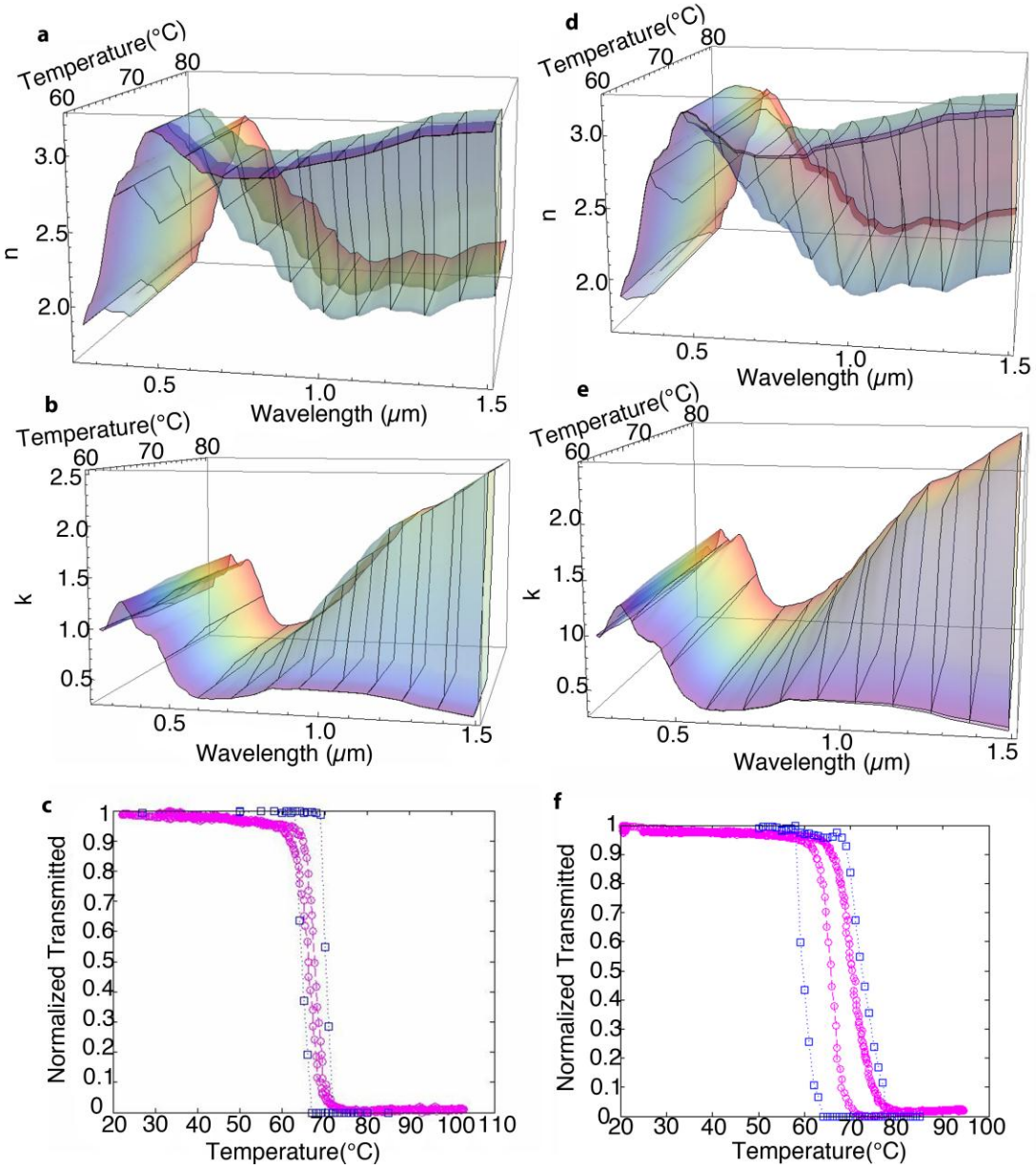

Figure 4.6: Top four panels: Three-dimensional plots of (a) real (n) and (b) imaginary (k) part of the effective refractive index in CE VO_2 and same in (d) and (e) respectively for NCE VO_2 extracted from HTXRD data by means of Bruggeman EMT analysis, as a function of temperature. The n, k hysteresis loops with higher contrasts are observed as one move towards the infrared. Bottom two panels: Superposition of the transmission hystereses, modeled (blue) and experimental (magenta) for (c) CE and (f) NCE VO_2.

pronounced in the infra-red region of the spectrum as expected. Superimposed on the calculated transmission [figure 4.5(c) and (f)] are the measured data from figure 4.3(d)

and 4.4(d), respectively to allow comparison of the hystereses for the MIT (measured optically) and the SPT calculated from the Bruggeman analysis.

4.1.5 Discussion

Comparison of the measured hystereses [Figures 4.3(c),(d) and 4.4(c),(d)] for both CE and NCE VO_2 films shows that the electronic (Mott) transition is completed with less thermal energy than the structural phase transition. The hystereses in dielectric functions extracted from a mean-field calculation of the monoclinic-to-tetragonal transitions are also wider than the measured IMT hysteresis, and thus consistent with this picture [Figures 4.5(c) and (f)]. Thus, we infer that the intermediate metallic state with its higher reflectivity appears before the signature of the stable rutile structure, as observed by Qazilbash *et al*[18] but this inference is now supported by the complementary structural measurement (XRD) and modeling of the SPT. Kim *et al*,[19] in μ-XRD studies on a nanofabricated epitaxial VO_2 channel on (1010) sapphire, combined with an electrical transport measurement, had likewise concluded that a monoclinic, correlated-metal (MCM) phase precedes the rutile phase. Our results, on the other hand were based on volume-averaged XRD and optical measurements made on the same spot in epitaxial films on a different plane of sapphire, namely (0001), thus with completely different lattice mismatches and strains from those in the Kim samples. Our experimental results combined with modeling of the dielectric function lead to a conclusion similar to that of Kim *et al*.[19] This suggests that we are justified in generalizing these results as an intrinsic feature of VO_2 phase transitions, which might well extend to other strongly-correlated oxides.

Using similar fabrication and measurement procedures, Okimura *et al*[52] have recently inferred the presence of the M_2 intermediate phase by fitting the measured asymmetric X-ray diffraction peaks. As they have noted, the M_2 phase could be stabilized by strain in the fabricated film. However, the M_2 is known to be an insulating phase, and our experiments show that the transitional phase is metallic instead. The search for intermediate metallic structures would be of general significance for the physics of phase transitions, just as the discovery of the insulating M_2 phase helped to establish the Mott character of VO_2 phase transitions. In the present measurements, the IMT hysteresis is

narrower than the SPT hysteresis in both the heating and cooling cycles. Therefore these new results leave open the possibility that the Mott transition can be partially or fully completed without a change of structure.

It is also possible that an intermediate crystal structure offers more freedom to electrons leading to this metallic character. Our experimental results hint at a dual character of the phase transition, as proposed by Pergament.[9] The duality is defined by two correlation lengths that correspond respectively to the Mott-Hubbard and Peierls contributions to the physics of the phase transition. The longer of the two correlation lengths is associated with the disappearance of the strong correlations in the monoclinic phase.

Starting with the Mott criterion:

$$a_H n_C^{\frac{1}{3}} \approx 0.25 \tag{4.7}$$

Pergament deduced the correlation length of a Mott insulator to be

$$\xi = \frac{2\hbar v_F}{(3\pi^2)^{\frac{1}{3}}\Delta} \tag{4.8}$$

Unlike in conventional semiconductors, band gap $E_g \neq kT_t$ for VO_2, as E_g = 0.7 eV whereas kT_t = 0.03 eV for VO_2.

Assuming $\Delta = E_g$, one gets the correlation length to be ~2Å and with $\Delta = kT_t$, the correlation length comes out to be ~18Å.

Thus according to to Pergament, the transition in VO_2 from a metal ($\Delta = 0$, $\xi \rightarrow \infty$) to a semiconductor/insulator ($\Delta = E_g$, $\xi = R$), with decreasing temperature, might be occurring through an intermediate (transient) state with $\Delta = kT_t$ and $\xi = \xi_1 =$ 15–20 Å. Once the modulation in the electronic configuration occurs, a Peierls-like distortion of the crystal structure accompanies by doubling of the lattice period along the c-direction. This structural transition then, in turn, results in the stabilization of the insulating state with $E_g =$ 1eV and complete localization of electrons on vanadium atoms. Thus the

intermediate state can be considered as a state in which the electrons are localized only partially.

We then can summarize this as: the structural change constitutes a bottleneck; and the driving force for completing the phase transition is the electron correlation produced by the Mott-Hubbard contribution. In our thermally driven, adiabatic phase transition, we thus see a trend similar to that observed when the phase transition is induced by ultrafast laser excitation,[58] causing rapid renormalization of the band gap and the excitation of a coherent phonon associated with vibrations of the oxygen octahedra.

To summarize, we observe that, as had been suggested by Kim *et al*,[19, 62] our results also indicate that it is possible that the VO_2 phase transition indeed undergoes a Mott transition between the M_2 insulator phase and the MCM phase, while the ultimate structural transition from the M_1 to the R phase occurs around it.

4.2 SYNCHROTRON EXPERIMENTS

In order to look for a structural correlate of this above-mentioned intermediate transient state during the phase transition, we planned further experiments in the synchrotron facility at the Swiss Light Source, Villigen, Switzerland. The Materials Science Beamline (X04SA) in the Swiss Light Source (SLS) has a unique facility for growing thin films in a PLD/XRD ultrahigh vacuum chamber mounted on a five-circle surface diffractometer for *in situ* characterization using the tunable X-ray beam from the SLS, as seen in figure 4.7.

Figure 4.7: Swiss Light Source Synchrotron Facility

A short description of the SLS XRD is as follows:

The Newport (2+3)-circle diffractometer is shown schematically in Figure 4.8. The naming conventions for the instrument circles follow those used by Vlieg.[211] The diffractometer provides two degrees of freedom for the sample motion and three for the detector. The γ and δ-circle are used to position the detector in the direction of the diffracted x-ray beam, $\mathbf{k}_{out}$, while the ν-axis rotation allows the detector and the slit system attached to it to turn around $\mathbf{k}_{out}$.

For a (2+3)-type instrument, the two sample circles are fully decoupled from the detector circles. For our experiment we used the vertical geometry (blue, dark shade in Fig. 4.8), the sample surface plane is vertical, and hence its surface normal direction lies in the horizontal plane. The grazing incidence angle of the synchrotron beam onto the surface is adjusted using the α-circle, while ω_ν provides the azimuthal sample rotation around the surface normal.[212]

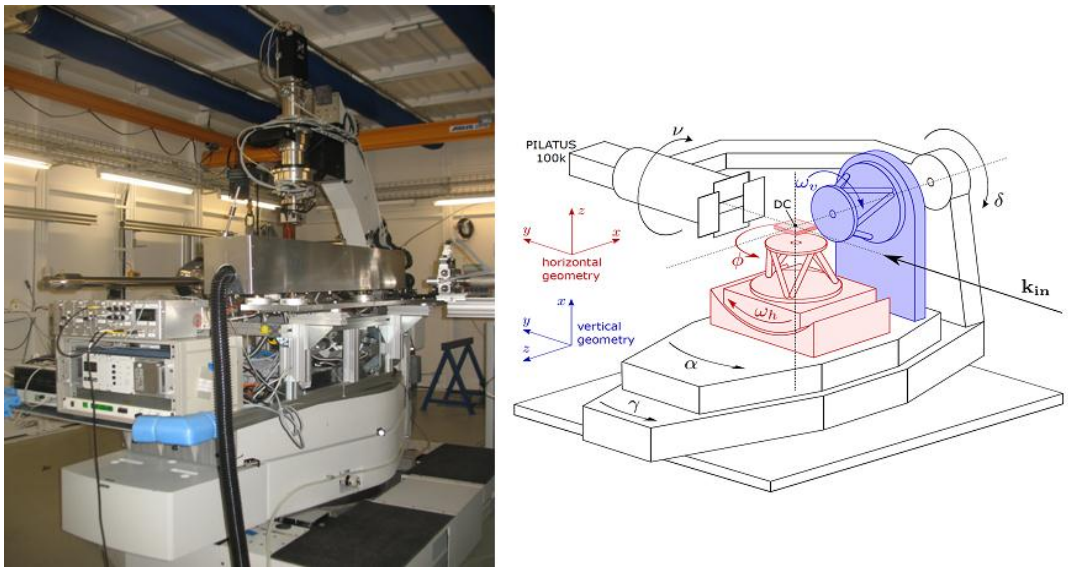

Figure 4.8: The five-circle X-ray diffractometer

Six additional sample degrees of freedom (three translations and three rotations) are provided by a hexapod, mounted onto the ω_v sample circle. The three linear motions are used to bring the sample center into coincidence with the diffractometer center. The sample surface normal is accurately aligned with the diffractometer's azimuthal sample rotation axis (ω_v) using the hexapod rotations. All measurements and angle calculations require this coincidence of sample surface normal and azimuthal rotation axis, so once the sample is accurately aligned, the hexapod positions are fixed for the rest of the experiment.

The spectra are collected using a two-dimensional pixilated CCD camera, the horizontal axis of which corresponds to δ and vertical to γ. The conversion from pixel coordinates to reciprocal space positions is discussed in detail on the SLS website. The angle-resolved scattering pattern on the detector is transformed into a curved two-dimensional slice through reciprocal space. In general, the δ corresponds to the in-plane 2θ and the γ corresponds to the out-of-plane 2θ implying that any change in the dimensions of the unit cell in-plane would be reflected on the horizontal axis and out-of-plane on the vertical axis.

Our intent was to conduct a systematic study of the effect of strain on structural transition of films grown epitaxially on different planes of sapphire and TiO_2 in conjunction with infrared reflection measurements, so as to have simultaneous structural and electronic phase transition information. This would have helped us understand the effect of strain on SPT and how it affects the electronic transition in turn and thus the effect of strain on the entire phase transition physics. During our experiments we observed some inconsistencies in temperature measurements and optical data acquisition, rendering some of the acquired data unusable.

Figure 4.9 shows the monoclinic to rutile transition in a 50 nm VO_2 film on glass. Since the film is polycrystalline, Bragg diffraction conditions are fulfilled for all random directions and hence the diffraction pattern consists of rings which are manifested as lines in two dimensions.

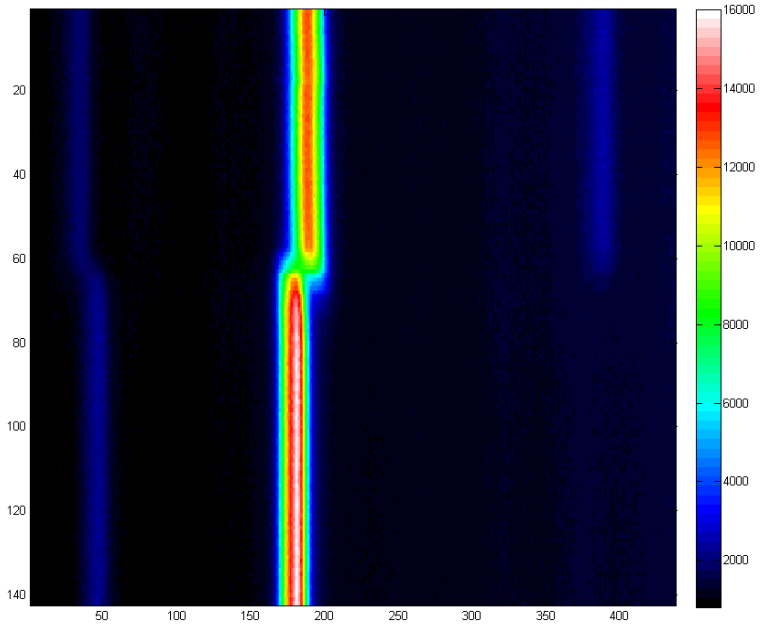

Figure 4.9: Monoclinic to rutile transition in a 50 nm VO_2 film on glass.

On the other hand , in case of epitaxial films on sapphire, for example we observe spots instead of lines , because of a preferred direction in which the film grows.

In figure 4.10, we present three snapshots of the structural phase transition of a 50 nm VO_2 film on c-cut sapphire. For the temperature-dependent XRD measurements an increase in frame numbers correspond to a monotonic increase in temperature during the heating cycle of the phase transition.

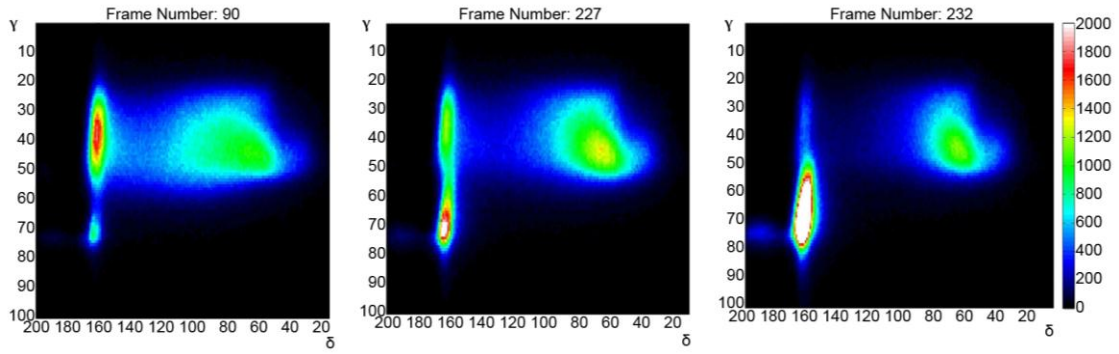

Figure 4.10: Evolution of the transient M2 phase as a function of temperature during phase transition

In Figure 4.10(a) the peak at the top left corresponds to the (002) M1-VO_2 peak. At the initiation of the phase transition a faint peak to the right of the figure appears, which does not correspond to any known M1-VO_2 peak, and grows in intensity as we come close to the transition temperature as seen in Figure 4.10(b). As we cross over to the other side of the transition temperature the (002) M1-VO_2 peak disappears and the (200) rutile-VO_2 peak appears in the bottom right (Figure 4.10(c)), the peak to the left still remains before vanishing completely only at a considerably higher temperature compared to the M1-VO_2 peak. This behavior of the "unknown" peak matches perfectly with the behavior of M2-VO_2 as described by Pouget et al and Eyert et al and described in Figure 1.6 in Chapter 1. This leads us to conclude that our "unknown" peak corresponds to an M2-VO_2 peak, thus giving us direct evidence of the M2-VO_2 transient phase in course of structural phase transition in epi-VO_2 films on c-sapphire. Figure 4.11 summarizes the discussion above for another M1-VO_2 peak, $(10\bar{2})$, which has no corresponding tetragonal peak when it transition. In this figure, the y-axis corresponds to the frame numbers for acquired data, which corresponds to the evolution of a specific peak in position and intensity as the

temperature is increased from below to above transition temperature and then cooled back below T_c. The $(10\bar{2})$ peak at 70-pixel should have vanished gradually and reappeared back during cooling, but instead a new peak, not corresponding to any known peak of M1-VO_2 transiently appeared and shifted from the $(10\bar{2})$ peak, grew in intensity and then disappeared abruptly above the transition temperature. During cooling also, it appeared transiently before the $(10\bar{2})$ peak grew in intensity and regained its room temperature position and intensity.

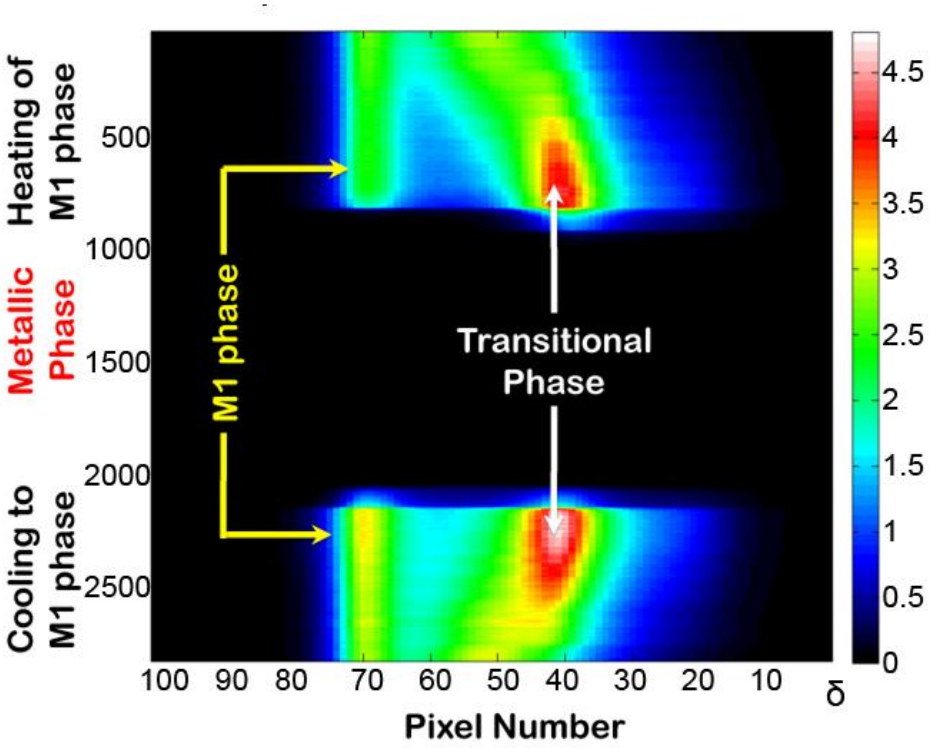

Figure 4.11: Evolution of a VO_2 peak (green peak to the left, at 70 pixel) as the temperature is increased from below to above the transition temperature T_c and then decreased back to below T_c. The 70-pixel peak corresponds to $(10\bar{2})$ peak of M1-VO_2 and should disappear above 67°C, but we see a second peak , not corresponding to an M1-VO_2 peak, at ~40 pixel, coming into transient existence just near T_c both during heating and cooling phases, thus giving evidence for a transient structure during SPT.

A hint of the same transitional M2 state is also seen in a 10 nm VO_2 film on C-sapphire as shown in figure 4.12.

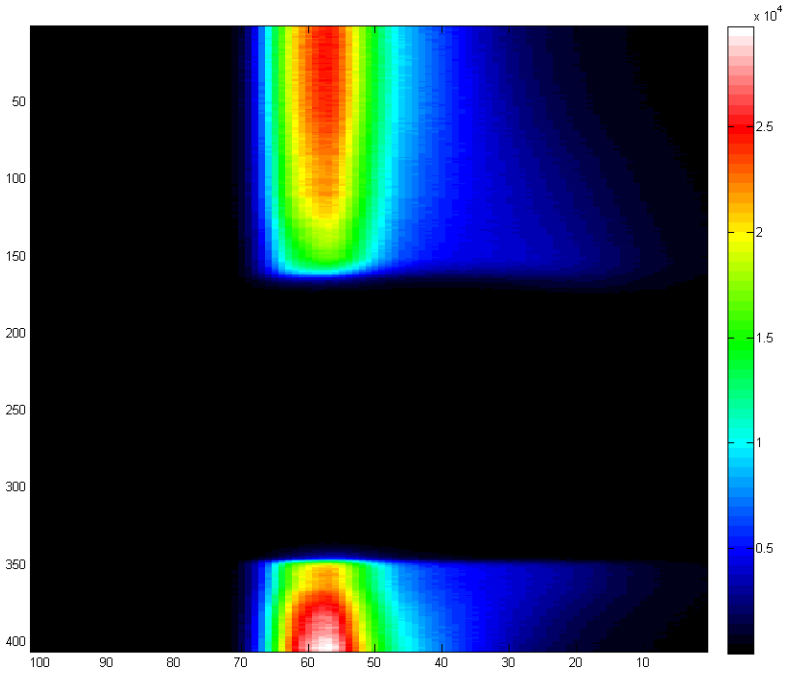

Figure 4.12: The same transitional M2 state is also seen in a 10 nm VO_2 film on C-sapphire.

Figure 4.13 shows the evolution of the signal from an M1-VO_2 peak near the film-substrate interface for the same 10 nm VO_2 film on C-sapphire.

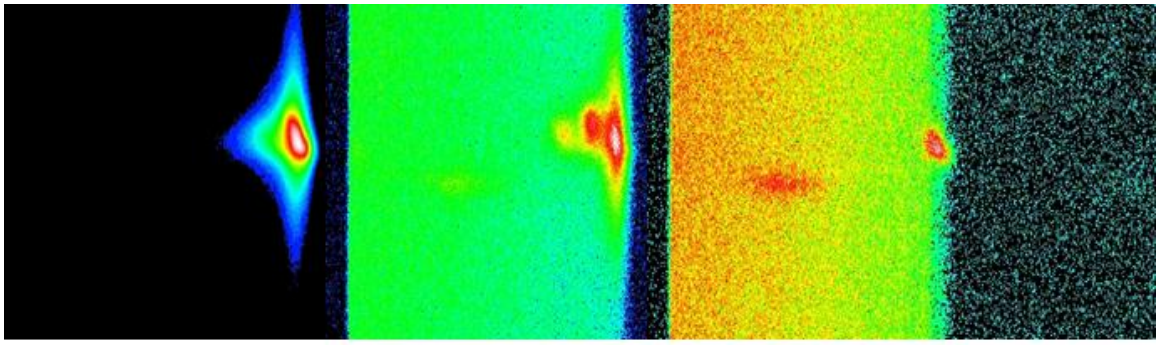

Figure 4.13: The evolution of the signal from an M1-VO_2 peak near the film-substrate interface for the same 10 nm VO_2 film on C-sapphire.

CONCLUSION

Our experiments demonstrate that the non-congruence of the structural and electronic phase transitions in VO_2 is a fundamental property of this material, independent of

dimensionality and morphology. This is a critical finding, given that a large share of the many potential applications envisaged for VO_2 necessarily involves thin-film devices. Moreover, the evolution of the SPT, coupled with modeling by an appropriate effective-medium theory to yield information on the evolving dielectric function, can reveal both correlations and differences between the electronic and structural signatures of solid-solid phase transitions. For example, doping alters the electronic signature of the metal-insulator transition in VO_2;[213] measurements like those described here can show whether or not these changes in electronic response have structural correlates. These results also contribute to deeper understanding of phase transitions found in other Magneli phases of Ti-O and V-O systems.[90] Indeed, as interest grows in understanding strongly correlated materials at the micro- and nano-scales, clarifying the relationship of evolving structural and electronic features of the phase transitions is imperative. Synchrotron measurements on epitaxial films have the ability to track structural intermediates during phase transitions, and more careful experiments can help uncover the structural pathways and components in the convoluted phase transition mechanism of vanadium dioxide.

CHAPTER V

TUNGSTEN DOPING OF VANADIUM DIOXIDE THIN FILMS

ABSTRACT

In this chapter we initially review the work by other groups that has been done in doping VO_2 with tungsten (W). This is followed by a discussion of our results involving the effect of deposition parameters on W-incorporation in VO_2 films. In the next section, we provide the first evidence from high-resolution transmission electron-microscopy that W occupies substitutional sites in epitaxial VO_2 films grown on (0001) sapphire substrates. The substitutional character of the W defect plays a critical role in the metal-insulator transition when it is induced by an ultrafast laser pulse. In particular, we demonstrate that both the transient response in the first few picoseconds after excitation and the longer-term evolution of the phase transition are determined by the injection of extra electrons into the conduction band from the dopant atoms. If the threshold fluence can be lowered/tailored to modify the ultrafast response of VO_2, it would be desirable for various applications ranging from switches and sensors to optoelectronics in telecommunications frequencies. In conclusion, we discuss the effect of W-doping on the thermally-induced structural phase transition of doped films.

5.1 EXISTING LITERATURE ON W-DOPING

The transition temperature T_c of approximately 67˚C for VO_2 is too high for many practical applications. Doping can lower the transition temperature, T_c significantly, and hence doping of VO_2 has been tried extensively for a long time to make it suitable for many important applications. Various dopants — W, Ti, F, Mo, Nb, Cr ,Li, Al — have been used to manipulate T_c. Earlier successful attempts at doping were made by many groups[22, 108, 122, 214-218] and they demonstrated that control of T_c make VO_2 films more suitable for a wide variety of applications.

The doping process is comparatively easier in CVD and sol-gel techniques, but has also been achieved with the help of co-sputtering, and use of multiple targets or metal-doped targets in pulsed laser deposition. The reported transition temperature-shifts on doping with different types of dopants have been quite significant (Table 1). But in some cases, with the decrease of T_c, the electrical and optical properties were degraded as well.

Table 5.1: The effect of doping VO_2 with various concentrations of different dopant atoms and their effect on the transition temperature

Dopant	*Concentration in atomic %*	*Transition temperature decreases by*
Tungsten(W)[22]	1.0	22°-28°C
Molybdenum(Mo)	1.5[219], 1.0[22]	35°C[219], 11°C[22]
Niobium(Nb)[22, 122]	1.0	8°C

In order to understand the cause of this degradation and find a solution to this issue, it is necessary to study the structural characteristics of the films before and after doping. Apart from the fact that dopant atoms supply extra charge carriers, it is also important to find the lattice locations of dopant atoms, that is, whether they enter the network or remain in the interstitial and induce stress release or form defect centers. This was studied in epitaxially-grown VO_2 by Wu *et al* in 1999,[219] who doped VO_2 with Mo and concluded that Mo is a substitutional dopant, which decreased T_c, and simultaneously reduced the sharpness of transitions. They concluded that since intrinsic VO_2 thin film is *n*-type, any acceptor doping will compensate for undoped *n*-type intrinsic VO_2, thereby lowering its transition temperature but without compromising its phase transition characteristics.

Livage *et al* in 1998[126] using sol-gel deposition demonstrated an extensive tailoring of the T_c and switching properties of VO2 films by doping them with cations like W^{6+}, Nb^{5+}, Ti^{4+},Cr^{3+},Al^{3+}, in varied proportions, and found that the transition temperature was reduced when doped with high-valence atoms (W^{6+}), whereas the transition temperature was elevated when the VO_2 doped with

lower valence atoms such as Al^{3+} and Cr^{3+}. Manning *et al*[110, 112] also demonstrated successfully doping VO_2 with tungsten and other cations such as Mo and Nb using the CVD process.

It was shown by Jin *et al*[220-222] initially by ion-implantation and later by magnetron sputtering ,and subsequently also by Soltani *et al*[168] in PLD, that T_c can be reduced by W-doping in proper proportions in films. More such efforts from several other research groups resulted in publications like Binions *et al,*[116, 223] Cavanna *et al,*[224] Piccirillo *et al,*[117] Beteille *et al,*[225] and others.

Recently, co-doping has also been attempted. Burkhardt *et al*[226, 227] were the first to try tungsten and fluorine co-doping by sputtering; they observed that the two doping elements act independently of each other, so that their conjugated influence on phase transition is the superposition of the respective influence of each element. Takahashi *et al*[228] investigated both W-Mo and W-Ti co-doping by the sol-gel deposition technique, and the interaction of W and Ti was found to be stronger than that between W and Mo. The advantage of W-Ti co-doping is that it permits one to control and to tailor the transition behavior, such as smoothing gradient and reducing optical and electrical hysteresis. This was also demonstrated by Soltani *et al*[213] in 2004.

Before concluding this section, we will discuss a very recent finding by Booth *et al*.[17] With the help of X-ray absorption fine structure spectrometry of W-doped VO_2 films they showed that significant expansion occurs along the [110] and $[1\bar{1}0]$ directions across the phase transition from low to high temperature. This distortion breaks the bonds between Peierls-paired vanadium ions and therefore might be one of the mechanisms by which tungsten doping lowers the transition temperature and enthalpy. From their results, Booth *et al*[17] draw an important conclusion, namely, that the phase transition in VO_2 is essentially structurally-driven.

5.2 EFFECT OF DEPOSITION PARAMETERS ON W-INCORPORATION

Recently, we have attempted to do W-doping of epitaxial films of VO_2 grown on sapphire and TiO_2 substrates. We have achieved tungsten doping following recipes similar to the high-temperature and room-temperature growth recipes described in Section 3.1.1 with just the V metal target replaced with W-V alloy metal targets of different proportions. Figure 5.1, shows

the changes in morphologies that occur due to doping in HT-grown film on A-sapphire, RT-grown film on C-sapphire and HT-grown film on TiO_2(001) substrates respectively.

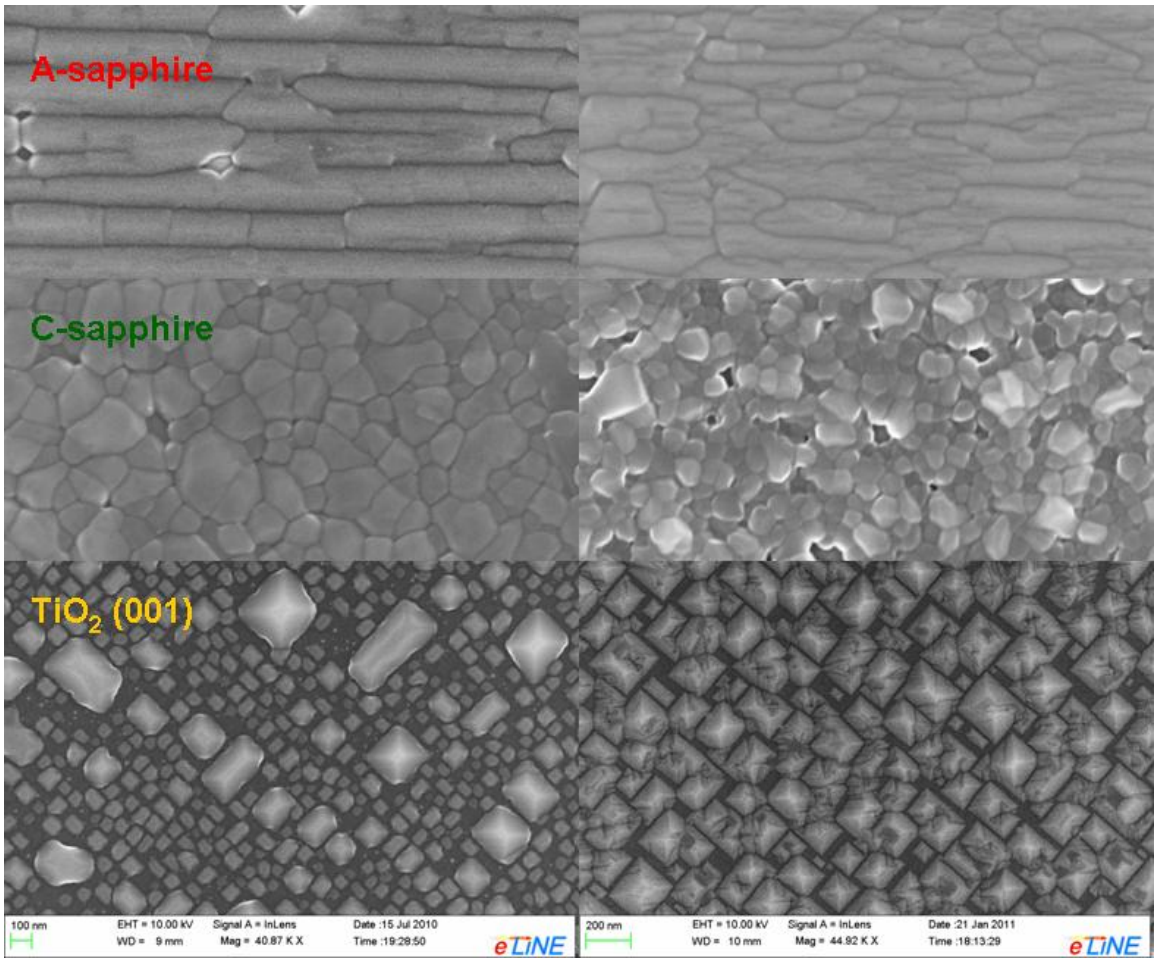

Figure 5.1: Morphology differences in undoped (left) and doped (right) VO_2 films grown on various substrates

5.2.1 Effect of Temperature

In this section, we discuss the noticeable effect that the temperature of the substrate during deposition has on W-incorporation in the films. Figures 5.2-5.4 show the differences in transition temperatures due to differing W-incorporations at different deposition temperatures.

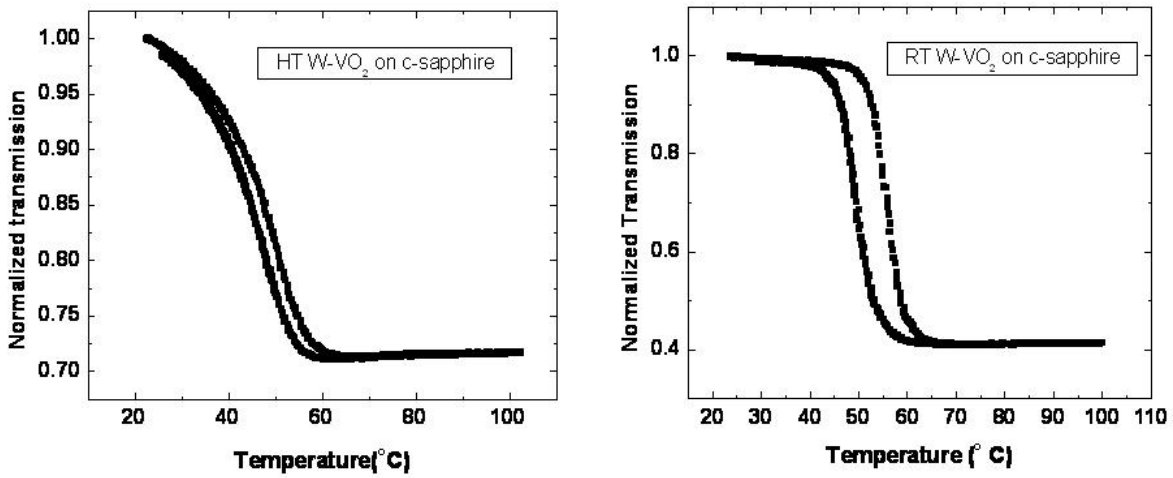

Figure 5.2: HT- (left) and RT- (right) grown W-doped films on C-sapphire

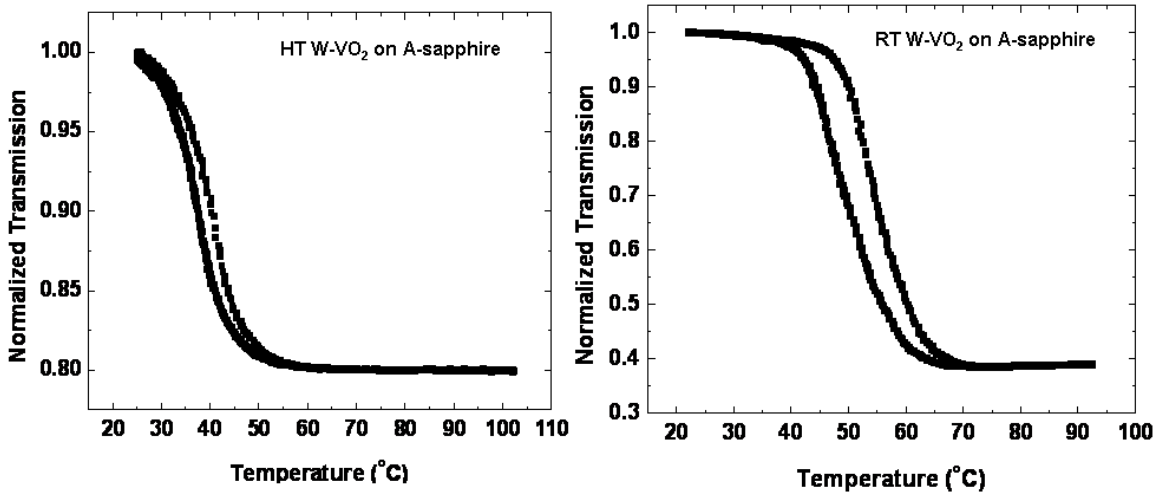

Figure 5.3: HT- (left) and RT- (right) grown W-doped VO_2 films on A-sapphire

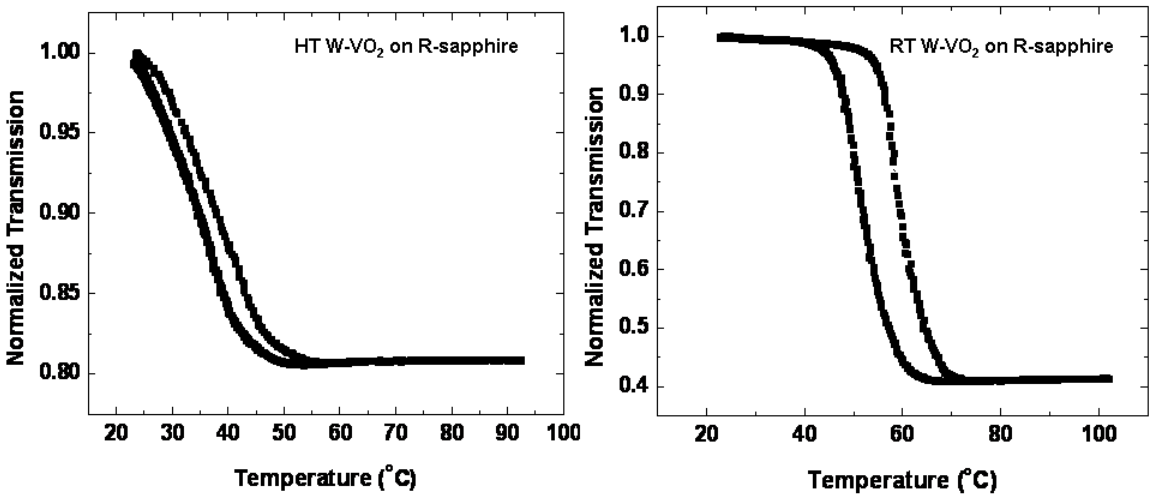

Figure 5.4: HT- (left) and RT- (right) grown W-doped VO_2 films on R-sapphire

According to Rutherford backscattering spectroscopy, the atomic percentages of W present in HT and RT grown films on C-sapphire are 0.66% and 0.34% respectively. In HT and RT grown films on R-sapphire, the concentrations were found to be 1.64% and 0.95% respectively. This indicates that higher substrate temperature definitely facilitates more W-incorporation in the films, but that dopant incorporation is also substrate dependent.

5.2.2 Effect of substrate

It has been observed that films grown under the same conditions on different substrates during the same deposition run yield differing W-doping levels as is evident from figures 5.5 and 5.6.

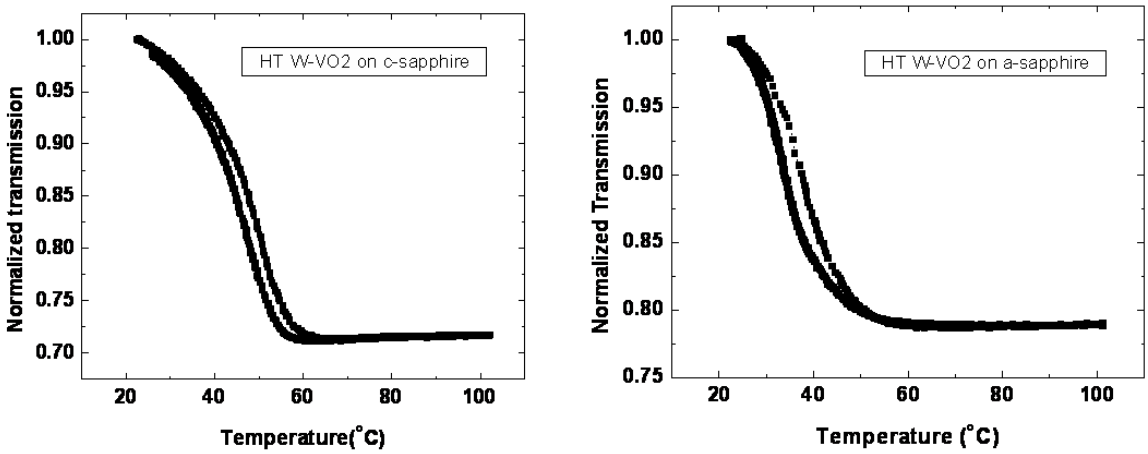

Figure 5.5: HT-grown W-doped films grown under the same deposition condition on C-sapphire and A-sapphire

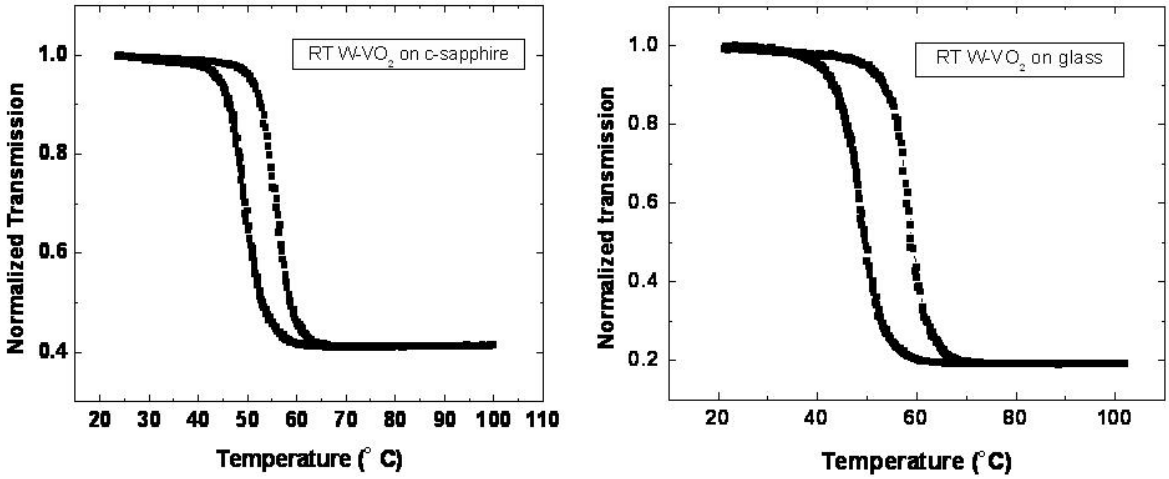

Figure 5.6: RT-grown W-doped films grown under the same deposition conditions on C-sapphire and glass

RBS studies on the HT-grown films on C-sapphire and A-sapphire yielded 0.66 and 0.71 atomic *per cent* of W, respectively, whereas the RT-grown films on C-sapphire and glass exhibited concentrations of 0.34 and 0.21 atomic per cent of W, respectively.

5.2.3 Effect of target-to-substrate distance

Contrary to conventional wisdom, as we vary the target-to-substrate distance we observe that, as the the distance grows, W incorporation increases. This is evident from both figures 5.7 and 5.8.

It is possible that the opportunity a tungsten ion has to interact with the oxygen background plays a role and it is the state of oxidation of tungsten that determines its incorporation in VO_2 film.

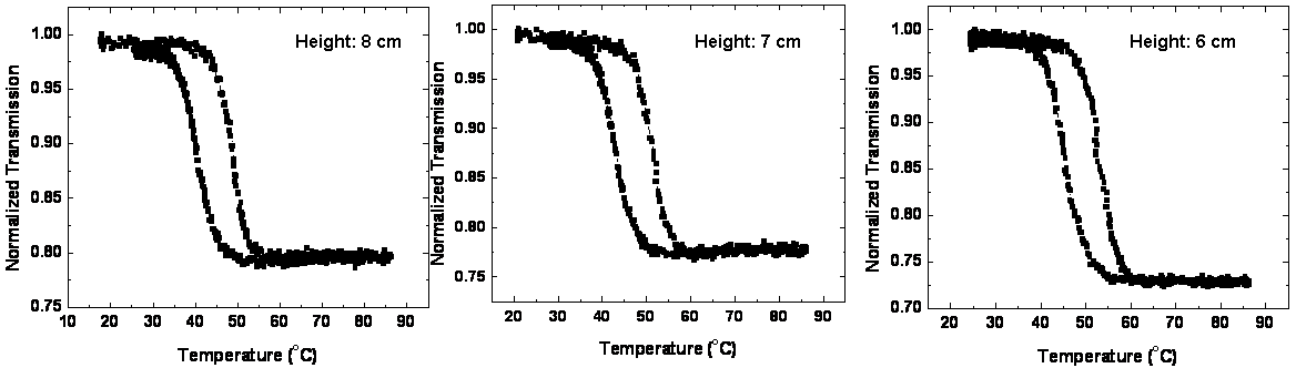

Figure 5.7: Effect of varying the target-to-substrate distance in RT-grown films on C-sapphire

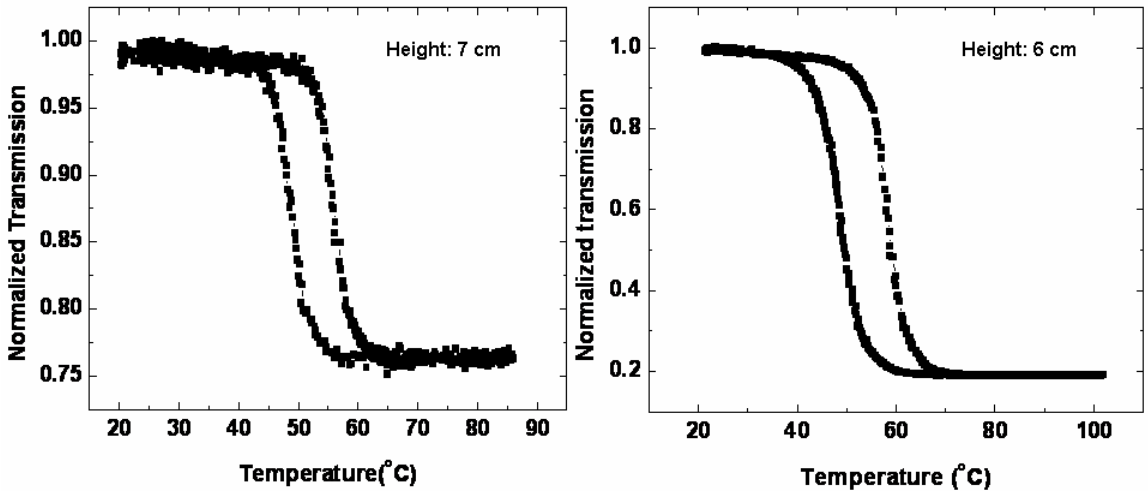

Figure 5.8: Effect of varying target-to-substrate distance in RT grown films on glass

The variation in switching contrast of the films in figure 5.8 is due to the difference in thicknesses of the films.

5.2.4 Tungsten doping in epitaxial VO_2 films on TiO_2

Ti and V are neighboring elements on the periodic table, which renders the peaks from these two elements very difficult to resolve and analyze using the Rutherford backscattering technique. Therefore it is difficult to calculate relative proportions of V and W present in these W-doped

VO_2 samples on TiO_2 substrates. Hence RBS data does not exist for the W-doped VO_2 films grown on the different TiO_2 substrates.

Figures 5.9-5.11 show the effect of increasing W-doping in epitaxial VO_2 films on TiO_2 (001), (110) and (100) respectively, where (a) always corresponds to the hysteresis of an undoped film.

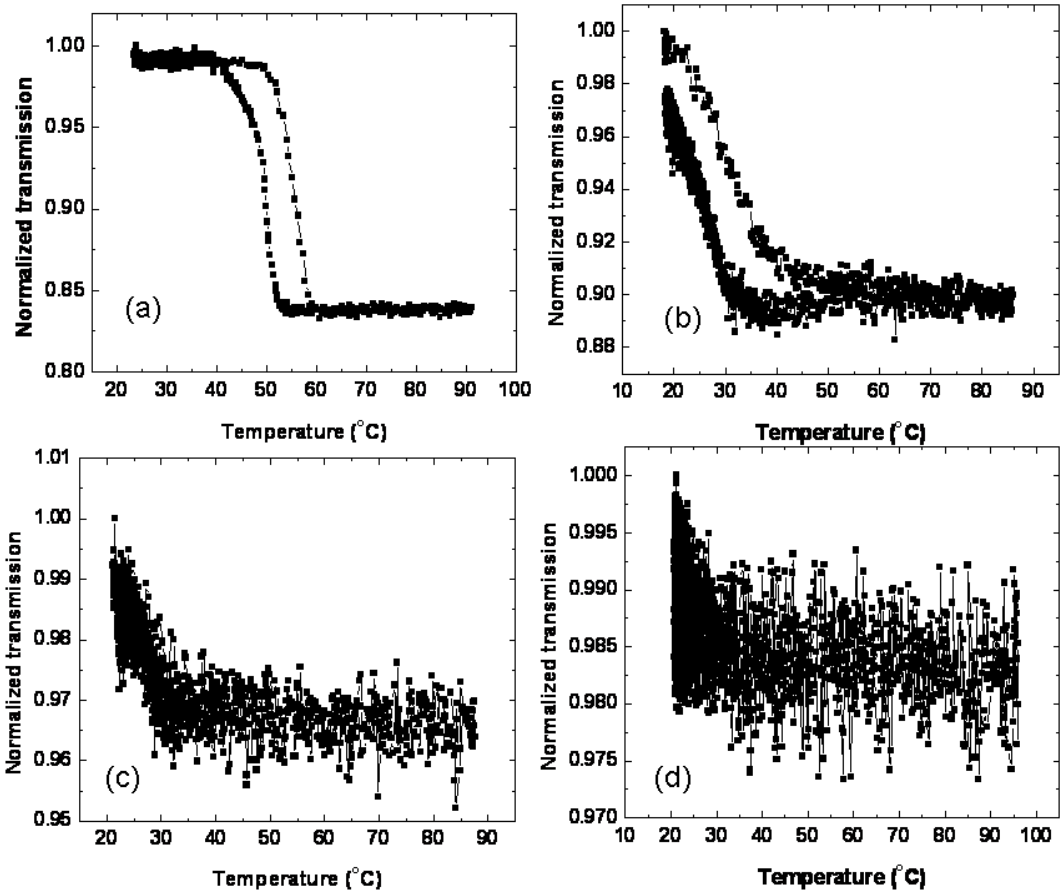

Figure 5.9: Hystereses of W-doped epitaxial VO_2 films on TiO_2 (001) as W-doping increases from (b) through (d). (a) corresponds to the hystersis in an undoped film.

Note that with the highest concentration of W, there is almost no switching, indicating that the doped film is metallic even at room temperature. In Figure 5.10, the hysteresis loop narrows with increasing W-concentration until the loop completely closes and there is no hysteresis.

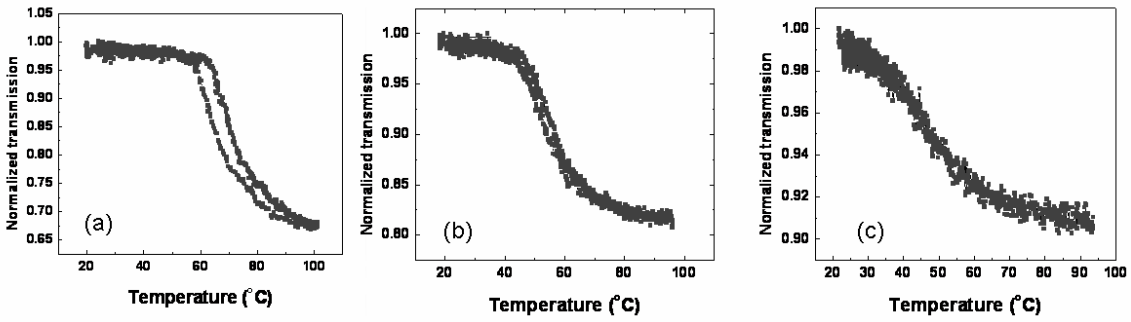

Figure 5.10: Hystereses of W-doped epitaxial VO_2 films on TiO_2 (110) as W-doping increases progressively in (b) and (c). (a) corresponds to an undoped film

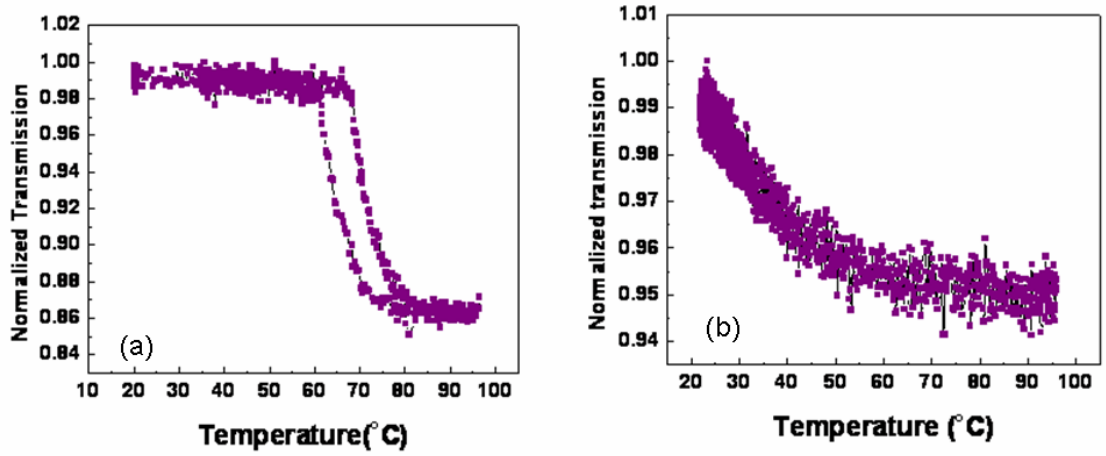

Figure 5.11: Hysteresis of (a) undoped and (b) W-doped VO_2 film on TiO_2 (100)

5.3 EFFECT OF W-DOPING ON THERMAL AND NON-THERMAL PHASE TRANSITIONS

5.3.1 Introduction

Understanding, controlling and tuning the VO_2 phase transition is important both for the intrinsic physics as well as for technological applications. Doping is the parameter that helps us tune the width, slope and critical temperature of the hysteresis loops, and acts as a probe to inspect the precise mechanism of the phase transition. We have studied both the thermal and photo-induced phase transitions of doped VO_2 to see the tuning of the energy requirements due to presence of the extra charge carriers donated by the dopant atoms.

Doping VO_2 to understand its electronic properties — a technique that has been critical to our understanding of electronic structure and dynamics in studies of group IV and III-V semiconductors — apparently has not been applied to this strongly-correlated semiconductor. Only by understanding the physics involved in the phase transition, will it be possible to tune the thermal and non-thermal phase transition features, such as the critical temperature, width and slope of hysteresis in case of thermal switching as well as the threshold fluence and relaxation time for optical switching.

In the case of thermally-induced phase transitions in undoped VO_2 films, the modification of hysteresis features due to substrate and film morphology has been studied in detail,[175] and analogous effects were studied for photo-induced phase transitions by Lysenko *et al*.[59, 60] But having an active element like precisely-controlled doping, to vary the critical temperature and contrast of switching more accurately and widely is advantageous for several conceivable reasons. Similarly, if the threshold fluence (energy requirement) can be tailored (lowered) to modify the ultrafast optical response of VO_2, it would be desirable for various applications ranging from optical switches, ultrafast sensors to high-speed optoelectronics in telecommunications frequencies. Apart from the lower power consumption advantage, it would provide us more insight regarding the path along which this ultrafast phase transition occurs and can be modified, for example if effecting a switch will be possible without causing the structural change, and if the switch-off response of VO_2 can be tuned or not.

Doping is used to modify the phase transition,by changing the lattice and electronic structure and their subtle balance in VO_2. In this work, we have studied the mechanism of the phase transition in this altered system by inducing the PT by both temperature and photo-induction. Here the effect of doping has been studied using a combination of atomic-resolution microscopy, time-resolved ultrafast measurements and DFT-calculations, with the goal of understanding, controlling and tuning the phase transition. The atomically-resolved Z-STEM coupled with EELS spectra helped us determine the location of dopant atoms in the VO_2 lattice. For the first time, DFT-based calculations are reported for W-doped VO_2, showing the relative stability of the M1 and R phases before and after doping and accurately predicting the change in transition temperature. The optically-induced PT study, with ultrafast pump-probe of varying pump-fluences show that doped-VO_2 switch at substantially lower fluences, indicating that W dopant

provides additional conduction-band electrons, thus accounting for softening of the insulating state analogous to the effect of temperature in case of Hilton *et al*.[61]

5.3.2 Characterization of the films

W-doped VO_2 was grown using the pulsed laser deposition system using a 2 wt % W-doped V target to grow $W_{0.006}V_{0.994}O_2$ films on the C (0001) plane of sapphire. Figure 5.12 compares the morphologies of undoped and doped VO_2 grown on the C-sapphire, and shows the transmission hysteresis for each case. For the above mentioned percentage of doping, the transition temperature was altered from ~67˚C to ~48˚C.

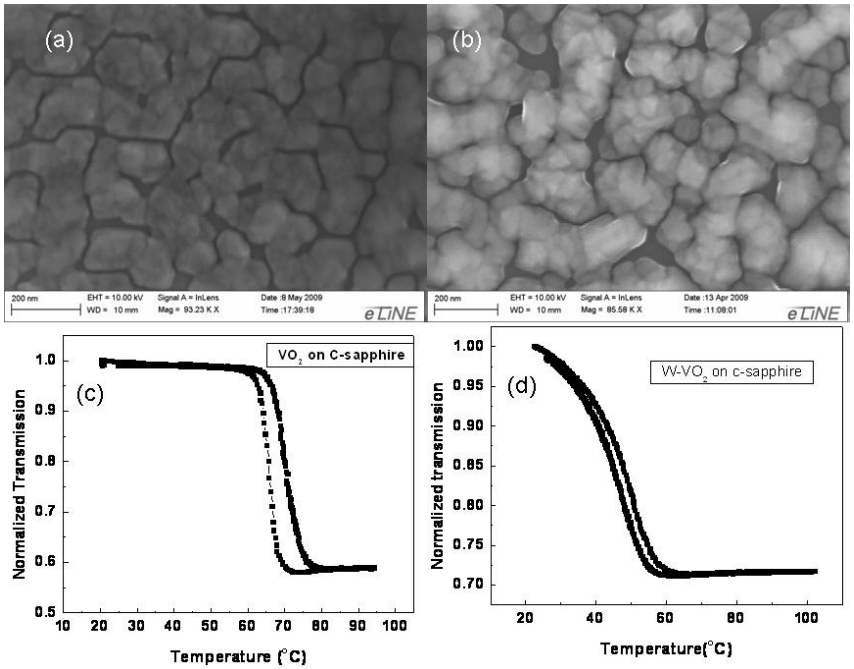

Figure 5.12: SEM images of (a) undoped and (b) doped VO_2 and the white light transmission hystereses on (c) undoped and (d) doped VO_2 films on C-sapphire

Figure 5.13 (a) shows the RBS spectra of the W-doped sample on C-sapphire from which the ratio of the area under the peaks of W and V yields the doping level of the sample. Figure 5.13(b) is the XRD of the doped sample and shows no W peak, indicating that the W is either distributed randomly in interstitial sites or occupies substitutional positions in the VO_2 lattice. Thus, apart from the sapphire substrate peak, the XRD spectrum shows only the (010) family of VO_2 peaks and the sapphire substrate peak.

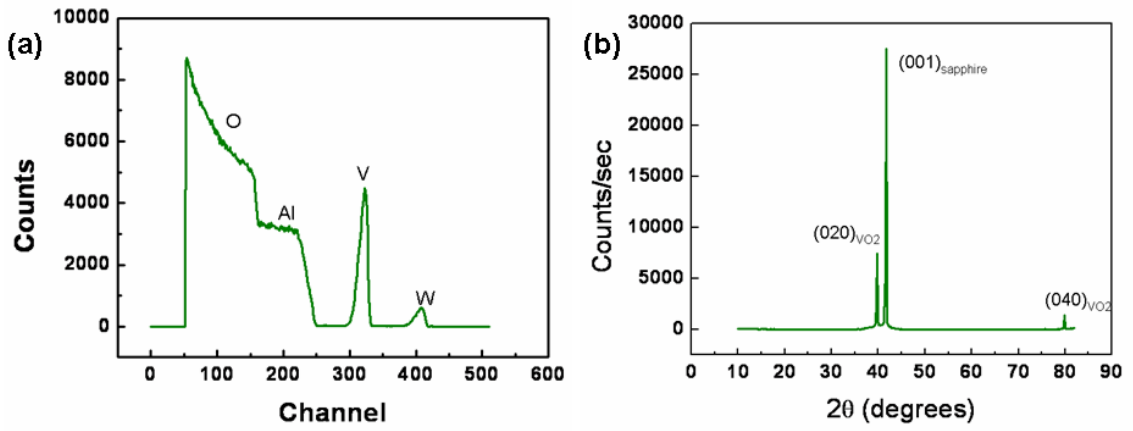

Figure 5.13: (a) Rutherford Backscattering spectrum on W-VO_2 film. The area under the W and V peaks give the relative concentrations. (b) θ-2θ XRD spectrum on the doped film shows no W peak

In order to experimentally determine where the W atoms are to be found, aberration-corrected atomic number contrast scanning transmission electron microscopy (Z-STEM) measurements were taken in combination with electron energy loss spectroscopy (EELS). Figure 5.14 the W ions (brighter spots due to higher Z = 74 compared Z = 23 of V) evidently show up in the column for V ions in the lattice.

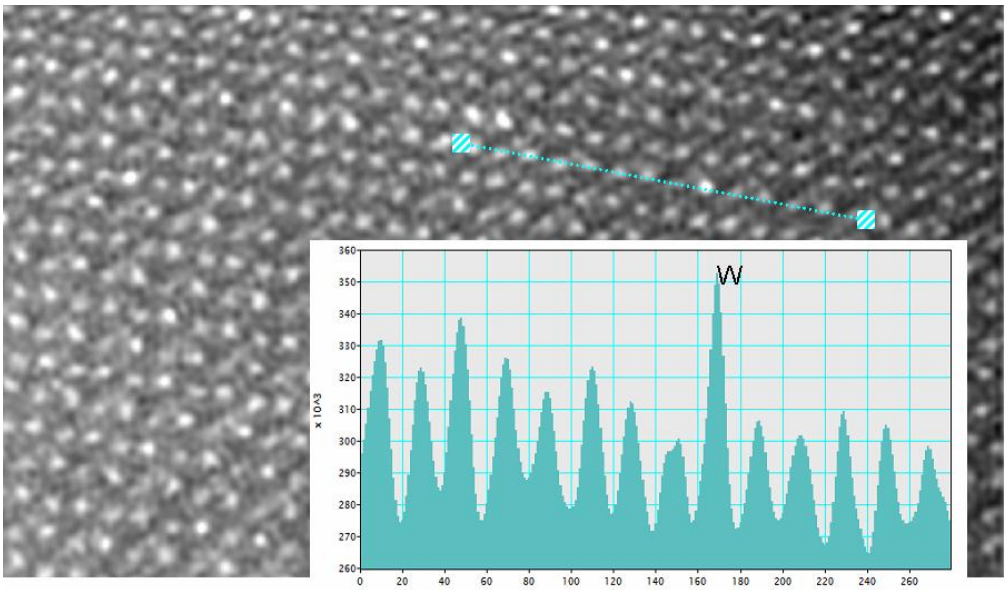

Figure 5.14: Z-contrast STEM image of W-doped VO_2 showing in conjunction with EELS that W substitutes V atomic sites (where, the brightest atomic site in Z-STEM and the highest EELS peak is observed). Courtesy: Dr. Gerd Duscher, Oak Ridge National Laboratory

5.3.3 Ultrafast pump-probe measurements

We apply optical pump-probe technique to investigate the light-induced phase transition in both the undoped and W-doped VO_2 thin film samples. The transient optical transmission was measured on a femtosecond and picosecond time scale by a delayed probe. Fig. 5.15 depicts the experimental setup where the femtosecond laser system (Quantronix) was applied as a light source. Mode locked pulses from the Ti::Sapphire 86 MHz laser oscillator was amplified by a regenerative amplifier at repetition rate of 1 KHz and a pulse duration of ~150 fs duration with the central wavelength at 800 nm. The output pulse was split into pump (~95%) and probe (~5%) beams. The pump, after passing through the optical delay line, was focused on the sample surface using a spherical mirror to a beam spot size of ~90 μm. The energy of the output pulse before splitting was varied using neutral density filters such that the probe energy was always at 5 % of the total output.

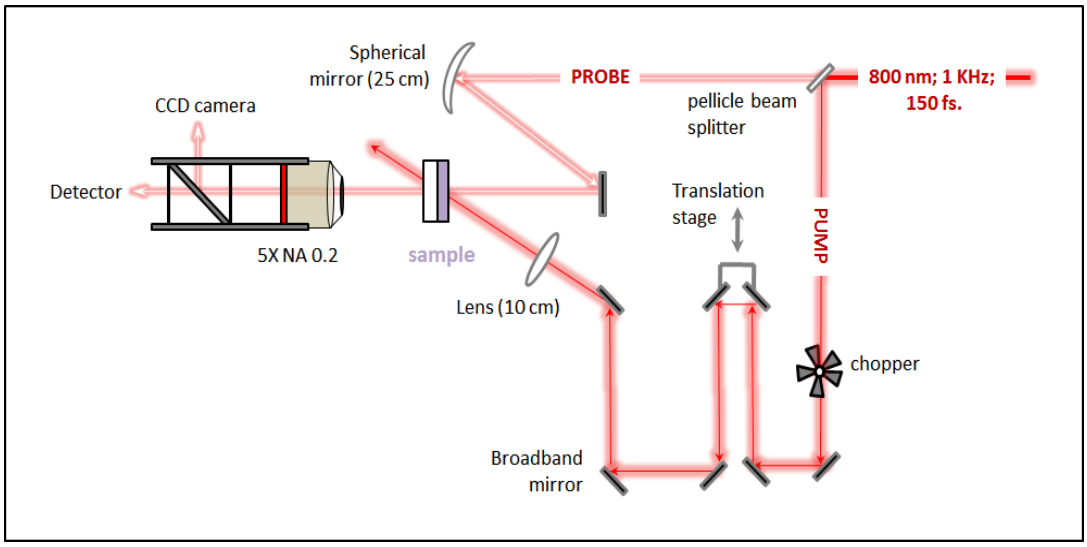

Figure 5.15: Schematic of our ultrafast pump-probe experimental set-up

The normal-incidence transmission measurements were recorded for various pump energies (and for the two thin film samples) and the results are shown in Figure 5.16. A subpicosecond insulator to metal transition is evident in the abrupt changes in the optical properties of the two films. The response comprises not only an ultrafast instantaneous change in the transmission

measurement, but also a slow component which is in the hundreds of the picoseconds range. This slow component is associated with the recovery process which typically lasts up to hundreds of nanoseconds.[60]

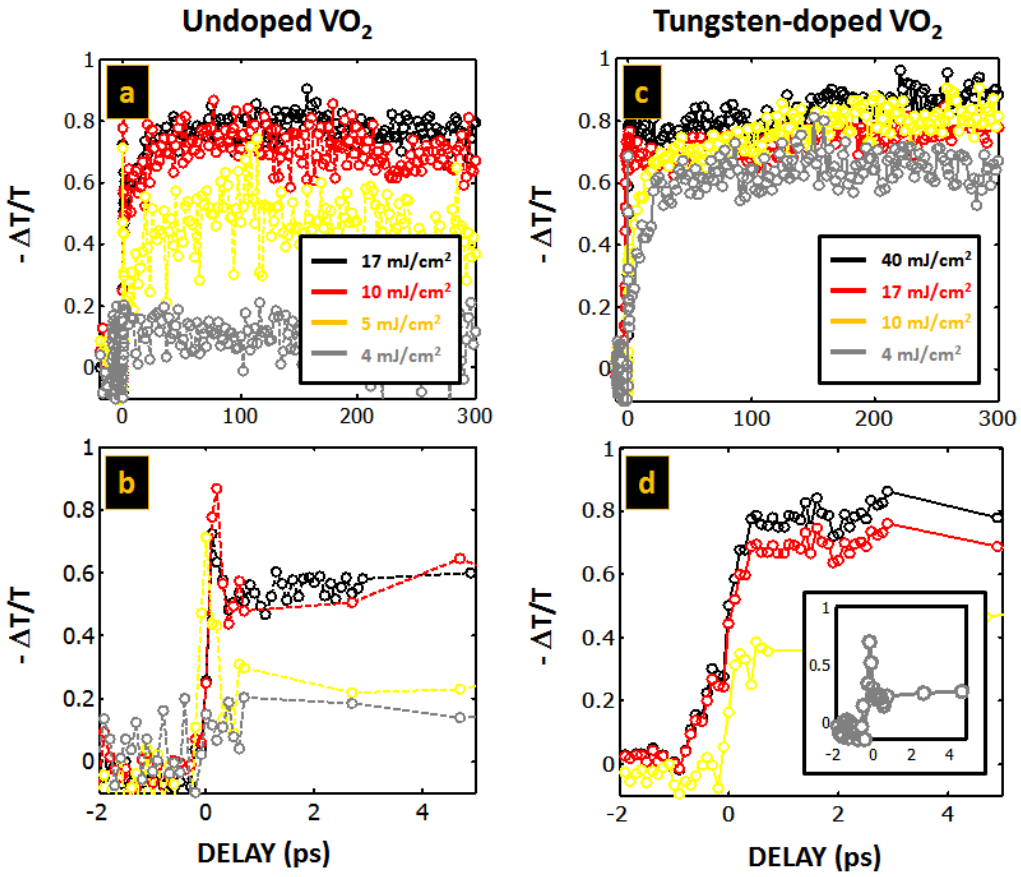

Figure 5.16: Ultrafast response of the VO_2 transmission in (a) and (b) undoped and (c) and (d) doped VO_2 films respectively plotted on two different time scales

According to Kubler *et al*,[57] the strong correlation between the two binding electrons of each V-V dimer can be reinstated on sub-picosecond, for lower fluence or much longer (~ns) timescale, for a higher fluence compared to a threshold excitation.

Dimerization is broken with W replacing one of the vanadium atoms in the pair, resulting in softening of the insulating state and hence lowering the energy required to switch doped VO_2. Also, from the discussion above it seems that, less energy dumped into the system might lead to faster recovery because more V-V dimers can be kept intact even when the phase transition has been achieved on the electronic scale, especially with contribution of the extra carriers coming

from W and the dimerization already destroyed by W-incorporation. Hence we speculate that with W-doping, ultrafast switching of VO_2 might have lower contrast but possibly the modulation in conductivity can be accomplished substantially faster, because of faster relaxation times. It will be interesting to see how future broadband THz conductivity measurements on doped VO_2 films of varying dopant concentrations (and also, varied dopants with different carrier contributions) contribute towards our better understanding of this phenomenon.

5.3.4 First-principles density-functional calculations

First-principles density functional theory calculations have been performed by Dr. Weidong Luo of the Pantelides group to study the relative stability of the low-temperature monoclinic phase (M1 phase) and the high-temperature rutile phase (R phase) of VO_2 before and after W substitution. Density functional theory[229] was employed within the non-spin-polarized, generalized-gradient approximation[230] plus Hubbard U (GGA+U)[231] approach and the projector augmented-wave method as implemented in VASP.[232-234] All calculations were carried out with a plane-wave cutoff energy of 500 eV. The Hubbard parameter and exchange interaction are chosen to be U=4.0 eV, and J=0.7 eV. For undoped VO_2, the unit cell of the monoclinic phase contains four V atoms and eight O atoms. The primitive unit cell of the rutile phase has tetragonal symmetry, which contains only two V atoms and four O atoms. For better convergence of the total energy difference with the monoclinic phase, a double unit cell, consistent in size and shape with the unit cell of the monoclinic phase, is used for the calculations of the rutile phase. An 8×8×8 k-point grid is generated using the Monkhorst-Pack scheme. The structures are relaxed so that the residual forces on all atoms are smaller than 5×10^{-3} eV/Å.

The theoretical crystal structures of undoped monoclinic and rutile phases are in good agreement with experiment. The calculated M1 phase lattice parameters are a = 5.68 Å, b = 4.61 Å, c = 5.45 Å, with monoclinic angle $\beta = 122.1^{o}$, which are in excellent agreement with experimental structure: a = 5.7529 Å, b = 4.5263 Å, c = 5.3825 Å, and $\beta = 122.602^{o}$. In the rutile structure, the relaxed structure from the calculations corresponds to lattice parameters of a = 4.64 Å, c = 2.80 Å, in good agreement with experimental values of a = 4.554 Å, c = 2.8557 Å. The calculated V-V distance in the rutile phase is 2.86 Å, while the alternating short and long V-V distances in the low-temperature monoclinic phase become 2.53 Å and 3.18 Å, respectively. These V-V

distances are in good agreement with the experimental values as introduced in chapter 1. The total energy of the monoclinic phase is calculated to be lower than the rutile phase by 96.9 meV per VO_2 unit, which is consistent with the stability of the monoclinic phase at low temperature.

The effects of W substitution doping are also investigated by employing a supercell containing 96 atoms with formula $WV_{31}O_{64}$ to compute the total energies of the W-doped monoclinic and rutile phases. This supercell corresponds to a W doping concentration of 3.125%.

The supercell sizes and atomic positions are optimized for both the monoclinic and rutile phases. The total energy of the monoclinic phase is lower than the rutile phase, consistent with the stability of the monoclinic phase at low temperature even with the W-doping. The total energy difference between the two structures from the calculations is 74.4 meV per $W_{1/32}V_{31/32}O_2$ unit, which is smaller compared to the undoped VO_2. This result shows that W doping stabilizes the high-temperature rutile phase relative to the low-temperature monoclinic phase, consistent with the observed reduction of transition temperatures in W-doped VO_2 samples.

Assuming the change of entropy between the monoclinic phase and the rutile phase at the phase transition remains the same between the undoped VO_2 and the W-doped VO_2, the phase transition temperature $T_{c,1}$ of the doped material can be estimated[235] as: $T_{c,1} = T_{c,0} \Delta E_1 / \Delta E_0$ where $T_{c,0}$ is the transition temperature of the undoped material, ΔE_0 and ΔE_1 are the total energy differences between the M1 and R phases in the undoped and the W-doped materials, respectively. An estimated transition temperature of 261 K is obtained for the $WV_{31}O_{64}$ material using the calculated total energy differences and the experimental transition temperature of 340 K in undoped VO_2. The reduction of transition temperature in VO_2 with W doping is equivalent to 25 K per 1% W doping, which is in excellent agreement with the accepted[236] and our experimentally observed reduction of 27 K per atomic percent of W doping. The success of this first-principle calculations in predicting the shift in transition temperature with a pre-specified percentage of doping has been demonstrated for the first time here. It is also significant from the perspective of further technological advancements aiming to exploit W-doping to precisely tailor VO_2 transition temperature.

5.4 EFFECT OF TUNGSTEN DOPING ON STRUCTURAL PHASE TRANSITION

Temperature-variable X-ray diffraction has been employed to study the effects of W-doping on the structural phase transition, as was done for undoped epitaxial VO_2 in chapter 4. Figure 5.19 gives the isoline views of the two transitions in case of undoped and doped films respectively. We note that compared to undoped VO_2 evolving between two discrete structures with peaks occurring at two discrete positions, in case of W-VO_2 the monoclinic peak gradually and smoothly shifts to the tetragonal peak position as it is heated and vice versa during cooling.

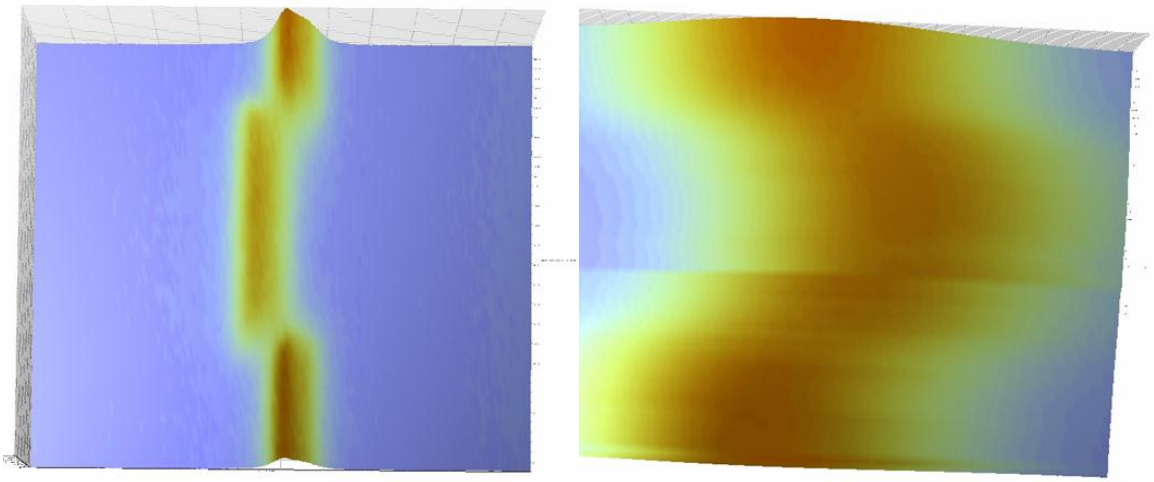

Figure 5.16: Three-dimensional isoline view of the evolution of monoclic-rutile-monoclinic phase transition in undoped (left) and doped (right) VO_2 films. Note the smooth, gradual change in doped vs a more abrupt change in undoped VO_2

CHAPTER VI

ULTRAFAST, COMPACT HYBRID SI: VO_2 OPTICAL MODULATOR

ABSTRACT

As interconnect densities rise, a transition from electrical to optical interconnects becomes imperative because of the inherent limitations of copper with respect to loss, speed and crosstalk. Si-based optical modulators are CMOS-compatible and therefore are the leading replacement candidates. We demonstrate modulation of a Si-based ring resonator coated with vanadium-dioxide (VO_2) as a first step toward achieving compact silicon-compatible optical modulators operating at THz speeds. VO_2 undergoes a metal-insulator transition (MIT) near 67^{o}C, with abrupt changes in its dielectric function that are maximized near 1.5 μm wavelength. We fabricated 3 μm diameter ring resonators coupled to 5 mm nanotapered waveguides on SOI substrates and coated the rings with 60nm of VO_2 in a dual-layer lithography process. Thermal induction of the MIT produced a wavelength shift $\Delta\lambda = -12\ nm$ at a carrier wavelength of 1337 nm, and a modal effective index change due solely to VO_2 switching $\Delta n_{VO2} \approx$ -0.053. With its low Q-factor and correspondingly shorter cavity lifetime, the VO_2-silicon hybrid ring resonator is expected to support extremely compact, optically switchable and more robust devices. Finite-difference time-domain simulations supporting our experimental results are also presented.

6.1 INTRODUCTION TO SI OPTICAL MODULATORS

Within the next decade, it is likely that optical interconnects will replace some traditional electrical interconnects in mainstream microelectronics applications. The leading candidate technology is silicon photonics, and the most important element of such interconnects is the optical modulator. Modulators have been improved dramatically in recent years, with a notable increase in bandwidth from the megahertz to the gigahertz regime, but demands of optical interconnects technology are significant[237, 238], and many questions remain unanswered as to whether silicon can meet the required performance metrics. Minimizing metrics such as the device footprint and energy requirement per bit, while also maximizing bandwidth and

modulation depth, is non-trivial. All of this must be achieved within an acceptable thermal tolerance and optical spectral width using CMOS-compatible fabrication processes.

The many application areas for optical interconnects range from high-performance computing and data centers down to mobile-to-server interconnects and desktop computers. The dominant application for silicon photonics is in optical interconnect technology, and this now is an urgent requirement for the industry because recent bandwidth improvements in electronic interconnects have only been achieved at the expense of increased latency and power consumption[237]. Other applications that may benefit from the success of silicon photonics include environmental monitoring, biological and chemical sensing, medical and military applications, and astronomy.

Optical interconnects could bring several major advantages over their electrical counterparts, by allowing optimization of the chip layout while retaining high data rates. They can also introduce some of the more conventional advantages of optical technology, such as the reduction of electromagnetic interference, cable length and cable weight, and optimized cooling. Finally, they may save energy and allow interconnect densities to be reduced.

According to Reed *et al:*[238] "The ultimate physical manifestation of the silicon photonic device would be as part of an optoelectronic integrated circuit formed monolithically in silicon, which would combine photonic functionality and electronic intelligence in a seamlessly integrated design. Although components continue to be developed, interim solutions such as hybrid combinations of different materials aim to fulfill the functions that silicon is currently unable to deliver."

This Si optical modulator has been realized in both monolithic and hybrid forms.

6.1.1 Optical Modulation

Optical modulation is one of the main required functionalities for any optical interconnect solution. An optical source can be either directly or externally modulated. External modulation offers several advantages over direct modulation. For example, the optical source can be relatively inexpensive and its operation does not need to be compromised by direct modulation, modulation speeds can be higher, and optical isolation and wavelength stabilization need to be performed only once for the entire system[239]. Furthermore, a single light source can feed multiple

channels via individual modulators, thus reducing the total power budget of the system. An optical modulator is a device that is used to modulate or vary the fundamental characteristics of a light beam propagating either in free space or in an optical waveguide. These devices can alter different beam parameters, allowing them to be categorized as either amplitude, phase or polarization modulators. In addition, modulators can be also classified as either electro-refractive or electro-absorptive.

6.1.1.1 Modulation in silicon

Applying an electric field to a material may change its real and imaginary refractive indices. A change in the real part of the refractive index (Δn) with an applied electric field is known as electro-refraction, whereas a change in the imaginary part of the refractive index ($\Delta \alpha$) is known as electro-absorption. The primary electric field effects that are traditionally useful in semiconductor materials for causing either electro-absorption or electro-refraction are the Kerr effect and the Franz–Keldysh effect. However, it has been shown that these are weak in pure silicon at the telecommunications wavelengths of 1.3 μm and 1.55 μm;[240, 241] alternative methods are therefore required to achieve modulation in silicon. One option is thermal modulation owing to the large thermo-optic coefficient of silicon, but this is too slow for the high frequencies required by modern telecommunications applications.[242] More recently, attempts have been made to investigate alternative modulation mechanisms in other materials potentially compatible with silicon technology, to achieve more efficient modulation.

The most common method of achieving modulation in silicon devices so far has been to exploit the plasma dispersion effect, in which the concentration of free charges in silicon changes the real and imaginary parts of the refractive index.[241] Soref and Bennett[240] evaluated changes in the refractive index Δn from experimentally produced absorption curves for a wide range of electron and hole densities, over a wide range of wavelengths. They also quantified changes in both the refractive index and absorption,[240] and produced the following expressions to evaluate changes in the carrier densities in silicon at a wavelength of 1.55 μm:

$$\Delta n = \Delta n_{\mathrm{e}} + \Delta n_{\mathrm{h}} = -\left[8.8 \times 10^{-22} \times \Delta n_{\mathrm{e}} + 8.5 \times 10^{-18} \times \left(\Delta n_{\mathrm{h}}\right)^{0.8}\right] \qquad (6.1)$$

$$\Delta \alpha = \Delta \alpha_{\mathrm{e}} + \Delta \alpha_{\mathrm{h}} = 8.5 \times 10^{-18} \times \Delta n_{\mathrm{e}} + 6.0 \times 10^{-18} \times \Delta n_{\mathrm{h}} \qquad (6.2)$$

where Δn_e and Δn_h are changes in refractive index resulting from changes in the free-electron and free-hole carrier concentrations, respectively, and $\Delta\alpha_e$ and $\Delta\alpha_h$ are the changes in absorption resulting from changes in the free-electron and free-hole carrier concentrations, However, this is accompanied by a detrimental change in intensity due to the absorption of free carriers.[243]

Electrical manipulation of the charge density interacting with the propagating light is achievable through mechanisms such as carrier injection, accumulation or depletion.

The process of changing refractive index and inducing absorption directly modulates the intensity of a propagating mode. There are two ways to convert a change in refractive index into intensity modulation. First, the refractive index change can be used to shift the relative phase of two propagating waves such that they interfere either constructively or destructively, as is the case for a Mach–Zehnder interferometer (MZI). Second, including a resonant structure in the device allows the refractive-index change induced in the modulator to change the resonance condition, thus allowing the device to be switched between on- and off –resonance states at any given wavelength.

6.1.2 Figures of merit

There are several figures of merit that are used to characterize a modulator, including its modulation speed and depth, optical bandwidth, insertion loss, area efficiency (footprint) and power consumption. The modulation speed or bandwidth is one of the most important figures of merit for an optical modulator. Modulation bandwidth is usually defined by the spread in frequency at which the modulation is reduced to 50% of its maximum value. The speed of a modulator is commonly characterized by its ability to carry data without significant distortion at a certain rate. High modulation speeds are required for applications in which high data rates are required, but for applications like sensing only relatively moderate modulation speeds are sufficient.

Modulation depth — also known as the extinction ratio — is defined as the ratio of I_{max}, the intensity transmitted when the modulator is adjusted for maximum transmission, to I_{min}, the intensity transmitted when the modulator is adjusted for minimum transmission. It is quoted in

decibels and expressed as $10.\log(I_{max}/I_{min})$. A large modulation depth is useful for long transmission distances, good bit error rates and high receiver sensitivity.

Insertion loss takes into account the optical power that is lost when the modulator is added to a photonic circuit. It is a passive loss that comprises reflection, absorption and mode-coupling losses, and is significant because it contributes the overall end-to-end losses in the system and therefore sets a limit for the receiver sensitivity that needs to be used. There has been a trend in silicon photonics to move to smaller, submicrometer waveguides (mostly in an attempt to reduce device size and increase performance). This move has been coupled with an increase in loss that mainly results from coupling and greater modal interaction with sidewall roughness.

Power consumption — the energy expended in producing each bit of data — is particularly important. If the power consumption of optical interconnects have to be lower than their electrical interconnect counterparts, then the optical modulators will need to reach power consumptions of less than 1 pJ bit^{-1}. Electro-optic modulators are promising from the point of power consumption because of their resonant behavior.

Another important feature of a device is its *footprint*. MZI-based modulators tend to require a long interaction length (millimeters) for a complete transition between a maximum and a minimum of the optical transmission. This hinders high-speed performance and results in greater insertion loss, cost and power consumption. The footprints of resonant devices, on the other hand, are typically much smaller. This discussion might therefore imply that modulators incorporated into resonant structures are superior to those based on MZIs.

However, there are other factors such as *optical bandwidth*. This refers to the useful operational wavelength range of a device. Resonant-structure-based modulators tend to function over a relatively narrow band compared with MZI-based devices. Narrowband devices are limited in their applications, and their main shortcoming is their high sensitivity to typical fabrication tolerances and temperature variations. High sensitivity to fabrication tolerance can have a significant effect on device operation; in ring resonators, for example, the resonant frequency shifts by approximately 0.25 nm for every nanometer increase in the average width of the ring waveguide. Achieving the right resonant wavelength can therefore be challenging using the 130 nm CMOS generation, as three standard deviations of the fabrication tolerance is 40 nm. Electro-

absorption modulators, on the other hand, are likely to be much less temperature-sensitive than resonator refractive devices.

6.2 Si: VO_2 Hybrid Optical Modulators

6.2.1 Introduction

As discussed above, Si optical modulators have many benefits for integration with microelectronic devices but do not offer ideal parameters[244-248] for operating at high speeds with large bandwidths, small footprint and low power consumption, thus motivating a search for hybrid materials combinations that could satisfy these requirements.[249, 250 251-254]

Here we report on a Si-based hybrid optical modulator incorporating vanadium dioxide (VO_2) as the silicon-compatible optical switching element. Using the sub-picosecond optically induced metal-insulator transition in vanadium dioxide, the intrinsic limitations of silicon optical response (of order GHz)[255-258] can be overcome while maintaining compatibility with silicon microelectronics architectures.

As discussed earlier as well, the change from monoclinic to tetragonal crystal structure in VO_2 and the corresponding change in dielectric function is shown in figure 6.1(a) and (b). Vanadium dioxide is also readily fabricated on silicon substrates and its phase transition gives rise to an abrupt change in its refractive index (~1.96-3.25) in the near infrared, as can be seen from figure 6.1(c), rendering this material appropriate for integration with silicon-based ring resonators at telecommunications frequencies. As we shall show, the hybrid Si-VO_2 ring resonator has the potential to operate at THz speeds, with large effective refractive index changes for smaller size and greater modulation depth, lower Q-factors for shorter cavity lifetimes, wide free spectral range, and low power consumption.

A recent paper has proposed that intensity modulation with speeds up to 1 THz may be feasible with a hybrid polymer-silicon waveguide structure based on the all-optical Kerr effect[259]. The hybrid Si-VO_2 ring-resonator structure, on the other hand, has the potential to operate at even higher speeds, by directly utilizing the ultra-fast switching capabilities of VO_2. In this manner, the hybrid Si-VO_2 ring resonator structure should bring about an order of magnitude improvement in the speed of Si-based modulators.

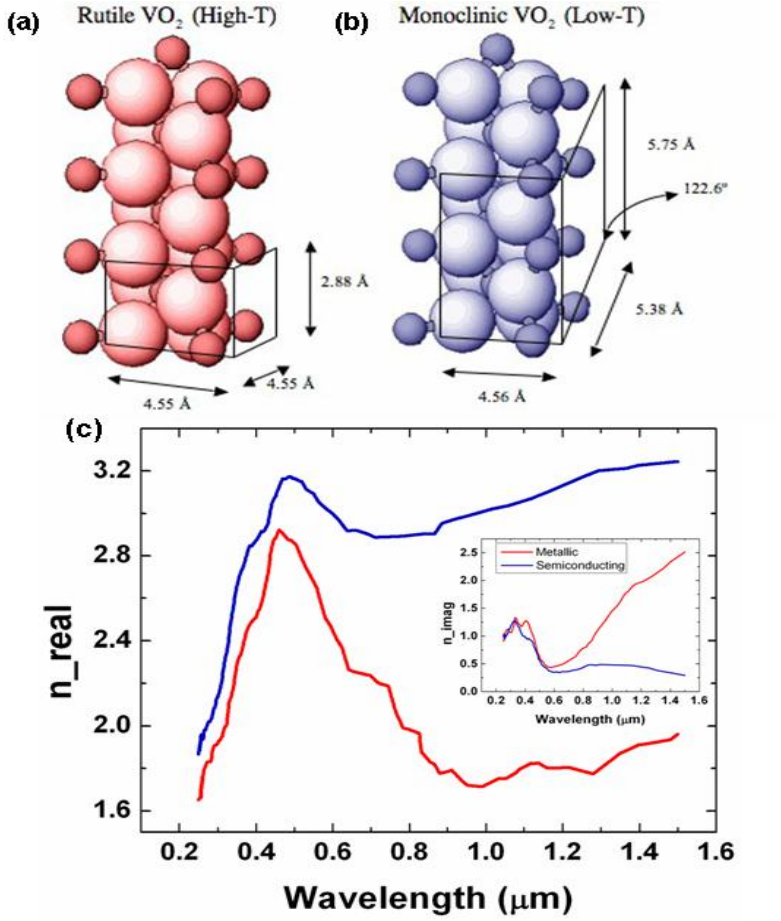

Figure 6.1: Atomic structure of VO_2 in its (a) high-temperature, metallic, tetragonal (rutile) phase, (b) low-temperature, semiconducting, monoclinic phase, (c) refractive index of VO_2 as a function of wavelength in the two phases (After Verleur *et al*[209]).

Xu *et al*[255] used resonant cavities to enhance the sensitivity of silicon photonics to small changes in refractive index and simultaneously enable high-speed operation. In a p-i-n configuration, utilizing the weak electro-optic (Kerr) effect in Si to induce the refractive index change in the Si ring, they demonstrated modulators 12 μm in diameter operating at GHz speeds.

We effected a much larger change in refractive index by covering the rings with VO_2 to obtain a larger modulation in frequency/wavelength following the relation $2\pi R\Delta n = m\Delta\lambda$ where m is an integer and the ring resonator has radius R. Given the large Δn induced by the VO_2, the hybrid Si-VO_2 modulator does not require as large a ring radius as the all-Si device and thus will have

an even smaller footprint. A natural consequence of the smaller ring radius is an increase in the free-spectral range (FSR), which frees up optical bandwidth and increases the number of optical channels that can be carried in the same photonic conduit. Furthermore, because the achievable index contrast of VO_2 is much larger than that of silicon, the resonator does not require sharp resonances (*i.e.* large Q-factors) to obtain good modulation depths, and thus is inherently less sensitive to small environmental fluctuations such as changes in ambient temperature or humidity.

Briggs *et al*[260] recently used VO_2 as an in-line absorption modulator for waveguides, and appropriately suggested that the ultra-low power consumption of such structures would enable their application in compact photonic devices. While this structure has the potential for large modulation depths, as well as low power consumption and high-speed operation, modulation occurs roughly independent of wavelength, and is thus ineffective for multiplexing or performing add/drop filtering operations. Additionally, the substantial VO_2 coverages required for larger modulation depths lead to significant attenuation of transmitted signals even in the "ON" state.

The ring resonator configuration, on the other hand, modulates optical signals by means of the large change in the real part of the refractive index that accompanies the phase transition in VO_2. Thus it can be easily adapted into a multiplexed routing system for routing specific wavelengths of light on-chip in a simple add/drop configuration.[261] Furthermore, the ability to define different fractional coverages of VO_2 coating on the ring naturally promotes highly tunable and flexible configurations while maintaining minimal optical attenuation in the "ON" state.

Although many of the above advantages of using VO_2 will be evident only when the phase transition is optically induced on an ultrafast time scale, we present here a proof-of-principle study demonstrating that the thermal switching of VO_2 on top of the rings leads to considerable modulation in resonance frequency; this was achieved for rings of ~ 3 μm diameter, which are, from an areal standpoint, more than an order of magnitude more compact than those demonstrated by Xu *et al.*[255]

Figure 6.2 shows our proposed Si/VO_2 hybrid optical modulator. Light is coupled evanescently from a bus ridge waveguide to ring resonator fabricated using electron beam lithography on a silicon-on-insulator (SOI) substrate. A thin cover layer of VO_2 is deposited on the ring using

pulsed laser deposition. When the temperature of the VO_2 is changed to 67^{o}C or an optical pulse is applied to the VO_2, the effective index of the resonator mode is changed based on modulation of the VO_2 index as indicated by our FDTD simulations. Thus, tuning the refractive index of VO_2 directly modulates the transmitted intensity of light passing through the device.

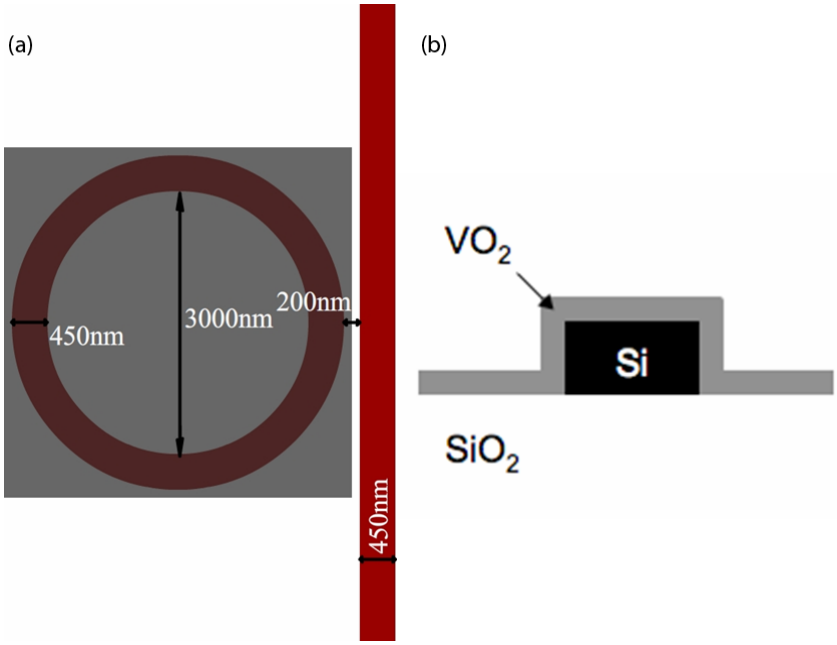

Figure 6.2 Schematic of (a) proposed device; (b) cross section of the vanadium dioxide covered ring.

6.2.2 Simulations of Si-VO_2 ring resonator modulator performance

Finite-difference time-domain simulations shown in figure 6.3 demonstrate the feasibility of our proposed structure. The simulated transmission [figure 6.3(a)] and electric field profiles [figure 6.3(b) and (c)] of a waveguide coupled to a ring resonator (non-optimized design) show that when light is coupled into the resonator at the normalized probe frequency ω~0.2337 there is almost no light transmitted through the modulator. From figure 6.3(a) we observe that, when the effective index of the ring is reduced by approximately 0.01, the resonator is detuned from the probe frequency and the transmitted output intensity significantly increases. If a 20nm VO_2 layer is switched completely from the semiconducting to metallic state, we expect a modal index

change on the order of 0.1. Thus from simulated transmission results we see that a change in refractive index of 0.01 shifts the resonance by 0.75%, i.e., a shift in wavelength of ~12nm near λ = 1550nm is expected. Our simulated electric field distribution at resonance frequency and detuned from it by $\Delta n = 0.01$ is shown in figure 6.3(b) and (c). The parameters of the hybrid ring resonator structure were optimized to ensure maximum output-intensity contrast from the modulator.

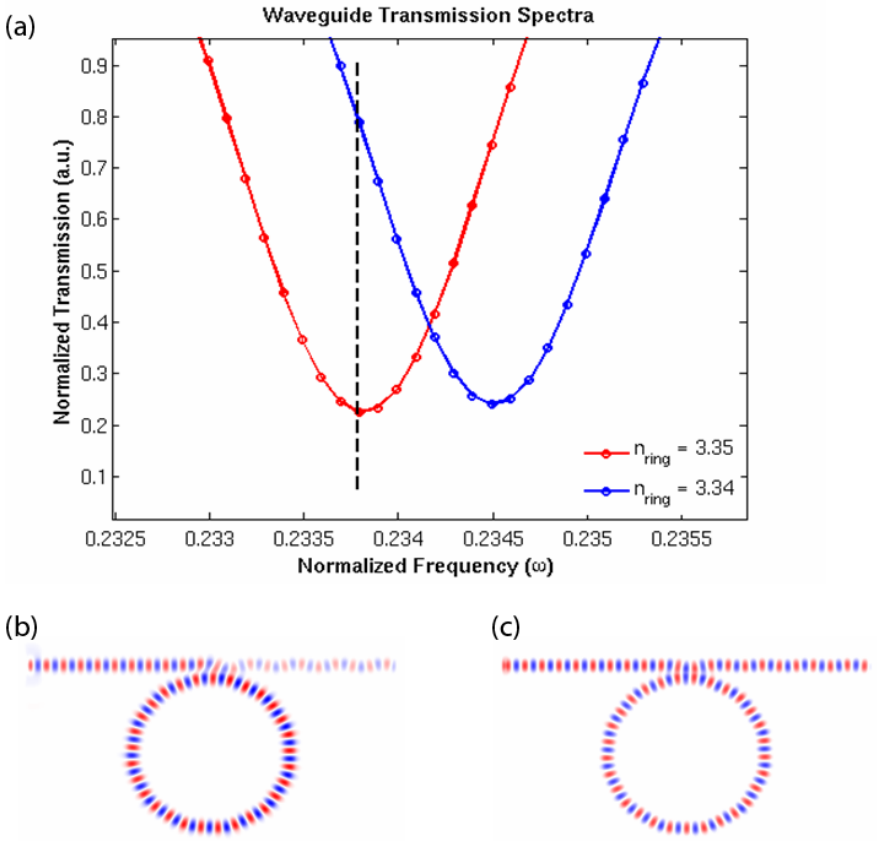

Figure 6.3 Simulated (a) normalized transmission spectra demonstrating detuning of the resonator from the probe wavelength (dashed line); (b) and (c) Electric field profiles at the probe wavelength corresponding to on and off resonance conditions respectively.

6.2.3 Experimental Details

The Si-VO_2 ring resonator structure described in figure 6.2 was fabricated on a silicon-on-insulator (SOI) substrate with 250nm thick Si or device layer and buried silicon dioxide layer of

1 μm thickness. The fabrication of the devices involved two steps of lithography as pictorially depicted in figure 6.4.

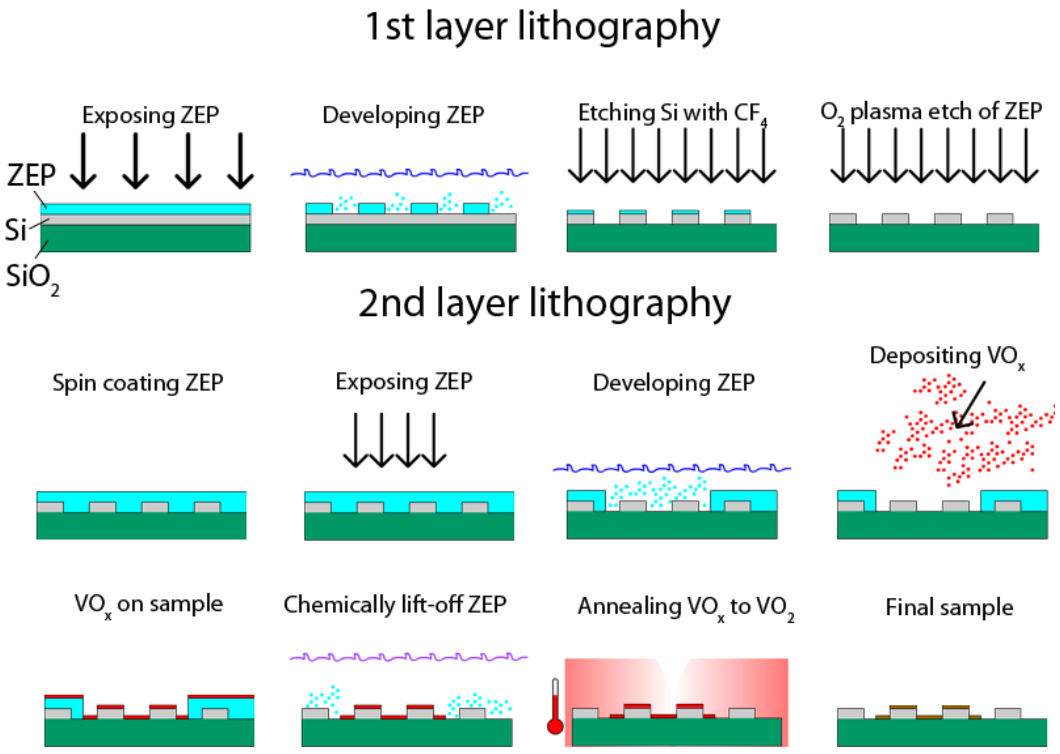

Figure 6.4: Schematic for the two-step lithography used to make the VO_2-covered ring resonators.

In the first step of lithography, we spin-coated 400nm of ZEP on our SOI wafer, and exposed it to the electron beam using the JEOL JBX-9300-100 kV electron beam lithography system with a special pattern to expose trenches surrounding our desired waveguides and rings. After developing and removing the exposed areas of ZEP, we performed a shallow reactive ion etch with a C_4F_8/SF_6/Ar mixture to etch the Si in the trenches, using the unexposed ZEP as our mask to protect our ring and waveguide. After etching off 250nm of Si, we removed the excess ZEP by oxygen plasma clean using the same RIE machine manufactured by Trion. This gave us our 250nm thick Si ring and waveguide devices on the buried oxide. Now to cover only the rings and not the waveguides with VO_2, a second layer of 400nm of ZEP was again spin coated and patterned with the Raith eLiNE electron beam lithography tool for squares on top of the rings. The same developing procedure as above is then followed by depositing VO_x using the pulsed laser deposition system. To deposit VO_x, a 99.99% pure vanadium metal target was ablated at

room-temperature in a background of 10mTorr of oxygen, following a standard recipe for pulsed laser deposition (PLD) in a high vacuum chamber (Epion PLD-3000) using a KrF excimer laser (Lambda Physik CompEx 201 laser, λ = 248nm, pulse repetition rate 25Hz, fluence ~2 J/cm^2). The target–to substrate distance was set at ~8 cm. This initial deposition produced an amorphous, oxygen-deficient film of $VO_{1.7}$ on the rings.

To keep VO_x from being affected by oxygen plasma, the ZEP in this step was chemically lifted-off using remover PG, acetone and deionized water. The deposited $VO_{1.7}$ was then annealed at a high temperature of 450^{o}C and 250 mTorr of oxygen for about 45 minutes to give stoichiometric, crystalline and switching VO_2. Control samples of plain thin films of VO_2 were simultaneously made to test the switching characteristics of the deposited VO_2 and a typical switching hysteresis was obtained as shown in figure 6.5.

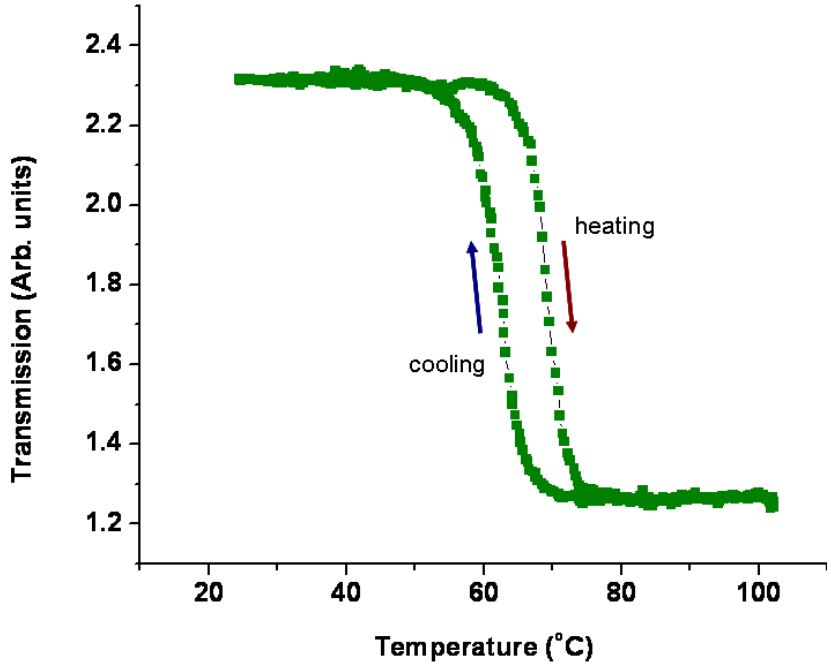

Figure 6.5: Hysteresis in transmission through a control sample of VO_2 demonstrating good quality of the deposited film.

Measurements were performed using an optical measurement system, as depicted in the schematic and the photograph in figure 6.6. Strip waveguides were made to bring the

input/output signal to the edges of the chip, which are cleaved before measurement. Cleaving through the waveguides provides a clean edge to minimize reflections. The sample was mounted on a brass carrier, which sits on a Y-Z stage for positioning. Tapered fibers carrying light in/out of the device are aligned on either side of the chip, mounted on XYZ stages with piezoelectric actuators for accurate positioning. A broadband LED source (Agilent 83437A) was used to provide an input spectrum ranging from 1200-1700 nm, suitable for the designed wavelength ranges of interest. The resulting transmission spectrum was measured by an optical spectrum analyzer (Agilent 86140B), in order to locate resonances in our patterned devices.

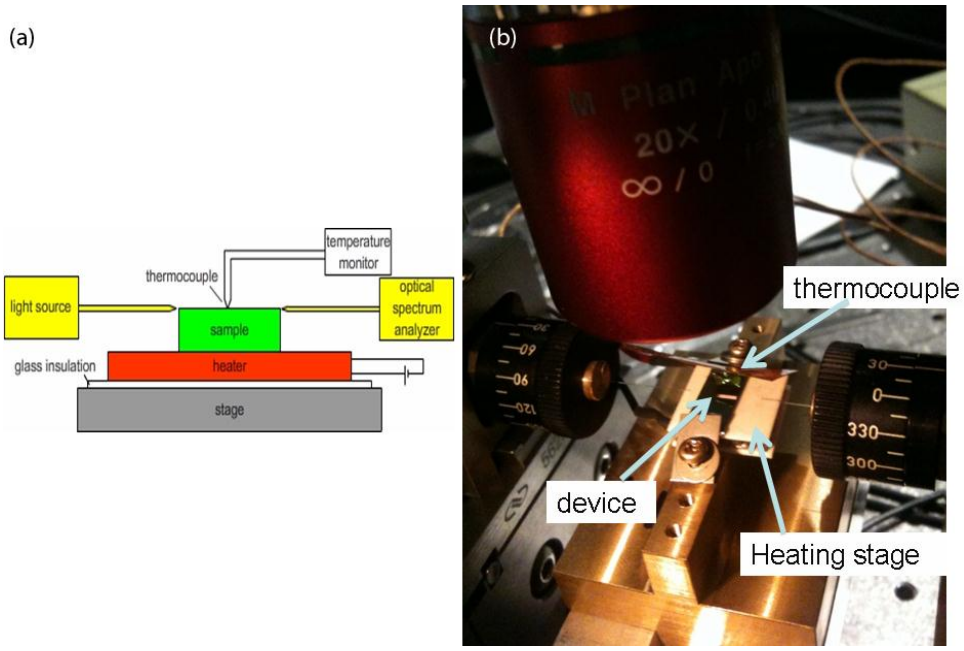

Figure 6.6 (a): Schematic of the optical set-up for observing the resonances; (b) Photograph of the actual set-up

6.2.4 Experimental Results and Discussions

Using the dual-layer e-beam lithography procedure described in the previous section, we made ring resonators with rings of 3 different inner diameters – 3 μm, 5 μm and 10 μm, each coupled to 5 mm long waveguides at a distance of ~ 125 nm. One of the prototypical devices with the smallest ring diameter is shown in figure 6.7. The resultant gap is smaller than the intended gap of 200 nm because the etching procedure did not provide the level of anisotropy expected, but it still allowed for coupling of evanescent waves between the waveguide and the ring. The

waveguides were 450 nm wide with nanotapers on both sides to 200 nm over the last 500 μm to facilitate better coupling to the input and output.

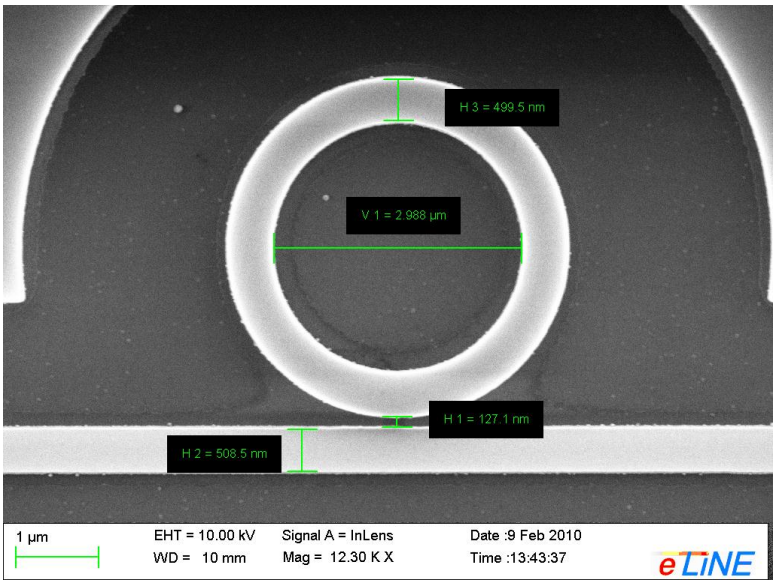

Figure 6.7: Scanning electron micrograph (SEM) of one of the fabricated devices with the smallest ring diameter of 3 μm, after the first step of lithography.

A second layer of squares was patterned on the rings and 60 nm of VO_2 was used to coat each of the rings and the final structure is as shown in figure 6.8 for three rings of three different sizes.

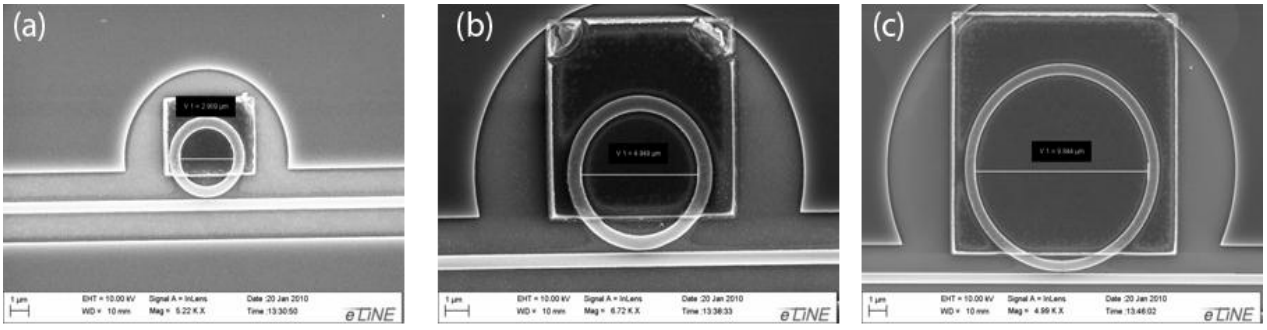

Figure 6.8: SEMs of the rings with three different inner diameters covered with VO_2.

In order to demonstrate proof-of-concept switching capabilities for the Si/VO_2 hybrid ring resonator, we measured the spectral characteristics at temperatures above and below the

switching point of VO_2. To accomplish this, the whole chip was heated using a thermoelectric Peltier element attached to the bottom of the chip as shown in the schematic and photograph in figure 6.7. Measurements were taken after the sample reached thermal equilibrium. Due to thermal fluctuations, maintaining good coupling was difficult at a high temperature (74^{o}C). This introduced additional noise and insertion losses into the measurement.

Figure 6.9 shows the optical transmission of the Si-VO_2 hybrid ring resonator at room temperature, for TE polarized light. The spectrum is characterized by resonances with a free-spectral range of ~52 nm, which is comparable to previous reports of Si resonators of similar dimensions[262]. Experimental Q-factors were found to be in the 10^2-10^3 range, which corresponds to cavity photon lifetimes $\tau_{cav} = \lambda^2 / (2\pi c \cdot \Delta\lambda)$ as low as 100 fs (which is ultimately required to enable THz optical switching in a resonant device). At room temperature, we monitored the most prominent resonance at wavelength ~1337 nm. After heating the sample to 74^{o}C to initiate the insulator-to-metal transition in VO_2, the resonance blue-shifted to ~1325 nm due to the reduced refractive index of the metallic VO_2 cladding layer: $\Delta\lambda = \lambda_0 \Delta n_{eff} / n_{eff}$. Notably however, this blue shift competes with the thermo-optic (TO) effect in silicon ($\Delta n/\Delta T \approx 1.86\times10^{-4}$ /°C)[263], which will red-shift resonances under a temperature increase[261]. The overall effective index change is represented by $\Delta n_{eff} = |\Delta n_{TO}| - |\Delta n_{VO_2}|$, where we know the effective index change from the VO_2 on the partially covered ring is larger than the opposing effective index change from the TO effect due to the blue-shift of the resonance.

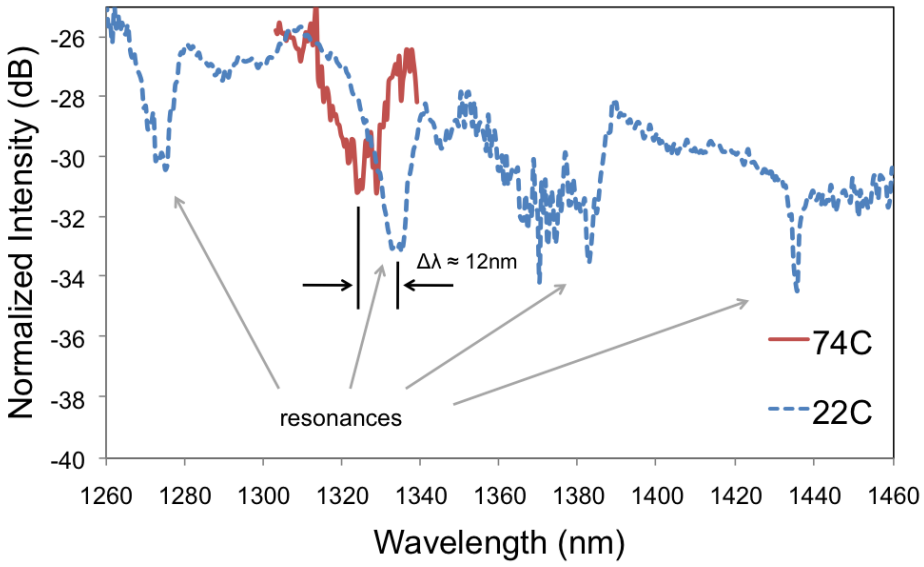

Figure 6.9: Resonances measured at room temperature using the 3 μm rings covered with VO_2, and the shift in 1337 nm resonance observed with VO_2 below and above transition temperature.

Optical or electrical initiation of the VO_2 insulator-to-metal transition could dramatically reduce the net temperature change and therefore minimize or eliminate the competing silicon thermo-optic effect altogether. The transition temperature and the shape of the hysteresis in VO_2 can also be altered by doping, as discussed in chapter 5. Such optimization strategies can be used to minimize the thermo-optic effect in silicon and maximize the modulation at resonance by reducing the transition temperature of VO_2 without degrading refractive-index contrast. Note here that optically inducing the phase transition in VO_2 will minimize the thermo-optic issue.

6.2.5 Simulations and Analysis

In order to estimate the change in n_{eff} due to solely to VO_2 modulation, we must consider both the fractional coverage of VO_2 on the ring as well as the competing thermo-optic effect in silicon. Thus, we employ the equation:

$$\Delta n_{eff} / n_{eff} = \left(\Delta n_{TO} + f_{VO2}\Delta n_{VO2}\right) / n_{eff} \tag{6.3}$$

where Δn_{TO} denotes change in effective index due solely to the thermo-optic effect, Δn_{VO2} denotes the change in effective index due to VO_2 modulation, and f_{VO2} represents the fractional coverage of VO_2 on the ring. A straightforward estimate of Δn_{TO} can be determined by

combining our 52°C increase in temperature and silicon's well-established thermo-optic response, $\Delta n/\Delta T \approx 1.86 \times 10^{-4}$ / °C [263], thus yielding a red-shifting thermo-optic contribution to the effective index $\Delta n_{TO} \approx 0.01$. A theoretical estimate for n_{eff} in the denominator of the right-hand side is determined by simulating our experimentally fabricated structure using the beam propagation method (RSoft BeamPROP). Note that for the simulation, we are limited to the assumption that VO_2 is only on the top of the ring and does not cover the sides or bottom, as is the case in the experiment. Considering 3.21 as the real component of the refractive indices of the VO_2 layer in the semiconducting state, we find the effective modal index to be 2.80, as shown in figure 2.8. Experimentally, we know $\Delta\lambda/\lambda = \Delta n_{eff}/n_{eff} = -0.009$, and thus can rearrange equation 6.3 to approximate the value of $\Delta n_{VO2} \approx -0.053$.

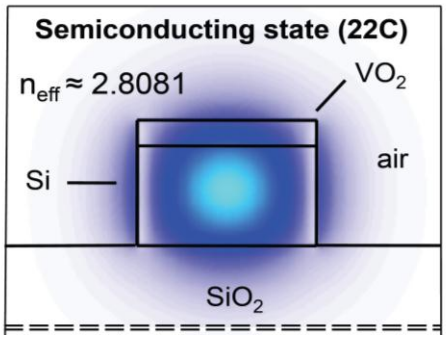

Figure 6.10: Electric field power distribution of the quasi-TE mode in the VO_2-cladded silicon ring at a wavelength ~1330nm for VO_2 in the semiconducting state.

For improved understanding and in order to demonstrate the tunability of our hybrid Si-VO_2 device with respect to varying VO_2 coverage, we calculate the expected variation in n_{eff} for thermal modulation of a VO_2 covered ring resonator, as shown in figure 6.12. In this calculation we assume $\Delta n_{VO2} \approx -0.053$ to illustrate the interplay between the thermo-optic effect and the fractional VO_2 coverage. Due to the competing contributions of Δn_{TO} (strictly positive) and f_{VO2} Δn_{VO2} (strictly negative) to the average effective index of the ring, there is a minimum fractional VO_2 coverage that is required to produce a net blue shift in the resonance position. For example, when performing thermal modulation from 25°C to 75°C, a net blue shift in the resonance position is only expected for fractional coverage greater than ~1/5. This 'cut-off coverage' is naturally influenced by the magnitude of the thermo-optic effect, or net temperature change ΔT, experienced during switching. In particular we note that it can be decreased if the required

temperature change is reduced, for example by doping the VO_2 so that it switches closer to room temperature.

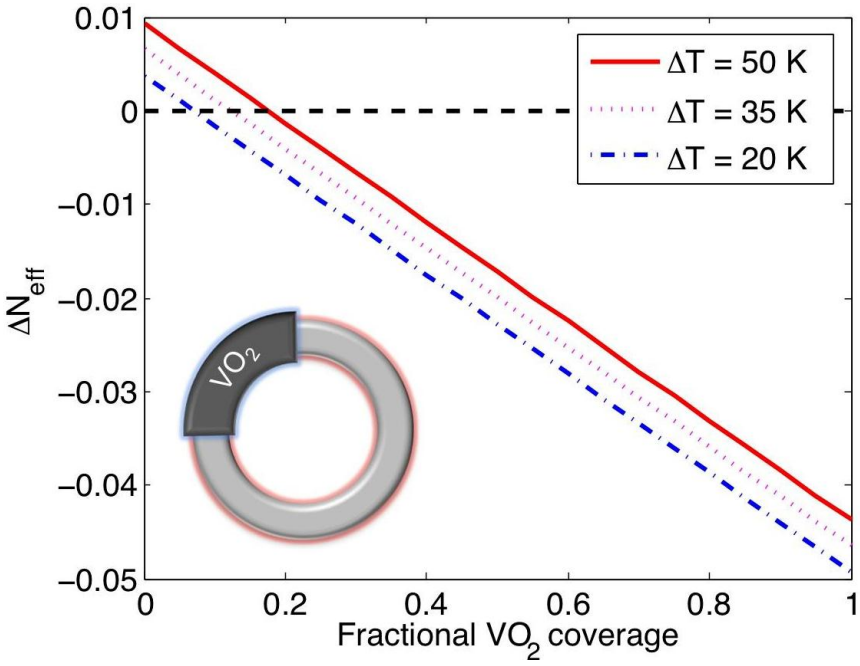

Figure 6.11: Expected change in the average effective modal index as a function of VO_2 coverage on a ring resonator.

CONCLUSION

The hybrid Si-VO_2 ring resonator design portends a new class of Si-based optical modulators that are substantially smaller than the state-of-the-art devices based on the electro-optic effect in Si. The resonant cavities in the hybrid structures have lower Q-factors, thus leading the way to more stable and faster devices. The flexibility of the Si-VO_2 device is further enhanced by the fact that the fractional VO_2-area coverage on the rings can be varied to induce wavelength shifts at different resonant frequencies. Moreover, coating the rings with W-doped VO_2 could reduce the thermal or electrical energy required to switch the VO_2 film, potentially reducing the power requirements even further for hybrid ring resonators based on W-doped VO_2. Finally, the smaller slope of the hysteretic response in doped VO_2 films compared to the abrupt phase change in undoped films can be accommodated in analog as well as digital designs.

Our ultimate goal is to demonstrate not only decreased size, but also enhanced speed of these Si-optical modulators by optically inducing the ultrafast phase transition in VO_2. Successful achievement of this next step would lead to a compact, low-power, ultrafast optical modulator well suited for chip-scale optoelectronic integration. The hybrid Si-VO_2 ring resonator thus has the potential to be a key building block for next-generation computers and communication networks. However, a key challenge will be to demonstrate that the required fluence for all-optical switching is sufficiently small that very fast recovery times can also be achieved.

CHAPTER VII

SUMMARY AND CONCLUSION

In this dissertation we began with a review of our present understanding about the physics of the phase transition in vanadium dioxide. The most prominent unresolved question about the mechanism of phase transition in VO_2 remains the perennial 'Mott *vs* Peierls' controversy. In attempting to answer these questions, it became increasingly clear that the issues of fabrication and characterization of epitaxial VO_2 on various substrates, and the effect of various deposition parameters on the growth of these films, would have to be addressed.

An important focus of the dissertation has therefore been to understand and develop pulsed-laser deposition processes that produce epitaxial VO_2 films on sapphire and titania. This led directly to an experiment in which the complex physics of the VO_2 phase transition was addressed by independently measuring the structural and electronic phase transitions as a function of temperature. These experiments showed that the hysteresis widths that are the defining signature of the transitions are different, implying that the insulator-to-metal and structural phase transitions are non-congruent. These results also suggest both conclusions and avenues for further investigation:

- Since the IMT develops before the SPT to the rutile phase is complete, these experiments may constitute further evidence for the existence of a strongly correlated metal phase that still has the tetragonal structure.
- Ultrafast experiments of our collaborators show that the laser-induced insulator-metal transition drives a coherent phonon associated with the SPT, indicating that the laser- and thermally-induced phase transitions are consistent.
- Given that the energy required to induce the IMT is less than that required to complete the SPT, is it possible to switch VO_2 on a femtosecond time scale without incurring the penalty of a long relaxation time to the initial state?

Doping has been used to engineer VO_2 thin films for applications ranging from thermal management films to sensors. Here we have demonstrated with ultrafast pump-probe

measurements that doping of epitaxial VO_2 films lowers the fluence requirement for switching. These experiments raise the following possibilities that remain to be investigated:

- The lowering of the threshold for the ultrafast laser induction of the phase transition by doping suggests that the next steps should be to measure the dependence of the threshold on dopant concentration.
- Is it possible that the lowering of the threshold for the IMT is sufficient to metallize the VO_2 in a transient so short that recovery time is also shortened to the picosecond regime?
- What are the effects of other dopants on the ultrafast dynamics (both on and off switching) of the phase transition, especially if these dopants (such as Cr) stabilize the M2 phase?

By systematically investigating the effect of various deposition parameters on dopant incorporation in both epitaxial and poly-crystalline films, this work has set the stage for these further explorations.

The last chapter of this dissertation was devoted to a novel application of VO_2 in an optical modulator, the ring resonator. In a proof-of-principle study, we showed that by thermal switching of the VO_2 cover layer of the hybrid silicon ring resonator, the size of the resonator and its photon cavity lifetime can be reduced to a level consistent with THz switching. This implies that hybrid Si:VO_2 ring resonators can go well beyond the current state-of-the-art in Si photonics. Fulfilling this potential will require all-optical, THz switching, of such devices in the telecommunications frequency range of around 1300 and 1550 nm, relying on the large dielectric contrast of VO_2 in that wavelength regime. Major challenges in meeting these goals include:

- Demonstrating optical switching by directly coupling pump light into the VO_2 component of the photonic structures by waveguide rather than free-space optics;
- Modifying the nanosecond switching-off time for VO2, to make it a truly ultrafast switching material, and the optical modulator a THz modulator. This might be done by doping VO_2 or by applying a bias to sweep away the extra charge carriers created to make it metallic.

- Showing that switching can be accomplished by lasers and at intensities that would typically be available in on-chip photon sources rather than by external lasers as at present; and
- Developing techniques for measuring the output of circuits operating at THz speeds.

Our demonstration of the application of VO_2 to the technologically critical Si optical modulator is definitely just the beginning of the exploration and extension of the potentials of this Si:VO_2 hybrid combination to the other important components essential to the realization of a complete set of optical interconnects like Mach-Zehnder interferometers (MZI) and nonlinear directional couplers (NLDC).

Two additional areas of investigation suggest themselves that apply to all of the questions raised here. The first is simulating the behavior of plasmonic and photonic devices that incorporate VO_2 in their structures. The second is related to is, and it is the experimental determination of the dielectric functions of undoped and doped VO_2 films, grown epitaxially or in polycrystalline form, in both semiconducting and metallic phases. The static dielectric functions will need to be measured ellipsometrically, while the dynamical changes in the dielectric function can be measured using ultrafast pump-probe ellipsometry. Meeting both of these challenges is a formidable task, but one that has been made easier by the results achieved in this dissertation.

REFERENCES

1. F. J. Morin, "Oxides which show a metal-to-insulator transition at the Néel temperature," Physical Review Letters **3**(1), 34-36 (1959).

2. J. B. Goodenough, "Two Components of Crystallographic Transition in VO_2," Journal of Solid State Chemistry **3**(4), 490-500 (1971).

3. D. Adler, "Mechanisms for Metal-Nonmetal Transitions in Transition-Metal Oxides and Sulfides," Reviews of Modern Physics **40**(4), 714-736 (1968).

4. D. Adler and H. Brooks, "Theory of Semiconductor-to-Metal Transitions," Physical Review **155**(3), 826-840 (1967).

5. D. Adler, J. Feinleib, H. Brooks, and W. Paul, "Semiconductor-to-Metal Transitions in Transition-Metal Compounds," Physical Review **155**(3), 851-860 (1967).

6. N. F. Mott, "Metal-insulator transition," Reviews of Modern Physics **40**(4), 677-683 (1968).

7. A. Liebsch, H. Ishida, and G. Bihlmayer, "Coulomb correlations and orbital polarization in the metal-insulator transition Of VO_2," Physical Review B **71**(8), 085109 (2005).

8. D. Paquet and P. Lerouxhugon, "Electron correlations and electron-lattice interactions in the metal-insulator, ferroelastic transition in VO_2 - a thermodynamical study," Physical Review B **22**(11), 5284-5301 (1980).

9. A. Pergament, "Metal-insulator transition: the Mott criterion and coherence length," Journal of Physics-Condensed Matter **15**(19), 3217-3223 (2003).

10. M. Gupta, A. J. Freeman, and D. E. Ellis, "Electronic-structure and lattice instability of metallic VO_2," Physical Review B **16**(8), 3338-3351 (1977).

11. J. P. Pouget, H. Launois, J. P. Dhaenens, P. Merenda, and T. M. Rice, "Electron localization induced by uniaxial stress in pure VO_2," Physical Review Letters **35**(13), 873-875 (1975).

12. J. P. Pouget, H. Launois, T. M. Rice, P. Dernier, A. Gossard, Villeneu.G, and Hagenmul.P, "Dimerization of a linear heisenberg chain in insulating phases of $V_{1-x}Cr_XO_2$," Physical Review B **10**(5), 1801-1815 (1974).

13. A. Zylbersztejn and N. F. Mott, "Metal-insulator transition in vanadium dioxide," Physical Review B **11**(11), 4383-4395 (1975).

14. C. Sommers and S. Doniach, "1ST principles calculation of intra-atomic correlation energy in VO_2," Solid State Communications **28**(1), 133-135 (1978).

15. T. M. Rice, H. Launois, and J. P. Pouget, "Comment on VO_2 - Peierls or Mott-Hubbard - A view from Band theory," Physical Review Letters **73**(22), 3042-3042 (1994).

16. A. Tselev, I. A. Luk'yanchuk, I. N. Ivanov, J. D. Budai, J. Z. Tischler, E. Strelcov, A. Kolmakov, and S. V. Kalinin, "Symmetry Relationship and Strain-Induced Transitions between Insulating M1 and M2 and Metallic R phases of Vanadium Dioxide," Nano Letters **10**(11), 4409-4416 (2010).

17. J. M. Booth and P. S. Casey, "Anisotropic Structure Deformation in the VO_2 Metal-Insulator Transition," Physical Review Letters **103**(8), 086402 (2009).

18. M. M. Qazilbash, M. Brehm, B. G. Chae, P. C. Ho, G. O. Andreev, B. J. Kim, S. J. Yun, A. V. Balatsky, M. B. Maple, F. Keilmann, H. T. Kim, and D. N. Basov, "Mott transition in VO_2 revealed by infrared spectroscopy and nano-imaging," Science **318**, 1750-1753 (2007).

19. B. J. Kim, Y. W. Lee, S. Choi, J. W. Lim, S. J. Yun, H. T. Kim, T. J. Shin, and H. S. Yun, "Micrometer x-ray diffraction study of VO_2 films: Separation between metal-insulator transition and structural phase transition," Physical Review B **77**(23), 235401(2008).

20. Macchesn.Jb and Guggenhe.Hj, "Growth and Electrical Properties of Vanadium Dioxide Single Crystals Containing Selected Impurity Ions," Journal of Physics and Chemistry of Solids **30**(2), 225-234 (1969).

21. H. Jerominek, F. Picard, and D. Vincent, "Vanadium oxide films for optical switching and detection," Optical Engineering **32**(9), 2092-2099 (1993).

22. G. V. Jorgenson and J. C. Lee, "Doped Vanadium Oxide for Optical Switching Fims," Solar Energy Materials **14**(3-5), 205-214 (1986).

23. S. Chen, X. Yi, H. Ma, H. Wang, X. Tao, M. Chen, and C. Ke, "A novel structural VO_2 micro-optical switch," Optical and Quantum Electronics **35**(15), 1351-1355 (2003).

24. S. H. Chen, H. Ma, X. J. Yi, T. Xiong, H. C. Wang, and C. J. Ke, "Smart VO_2 thin film for protection of sensitive infrared detectors from strong laser radiation," Sensors and Actuators a-Physical **115**(1), 28-31 (2004).

25. R. H. Walden, "Two Switching Devices Utilizing VO_2," IEEE Transactions on Electron Devices **ED17**(8), 603-612 (1970).

26. M. Soltani, M. Chaker, E. Haddad, R. Kruzelecky, and J. Margot, "Micro-optical switch device based on semiconductor-to-metallic phase transition characteristics of W-doped VO_2 smart coatings," Journal of Vacuum Science & Technology A **25**(4), 971-975 (2007).

27. M. Soltani, M. Chaker, E. Haddad, and R. V. Kruzelesky, "Thermochromic vanadium dioxide smart coatings grown on Kapton substrates by reactive pulsed laser deposition," Journal of Vacuum Science & Technology A **24**(3), 612-617 (2006).

28. M. A. Sobhan, R. Kivaisi, B. Stjerna, and C. G. Granqvist, "Thermochromism of sputter deposited $W_xV_{1-x}O_2$ films," Solar Energy Materials and Solar Cells **44**(4), 451-455 (1996).

29. T. D. Manning, I. P. Parkin, R. J. H. Clark, D. Sheel, M. E. Pemble, and D. Vernadou, "Intelligent window coatings: atmospheric pressure chemical vapour deposition of vanadium oxides," Journal of Materials Chemistry **12**(10), 2936-2939 (2002).

30. R. T. Kivaisi and M. Samiji, "Optical and electrical properties of vanadium dioxide films prepared under optimized RF sputtering conditions," Solar Energy Materials and Solar Cells **57**(2), 141-152 (1999).

31. B. J. Kim, Y. W. Lee, B. G. Chae, S. J. Yun, S. Y. Oh, H. T. Kim, and Y. S. Lim, "Temperature dependence of the first-order metal-insulator transition in VO2 and programmable critical temperature sensor," Applied Physics Letters **90**(2), 023515 (2007).

32. R. T. Rajendra Kumar, B. Karunagaran, D. Mangalaraj, S. K. Narayandass, P. Manoravi, M. Joseph, and V. Gopal, "Pulsed laser deposited vanadium oxide thin films for uncooled infrared detectors," Sensors and Actuators A: Physical **107**(1), 62-67 (2003).

33. W. A. Radford, D. F. Murphy, M. Ray, S. H. Propst, A. Kennedy, J. K. Kojiro, J. T. Woolaway Ii, K. L. Soch, R. Coda, G. Lung, E. A. Moody, D. Gleichman, and S. T. Baur, "320 x 240 silicon microbolometer uncooled IR FPAs with on-chip offset correction," presented at the Infrared Detectors and Focal Plane Arrays IV, Orlando, FL, USA, 1996.

34. Z. P. Wu, A. Miyashita, S. Yamamoto, I. Nashiyama, K. Narumi, and H. Naramoto, "Optical properties of vanadium dioxide thin film as a windows thermochromic coating," Materiales De Construccion **50**(258), 5-10 (2000).

35. W. R. Roach, "Holographic Storage in VO_2," Applied Physics Letters **19**(11), 453-455 (1971).

36. J. S. Chivian, M. W. Scott, W. E. Case, and N. J. Krasutsky, "An Improved Scan Laser with a VO_2 Programmable Mirror " IEEE Journal of Quantum Electronics **21**(4), 383-390 (1985).

37. D. Ruzmetov, G. Gopalakrishnan, C. H. Ko, V. Narayanamurti, and S. Ramanathan, "Three-terminal field effect devices utilizing thin film vanadium oxide as the channel layer," Journal of Applied Physics **107**(11), 114516 (2010).

38. S. X. Zhang, J. Y. Chou, and L. J. Lauhon, "Direct Correlation of Structural Domain Formation with the Metal Insulator Transition in a VO_2 Nanobeam," Nano Letters **9**(12), 4527-4532 (2009).

39. P. J. Hood and J. F. Denatale, "Millimeter-Wave Dielectric-Properties of Epitaxial Vanadium Dioxide Thin-Films," Journal of Applied Physics **70**(1), 376-381 (1991).

40. J. C. C. Fan, H. R. Fetterman, F. J. Bachner, P. M. Zavracky, and C. D. Parker, "Thin-Film VO_2 Submillimeter-wave Modulators and Polarizers " Applied Physics Letters **31**(1), 11-13 (1977).

41. M. Rini, A. Cavalleri, R. W. Schoenlein, R. Lopez, L. C. Feldman, R. F. Haglund, L. A. Boatner, and T. E. Haynes, "Photoinduced phase transition in VO_2 nanocrystals: ultrafast control of surface-plasmon resonance," Optics Letters **30**(5), 558-560 (2005).

42. P. Jin, M. Tazawa, and G. Xu, "Reversible tuning of surface plasmon resonance of silver nanoparticles using a thermochromic matrix," Journal of Applied Physics **99**(9), 096106 (2006).

43. R. S. Lakes, T. Lee, A. Bersie, and Y. C. Wang, "Extreme damping in composite materials with negative-stiffness inclusions," Nature **410**(6828), 565-567 (2001).

44. J. Cao, E. Ertekin, V. Srinivasan, W. Fan, S. Huang, H. Zheng, J. W. L. Yim, D. R. Khanal, D. F. Ogletree, J. C. Grossmanan, and J. Wu, "Strain engineering and one-dimensional organization of metal-insulator domains in single-crystal vanadium dioxide beams," Nature Nanotechnology **4**(11), 732-737 (2009).

45. E. Strelcov, Y. Lilach, and A. Kolmakov, "Gas Sensor Based on Metal-Insulator Transition in VO_2 Nanowire Thermistor," Nano Letters **9**(6), 2322-2326 (2009).

46. V. Eyert, "The metal-insulator transitions of VO_2: a band-theoretical approach," Ann. Phys. (Leipzig) **9**, 650-702 (2002).

47. R. M. Wentzcovitch, W. W. Schulz, and P. B. Allen, "VO_2 - Peierls or Mott-Hubbard - A view from Band Theory," Physical Review Letters **72**(21), 3389-3392 (1994).

48. G. Kotliar and D. Vollhardt, "Strongly correlated materials: Insights from dynamical mean-field theory," Physics Today **57**(3), 53-59 (2004).

49. S. Biermann, A. Poteryaev, A. I. Lichtenstein, and A. Georges, "Dynamical singlets and correlation-assisted Peierls transition in VO2," Physical Review Letters **94**(2), 026404 (2005).

50. B. Lazarovits, K. Kim, K. Haule, and G. Kotliar, "Effects of strain on the electronic structure of VO_2," Physical Review B **81**(11), 115117 (2010).

51. S. A. Corr, D. P. Shoemaker, B. C. Melot, and R. Seshadri, "Real-Space Investigation of Structural Changes at the Metal-Insulator Transition in VO_2," Physical Review Letters **105**(5), 056404 (2010).

52. K. Okimura, J. Sakai, and S. Ramanathan, "In situ x-ray diffraction studies on epitaxial VO_2 films grown on c-Al2O3 during thermally induced insulator-metal transition," Journal of Applied Physics **107**(6), 063503 (2010).

53. T. C. Koethe, Z. Hu, M. W. Haverkort, C. Schussler-Langeheine, F. Venturini, N. B. Brookes, O. Tjernberg, W. Reichelt, H. H. Hsieh, H. J. Lin, C. T. Chen, and L. H. Tjeng, "Transfer of spectral weight and symmetry across the metal-insulator transition in VO_2," Physical Review Letters **97**(11), 116402 (2006).

54. M. F. Becker, A. B. Buckman, R. M. Walser, T. Lepine, P. Georges, and A. Brun, "Femtosecond laser excitation dynamics of the semiconductor-metal phase transition in VO_2," Journal of Applied Physics **79**(5), 2404-2408 (1996).

55. M. F. Becker, A. B. Buckman, R. M. Walser, T. Lepine, P. Georges, and A. Brun, "Femtosecond Laser Excitationof the Semiconductor-Metal Phase Transition in VO_2," Applied Physics Letters **65**(12), 1507-1509 (1994).

56. A. Cavalleri, C. Toth, C. W. Siders, J. A. Squier, F. Raksi, P. Forget, and J. C. Kieffer, "Femtosecond structural dynamics in VO_2 during an ultrafast solid-solid phase transition," Physical Review Letters **87**(23), 237401 (2001).

57. C. Kübler, H. Ehrke, R. Huber, R. Lopez, A. Halabica, R. F. Haglund, and A. Leitenstorfer, "Coherent structural dynamics and electronic correlations during an ultrafast insulator-to-metal phase transition in VO_2," Physical Review Letters **99**(11), 116401 (2007).

58. A. Cavalleri, T. Dekorsy, H. H. W. Chong, J. C. Kieffer, and R. W. Schoenlein, "Evidence for a structurally-driven insulator-to-metal transition in VO_2: A view from the ultrafast timescale," Physical Review B **70**(16), 161102 (2004).

59. S. Lysenko, A. Rua, V. Vikhnin, F. Fernandez, and H. Liu, "Insulator-to-metal phase transition and recovery processes in VO_2 thin films after femtosecond laser excitation," Physical Review B **76**(3), 035104 (2007).

60. S. Lysenko, V. Vikhnin, F. Fernandez, A. Rua, and H. Liu, "Photoinduced insulator-to-metal phase transition in VO_2 crystalline films and model of dielectric susceptibility," Physical Review B **75**(7), 075109 (2007).

61. D. J. Hilton, R. P. Prasankumar, S. Fourmaux, A. Cavalleri, D. Brassard, M. A. El Khakani, J. C. Kieffer, A. J. Taylor, and R. D. Averitt, "Enhanced photosusceptibility near T_c for the light-induced insulator-to-metal phase transition in vanadium dioxide," Physical Review Letters **99**(22), 226401 (2007).

62. H. T. Kim, Y. W. Lee, B. J. Kim, B. G. Chae, S. J. Yun, K. Y. Kang, K. J. Han, K. J. Yee, and Y. S. Lim, "Monoclinic and correlated metal phase in VO_2 as evidence of the Mott transition: Coherent phonon analysis," Physical Review Letters **97**(26), 266401 (2006).

63. P. U. Jepsen, B. M. Fischer, A. Thoman, H. Helm, J. Y. Suh, R. Lopez, and R. F. Haglund, "Metal-insulator phase transition in a VO_2 thin film observed with terahertz spectroscopy," Physical Review B **74**(20), 205103 (2006).

64. J. Y. Suh, "Plasmonic Properties of Metal-VO_2 Nanostructures," Dissertation (Vanderbilt University, Nashville, 2007).

65. G. Stefanovich, A. Pergament, and D. Stefanovich, "Electrical switching and Mott transition in VO_2," Journal of Physics-Condensed Matter **12**(41), 8837-8845 (2000).

66. F. Chudnovskiy, S. Luryi, and B. Spivak, "Switching device based on first-order metal insulator transition induced by external electric field," in *Future Trends in Microelectronics: the Nano Millennium* (Wiley Interscience, 2002), pp. 148-155.

67. D. Ruzmetov, G. Gopalakrishnan, J. D. Deng, V. Narayanamurti, and S. Ramanathan, "Electrical triggering of metal-insulator transition in nanoscale vanadium oxide junctions," Journal of Applied Physics **106**(8), 083702 (2009).

68. B. G. Chae, H. T. Kim, D. H. Youn, and K. Y. Kang, "Abrupt metal-insulator transition observed in VO_2 thin films induced by a switching voltage pulse," Physica B-Condensed Matter **369**(1-4), 76-80 (2005).

69. B. J. Kim, Y. W. Lee, S. Choi, S. J. Yun, and H. T. Kim, "VO_2 Thin-Film Varistor Based on Metal-Insulator Transition," IEEE Electron Device Letters **31**(1), 14-16 (2010).

70. G. Gopalakrishnan, D. Ruzmetov, and S. Ramanathan, "On the triggering mechanism for the metal-insulator transition in thin film VO_2 devices: electric field versus thermal effects," Journal of Materials Science **44**(19), 5345-5353 (2009).

71. J. Kim, C. Ko, A. Frenzel, S. Ramanathan, and J. E. Hoffman, "Nanoscale imaging and control of resistance switching in VO_2 at room temperature," Applied Physics Letters **96**(21), 213106 (2010).

72. C. H. Chen, R. F. Wang, L. Shang, and C. F. Guo, "Gate-field-induced phase transitions in VO_2: Monoclinic metal phase separation and switchable infrared reflections," Applied Physics Letters **93**(17), 171101 (2008).

73. C. Ko and S. Ramanathan, "Stability of electrical switching properties in vanadium dioxide thin films under multiple thermal cycles across the phase transition boundary," Journal of Applied Physics **104**(8), 086105 (2008).

74. Z. Yang, C. H. Ko, V. Balakrishnan, G. Gopalakrishnan, and S. Ramanathan, "Dielectric and carrier transport properties of vanadium dioxide thin films across the phase transition utilizing gated capacitor devices," Physical Review B **82**(20), 205101 (2010).

75. M. Ghedira, H. Vincent, M. Marezio, and J. C. Launay, "Structural aspects of metal-insulator transitions in $V0._{985}AL_{0.015}O_2$," Journal of Solid State Chemistry **22**(4), 423-438 (1977).

76. M. Ghedira, J. Chenavas, and M. Marezio, "Cation disproportionation and pairing in insulating T-phase of $V_{0.985}AL_{0.015}O_2$," Journal of Physics C-Solid State Physics **10**(11), L309-L314 (1977).

77. M. Marezio, B. McWhan, P. D. Dernier, and J. P. Remeika, "Structural aspects of metal-insulator transitions in Cr-doped VO_2," Physical Review B **5**(7), 2541 (1972).

78. B. L. Chamberland, "New Defect Vanadium Dioxide Phases," Journal of Solid State Chemistry **7**, 377-384 (1973).

79. J. M. Reyes, J. R. Marko, and M. Sayer, "Hysteresis effects inthe semiconductor—metal transition of Cr-doped $V0_2$," Solid State Communications **13**, 1953-1957 (1973).

80. C. Marini, E. Arcangeletti, D. Di Castro, L. Baldassare, A. Perucchi, S. Lupi, L. Malavasi, L. Boeri, E. Pomjakushina, K. Conder, and P. Postorino, "Optical properties of V_{1-x}Cr_{x}O_{2} compounds under high pressure," Physical Review B **77**(23), 235111 (2008).

81. D. Paquet and P. Lerouxhugon, "Electron correlations and spin dimerization in the metal-insulator-transition in VO_2 - A thermodynamical study," Journal of Magnetism and Magnetic Materials **15-8**(JAN-), 999-1000 (1980).

82. J. P. Dhaenens, D. Kaplan, and P. Merenda, "Electron-spin resonance in $V_{1-X}Cr_XO_2$," Journal of Physics C-Solid State Physics **8**(14), 2267-2273 (1975).

83. J. P. Dhaenens, D. Kaplan, and Tuchendl.J, "Electron-spin resonance in chromium doped VO_2," Solid State Communications **15**(3), 635-638 (1974).

84. B. S. Guiton, Q. Gu, A. L. Prieto, M. S. Gudiksen, and H. Park, "Single-crystalline vanadium dioxide nanowires with rectangular cross sections," Journal of the American Chemical Society **127**(2), 498-499 (2005).

85. J. I. Sohn, H. J. Joo, D. Ahn, H. H. Lee, A. E. Porter, K. Kim, D. J. Kang, and M. E. Welland, "Surface-Stress-Induced Mott Transition and Nature of Associated Spatial Phase Transition in Single Crystalline VO_2 Nanowires," Nano Letters **9**(10), 3392-3397 (2009).

86. J. Wei, Z. H. Wang, W. Chen, and D. H. Cobden, "New aspects of the metal-insulator transition in single-domain vanadium dioxide nanobeams," Nature Nanotechnology **4**(7), 420-424 (2009).

87. A. C. Jones, S. Berweger, J. Wei, D. Cobden, and M. B. Raschke, "Nano-optical Investigations of the Metal-Insulator Phase Behavior of Individual VO_2 Microcrystals," Nano Letters **10**(5), 1574-1581 (2010).

88. J. Cao, Y. Gu, W. Fan, L. Q. Chen, D. F. Ogletree, K. Chen, N. Tamura, M. Kunz, C. Barrett, J. Seidel, and J. Wu, "Extended Mapping and Exploration of the Vanadium Dioxide Stress-Temperature Phase Diagram," Nano Letters **10**(7), 2667-2673 (2010).

89. Griffith.Ch and H. K. Eastwood, "Influence of Stoichiometry on Metal-Semiconductor Transition in Vanadium Dioxide," Journal of Applied Physics **45**(5), 2201-2206 (1974).

90. U. Schwingenschlogl and V. Eyert, "The vanadium Magneli phasesV(n)O(2n-1)," Annalen Der Physik **13**(9), 475-510 (2004).

91. R. Lopez-Noriega, "Metal Semiconductor Phase Transition in VO_2 Nanocrystals," Dissertation (Vanderbilt University, Nashville, 2002).

92. F. C. Case, "Influence of Ion-Beam Parameters on the Electrical and Optical- Properties of Ion-Assisted Reactively Evaporated Vanadium Dioxide Thin-Films," Journal of Vacuum Science & Technology a-Vacuum Surfaces and Films **5**(4), 1762-1766 (1987).

93. F. C. Case, "Improved VO_2 Thin-Films for Infrared Switching," Applied Optics **30**(28), 4119-4123 (1991).

94. G. Golan, A. Axelevitch, B. Sigalov, and B. Gorenstein, "Metal-insulator phase transition in vanadium oxides films," Microelectronics Journal **34**(4), 255-258 (2003).

95. G. Golan, A. Axelevitch, B. Sigalov, and B. Gorenstein, "Investigation of phase transition mechanism in vanadium oxide thin films," Journal of Optoelectronics and Advanced Materials **6**(1), 189-195 (2004).

96. M. Fukuma, S. Zembutsu, and S. Miyazawa, "Preparation of VO thin film and its direct optical bit recording characteristics," Applied Optics **22**(2), 265-268 (1982).

97. G. A. Nyberg and R. A. Buhrman, "Preparation and Optical Properties of Reactively Evaporated VO_2 Thin Films " Journal of Vacuum Science & Technology A-Vacuum Surfaces and Films **2**(2), 301-302 (1984).

98. R. Lopez, L. A. Boatner, T. E. Haynes, L. C. Feldman, and R. F. Haglund, "Synthesis and characterization of size-controlled vanadium dioxide nanocrystals in a fused silica matrix," Journal of Applied Physics **92**(7), 4031-4036 (2002).

99. L. A. Gea and L. A. Boatner, "Optical switching of coherent VO_2 precipitates formed in sapphire by ion implantation and annealing," Applied Physics Letters **68**(22), 3081-3083 (1996).

100. L. A. Gea, L. A. Boatner, H. M. Evans, and R. Zuhr, "Optically active surfaces formed by ion implantation and thermal treatment," Nuclear Instruments & Methods in Physics Research Section B- Beam Interactions with Materials and Atoms **127**, 553-556 (1997).

101. R. Lopez, L. A. Boatner, T. E. Haynes, R. F. Haglund, and L. C. Feldman, "Enhanced hysteresis in the semiconductor-to-metal phase transition of VO_2 precipitates formed in SiO_2 by ion implantation," Applied Physics Letters **79**(19), 3161-3163 (2001).

102. R. Lopez, T. E. Haynes, L. A. Boatner, L. C. Feldman, and R. F. Haglund, "Size effects in the structural phase transition of VO_2 nanoparticles," Physical Review B **65**(22), 224113 (2002).

103. R. Lopez, L. C. Feldman, and R. F. Haglund Jr, "Size-dependent optical properties of VO_2 nanoparticle arrays," Physical Review Letters **93**(17), 177403 (2004).

104. H. Takei and S. Koide, "Growth and Electrical Properties of Vanadium-Oxide Single Crystals by Oxychloride Decomposition Method " Journal of the Physical Society of Japan **21**(5), 1010 (1966).

105. S. Koide and H. Takei, "Epitaxial Growth of VO_2 Single Crystals and Their Anisotropic Properties in Electrical Resistivities " Journal of the Physical Society of Japan **22**(3), 946-947 (1967).

106. J. B. MacChesne, J. F. Potter, and H. J. Guggenheim, "Preparation and Properties of Vanadium Dioxide Films " Journal of the Electrochemical Society **115**(1), 52-55 (1968).

107. L. A. Ryabova, I. A. Serbinov, and A. S. Darevsky, "Preparation and Properties of Pyrolysis of Vanadium-Oxide Films " Journal of the Electrochemical Society **119**(4), 427-429 (1972).

108. C. B. Greenberg, "Undoped and Doped VO_2 Films Grown from $VO(OC_3H_7)_3$ " Thin Solid Films **110**(1), 73-82 (1983).

109. T. Maruyama and Y. Ikuta, "Vanadium Dioxide Thin Films Prepared by Chemical Vapor Deposition from Vanadium(III) Acetylacetonate " Journal of Materials Science **28**(18), 5073-5078 (1993).

110. T. D. Manning and I. P. Parkin, "Atmospheric pressure chemical vapour deposition of tungsten doped vanadium(IV) oxide from $VOCl_3$, water and WCl_6," Journal of Materials Chemistry **14**(16), 2554-2559 (2004).

111. T. D. Manning and I. P. Parkin, "Vanadium(IV) oxide thin films on glass and silicon from the atmospheric pressure chemical vapour deposition reaction of $VOCl_3$ and water," Polyhedron **23**(18), 3087-3095 (2004).

112. T. D. Manning, I. P. Parkin, C. Blackman, and U. Qureshi, "APCVD of thermochromic vanadium dioxide thin films - solid solutions $V_{2-x}M_xO_2$ (M = Mo, Nb) or composites VO_2 : SnO_2," Journal of Materials Chemistry **15**(42), 4560-4566 (2005).

113. H. Zhang, H. L. M. Chang, J. Guo, and T. J. Zhang, "Microstructure of Epitaxial VO_2 Thin Films Deposited on (11(2)over-bar) sapphire by MOCVD " Journal of Materials Research **9**(9), 2264-2271 (1994).

114. M. B. Sahana, M. S. Dharmaprakash, and S. A. Shivashankar, "Microstructure and properties of VO_2 thin films deposited by MOCVD from vanadyl acetylacetonate," Journal of Materials Chemistry **12**(2), 333-338 (2002).

115. M. B. Sahana, G. N. Subbanna, and S. A. Shivashankar, "Phase transformation and semiconductor-metal transition in thin films of VO_2 deposited by low-pressure metalorganic chemical vapor deposition," Journal of Applied Physics **92**(11), 6495-6504 (2002).

116. R. Binions, C. Piccirillo, and I. P. Parkin, "Tungsten doped vanadium dioxide thin films prepared by atmospheric pressure chemical vapour deposition from vanadyl acetylacetonate and tungsten hexachloride," Surface & Coatings Technology **201**(22-23), 9369-9372 (2007).

117. C. Piccirillo, R. Binions, and I. P. Parkin, "Nb-doped VO_2 thin films prepared by aerosol-assisted chemical vapour deposition," European Journal of Inorganic Chemistry (25), 4050-4055 (2007).

118. B. G. Chae, H. T. Kim, S. J. Yun, B. J. Kim, Y. W. Lee, D. H. Youn, and K. Y. Kang, "Highly oriented VO_2 thin films prepared by sol-gel deposition," Electrochemical and Solid State Letters **9**(1), C12-C14 (2006).

119. Y. Dachuan, X. Niankin, Z. Jingyu, and Z. Xiulin, "Vanadium dioxide films with good electrical switching property," J. Phys. D: Appl. Phys. **29**, 1051-1057 (1996).

120. J. Livage, "Sol-gel chemistry and electrochemical properties of vanadium oxide gels," Solid State Ionics **86-8**, 935-942 (1996).

121. J. Livage, "Optical and electrical properties of vanadium oxide films deposited from alkoxides," Boletin De La Sociedad Espanola De Ceramica Y Vidrio **37**(2-3), 87-92 (1998).

122. G. Guzman, F. Beteille, R. Morineau, and J. Livage, "Thermochromic $V_{1-x}Nb_xO_2$ Sol-Gel Thin Fims " European Journal of Solid State and Inorganic Chemistry **32**(7-8), 851-861 (1995).

123. G. Guzman, F. Beteille, R. Morineau, and J. Livage, "Electrical switching in VO_2 sol-gel films," Journal of Materials Chemistry **6**(3), 505-506 (1996).

124. G. Guzman, R. Morineau, and J. Livage, "Synthesis of Vanadium Dioxide Thin Films from Vanadium Alkoxides " Materials Research Bulletin **29**(5), 509-515 (1994).

125. J. Livage, G. Guzman, F. Beteille, and P. Davidson, "Optical properties of sol-gel derived vanadium oxide films," Journal of Sol-Gel Science and Technology **8**(1-3), 857-865 (1997).

126. F. Beteille and J. Livage, "Optical switching in VO_2 thin films," Journal of Sol-Gel Science and Technology **13**(1-3), 915-921 (1998).

127. F. Beteille, R. Morineau, J. Livage, and M. Nagano, "Switching properties of $V_{1-x}Ti_xO_2$ thin films deposited from alkoxides," Materials Research Bulletin **32**(8), 1109-1117 (1997).

128. D. P. Partlow, S. R. Gurkovich, K. C. Radford, and L. J. Denes, "Switchable Vanadium-Oxide Films by a Sol-Gel Process " Journal of Applied Physics **70**(1), 443-452 (1991).

129. H.-K. Chen, H.-C. Hung, T. C. K. Yang, and S.-F. Wang, "The preparation and characterization of transparent nano-sized thermochromic VO_2 - SiO_2 films from the sol-gel process," Journal of Non-Crystalline Solids **347**, 138-143 (2004).

130. S. W. Lu, L. S. Hou, and F. X. Gan, "Surface analysis and phase transition of gel-derived VO_2 thin films," Thin Solid Films **353**(1-2), 40-44 (1999).

131. B. G. Chae, H. T. Kim, S. J. Yun, B. J. Kim, Y. W. Lee, and K. Y. Kang, "Comparative analysis of VO_2 thin films prepared on sapphire and SiO_2/Si substrates by the sol-gel process," Japanese Journal of Applied Physics Part 1-Regular Papers Brief Communications & Review Papers **46**(2), 738-743 (2007).

132. J. A. Thornton, "Plasma-Assisted Deposition Processes - Theory, Mechanisms and Applications," Thin Solid Films **107**(1), 3-19 (1983).

133. E. N. Fuls, D. H. Hensler, and A. R. Ross, "Reactively Sputtered Vanadium Dioxide Thin Films " Applied Physics Letters **10**(7), 199-201 (1967).

134. J. E. Mahan, *Physical vapor deposition of thin films* (Wiley, New York ; Chichester, 2000).

135. K. Wasa, M. Kitabatake, and H. Adachi, *Thin Films Materials Technology* (William Andrew, Inc., New York, 2004).

136. G. A. Rozgonyi and D. H. Hensler, "Structural and Electrical Properties of Vanadium Dioxide Thin Films " Journal of Vacuum Science & Technology **5**(6), 194-199 (1968).

137. G. A. Rozgonyi and W. J. Polito, "Preparation of Thin Films of Vanadium (Di-, Sesqui- and Pent-) Oxide," Journal of the Electrochemical Society **115**(1), 56-&57 (1968).

138. J. Duchene, Terraill.M, and M. Pailly, "RF And DC Reactive sputtering for crystalline and amorphous VO_2 thin-film deposition," Thin Solid Films **12**(2), 231-& (1972).

139. E. E. Chain, "The Influence of Deposition Temperature on the Structure and Optical Properties of Vanadium-Oxide Films " Journal of Vacuum Science & Technology a-Vacuum Surfaces and Films **4**(3), 432-435 (1986).

140. E. E. Chain, "Effects of Oxygen in Ion-Beam Sputter Deposition of Vanadium Oxide " Journal of Vacuum Science & Technology a-Vacuum Surfaces and Films **5**(4), 1836-1839 (1987).

141. F. Guinneton, L. Sauques, J. C. Valmalette, F. Cros, and J. R. Gavarri, "Optimized infrared switching properties in thermochromic vanadium dioxide thin films: role of deposition process and microstructure," Thin Solid Films **446**(2), 287-295 (2004).

142. P. Jin, K. Yoshimura, and S. Tanemura, "Dependence of microstructure and thermochromism on substrate temperature for sputter-deposited VO_2 epitaxial films," Journal of Vacuum Science & Technology a-Vacuum Surfaces and Films **15**(3), 1113-1117 (1997).

143. P. Jin, M. Tazawa, M. Ikeyama, S. Tanemura, K. Macak, X. Wang, S. Olafsson, and U. Helmersson, "Growth and characterization of epitaxial films of tungsten-doped vanadium oxides on sapphire (110) by reactive magnetron sputtering," Journal of Vacuum Science & Technology a-Vacuum Surfaces and Films **17**(4), 1817-1821 (1999).

144. P. Jin and S. Tanemura, "Formation and Thermochromism of VO_2 Films Deposited by RF Magnetron Sputtering at Low Substrate Temperature " Japanese Journal of Applied Physics Part 1-Regular Papers Short Notes & Review Papers **33**(3A), 1478-1483 (1994).

145. A. Razavi, L. Bobyak, and P. Fallon, "The Effects of Biasing and Annealing on the Optical Properties of Radiofrequency Sputtered VO_2 " Journal of Vacuum Science & Technology a-Vacuum Surfaces and Films **8**(3), 1391-1394 (1990).

146. A. Razavi, T. Hughes, J. Antinovitch, and J. Hoffman, "Temperature Effects on Structure and Optical Properties of Radio-Frequency Sputtered VO_2 " Journal of Vacuum Science & Technology a-Vacuum Surfaces and Films **7**(3), 1310-1313 (1989).

147. S. D. Hansen and C. R. Aita, "Low-Temperature Reactive Sputter Deposition of Vanadium Oxide " Journal of Vacuum Science & Technology a-Vacuum Surfaces and Films **3**(3), 660-663 (1985).

148. T. Christmann, B. Felde, W. Niessner, D. Schalch, and A. Scharmann, "Thermochromic VO_2 thin films studied by photoelectron spectroscopy," Thin Solid Films **287**(1-2), 134-138 (1996).

149. J. Z. Cui, D. A. Da, and W. S. Jiang, "Structure characterization of vanadium oxide thin films prepared by magnetron sputtering methods," Applied Surface Science **133**(3), 225-229 (1998).

150. R. O. Dillon, K. Le, and N. Ianno, "Thermochromic VO_2 sputtered by control of a vanadium-oxygen emission ratio," Thin Solid Films **398**, 10-16 (2001).

151. N. R. Mlyuka and R. T. Kivaisi, "Correlation between optical, electrical and structural properties of vanadium dioxide thin films," Journal of Materials Science **41**(17), 5619-5624 (2006).

152. F. Guinneton, L. Sauques, J. C. Valmalette, F. Cros, and J. R. Gavarri, "Comparative study between nanocrystalline powder and thin film of vanadium dioxide VO_2: Electrical and infrared properties," Journal of Physics and Chemistry of Solids **62**(7), 1229-1238 (2001).

153. F. Guinneton, J.-C. Valmalette, and J.-R. Gavarri, "Nanocrystalline vanadium dioxide: synthesis and mid-infrared properties," Optical Materials **15**(2), 111-114 (2000).

154. K. Okimura and N. Kubo, "Preparation of VO_2 films with metal-insulator transition on sapphire and silicon substrates by inductively coupled plasma-assisted sputtering," Japanese Journal of Applied Physics Part 2-Letters & Express Letters **44**(33-36), L1150-L1153 (2005).

155. K. Okimura and N. Kubo, "Growth of VO_2 films with metal-insulator transition on silicon substrates in inductively coupled plasma-assisted sputtering," Thin Solid Films **515**(12), 4992-4995 (2007).

156. G. H. Fu, A. Polity, N. Volbers, and B. K. Meyer, "Annealing effects on VO_2 thin films deposited by reactive sputtering," Thin Solid Films **515**(4), 2519-2522 (2006).

157. H. J. Schlag and W. Scherber, "New sputter process for VO_2 thin films and examination with MIS-elements and C-V-measurements," Thin Solid Films **366**(1-2), 28-31 (2000).

158. M. Gurvitch, S. Luryi, A. Polyakov, A. Shabalov, M. Dudley, G. Wang, S. Ge, and V. Yakovlev, "VO_2 films with strong semiconductor to metal phase transition prepared by the precursor oxidation process," Journal of Applied Physics **102**(3), 13 (2007).

159. E. Lugscheider, O. Knotek, S. Barwulf, and K. Bobzin, "Characteristic curves of voltage and current, phase generation of tungsten and vanadium oxides deposited by reactive d.c.-MSIP-PVD-process for self-lubricating applications," Surface and Coatings Technology **142 -144**, 137-142 (2001).

160. D. B. Chrisey and G. K. Gubler, *Pulsed Laser Deposition of Thin Films* (John Wiley and Sons, New York, 1994).

161. R. Eason, ed., *Pulsed Laser Deposition of Thin Films: Applications-Led Growth of Functional Materials* (John Wiley and Sons: Wiley-Interscience, Hoboken, New Jersey, 2007).

162. M. Borek, F. Qian, V. Nagabushnam, and R. K. Singh, "Pulsed-Laser Deposition of Oriented VO_2 Thin Films on R-Cut Sapphire Substrates " Applied Physics Letters **63**(24), 3288-3290 (1993).

163. D. H. Kim and H. S. Kwok, "Pulsed Laser Deposition of VO_2 Thin Films " Applied Physics Letters **65**(25), 3188-3190 (1994).

164. M. Maaza, K. Bouziane, J. Maritz, D. S. McLachlan, R. Swanepool, J. M. Frigerio, and M. Every, "Direct production of thermochromic VO_2 thin film coatings by pulsed laser ablation," Optical Materials **15**(1), 41-45 (2000).

165. J. Y. Suh, R. Lopez, L. C. Feldman, and R. F. Haglund, "Semiconductor to metal phase transition in the nucleation and growth of VO_2 nanoparticles and thin films," Journal of Applied Physics **96**(2), 1209-1213 (2004).

166. S. A. Pauli, R. Herger, P. R. Willmott, E. U. Donev, J. Y. Suh, and R. F. Haglund, "X-ray diffraction studies of the growth of vanadium dioxide nanoparticles," Journal of Applied Physics **102**(7), 6 (2007).

167. B. G. Chae, D. H. Youn, H. T. Kim, S. L. Maeng, and K. Y. Kang, "Fabrication and electrical properties of Pure VO2 phase films," Journal of the Korean Physical Society **44**(4), 884-888 (2004).

168. M. Soltani, M. Chaker, E. Haddad, R. V. Kruzelecky, and D. Nikanpour, "Optical switching of vanadium dioxide thin films deposited by reactive pulsed laser deposition," Journal of Vacuum Science & Technology A **22**(3), 859-864 (2004).

169. J. Q. Wu, Q. Gu, B. S. Guiton, N. P. de Leon, O. Y. Lian, and H. Park, "Strain-induced self organization of metal-insulator domains in single-crystalline VO_2 nanobeams," Nano Letters **6**(10), 2313-2317 (2006).

170. J. H. Son, J. Wei, C. D., G. Cao, and Y. Xia, "Hydrothermal Synthesis of Monoclinic VO_2 Micro- and Nanocrystals in One Step and Their Use in Fabricating Inverse Opals," Chemistry of Materials **22**, 3043-3050 (2010).

171. J. M. Booth and P. S. Casey, "Production of VO_2 M-1 and M-2 Nanoparticles and Composites and the Influence of the Substrate on the Structural Phase Transition," ACS Applied Materials & Interfaces **1**(9), 1899-1905 (2009).

172. M. A. Herman, W. Richter, and H. Sitter, *Epitaxy*, Materials Science (Springer-Verlag, Berlin Heidelberg 2004).

173. L. Royer, Bull. Soc. Franc. Min. **51**, 7 (1928).

174. S. Smirnov, "Physical Modeling of Electron Transport in Strained Silicon and Silicon-Germanium," Dissertation (Technischen Universität Wien, Wien, 2003).

175. J. Narayan and V. M. Bhosle, "Phase transition and critical issues in structure-property correlations of vanadium oxide," Journal of Applied Physics **100**(10), 101063 (2006).

176. Z. P. Wu, S. Yamamoto, A. Miyashita, Z. J. Zhang, K. Narumi, and H. Naramoto, "Single-crystalline epitaxy and twinned structure of vanadium dioxide thin film on (0001) sapphire," Journal of Physics-Condensed Matter **10**(48), L765-L771 (1998).

177. G. Xu, P. Jin, M. Tazawa, and K. Yoshimura, "Thickness dependence of optical properties of VO_2 thin films epitaxially grown on sapphire (0001)," Applied Surface Science **244**(1-4), 449-452 (2005).

178. K. D. Rogers, J. A. Coath, and M. C. Lovell, "Characterization of epitaxially grown films of vanadium-oxides," Journal of Applied Physics **70**(3), 1412-1415 (1991).

179. G. Garry, O. Durand, and A. Lordereau, "Structural, electrical and optical properties of pulsed laser deposited VO2 thin films on R- and C-sapphire planes," Thin Solid Films **453-54**, 427-430 (2004).

180. Z. P. Wu, "Epitaxial growth and defect microstructures of vanadium dioxide thin films on sapphire substrates," in *Defects and Diffusion in Ceramics* (Scitec Publications Ltd, Uetikon-Zuerich, 2000), pp. 137-143.

181. Z. P. Wu and P. A. Fang, "Epitaxial growth and phase transition properties of vanadium dioxide thin film on sapphire substrate," Journal of Inorganic Materials **14**(5), 823-827 (1999).

182. Y. Muraoka and Z. Hiroi, "Metal-insulator transition of VO_2 thin films grown on TiO_2 (001) and (110) substrates," Applied Physics Letters **80**(4), 583-585 (2002).

183. K. Nagashima, T. Yanagida, H. Tanaka, and T. Kawai, "Influence of ambient atmosphere on metal-insulator transition of strained vanadium dioxide ultrathin films," Journal of Applied Physics **100**(6), 063714 (2006).

184. J. W. Lu, K. G. West, and S. A. Wolf, "Very large anisotropy in the dc conductivity of epitaxial VO_2 thin films grown on (011) rutile TiO_2 substrates," Applied Physics Letters **93**(26), 262107 (2008).

185. J. H. Claassen, J. W. Lu, K. G. West, and S. A. Wolf, "Relaxation dynamics of the metal-semiconductor transition in VO_2 thin films," Applied Physics Letters **96**(13), 132102 (2010).

186. T. H. Yang, R. Aggarwal, A. Gupta, H. H. Zhou, R. J. Narayan, and J. Narayan, "Semiconductor-metal transition characteristics of VO2 thin films grown on c- and r-sapphire substrates," Journal of Applied Physics **107**(5), 053514 (2010).

187. T. H. Yang, C. M. Jin, R. Aggarwal, R. J. Narayan, and J. Narayan, "On growth of epitaxial vanadium oxide thin film on sapphire (0001)," Journal of Materials Research **25**(3), 422-426 (2010).

188. A. Gupta, R. Aggarwal, P. Gupta, T. Dutta, R. J. Narayan, and J. Narayan, "Semiconductor to metal transition characteristics of VO2 thin films grown epitaxially on Si (001)," Applied Physics Letters **95**(11) 111915 (2009).

189. E. U. Donev, "Metal-semiconductor transitions in nanoscale vanadium dioxide - thin films, subwavelength holes, and nanoparticles," Dissertation (Vanderbilt University, Nashville, 2008).

190. V. Msomi, "Vanadium dioxide thermochromic thin films correlation between microstructure, electrical and optical properties," MS thesis (University of Zululand, 2008).

191. Y. Suzuki, M. Shinbara, H. Kii, and Y. Chikaura, "X-ray reciprocal space maps and x-ray scattering topographic observation of GaN layer on GaAs (001) in plasma-assisted molecular beam epitaxy," Journal of Applied Physics **101**(6), 063516 (2007).

192. W. R. Bowen and N. Hilal, "Atomic Force Microscopy in Process Engineering - An Introduction to AFM for Improved Processes and Products," (Elsevier, 2008).

193. "Transmission Electron Microscopy", retrieved March 09, 2011, http://en.wikipedia.org/wiki/Transmission_electron_microscopy.

194. D. B. Williams and C. B. Carter, *Transmission Electron Microscopy: A Textbook for Materials Science* (Springer, New York, 1996).

195. F. Rivera, " Solid phase crystallization of vanadium dioxide thin films and characterization through scanning electron microscopy," MS thesis (Brigham Young University, 2007).

196. R. P. Goehner and J. R. Michael, "Phase Identification in a Scanning Electron Microscope Using Backscattered Electron Kikuchi Patterns," Journal of Research of the National Institute of Standards and Technology **101**, 301-308 (1996).

197. V. A. Klimov, I. O. Timofeeva, S. D. Khanin, E. B. Shadrin, A. V. Ilinskii, and F. Silva-Andrade, "Hysteresis loop construction for the metal-semiconductor phase transition in vanadium dioxide films," Technical Physics **47**(9), 1134-1139 (2002).

198. J. Tersoff and F. K. Legoues, "Competing relaxation mechanisms in strained layers," Physical Review Letters **72**(22), 3570-3573 (1994).

199. E. Dagotto and Y. Tokura, "Strongly Correlated Electronic Materials: Present and Future," Mrs Bulletin **33**(11), 1037-1045 (2008).

200. G. A. Thomas, D. H. Rapkine, S. A. Carter, A. J. Millis, T. F. Rosenbaum, P. Metcalf, and J. M. Honig, "Observation of the Gap and Kinetic-Energy in a Correlated Insulator," Physical Review Letters **73**(11), 1529-1532 (1994).

201. D. B. McWhan, A. Jayaraman, J. P. Remeika, and T. M. Rice, "Metal-Insulator Transition in $(V_{1-x}Cr_x)_2O_3$," Physical Review Letters **34**(9), 547-550 (1975).

202. E. Dagotto, T. Hotta, and A. Moreo, "Colossal magnetoresistant materials: The key role of phase separation," Physics Reports-Review Section of Physics Letters **344**(1-3), 1-153 (2001).

203. P. Baum, D. S. Yang, and A. H. Zewail, "4D visualization of transitional structures in phase transformations by electron diffraction," Science **318**, 788-792 (2007).

204. Z. P. Wu, A. Miyashita, I. Nashiyama, and H. Naramoto, "Heterophase polydomain structure and metal-semiconductor phase transition in vanadium dioxide thin films deposited on (10(1)over-bar0) sapphire," Philosophical Magazine Letters **79**(10), 813-817 (1999).

205. D. A. G. Bruggeman, Ann. Phys. **24**, 636 (1935).

206. P. J. Hood and J. F. DeNatale, "Millimeter-wave dielectric properties of epitaxial vanadium dioxide thin films," Journal of Applied Physics **70**(1), 376-381 (1991).

207. J. Rozen, R. Lopez, R. F. Haglund, and L. C. Feldman, "Two-dimensional current percolation in nanocrystalline vanadium dioxide films," Applied Physics Letters **88**(8), 3 (2006).

208. J. C. Maxwell-Garnett, Philos. Trans. R. Soc. London **205**, 237 (1906).

209. H. W. Verleur, A. S. Barker, and C. N. Berglund, "Optical Properties of VO_2 between 0.25 and 5 Ev," Physical Review **172**(3), 788-798 (1968).

210. M. M. Qazilbash, A. A. Schafgans, K. S. Burch, S. J. Yun, B. G. Chae, B. J. Kim, H. T. Kim, and D. N. Basov, "Electrodynamics of the vanadium oxides VO_2 and V_2O_3," Physical Review B **77**(11), 115121 (2008).

211. E. Vlieg, "A (2+3)-type surface diffractometer: Mergence of the z-axis and (2+2)-type geometries," Journal of Applied Crystallography **31**, 198-203 (1998).

212. C. M. Schleputz, S. O. Mariager, S. A. Pauli, R. Feidenhans'l, and P. R. Willmott, "Angle calculations for a (2+3)-type diffractometer: focus on area detectors," Journal of Applied Crystallography **44**(1), 73-83 (2010).

213. M. Soltani, M. Chaker, E. Haddad, R. V. Kruzelecky, and J. Margot, "Effects of Ti-W codoping on the optical and electrical switching of vanadium dioxide thin films grown by a reactive pulsed laser deposition," Applied Physics Letters **85**(11), 1958-1960 (2004).

214. C. G. Granqvist, "Chromogenic materials for transmittance control of large-area windows," Critical Reviews in Solid State and Materials Sciences **16**(5), 291-308 (1990).

215. C. G. Granqvist, "Window coatings for the future," Thin Solid Films **193**(1-2), 730-741 (1990).

216. T. Horlin, Niklewsk.T, and M. Nygren, "Electrical and magnetic properties of $V_{1-X}W_XO_2$, O'= X '=0.060," Materials Research Bulletin **7**(12), 1515-1524 (1972).

217. T. Horlin, Niklewsk.T, and M. Nygren, "Magnetic, electrical and thermal studies on $V_{1-x}Mo_x0_2$ system with 0 less than or equal to x less than or equal to 0.20," Materials Research Bulletin **8**(2), 179-189 (1973).

218. T. Horlin, T. Niklewski, and M. Nygren, "Magnetic, electrical and thermal studies of $V_{1-x}tTi_xO_2$ (0less-than-or-equal-to x less-than-or-equal-to 0.06)," Acta Chemica Scandinavica Series a-Physical and Inorganic Chemistry **30**(8), 619-624 (1976).

219. Z. P. Wu, A. Miyashita, S. Yamamoto, H. Abe, I. Nashiyama, K. Narumi, and H. Naramoto, "Molybdenum substitutional doping and its effects on phase transition properties in single crystalline vanadium dioxide thin film," Journal of Applied Physics **86**(9), 5311-5313 (1999).

220. P. Jin, S. Nakao, and S. Tanemura, "Tungsten doping into vanadium dioxide thermochromic films by high-energy ion implantation and thermal annealing," Thin Solid Films **324**(1-2), 151-158 (1998).

221. P. Jin, M. Tazawa, K. Yoshimura, K. Igarashi, S. Tanemura, K. Macak, and U. Helmersson, "Epitaxial growth of W-doped VO2/V2O3 multilayer on alpha-Al2O3(110) by reactive magnetron sputtering," Thin Solid Films **375**(1-2), 128-131 (2000).

222. P. Jin and S. Tanemura, "$V_{1-x}Mo_xO_2$ thermochromic films deposited by reactive magnetron sputtering," Thin Solid Films **282**(1-2), 239-242 (1996).

223. R. Binions, G. Hyett, C. Piccirillo, and I. P. Parkin, "Doped and un-doped vanadium dioxide thin films prepared by atmospheric pressure chemical vapour deposition from vanadyl acetylacetonate and tungsten hexachloride: the effects of thickness and crystallographic orientation on thermochromic properties," Journal of Materials Chemistry **17**(44), 4652-4660 (2007).

224. E. Cavanna, J. P. Segaud, and J. Livage, "Optical switching of Au-doped VO_2 sol-gel films," Materials Research Bulletin **34**(2), 167-177 (1999).

225. F. Beteille, R. Morineau, J. Livage, and M. Nagano, "Switching properties of $V_{1-x}Ti_xO_2$ thin films deposited from alkoxides," Materials Research Bulletin **32**(8), 1109-1117 (1997).

226. W. Burkhardt, T. Christmann, B. K. Meyer, W. Niessner, D. Schalch, and A. Scharmann, "W- and F-doped VO2 films studied by photoelectron spectrometry," Thin Solid Films **345**(2), 229-235 (1999).

227. W. Burkhardt, T. Christmann, S. Franke, W. Kriegseis, D. Meister, B. K. Meyer, W. Niessner, D. Schalch, and A. Scharmann, "Tungsten and fluorine co-doping of VO_2 films," Thin Solid Films **402**(1-2), 226-231 (2002).

228. I. Takahashi, M. Hibino, and T. Kudo, "Thermochromic properties of double-doped VO_2 thin films prepared by a wet coating method using polyvanadate-based sols containing W and Mo or W and Ti," Japanese Journal of Applied Physics Part 1-Regular Papers Short Notes & Review Papers **40**(3A), 1391-1395 (2001).

229. W. Kohn and L. J. Sham, "Self-consistent equations including exchange and correlation effects," Physical Review **140**(4A), 1133 (1965).

230. J. P. Perdew, K. Burke, and M. Ernzerhof, "Generalized gradient approximation made simple," Physical Review Letters **77**(18), 3865-3868 (1996).

231. V. I. Anisimov, J. Zaanen, and O. K. Andersen, "Band theory and Mott insulators - Hubbard-U instead of Stoner-I," Physical Review B **44**(3), 943-954 (1991).

232. P. E. Blochl, "Projector augmented-wave method," Physical Review B **50**(24), 17953-17979 (1994).

233. G. Kresse and J. Furthmuller, "Efficient iterative schemes for ab initio total-energy calculations using a plane-wave basis set," Physical Review B **54**(16), 11169-11186 (1996).

234. G. Kresse and D. Joubert, "From ultrasoft pseudopotentials to the projector augmented-wave method," Physical Review B **59**(3), 1758-1775 (1999).

235. M. Netsianda, P. E. Ngoepe, C. Richard, A. Catlow, and S. M. Woodley, "The displacive phase transition of vanadium dioxide and the effect of doping with tungsten," Chemistry of Materials **20**(5), 1764-1772 (2008).

236. J. C. Rakotoniaina, R. Mokranitamellin, J. R. Gavarri, G. Vacquier, A. Casalot, and G. Calvarin, "The thermochromic vanadium dioxide .1. Role of stresses and substitution on switching properties," Journal of Solid State Chemistry **103**(1), 81-94 (1993).

237. D. A. B. Miller, "Device Requirements for Optical Interconnects to Silicon Chips," Proceedings of the IEEE **97**(7), 1166-1185 (2009).

238. G. T. Reed, G. Mashanovich, F. Y. Gardes, and D. J. Thomson, "Silicon optical modulators," Nature Photonics **4**(8), 518-526 (2010).

239. C. Pollock and M. Lipson, *Integrated Photonics* (Kluwer Academic Publishers, 2003).

240. R. A. Soref and B. R. Bennett, "Electrooptical effects in Silicon," IEEE Journal of Quantum Electronics **23**(1), 123-129 (1987).

241. G. T. Reed and A. P. Knights, *Silicon Photonics: An Introduction* (Wiley, 2004).

242. G. Cocorullo and I. Rendina, "Thermooptic modulation at 1.5 mu-m in silicon etalon," Electronics Letters **28**(1), 83-85 (1992).

243. G. T. Reed, *Silicon Photonics: The State of the Art* (Wiley, 2008).

244. R. A. Soref, "SILICON-BASED OPTOELECTRONICS," Proceedings of the IEEE **81**(12), 1687-1706 (1993).

245. R. Soref, "The past, present, and future of silicon photonics," IEEE Journal Of Selected Topics In Quantum Electronics **12**(6), 1678-1687 (2006).

246. R. Jones, A. S. Liu, H. S. Rong, M. Paniccia, O. Cohen, and D. Hak, "Lossless optical modulation in a silicon waveguide using stimulated Raman scattering," Optics Express **13**(5), 1716-1723 (2005).

247. T. Baehr-Jones, M. Hochberg, G. X. Wang, R. Lawson, Y. Liao, P. A. Sullivan, L. Dalton, A. K. Y. Jen, and A. Scherer, "Optical modulation and detection in slotted Silicon waveguides," Optics Express **13**(14), 5216-5226 (2005).

248. O. Boyraz and B. Jalali, "Demonstration of a silicon Raman laser," Optics Express **12**(21), 5269-5273 (2004).

249. Y. H. Kuo, Y. K. Lee, Y. S. Ge, S. Ren, J. E. Roth, T. I. Kamins, D. A. B. Miller, and J. S. Harris, "Strong quantum-confined Stark effect in germanium quantum-well structures on silicon," Nature **437**(7063), 1334-1336 (2005).

250. J. E. Roth, O. Fidaner, R. K. Schaevitz, Y. H. Kuo, T. I. Kamins, J. S. Harris, and D. A. B. Miller, "Optical modulator on silicon employing germanium quantum wells," Optics Express **15**(9), 5851-5859 (2007).

251. Y. W. Rong, Y. S. Ge, Y. J. Huo, M. Fiorentino, M. R. T. Tan, T. I. Kamins, T. J. Ochalski, G. Huyet, and J. S. Harris, "Quantum-Confined Stark Effect in Ge/SiGe Quantum Wells on Si," IEEE Journal Of Selected Topics In Quantum Electronics **16**(1), 85-92 (2010).

252. R. S. Jacobsen, K. N. Andersen, P. I. Borel, J. Fage-Pedersen, L. H. Frandsen, O. Hansen, M. Kristensen, A. V. Lavrinenko, G. Moulin, H. Ou, C. Peucheret, B. Zsigri, and A. Bjarklev, "Strained silicon as a new electro-optic material," Nature **441**(7090), 199-202 (2006).

253. H. W. Chen, Y. H. Kuo, and J. E. Bowers, "25Gb/s hybrid silicon switch using a capacitively loaded traveling wave electrode," Optics Express **18**(2), 1070-1075 (2010).

254. L. Liu, J. Van Campenhout, G. Roelkens, R. A. Soref, D. Van Thourhout, P. Rojo-Romeo, P. Regreny, C. Seassal, J. M. Fedeli, and R. Baets, "Carrier-injection-based electro-optic modulator on silicon-on-insulator with a heterogeneously integrated III-V microdisk cavity," Optics Letters **33**(21), 2518-2520 (2008).

255. Q. F. Xu, B. Schmidt, S. Pradhan, and M. Lipson, "Micrometre-scale silicon electro-optic modulator," Nature **435**(7040), 325-327 (2005).

256. A. S. Liu, R. Jones, L. Liao, D. Samara-Rubio, D. Rubin, O. Cohen, R. Nicolaescu, and M. Paniccia, "A high-speed silicon optical modulator based on a metal-oxide-semiconductor capacitor," Nature **427**(6975), 615-618 (2004).

257. A. S. Liu, L. Liao, D. Rubin, H. Nguyen, B. Ciftcioglu, Y. Chetrit, N. Izhaky, and M. Paniccia, "High-speed optical modulation based on carrier depletion in a silicon waveguide," Optics Express **15**(2), 660-668 (2007).

258. C. Gunn, "CMOS photonics for high-speed interconnects," IEEE Micro **26**(2), 58-66 (2006).

259. M. Hochberg, T. Baehr-Jones, G. X. Wang, M. Shearn, K. Harvard, J. D. Luo, B. Q. Chen, Z. W. Shi, R. Lawson, P. Sullivan, A. K. Y. Jen, L. Dalton, and A. Scherer, "Terahertz all-optical modulation in a silicon-polymer hybrid system," Nature Materials **5**(9), 703-709 (2006).

260. R. M. Briggs, I. M. Pryce, and H. A. Atwater, "Compact silicon photonic waveguide modulator based on the vanadium dioxide metal-insulator phase transition," Optics Express **18**(11), 11192-11201 (2010).

261. M. Lipson, "Compact electro-optic modulator's on a silicon chip," IEEE Journal Of Selected Topics In Quantum Electronics **12**(6), 1520-1526 (2006).

262. M. S. Nawrocka, T. Liu, X. Wang, and R. R. Panepucci, "Tunable silicon microring resonator with wide free spectral range," Applied Physics Letters **89**(7), 071110 (2006).

263. G. Cocorullo, F. G. Della Corte, I. Rendina, and P. M. Sarro, "Thermo-optic effect exploitation in silicon microstructures," Sensors and Actuators a-Physical **71**(1-2), 19-26 (1998).